Imaging Dynamic Pore-Formation Processes in Droplet-Interface Bilayers

Jason Thomas Sengel

Keble College
University of Oxford



A thesis submitted for the degree of
Doctor of Philosophy

Trinity Term 2017

Declaration

The work described in this thesis was carried out between 2012 and 2016 in the laboratory of Professor Mark Wallace in the Chemistry Research Laboratory at the University of Oxford. All the work described within this thesis is entirely my own, unless expressly attributed to my co-workers. This work has not been submitted previously for any other degree at the University of Oxford or any other institution. Publications stemming from this work are detailed in Appendix A.

Jason Thomas Sengel
August 2017

Acknowledgements

Some time ago I missed an opportunity to thank those around me who had given their guidance, passed on their knowledge, offered their support and freely gave their time to me when working on a small research project. Since the opportunity has come around again, I certainly shall not miss it this time.

It is customary to thank one's supervisor first. It is customary, but it is also right. Prof. Mark Wallace has seen me through a good many years in his lab, a period of enjoyment and stimulation that is in large part due to him. I thank him for his direction, but also freedom for me to explore my ideas — and for never failing to impart to our conversations an excitement for what the next result might hold.

Thanks go to those former lab members who got me on my feet when I started in the lab, especially Drs. Ollie Castell and Bríd Cronin, and Charlotte Dodson. Thanks also to those members of the Wallace Group who have made these years fun, and who have become good friends. Special thanks go to Dr. Eve Weatherill, who keeps my head screwed on. I couldn't do without her. Finally, thanks to my family. They have in part put me where I am today. What's more, they have listened to me bore them about electropores for a very long time.

Abstract

Observing dynamic pore-forming processes in lipid bilayers is a challenging task. It requires a bilayer system that is stable, compositionally adjustable, and one that may be interrogated using electrical and optical techniques. Aside from these practical challenges, and that pore formation is inherently destructive to the bilayer system, membrane pores are often highly transient, with milli- or microsecond lifetimes, and are seldom larger than a few tens of nanometres in diameter.

This work presents droplet-interface bilayers (DIBs) as a platform for overcoming some of these challenges. The technique is in particular applied to the study of electroporation, a well-known and widely used but less comprehensively understood phenomenon in which transmembrane pores are generated under the influence of an applied electric field. DIBs are shown to be a useful system for the study of the formation, development, energetics and dynamics of electropores. Through simultaneous electrophysiological recording and calcium-flux imaging, the real-time behaviour of individual electropores within an ensemble of transmembrane defects is observed for the first time. This reveals information about the pore dynamics, their diffusion in the membrane, and their gating kinetics. Analysis of these kinetics further allows the determination of the energy barriers to pore formation. This is the first such imaging study to be carried out on electroporation, granting access to electropore behaviour that previously no imaging methodologies have accessed.

In turn, this paves the way for imaging studies of more complex pore-forming processes, such as those mediated by pore-forming peptides and proteins. Work on these systems shall be presented towards the end of this thesis, in particular, an investigation into the interactions of four typical antimicrobial peptides (AMPs) with DIBs, which serves to expand the toolkit for membrane-active peptide studies. In this work, for the first time, the location of dynamic membrane pores is correlated with the position of the pore-forming peptides by combining calcium-flux and single-molecule imaging, revealing real-time information about peptide-mediated pores that is difficult to access through alternative bilayer membrane methods.

Contents

List of Figures **xiii**

List of Abbreviations **xv**

List of Symbols **xvii**

1 Introduction **1**
1.1 Opening Remarks . . . 1
1.1.1 The Importance of Poration Processes . . . 2
1.2 The Cell Membrane . . . 5
1.2.1 Lipids . . . 9
1.3 Artificial Membrane Mimics . . . 12
1.3.1 BLMs, SLBs and GUVs . . . 12
1.3.2 DIBs . . . 14
1.3.3 Molecular Dynamics Simulations . . . 16
1.4 Electroporation . . . 17
1.4.1 A Brief History of Electroporation . . . 17
1.4.2 Early Observations . . . 19
1.4.3 Electroporation Models . . . 20
1.4.4 Applications & Protocols . . . 24
1.4.5 Current Outlook . . . 26
1.5 Bilayer Interrogation Techniques . . . 28
1.5.1 Electrophysiology . . . 28
1.5.2 Total Internal Reflection Fluorescence Microscopy . . . 31

2 Electroporation in DIBs: Electrical Characterisation **37**
2.1 Introduction . . . 37
2.2 Theory of Electroporation . . . 38
2.2.1 Formation of Transient Aqueous Pores . . . 38
2.2.2 The Role of the Electric Field . . . 43
2.2.3 The Stages of Pore Formation in MD Simulations . . . 45
2.3 Materials & Methods . . . 48
2.3.1 Materials . . . 48

2.3.2 Conductivity Measurements 48
2.3.3 Lipid Stock Solutions 49
2.3.4 Agarose Solutions 49
2.3.5 Ag/AgCl Electrodes 49
2.3.6 Device Preparation 50
2.3.7 Experimental Setup 52
2.3.8 Monolayer Formation 54
2.3.9 Bilayer Formation 54
2.3.10 Electrical Recording & Data Analysis 56
2.4 Results & Discussion 57
2.4.1 Ensemble Response 58
2.4.2 I–V Characteristics 63
2.4.3 Specific Behaviours 68
2.4.4 Physiological Electrolyte Solutions 70
2.4.5 Influence of the Protocol 77
2.5 Summary & Limitations 78

3 Electroporation in DIBs: Optical Characterisation 81
3.1 Introduction 81
3.1.1 Previous Imaging Studies 82
3.1.2 Optical Single-Channel Recording 83
3.2 Materials & Methods 84
3.2.1 Materials 84
3.2.2 Conductivity Measurements 84
3.2.3 Fluo-8H Solutions 85
3.2.4 Device Preparation 85
3.2.5 Simultaneous Imaging & Electrical Recording 86
3.2.6 Phase-Separated Bilayers 87
3.2.7 Bilayers at Elevated Temperatures 88
3.2.8 Image Processing 89
3.2.9 Data Analysis 91
3.3 Results & Discussion 91
3.3.1 Effect of Calcium 91
3.3.2 Optical Detection of Electropores 94
3.3.3 Correlating Electrical & Optical Measurements 95
3.3.4 Individual Pore Behaviours 97
3.3.5 Electropore Diffusion 98
3.3.6 Electropores in Phase-Separated Bilayers 106
3.3.7 Pore-Pore Interactions 108

3.3.8 Bilayer Rupture . . . 110
3.4 Summary . . . 112
3.4.1 Sensitivity & Limitations . . . 114

4 Electroporation in DIBs: Investigating the Energy Landscape 117
4.1 Introduction . . . 117
4.2 Materials & Methods . . . 118
4.2.1 Gaussian Fitting of SCCaFTs . . . 118
4.2.2 Counting Electropore Lifetimes . . . 118
4.2.3 Controlling Bilayer Temperature . . . 118
4.2.4 Imaging Super-Hydrated Bilayers . . . 119
4.3 Results & Discussion . . . 119
4.3.1 The Distribution of Pore Sizes . . . 119
4.3.2 Gating Kinetics . . . 124
4.3.3 Temperature Dependence of Electroporation . . . 128
4.4 Influence of the Agarose Substrate . . . 132
4.5 Summary & Limitations . . . 134

5 The Interaction of Antimicrobial Peptides with DIBs 137
5.1 Introduction . . . 137
5.1.1 Antimicrobial Peptides . . . 137
5.1.2 AMP-Bilayer Interactions . . . 139
5.1.3 Pore-Forming AMPs . . . 140
5.1.4 oSCR of AMP-Mediated Pores . . . 141
5.1.5 Contributions to This Work . . . 148
5.2 Materials & Methods . . . 148
5.2.1 Materials . . . 148
5.2.2 Bilayer formation . . . 149
5.2.3 Imaging Setup . . . 149
5.2.4 Radial Distribution Function Analysis . . . 151
5.3 Results & Discussion . . . 151
5.3.1 Electrical Behaviour of AMPs in DIBs . . . 151
5.3.2 oSCR Imaging of AMP Pores . . . 158
5.3.3 Single-Molecule and oSCR Imaging . . . 159
5.4 Summary & Limitations . . . 167

6 Conclusions & Further Work 169
6.1 Electroporation in DIBs . . . 169
6.1.1 The Electroporation Model . . . 169
6.1.2 Electroporation in Biological Membranes . . . 171
6.2 AMP Interactions with DIBs . . . 173
6.3 Closing Remarks . . . 174

Appendices

A Publications **177**

B Modelling Membrane Voltage Drop **179**

C Spectra **181**

References **183**

List of Figures

1.1 Overview of common membrane poration processes 3
1.2 Lipidic structures 6
1.3 The biological cell membrane 8
1.4 The hydrophobic effect 10
1.5 Lipid molecule structure 11
1.6 Model membrane systems 14
1.7 Droplet-interface bilayers 16
1.8 Early electroporation recordings 20
1.9 Transient aqueous pores 23
1.10 Electropore imaging studies 27
1.11 Voltage clamps and current measurement 30
1.12 Jablonski diagram 32
1.13 Objective-based total internal reflection 35

2.1 Electroporation theory 41
2.2 Interfacial water alignment in pore initiation 44
2.3 The PMMA device used to form DIBs 51
2.4 Electrical experiment setup 53
2.5 Monolayer and bilayer formation 55
2.6 Bilayer formation time 56
2.7 Example voltage protocol 57
2.8 Typical current response of DIBs 59
2.9 Capacitative charging of the bilayer 61
2.10 I–V curve for a DPhPC droplet-interface bilayer 64
2.11 I–V curves for DPhPC bilayers under various protocols 66
2.12 Variations in ensemble electropore conductance 68
2.13 I–V curves at physiological electrolyte concentrations 71
2.14 Equivalent circuit for electroporation 75
2.15 Model of voltage drop across the membrane 76

3.1 Excitation and emission pathways for oSCR imaging 87
3.2 Background correction procedure 90

3.3 Setup for oSCR imaging of electropores 92
3.4 Ensemble electrical behaviour in the presence of Ca^{2+} 93
3.5 Visualising electropores in DIBs 95
3.6 Increasing pore formation with voltage 95
3.7 Correlating electrical and optical signals 96
3.8 Deconvoluting multiple electrical signals 97
3.9 Individual electropore gating behaviour 99
3.10 Diffusional behaviour of electropores 102
3.11 Electric field lines in an electropore 103
3.12 Diffusion at elevated temperatures 105
3.13 Electropore formation in phase-separated bilayers 107
3.14 Anticorrelation in oSCR signals 109
3.15 Tandem diffusion of an electropore pair 110
3.16 Imaging bilayer rupture 111
3.17 oSCR signal lag in the case of large pores 115

4.1 Variation of pore conductance with radius 120
4.2 Current vs. intensity relationship for large pores 121
4.3 Pore size distributions 122
4.4 Electropore lifetimes 125
4.5 Lifetimes of individual pores 127
4.6 Temperature dependence of pore kinetics 130
4.7 Estimating the barrier to electroporation 131

5.1 Models of antimicrobial peptide pore formation 141
5.2 AMPs structures 142
5.3 Dual-colour setup for oSCR and single-molecule imaging 150
5.4 I–V curves for alamethicin and melittin in DIBs 153
5.5 I–V curves for magainin-II and indolicidin in DIBs 154
5.6 Concentration dependence of V_c 155
5.7 Electrical behaviour of AMP-containing DIBs 157
5.8 Optical single-channel recording traces for AMPs 159
5.9 Dual-colour fluorescence imaging of AMP pore formation 160
5.10 Radial distribution function analysis procedure 163
5.11 Radial distribution functions for AMPs 164

List of Abbreviations

AFM . . . . . atomic force microscopy

AMP . . . . . antimicrobial peptide

ANTS . . . . . 8-aminonaphthalene-1,3,6-trisulfonic acid

BLM . . . . . black lipid membrane

bSM . . . . . brain sphingomyelin

chol . . . . . cholesterol

CD . . . . . circular dichroism

CL . . . . . cardiolipin

DHB . . . . . droplet-hydrogel bilayer

DiI . . . . . 1,1'-dioctadecyl-3,3,3',3'-tetramethylindocarbocyanine iodide

DIB . . . . . droplet-interface bilayer

DMPC 1,2-dimyristoyl-*sn*-glycero-3-phosphocholine

DMPS 1,2-dimyristoyl-*sn*-glycero-3-phospho-L-serine

DOPC 1,2-dioleoyl-*sn*-glycero-3-phosphocholine

DOPE 1,2-dioleoyl-*sn*-glycero-3-phosphoethanolamine

DPPC 1,2-dipalmitoyl-*sn*-glycero-3-phosphocholine

DPPE 1,2-dipalmitoyl-*sn*-glycero-3-phosphoethanolamine

DPPG . . . . . 1,2-dipalmitoyl-*sn*-glycero-3-phospho-(1'-*rac*-glycerol)

DPhPC 1,2-diphytanoyl-*sn*-glycero-3-phosphocholine

DPhPG . . . . 1,2-diphytanoyl-*sn*-glycero-3-phospho-(1'-*rac*-glycerol)

DSPC 1,2-distearoyl-*sn*-glycero-3-phosphocholine

EDTA . . . . . ethylenediaminetetraacetic acid

(EM)CCD . . (electron-multiplying) charge-coupled device

FFT . . . . . fast Fourier transform

FRAP . . . . . fluorescence recovery after photobleaching

GUV . . . . . giant unilamellar vesicle

HEPES . . . . 4-(2-hydroxyethyl)-1-piperazineethanesulfonic acid

HIV . . . . . human immunodeficiency virus

IC . . . . . internal conversion

ISC . . . . . intersystem crossing

L_o/L_d . . . . . liquid ordered/liquid disordered (phase)

LPC . . . . . lysophosphatidylcholine

LPS . . . . . lipopolysaccharide

MD . . . . . molecular dynamics (simulation)

MIC . . . . . minimum inhibitory concentration

MSD . . . . . mean-squared displacement

NA . . . . . numerical aperture

NMR . . . . . nuclear magnetic resonance

oSCR . . . . . optical single-channel recording

PBS . . . . . phosphate-buffered saline

PSF . . . . . point-spread function

P/L . . . . . peptide-to-lipid ratio

PMMA . . . . poly(methyl methacrylate)

POPC 1-palmitoyl-2-oleoyl-*sn*-glycero-3-phosphocholine

POPE 1-palmitoyl-2-oleoyl-*sn*-glycero-3-phosphoethanolamine

POPG . . . . . 1-palmitoyl-2-oleoyl-*sn*-glycero-3-phospho-(1'-*rac*-glycerol)

PTFE . . . . . polytetrafluoroethylene

RDF . . . . . radial distribution function

SCCaFT . . . single-channel calcium flux/fluorescence transient

SLB . . . . . supported lipid bilayer

SM . . . . . sphingomyelin

SNR . . . . . signal-to-noise ratio

SUV . . . . . small unilamellar vesicle

TIRF(m) . . . total internal reflection fluorescence (microscopy)

TRITC . . . . tetramethylrhodamine isothiocyanate

wt./vol. . . . . weight-to-volume

List of Symbols

$a_\mathbf{0}$ . . . . . area per lipid

a_p . . . . . electroporation capacitance term, equal to $\frac{1}{2d_\mathrm{m}}(\epsilon_\mathrm{w} - \epsilon_\mathrm{m})\epsilon_0$

A . . . . . membrane area

$A_\mathbf{p}$ . . . . . membrane area occupied by pores

β . . . . . empirically determined capacitance variance factor

b . . . . . surface frictional coefficient

γ . . . . . (pore) line tension

C . . . . . constant in (hydrophilic) pore closure term

$C_\mathbf{0}$ . . . . . specific capacitance

$C_\mathbf{m}$ . . . . . membrane capacitance

d . . . . . depth of evanescent field penetration

$d_\mathbf{m}$ . . . . . bilayer thickness

$D_\mathbf{lat}$ . . . . . lateral (2D) diffusion coefficient

$\epsilon_\mathbf{0}$ . . . . . permittivity of free space

$\epsilon_\mathbf{m/w/r}$ . . . . . relative permittivity of membrane/water/continuous dielectric

$e_\mathbf{0}$ . . . . . elementary charge

$\Delta E_\mathbf{c}$ . . . . . energy barrier to unbounded pore expansion

$E_\mathbf{hydrophilic}$ . . . energy of a hydrophilic (toroidal) pore

$E_\mathbf{hydrophobic}$ . . energy of a hydrophobic (cylindrical) pore

$\mathbf{E}$ . . . . . local electric field (vector)

F_z . . . . . force component normal to the membrane

$\mathbf{F}$ . . . . . (vector) force experienced by a molecule in an electric field

$\Delta_\mathbf{solv.} G^\ominus$ . . . . Gibbs free energy of solvation

g . . . . . electrolyte conductivity

$g(r)$ . . . . . radial distribution function

G . . . . . pore conductance

$\eta_{\mathbf{w}}$ . . . . . fluid viscosity

$h_{\mathbf{e}}$ . . . . . bilayer dielectric (hydrocarbon tail) thickness

$\theta_{\mathbf{i/c}}$ . . . . . angle of incidence/critical angle

$I_{\mathbf{0}}$ . . . . . evanescent field intensity (at the TIR interface)

$I_{\mathbf{m}}$ . . . . . membrane current

k . . . . . rate of hydrophilic pore formation

$k_{\mathbf{B}}$ . . . . . the Boltzmann constant

$\lambda_{\mathbf{0}}$ . . . . . wavelength of incident light in a vacuum

$\lambda_{\mathbf{em./ex.}}$ . . . . . wavelength of excitation/emission

$\boldsymbol{\mu}$ . . . . . molecular dipole moment (vector)

$n_{\mathbf{1/2}}$ . . . . . refractive index of material 1/2

$N_{\mathbf{A}}$ . . . . . the Avogadro constant

$p_{\mathbf{elec.}}$ . . . . . electrocompressive pressure on the dielectric of a capacitor

Π . . . . . osmotic pressure

Q . . . . . capacitor charge

r . . . . . pore radius

r^* . . . . . pore radius at the hydrophobic-hydrophilic intersection point

$r_{\mathbf{c}}$ . . . . . critical radius

r_i . . . . . radius of ion i

$R_{\mathbf{access}}$ . . . . . access resistance of a pore

$R_{\mathbf{ext.}}$ . . . . . external series resistance

$R_{\mathbf{m}}$ . . . . . membrane resistance

$R_{\mathbf{pore}}$ . . . . . pore resistance

σ . . . . . (bilayer) surface tension

$\sigma_{\mathbf{eff}}$ . . . . . modified (effective) membrane tension due to the presence of pores

$\sigma_{\mathbf{elec.}}$ . . . . . surface tension induced by transmembrane voltage

σ' . . . . . energy per unit area of the lipid hydrocarbon-water interface

$\sigma(r)$ . . . . . interfacial tension between lipid tails and water (as a function of pore radius)

List of Symbols

$\tau_{\mathbf{cap}}$	capacitor time constant
$\tau_{\mathbf{1/2,\ open/closed}}$	lifetime 1/2 for pore opening/closing
$\tau_{\mathbf{m}}$	membrane lifetime
Δt	time lag
T	absolute temperature
$T_{\mathbf{m}}$	lipid melting temperature
$V_{\mathbf{applied/app.}}$	applied voltage
$V_{\mathbf{c}}$	critical (bilayer rupture) voltage
$V_{\mathbf{m}}$	transmembrane voltage
$\bar{V}_{\mathbf{onset}}$	mean voltage at which electroporation was observed
ϕ^*	energy barrier at the hydrophobic-hydrophilic intersection point
$\phi_{\mathbf{c\to o}}$	energy barrier to hydrophilic pore opening (closed to open)
$\phi_{\mathbf{o\to c}}$	energy barrier to hydrophilic pore closing (open to closed)
φ_i	osmotic coefficient of species i
v	frequency of lateral lipid fluctuations
w	energy of a monovalent ion inside a bilayer
z	ion charge (in terms of e_0)

1 Introduction

This chapter outlines the rationale for studying pore formation in lipid bilayers, considering both the processes that arise in Nature and those induced and exploited by Man. Alongside, it presents the requisite background information for understanding such processes and their experimental investigation.

1.1 Opening Remarks

The cell (or plasma) membrane is the biological fabric that surrounds all cells. It functions first and foremost as a barrier, protecting cells from their external environment, and ensuring the retention of all the materials and structures that are vital to the organism. Secondly, it is the location of many thousands of components that shuttle, organise, transfer, block, and redistribute material and messages into and out of the cell. Without the plasma membrane, the cell cannot function: these processes no longer have a fabric in which to take place. But moreover, without the cell membrane, the compartmentalisation that it affords ceases to exist. Internal and external environments are no longer separated: the biological material of the cell is free to become lost and disorganised. Without the cell membrane, the cell cannot exist.

This thesis deals with the *disruption* of the cell membrane. An interest in disrupting this structure may seem at first contradictory, given the importance that it has for the cell. However, although it is certainly within an organism's best interest to maintain the plasma membrane as its barrier to the outside world, there are circumstances under which that barrier may — intentionally or unintentionally — be compromised.

1.1.1 The Importance of Poration Processes

Unexpected pore formation within the plasma membrane is a serious and possibly terminal disruption for a cell. Such an event would likely result in the loss of vital internal components to the outside world. Should the loss of material be significant, either through defects sufficient in size or in number, the cell would likely be unable to recover and it would die. Else, a hole in the membrane might permit the entry of foreign material, which could be immediately toxic, or could induce longer-term damage by modifying or disrupting natural cellular processes. As already alluded to, however, there may be good reasons for targeting a cell membrane in this way. An overview of these processes is shown in Figure 1.1.

The ability of an organism to combat the internal invasion of bacteria or other foreign cellular species is a vital defence system for any living thing which wishes to survive, and the cell membrane belonging to the foreign body is the most immediate and oft-effective structure to target during the initial stages of infection. The great majority of lifeforms defending themselves against such invaders employ, as part of their innate immune response, a group of proteins known as host-defence or antimicrobial peptides (AMPs) [1, 2]. The structure of these proteins is such that they target the plasma membranes of the invading cells whilst leaving those of the host intact [3–5]. Mechanistically, many of these host-defence peptides are believed to operate by permeabilising the foreign membranes, inducing cell death by leakage of cytosolic material [6]. Alternatively, organisms may use similar means when attacking or attempting to defend themselves. For example, pore-forming proteins have been found in the venom of bees, spiders and scorpions [7, 8] as

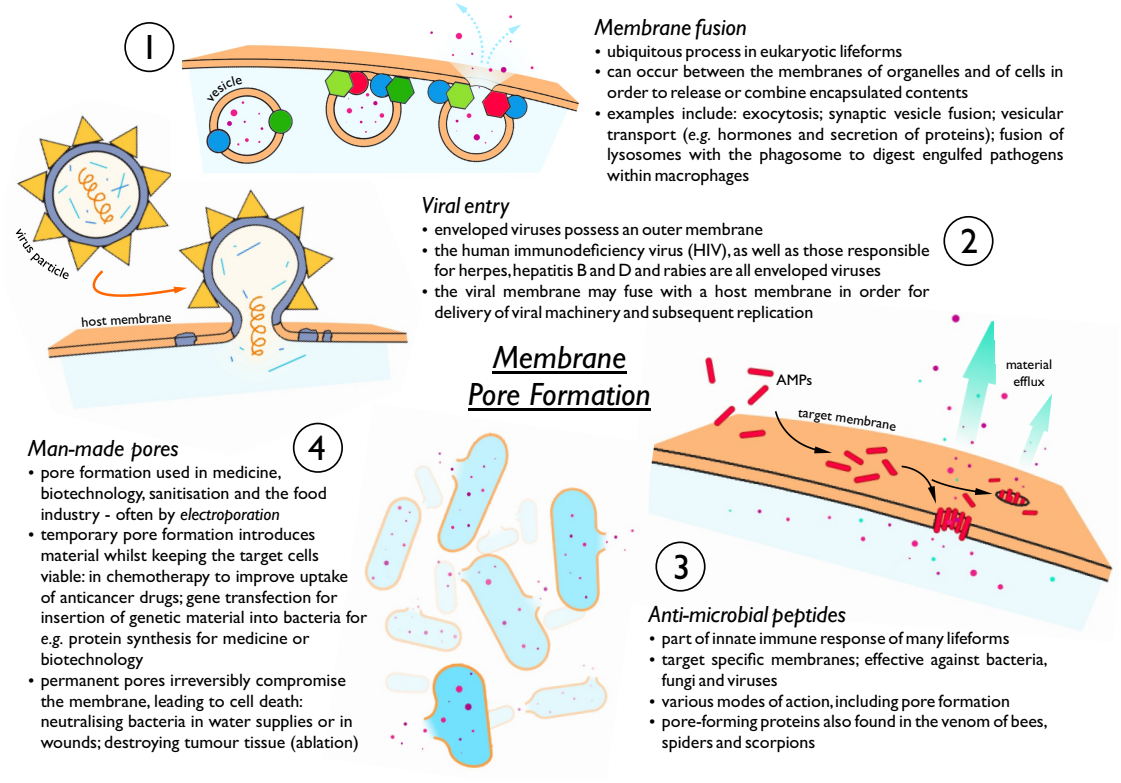


Figure 1.1: Overview of common membrane poration processes. (1) Organelle-organelle and organelle-plasma membrane fusion permit biomolecular exchange throughout eukaryotes. (2) In a related manner, enveloped viruses may infect a eukaryotic host by fusing with its membrane. (3) Antimicrobial peptides (AMPs) are secreted by many organisms to defend against pathogens. AMPs have many (and sometimes combinatorial) modes of action; in the case of pore-forming AMPs, they assemble on the target membrane surface and then puncture the membrane. *N.B.* The protein-based pores formed by transmembrane proteins — pumps, channels, transporters and porins — arguably the largest area of study in Biophysics, are not part of the work contained in this thesis; the focus here shall be on externally-induced pore formation. (4) Man has found wide-ranging applications for membrane-porating techniques. (1) and (2) adapted from [11].

part of their systems to defend against larger, and often predatory animals, and in the skins of certain frogs [9, 10], as a constant outer defence against potential pathogens*. The pores formed by AMPs are the subject of Chapter 5, in which the structures, membrane interactions and modes of action of these peptides shall be discussed in greater detail.

The formation of membrane pores is also a ubiquitous part of membrane fusion

*Before the advent of refrigeration, the native peoples of Russia are said to have prevented the spoiling of milk by placing the Russian brown frog (*Rana temporaria*) in the container.

[11, 12]. Within eukaryotic cells, the membrane structure that bounds the cell is also found to compartmentalise volumes within it; these membrane-enclosed compartments are known as organelles[†], and serve as isolated volumes to store, shuttle, generate or modify biological material. Should a carrying vessel (usually a membrane-bound volume called a vesicle, see Figure 1.2) be needed in order to transfer this material between organelles, or to deliver it into or out of a cell, the respective membranes of the carrier and the recipient must fuse, which takes place via a fusion pore [13]. Proteins, neurotransmitters and hormones are all trafficked in this manner.

Membrane fusion is also one mechanism by which certain virus particles enter their host cell. Those that possess a viral envelope (an outer membrane derived from or similar to that of the host), such as HIV, may attach to the host and puncture its membrane, delivering the machinery required for viral replication [14, 15]. Whilst membrane fusion is not within the focus of this thesis, the study of the pores that are formed during fusion processes is an extensive field [12, 16, 17].

An understanding of these natural processes is of great value. Information about vesicular transport allows us to piece together the mechanisms involved in moving all manner of biological molecules within and between cells. Knowledge of how antimicrobial peptides behave — the means by which they target *specific* membranes, and their subsequent modes of action — is one focus of this thesis, and is requisite in the early steps towards the design of novel peptides, each tailored to selectively target the pathogen that gives rise to a particular illness or disease. This knowledge is also the foundation of understanding the ways in which evolution might circumvent such attempts to protect ourselves. In an age when antibiotics are increasingly losing their efficacy, alternative methods of tackling bacteria are sorely needed.

One final and important class of processes that lead to membrane pore formation are those techniques that Man has invented across medicine, the food industry and biotechnology. The ability to neutralise cells by membrane rupture is highly applicable, for example, in the context of sterilising water [18], in disinfection [19],

[†]Prokaryotic organisms on the other hand are exclusively single-celled, and distinguished from eukaryotes by virtue of their lack of membrane-bound organelles.

or in the food industry [20]. A method to eliminate an isolated region of cells by porating their membranes is a simple albeit effective means to destroy or degrade tumours [21]. Transient pore formation, through which matter may be introduced into target cells before the holes reseal, is incredibly useful in microbiology for inserting genetic material into bacterial and mammalian cells [22, 23]. Clinically, this has been successfully used in gene therapy[‡] [24], and to improve transdermal drug delivery, especially in the context of chemotherapy [25]. A technique that has found applicability in all of the above, called electroporation, is the main focus of this thesis.

1.2 The Cell Membrane

Although the specific components of cell membranes vary throughout Nature [26, 27], their fundamental building blocks and general architecture are common to all lifeforms: two tightly associated, opposing layers (a bilayer), each assembled from molecules (lipids) that possess a polar, hydrophilic 'head' region and at least one non-polar, hydrophobic chain, or 'tail'. The thickness of this lipid bilayer is on the order of a few nanometres; depending on its component lipids, membranes typically range from 3–5 nm [28, 29]. Figure 1.2 depicts the common structures that lipids spontaneously form in water. The origin of the phenomenon which drives their assembly shall be detailed in the following section.

In order to provide a barrier between aqueous volumes, the bilayer structure must be stable in its water-based environment whilst being largely impermeable to the ions, proteins and other matter either side of it; the lipid heads take care of the former requirement, and the non-polar membrane interior, composed of the tails, deals with the latter (Figure 1.2). That said, the bilayer is a semi-permeable membrane, allowing the passage of small molecules that are soluble in the hydrophobic core [30]. Small hydrophobic molecules such as gases (O_2, CO_2) diffuse through (effectively) unhindered, with permeation rates of 0.1 to 10 $cm{\cdot}s^{-1}$ [31]. Small, uncharged polar molecules, like water and ethanol, may also transit across the membrane, and do

[‡]Gene therapy is the introduction of genetic material into tissues in order to induce a particular cellular response. This response could have an antitumour effect, or combat a cellular dysfunction such as a specific protein deficiency.

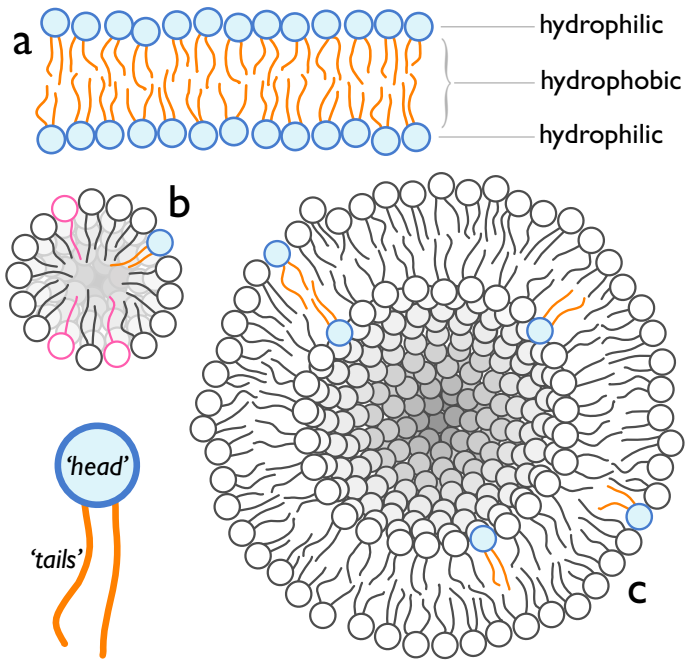


Figure 1.2: Lipidic structures. (a) Cartoon of a bilayer, the structural basis of all cell membranes, showing only the lipid molecules, which are arranged as two opposing leaflets. Hydrophilic headgroups are shown by the shaded circles; wavy lines depict the hydrophobic acyl tails. (b) Cross-sectional representation of a micelle, a single lipid layer curved inwards upon itself to shield the tail groups. This structure is particularly favoured when the amphiphile has an inverted-cone shape (a large headgroup with respect to the tail region), such as with lysolipids – those bearing a single tail (highlighted here in pink). (c) Cut-through of a vesicle, a spherical arrangement of a bilayer with an aqueous centre. Colour coding: blue, hydrophilic segments; orange, hydrophobic regions.

so at around 10^{-2} cm·s^{-1} [29, 32]. However, larger, uncharged polar molecules, for example glucose (10^{-7} cm·s^{-1}), and charged species (and therefore all ions) have very low permeation rates across the bilayer (10^{-10}–10^{-12} cm·s^{-1}) [32].

The bilayers found in cellular systems have a great number of components in addition to the lipids which form the basis of their structure (Figure 1.3), due to the great many roles that the bilayer performs [30, 33]. The barrier function that the membrane provides between compartments allows the separation of charge, the generation of chemical gradients (of ions or pH, for example), the isolation of reactive biomolecules and a volume in which to perform their reactions, and a space to retain toxic matter, waste, or substances needed only at particular times. Transfer of large quantities of matter across cell membranes and their subspaces can

occur by vesicle fusion, however, for individual molecules and for the maintenance of gradients there is a myriad of proteins of incredible variety, designed to transport membrane-impermeable molecules across the bilayer. The membrane is also the site of cell-cell communication, for example in the recognition of a cell by the organism's own defence system. The outer face of the membrane is the site of cell-cell adhesion, whilst the internal surface is used as an anchor for the cytoskeleton, conferring mechanical stability to cells and acting as a conduit for material transport. It should be noted that despite the tight association between the two leaflets of a bilayer, its component lipids and most of the molecules and proteins that pepper it are by no means fixed. Rather, in the plane of the bilayer the material is fluid, with lipids and other species able to diffuse laterally within the structure [34].

In order to support these additional membrane species, the bilayer contains various lipid types [26, 27]. These may have a specific association with particular membrane proteins [35], or exhibit particular properties (such as headgroup charge [36]) that aid in the distribution or function of other membrane-associated species. Lipid tails vary in number, length, saturation or branching, and different tails may be bonded to the same headgroup. This variation confers to the membrane different physical properties, such as the bilayer thickness, curvature, resistance to temperature, or fluidity [32]. The introduction of branching or a double bond into a lipid tail alters the packing between the molecule and its neighbours, altering the strength of the van der Waals interactions in the plane of the bilayer, and hence its fluidity; similarly, longer chains interact more strongly, contributing $\sim$2 kJ·mol^{-1} per –CH_2 group [30]. Organisms may therefore modulate their lipid composition in order to suit their surroundings: in bacterial membranes, the ratio of saturated to unsaturated lipids decreases as the growth temperature is lowered [37, 38]. Lipids undergo a phase transition at their 'melting temperature' (T_m), at which the membrane fluidity alters and the bilayer changes from a relatively ordered gel (solid-like) phase to a relatively disordered liquid-crystalline (fluid-like) phase [39]. In bacteria incubated at cooler temperatures, the increase in the proportion of

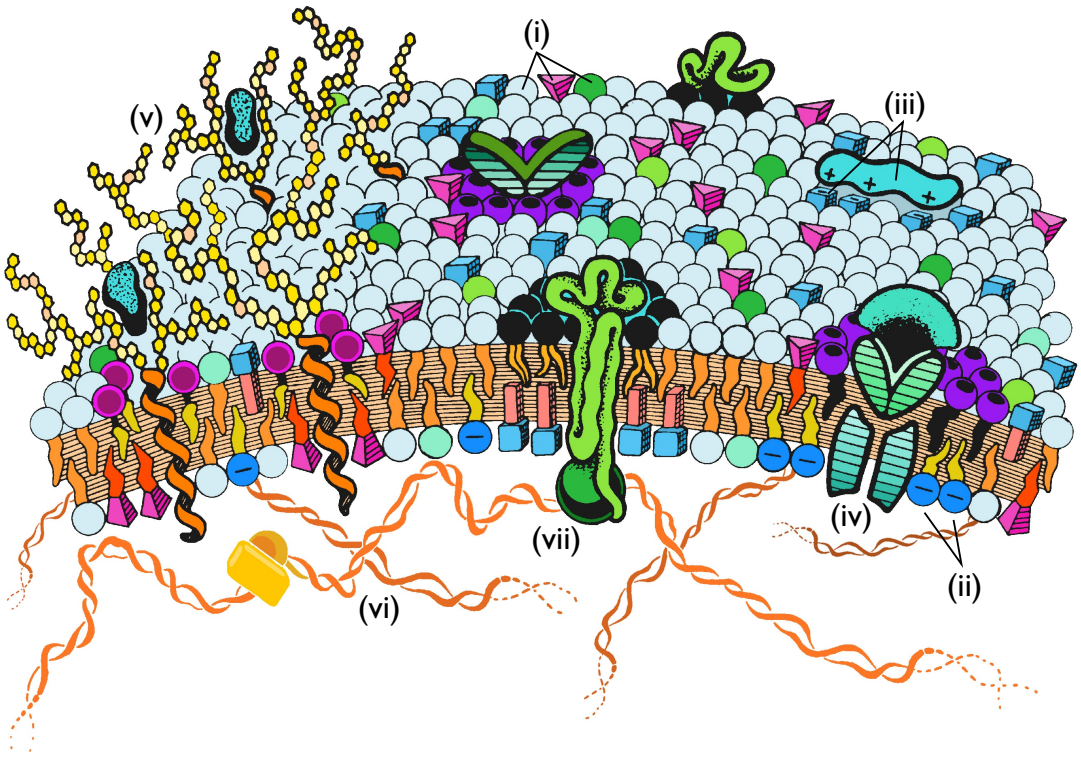


Figure 1.3: Cartoon of the biological cell membrane. The bilayers that encapsulate cells and their organelles are complex environments containing a great many components other than lipids, which themselves come in many types (*i*). The lipids may be charged (*ii*), attracting proteins or other molecules to the surface (*iii*), and they may be associated with particular membrane proteins (*iv*). Many of these proteins pump, shuttle and translocate impermeant molecules either side of the bilayer (*iv*). Others embedded in the membrane have bonded to them structures, such as oligosaccharides, that extend out into the extracellular space for cell-cell recognition and intercellular interaction (*v*). On the intracellular face, the cytoskeleton (*vi*) is anchored to the cell membrane by another branch of membrane proteins (*vii*). It should be noted that this list of membrane components and their functions is by no means exhaustive. Figure adapted from [33].

unsaturated lipids lowers the transition temperature T_{m}, ensuring that the bilayer remains fluid in their lower temperature environment.

It is worth mentioning that cholesterol, another type of lipid molecule, also plays a large role in the mechanical properties of animal bilayers. Whereas bacteria regulate membrane fluidity by varying the length and saturation of lipid chains [32], cholesterol in animal membranes intercalates lipids, stabilising the structure by maintaining lateral van der Waals interactions [40], but preventing widespread clustering, thus maintaining fluidity [32, 41]. On smaller scales lipid clusters rich in

cholesterol, saturated lipids and sphingolipids exist in the membrane, called lipid 'rafts' [42]. These nanoscale subdomains (10s to a few 100 nanometres across) exhibit tighter packing and thus a more ordered structure than the surrounding membrane, bearing membrane-signalling and trafficking proteins which partition into them [43].

Additionally, curvature can also be dictated by the nature of the membrane-forming lipids: single or small chains with respect to the area of the headgroup create positive curvature, whilst heavily branched lipids force the tail regions to occupy a larger area than the headgroups, generating negative curvature [44]. The great diversity of lipid species that is found within one leaflet of the membrane can also be found in its opposing leaflet: biological membranes are asymmetric in the composition of the cytoplasmic and exoplasmic surfaces, according to the functions each must perform and the molecules they interact with.

1.2.1 Lipids

Lipids are amphiphilic molecules: they contain both polar and apolar regions. In the aqueous environments that cells operate within, lipid molecules spontaneously associate into membraneous structures in order to minimise contact between the apolar, aliphatic tails and water, a phenomenon known as the hydrophobic effect [45] (Figure 1.4). As the non-polar lipid tails are unable to form hydrogen-bonds with the surrounding (polar) solvent, they therefore disrupt the dynamic hydrogen-bonding network that exists in pure water, reducing the number of (configurational) degrees of freedom available to the water as it is forced to adopt a more ordered structure, as shown in Figure 1.4b. Thermodynamic laws dictate that a system will find stability by minimising its free energy — in effect a restatement of the second law of thermodynamics. The reduction in molecular mobility as a result of water ordering itself around the acyl chains decreases the system's overall disorder, or entropy — an unfavourable scenario in this case as this increases the free energy. However, the rise in free energy when lipids are introduced to the system can be limited by reducing the total hydrophobic surface exposed to water. This results in

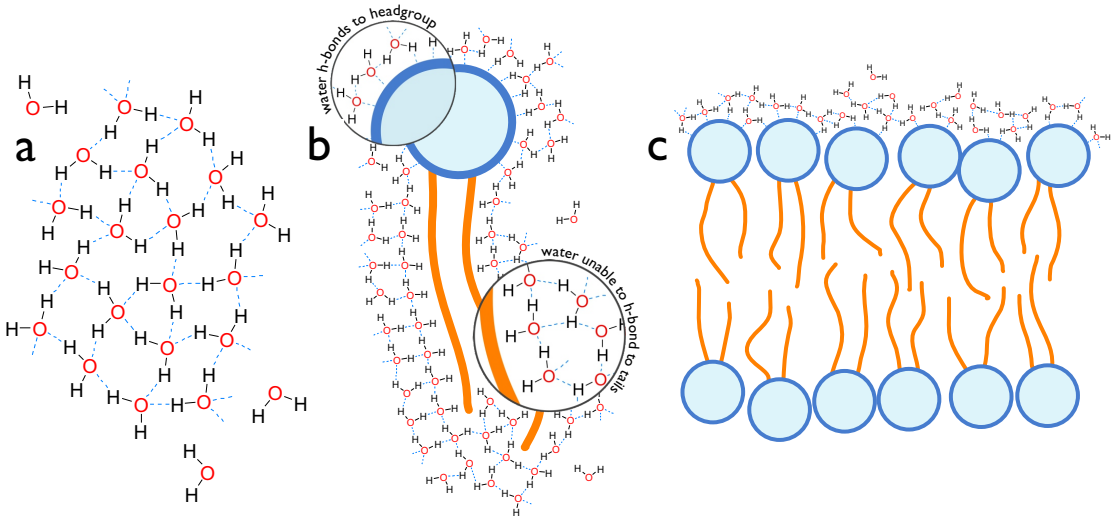


Figure 1.4: The hydrophobic effect. (a) The hydrogen bonding network in water is dynamic and transient: molecules may rapidly reorientate and form new hydrogen bonds (blue) with other neighbours. (b) Water may hydrogen bond (h-bond) to the hydrophilic headgroup of a lipid molecule, but is unable to do so with the acyl chains, thus restricting its degrees of freedom. (c) A bilayer structure minimises the contact between water and the lipid tails.

structures that ensure the hydrophilic regions encapsulate those that are 'water-fearing'. Furthermore, attractive van der Waals forces encourage packing of the lipid tails, and electrostatic and hydrogen-bonding interactions between the headgroups favour ordered clustering of phospholipid molecules.

The most commonly encountered class of bilayer-forming lipid molecules, and those that form the major component of all membranes, are the phospholipids. They are composite molecules, comprising four sections (Figure 1.5a). A central alcohol (usually glycerol or sphingosine) is bonded to one or more long-chain acids, normally an even number of backbone carbons in length, which can exhibit saturated and/or unsaturated regions. These alkyl chains are what are referred to as the lipid 'tail(s)'. Also bonded to the glycerol (or sphingosine) is a phosphorylated alcohol, commonly choline, serine or ethanolamine. The phosphate group bears a negative charge, and the alcohol may also bear a charge, producing an ionic or zwitterionic region which constitutes the hydrophilic 'head' of the lipid molecule.

The main lipids referred to in this work are depicted in Figure 1.5. The acyl chains of 1,2-diphytanoyl-*sn*-glycero-3-phosphocholine (diphytanoyl phosphatidylcholine,

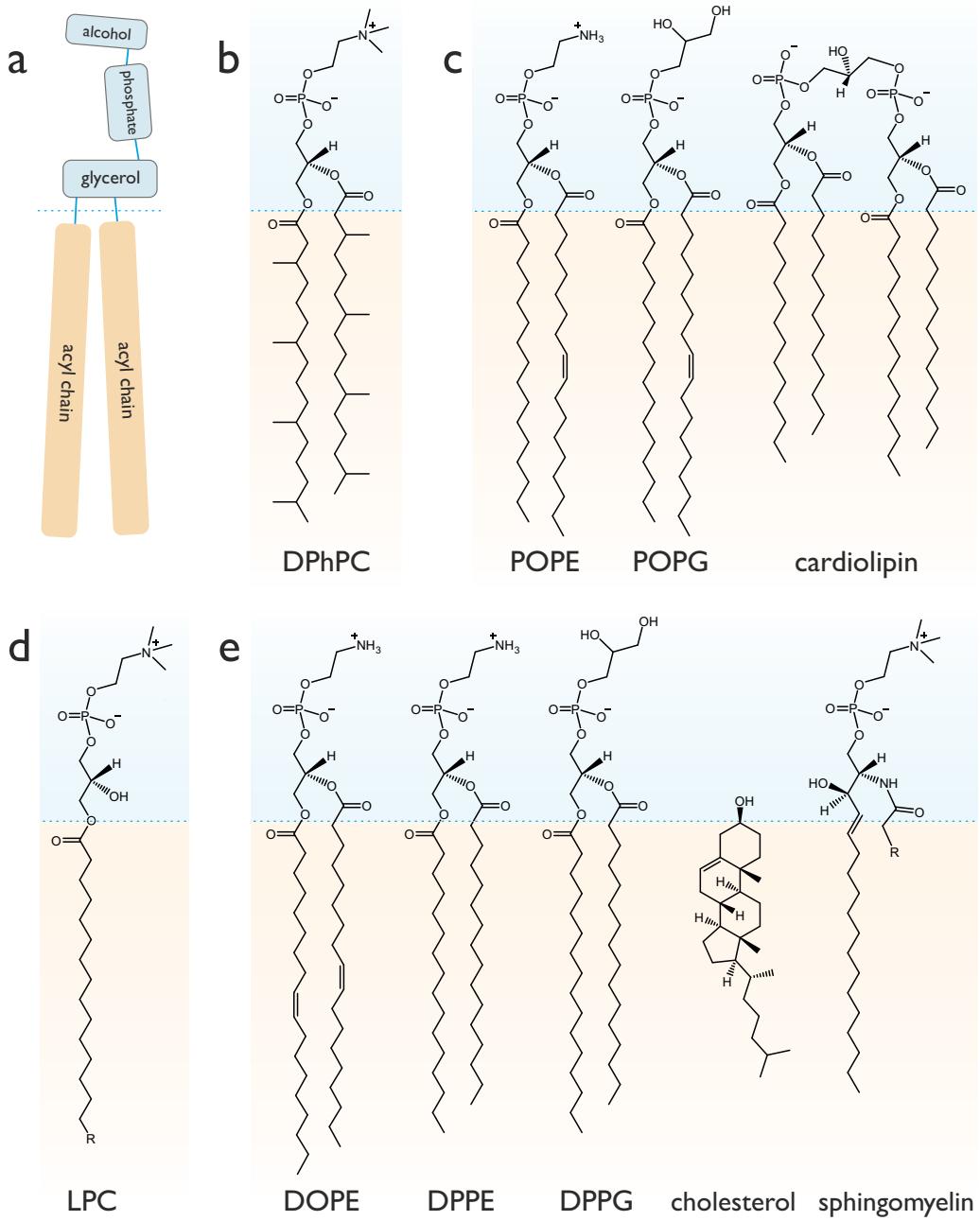


Figure 1.5: Lipid molecule structure. (a) Generalised (glycero-) phospholipid architecture. (b) The branched lipid diphytanoyl phosphatidylcholine (DPhPC), the main lipid used in this work. (c) The trio of lipids used to mimic bacterial membranes: palmitoyl-oleoyl phosphoethanolamine (POPE), palmitoyl-oleoyl phosphoglycerol (POPG) and cardiolipin (CL). (d) General structure of the single-tailed lipid lysophosphatidylcholine (LPC), with R representing an acyl chain (most commonly CH_3, CH_2CH_3 or $CH_2CH_2CH_3$). (e) Other lipid species referred to in this thesis: dioleoyl phosphoethanolamine (DOPE), dipalmitoyl phosphoethanolamine (DPPE), dipalmitoyl phosphoglycerol (DPPG), cholesterol (chol), and the sphingolipid sphingomyelin (SM). R represents an acyclic aliphatic chain. As before, blue shaded regions highlight hydrophilic areas of the molecules; orange denotes the hydrophobic regions.

DPhPC), Figure 1.5b, are based on the branched, saturated isoprenoid phytane. Despite not being found in mammalian membranes[§], which are derived from unbranched, linear fatty acids, this particular lipid is resistant to photon-induced oxidation, and degradation when compared with unsaturated analogues. In addition, the methyl group branching dictates that the lipid molecules pack in such a way that its bilayers are in the fluid phase relevant to biological systems over a very wide range of temperatures (–120 to +120 °C) [46]. They therefore form highly stable model membranes, and consequently DPhPC has been used in many studies for characterising lipid behaviour [47, 48] and membrane-protein interactions [49, 50].

In the work on antimicrobial peptides (see Chapter 5), a ternary lipid mixture (Figure 1.5c) was used in order to mimic the bacterial membranes that these proteins are designed to permeabilise. A great many AMPs are cationic, whilst the bacterial plasma membranes that they target tend to possess ∼20–30 % negatively-charged lipids [27]. The compositional mimic used in this work therefore comprised the three major bacterial phospholipids: the zwitterionic, monounsaturated POPE (1-palmitoyl-2-oleoyl-*sn*-glycero-3-phosphoethanolamine), its anionic, glycerol headgroup counterpart POPG (1-palmitoyl-2-oleoyl-*sn*-glycero-3-phospho-(1'-*rac*-glycerol)), and the doubly anionic cardiolipin. Such a mixture is an effective model of *E. coli* membranes [51, 52].

1.3 Artificial Membrane Mimics

1.3.1 BLMs, SLBs and GUVs

When attempting to study natural bilayer systems, the presence of the great number of components within and associated with the membrane presents an obvious challenge: the level of complexity of the system. Attempting to understand the dynamics of a single protein, or to investigate a specific membrane process can be hindered by the thousands of other processes and biomolecules comprising

[§]Lipids with phytanyl groups tend to be found in halo- and thermophilic archaea; their branched chains are more resistant to oxidation, and are joined to glycerol by ether (rather than ester) linkages, which are more resistant to hydrolysis [32]

the bilayer. In order to comprehend the complete system, fundamental knowledge about its separate components must be gained, and then pieced together, before the entire structure can be understood as a whole. Whilst a label (very commonly a fluorescent marker) might allow the tracking of a substrate or the operation of some biological machinery, isolating its dependence on a single, externally varied parameter can be complicated by the relationship that the species under study has with other bilayer and cellular components. Furthermore, the means of isolating the bilayer (or one of its vast number of smaller elements) so that it may be interrogated, is an additional consideration when embarking on lipid bilayer studies.

Consequently, there exist several *artificial* bilayer platforms through which the complexities of the biological lipid bilayer might be reduced. The main techniques are depicted in Figures 1.6 and 1.7. Black lipid membranes (BLMs, Figure 1.6a) are formed by the application of lipid across an aperture separating two aqueous volumes [53, 54]. Their name derives from their dark appearance in reflected light, a result of interference between light reflected from the water-lipid and lipid-water interfaces, a path which as the leaflets come together becomes small enough to cause destructive interference [54, 55]. BLMs have been used to investigate voltage-gated ion channels [56] and in the earliest electroporation studies [57], but suffer from a lack of long-term bilayer stability.

Supported lipid bilayers (SLBs, Figure 1.6b, *lower*) overcome this by virtue of the support on which the bilayer rests [58]. Bilayers formed on solid supports may be interrogated using physical techniques such as atomic force microscopy, or using optical methods — techniques largely inaccessible to BLMs. However, interactions with the substrate can be of concern when incorporating transmembrane proteins into the SLB, for fear of altering their native behaviour [59]. Vesicle platforms (Figure 1.6b, *upper*), ranging from small unilamellar vesicles (SUVs, 10s of nanometres) to giant unilamellar vesicles (GUVs, 10s to 100s of micrometres) on the other hand, need no substrate on which to form (although they may also be localised to a substrate by molecular tethering) [60, 61]. Whilst certain surface-sensitive methods and electrical interrogation of isolated membranes are difficult with vesicular models,

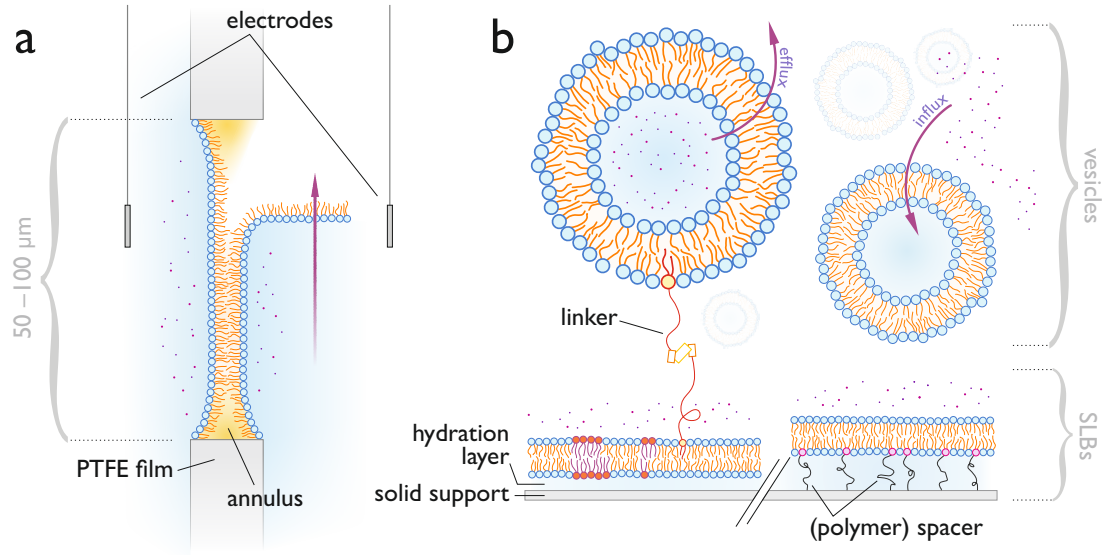


Figure 1.6: Model membrane systems. (a) The black lipid membrane (BLM). A bilayer is formed within an aperture in a polytetrafluoroethylene (PTFE) film, by either: (1) Lipid dissolved in a viscous solvent is 'painted' across the hole before addition of the aqueous phase, then reapplied once the electrolyte solution is present; (2) After lipid in a volatile carrier forms a monolayer on the aqueous surfaces either side of the PTFE film, the level of the electrolyte is raised with respect to the aperture, 'zipping' the two monolayers together. This diagram shows the second method, with the arrow indicating the raising of the right-hand volume of aqueous phase. In the first method, residual oil lines the edge of the bilayer; in the second, oil may be added for stabilisation, as this annulus bridges the gap between the nanometre-thick membrane and micrometre PTFE film. (b) Supported lipid membranes (SLBs) and giant unilamellar vesicles (GUVs). SLBs, often made by vesicle fusion with the surface, have a small water cushion beneath them, that can be expanded for incorporation of transmembrane proteins by the addition of polymers, which may or may not be anchored to a small proportion of the lipids via their headgroups. GUVs, produced by electroformation, extrusion, sonication or swelling of lipid films in aqueous media, may be studied as solutions or as individuals tethered to a surface or a planar bilayer. *N.B.* The components of these cartoons are not depicted to scale.

their similarity to cell membranes in size and geometry has seen them used in very many studies, from modelling cellular electroporation [62], to investigating rafts, curvature [61], and peptide binding [63].

1.3.2 DIBs

Droplet-interface bilayers (DIBs, Figure 1.7) are the latest addition to this toolkit, and the technique used in the experiments described in this work. DIBs are formed

between two aqueous surfaces in the presence of solution consisting of lipid dissolved in an alkane oil [64]. Lipids self-assemble as a monolayer on both surfaces, presenting the lipid tails to the solution; bringing these monolayers together forms a bilayer. DIBs present an adaptable platform with which to study membrane phenomena, with droplet-droplet bilayers used, for example, to measure bilayer water permeability [48], form linked bilayer networks [65, 66] and study membrane proteins [67].

In this work, the membrane is formed between an aqueous droplet and a planar hydrogel substrate, shown in Figure 1.7b. Both are incubated in lipid-in-oil; when they come into contact under gravity, the bilayer is formed[¶]. Bilayers formed in this way have several advantages. Formation of a bilayer on a hydrogel ensures the maintenance of a water cushion beneath the lower leaflet, maintaining fluidity and reducing interactions with the substrate. Both substrate and cushion can be chosen to suit the experiment and alter the properties of the bilayer. Moreover, DIBs are highly stable (surviving for very long lifetimes — weeks compared to a few hours for BLMs) and the technique simple to implement, with bilayers forming in seconds to minutes.

Importantly, as for any artificial membrane method, the system is adaptable to the needs of the bilayer model. The lipids or their composition can be varied, and can assemble to form the monolayers either from the incubating oil (termed 'lipid-out'), or from inside the droplet as SUVs ('lipid-in'), which can be used to produce an asymmetric membrane. Asymmetry may also be generated in the aqueous components either side of the bilayer. Further, the technique allows for the incorporation of membrane species of interest, such as proteins, either by injecting them into the droplet once the bilayer has formed, or by forming the droplet with the required components in solution. Electrical access may be gained by the insertion of electrodes into the droplet and the hydrogel. The droplet may then be mechanically perturbed or translated, providing a means to alter the bilayer area or tension, or to relocate one leaflet of the membrane to a region of the underlying substrate different in character or structure.

[¶]For full methods and detail of the experimental setup, see the relevant sections in Chapters 2 and 3.

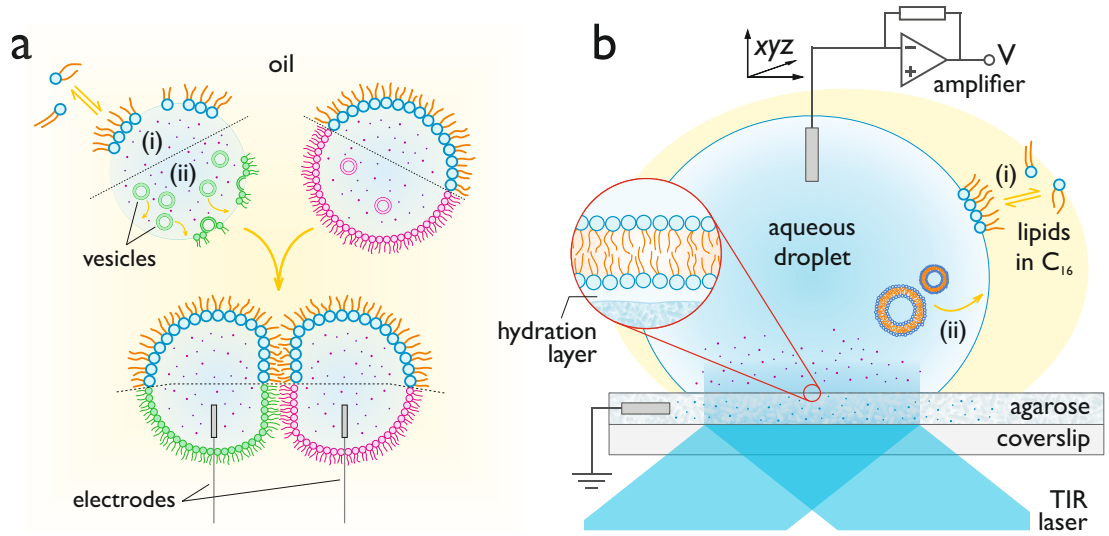


Figure 1.7: Droplet-interface bilayers. (a) Droplet-droplet bilayers, formed by the bringing together of monolayer-bearing aqueous volumes in oil. The lipid may be carried in and assemble at the water-oil interface from the oil phase (termed 'lipid-out', labelled *i*) or be absent from the oil and present in the aqueous phase as SUVs, which fuse with the interface (termed 'lipid-in', *ii*). The latter gives the ability to form asymmetric bilayers. (d) DIBs formed on an agarose hydrogel substrate, the system used in this work. Lipid assembles around the droplet by lipid-out (*i*) or lipid-in (*ii*) methods. Electrodes in the agarose and the droplet (the latter mounted on an *xyz*-micromanipulator) grant electrical access, and bilayer components may be sensitively and selectively probed using a totally internally reflected (TIR) laser beam. Again, the components of these cartoons have not been drawn to scale.

In the setup employed for this work, the hydrogel substrate is formed on a glass coverslip, which grants optical access to the bilayer. This permits not only simple manipulation but the ability to sensitively image fluorescently labelled membrane components by means of TIRF (total internal reflection fluorescence) microscopy (see Section 1.5.2). Droplet-hydrogel bilayers have already been exploited to image lipid rafts [68] and to sequence nucleic acids [69]. However, this work presents the first in-depth investigation into electroporation using the DIB membrane technique.

1.3.3 Molecular Dynamics Simulations

In the last couple of decades, computer-run models, termed molecular dynamics (MD) simulations, have joined experimental techniques as part of the toolkit for probing bilayer phenomena (for a review covering the basic features of MD simulations,

see [70]). Developing as computing power increases, MD simulations run from coarse-grained studies, whereby molecules or parts of molecules are reduced to single entities in order to simplify the system, to atomistic simulations, in which the trajectories of all atoms are computed [71, 72]. The level of detail of the modelled system is a trade-off with the period that the simulation is able to cover. However, with ever increasing hardware capabilities and algorithm development, these scales are expanding: twenty years ago, simulations covering 100–200 lipid molecules represented an area of 5–10 nm and could be run for a few nanoseconds [70, 73]. A decade ago, systems a few tens of nanometres across were limited to between the 100s of nanoseconds to the low microsecond timescale [74]. Now, systems can possess many hundreds to thousands of lipids, involve the additional complexities of modelling protein folding, or run into micro- to millisecond periods [72, 75, 76].

The great advantage of MD is its ability to investigate mechanistic details on time and length scales that are, for the time being, largely inaccessible by experimental methods; in the context of the biophysical processes covered in this thesis, MD has for example been used to predict the early stages of electropore formation at picosecond time resolution [77], and follow the interaction between antimicrobial peptides and the bilayer [78]. One area of caution regarding molecular dynamics is that the predictions made by a simulation are only as good as the physical model behind it, which has occasionally led to discrepancies between simulation outcomes [79], but critical comparisons between algorithms and methodologies are in place [80, 81].

1.4 Electroporation

Electroporation constitutes the focus of a large part of this thesis. The following sections therefore provide background and context to the results presented in subsequent chapters.

1.4.1 A Brief History of Electroporation

In 1974, Masao Yafuso and co-workers published a study in which they exposed oxidised cholesterol bilayers, formed as black lipid membranes, to a transmembrane

potential of 70 mV [82]. They reported '*spontaneous conductance changes, multilevel conductance phenomena... which we believed at that time [of experimentation] to be outside the realm of the capabilities of the unmodified lipid bilayer film.*' These spontaneous conductance changes are what we now call electroporation, or electropermeabilisation.

The notion that a transmembrane potential could disrupt cells[‖] may have in fact been first reported over two centuries prior to that, in 1754, when Nollet made observations regarding the discharge of static electricity on skin [83]. In 1898, George Fuller presented a report to the Louisville Water Company detailing tests conducted on river water, investigating whether voltage discharge could have a bactericidal effect [84]. Half a century later, whilst investigating the transmembrane potential of Ranvier nodes within nerve fibres, Stämpfli and Willi in 1957 noted that the application of a voltage pulse of sufficient amplitude across the cell would result in a reduction in the membrane resistance, which recovered if short pulses were used [85]. At higher potentials, of the order of 10 V, the membrane was destroyed.

Over the subsequent decades this phenomenon received greater interest. Pulsed electric fields were shown to kill bacterial and yeast cells in suspension [86], in a study in which — importantly — it was determined that thermal and electrolytic effects were not major contributory factors to cell lysis, rather that pulse length, field strength and the number of pulses dictated the proportion of cell death. Come 1972, Eberhard Neumann and Kurt Rosenheck demonstrated that the contents could be released from amine-encapsulating vesicles with the application of a pulse of $\sim$20 kV·cm^{-1} lasting a few hundred microseconds [87] (although at the time they did not attribute this to pore formation). Neumann would, a decade later, implement this technique to allow for greatly enhanced uptake of DNA into eukaryotic cells compared to injection or vesicle fusion methods, coining the term 'electroporation' in the same paper [22]. This method of introducing genetic material, now called gene electrotransfer, has become one of the most common methods for transfecting cells [88]. Interestingly, such electrotransformation has

[‖]The concept of a cell membrane had not been fully formed at the time.

also been suggested to be a side-effect of lightning strikes, which may permit horizontal gene transfer by fusing or transfecting neighbouring microorganisms near the site of sea or land discharge [89, 90].

From this point onwards, electroporation gained traction as a biophysical phenomenon not only of interest, but of applicability; a literature search of the word now retrieves more than 16,700 publications, covering its theoretical basis to applications in medicine, computational models to development of new electroporation apparatus. For an comprehensive review of the history of electroporation studies, the reader is directed to [91].

1.4.2 Early Observations

Whilst a full review of the early experimental observations of electroporation is not necessary here (the review by James Weaver and Yu Chizmadzhev [92] is a sound place to start), it is of use to summarise some of the early findings, in order to consider the origins of the pore-based model in the context of the information that was available at the time. These studies were conducted on cell suspensions, individual cells, and artificial membranes, and usually considered the electrical behaviour as a function of time, or the uptake of a variety molecules [92].

When monitoring the transmembrane current (I_{m}) in BLMs, a stepwise change in a sufficiently large applied voltage (V_{applied}) was found to result in an initial charging of the membrane (consistent with the bilayer acting as a capacitor), followed by fluctuations in I_{m}, terminating in a drastic and irreversible increase in I_{m} [57, 82]. This corresponded to rupture of the bilayer. Such a sequence is shown in Figure 1.8a. Investigation of the lifetime of the membrane, τ_{m}, defined as the period of time that the bilayer survived after a voltage pulse, found that there was a distribution of τ_{m} values for the same membrane voltage [57]. The character of the conductance fluctuations and the duration of this conductive state also varied between experiments, implying an underlying process stochastic in nature, rather than one that is deterministic.

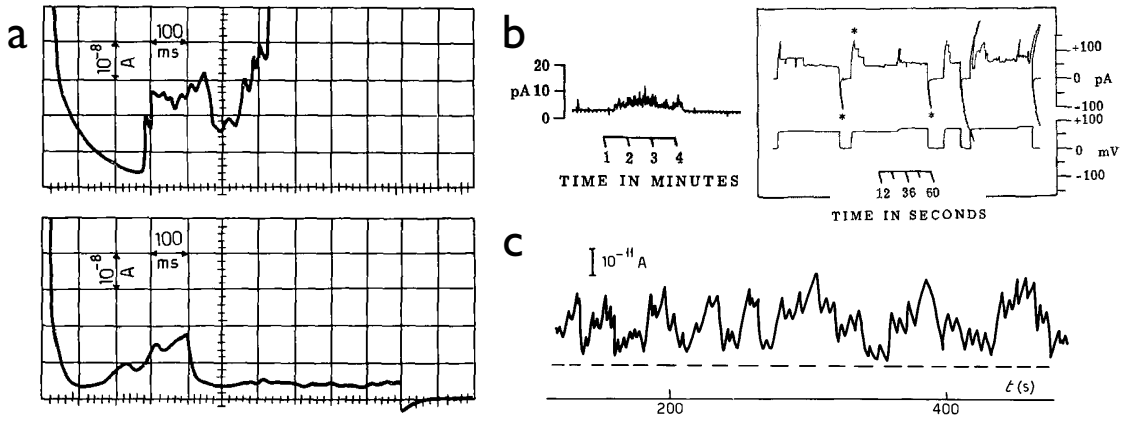


Figure 1.8: Early electroporation recordings. (a) Two recordings of the transmembrane current I_{m} following a 1 μs pulse of 400 mV in black lipid membranes. *Upper panel*: the capacitative charging spike decays to a baseline conductance level, after which current fluctuations begin, ending in a rapid rise to very high conductance corresponding to membrane rupture. *Lower panel*: The membrane was observed to return to the background conductance if exposed to a shorter pulse. (b) Some of the earliest electrical recordings to reveal electroporation. *Left trace*: transient current fluctuations in an oxidised cholesterol BLM held at 70 mV. *Right panel*: a similar bilayer responds to voltage steps. Asterisks indicate capacitative currents; the current is distorted in an arc due to I_{m} being captured on a chart recorder. (c) Current fluctuations maintained at 100 mV, after an initial pulse of 400 mV for 1 μs. The dashed line represents the baseline conductance before the pulse. (a) and (c) may be found in [57]; (b) was adapted from [82].

Furthermore, these phenomena were found to have a significant dependence on the magnitude of the electric field. The mean value of τ_{m} decreased as V_{applied} was increased [57]. At low field strengths (or with short pulses**), membranes still exhibited conductance fluctuations, but did not rupture. However, there appeared a critical voltage, V_{c}, above which irreversible breakdown became very likely [92].

1.4.3 Electroporation Models

The first major efforts to explain the outcomes of electroporation in terms of a mechanistic theory were made by Chizmadzhev, Arakelyan, Pastushenko *et al.* in

**Upon the application of a voltage step, the membrane, acting as a capacitor, accumulates a charge across its leaflets. This build-up of charge causes a current to be produced, recorded as a capacitative 'spike' in the I_{m} trace (see Figure 1.8). As the charge gathers to its maximum value, the current drops until the capacitor (bilayer) is fully charged (See Section 2.4.1). Ignoring losses elsewhere in the circuit, when the membrane is fully charged, it experiences the full applied voltage, *i.e.* $V_{\mathrm{m}} = V_{\mathrm{applied}}$. However, the bilayer takes a finite period of time to fully charge; should the voltage pulse to the membrane last less than this charging time, the bilayer will not experience the entirety of V_{applied}.

a series of seven papers in 1979, based on their experimental observations [57, 93–98]. Whilst models based on compression of the membrane in response to the transmembrane potential were put forward [99], along with those that suggested defects may result from the coming together of opposing leaflets during fluctuating, wave-like undulations in the bilayer [100] these failed to explain the stochastic nature of the process, and at times made poor estimates of the potential at which a membrane is expected to rupture [92, 101].

Furthermore, measurements of the change in capacitance C_{m} of the membrane determined that ΔC_{m} occurred rapidly (hundreds of milliseconds), with increases of at most (and in many cases far below) 3–5 % under voltages of several hundred millivolts [92, 102, 103]. Increases in C_{m} are a result of membrane thinning and area increase; such changes are an expected response of the bilayer as a capacitor to the application of a transmembrane voltage and resultant charge accumulation on its surfaces [103]. Although a change in C_{m} takes place, it was found that after compression, the capacitance remained constant until rupture, which would argue strongly against any large-scale electrocompression that precedes bilayer breakdown. The greatest failing, however, was that electrocompression models could not explain how pore formation might be reversible. They predicted that breakdown would only initiate beyond a critical voltage, in conflict with the observations stochastic membrane lifetimes and conductance fluctuations that are influenced by V_{applied}.

This lack of compatibility largely spelled the end for electrocompression theories, and along with studies showing that membranes are transiently permeant to ions and DNA under electric fields, pore formation was seen as the most likely mechanism.

1.4.3.1 Hydrophobic & Hydrophilic Pore Formation

Chizmadzhev *et al.* proposed that the observations of increased electrical conductance, transient permeability to small molecules, or total breakdown of the membrane, were the result of the generation of numerous *hydrophilic pores*, membrane-spanning defects in which the lipid headgroups line the edge of a water-filled inclusion [57]. The mechanism of their voltage-dependent formation, sometimes

called the transient aqueous pore hypothesis, remains the foundation of current electroporation theory.

The formation of hydrophilic pores is depicted in Figure 1.9. This toroidal geometry is a significant rearrangement from the unperturbed bilayer, and does not form directly; the energy barrier to its formation shall be considered later in this work. Toroidal pores form via a cylindrical transmembrane defect involving only an in-plane parting of the lipid molecules, termed a *hydrophobic pore*. This process is sometimes called an 'inversion' of the hydrophobic pore.

The distinction between the two pore types arises from the nature of the pore walls. Hydrophobic pores expose the (hydrophobic) bilayer interior to the surrounding electrolyte. In the absence of such a defect, it has been estimated by continuum dielectric models that the energy of a monovalent ion within the hydrophobic bilayer core may be given by:

$$w = \frac{z^2 e_0^2}{8\pi\epsilon_0 r_\mathrm{i}} \left(\frac{1}{\epsilon_\mathrm{m}} - \frac{1}{\epsilon_\mathrm{w}} \right) - \frac{z^2 e_0^2}{4\pi\epsilon_0 \epsilon_\mathrm{m} d_\mathrm{m}} \ln \left(\frac{2\epsilon_\mathrm{w}}{\epsilon_\mathrm{w} + \epsilon_\mathrm{m}} \right) \tag{1.1}$$

where z is the ion valency, e_0 is the elementary charge, ϵ_0 is the permittivity of free space, r_i the radius of the ion, d_m the bilayer thickness, and ϵ_m and ϵ_w are the relative permittivities of the bilayer core (∼2) and electrolyte (∼80 for water) respectively. The first term derives from the Born equation[††] and estimates the energy of moving the ion from the bulk electrolyte into the bilayer, whilst the second term makes a correction due to the membrane being relatively thin [105]. Such models, along with MD simulations, estimates the barrier to ion entry into the bilayer to be $w \simeq$ 40–70 $k_\mathrm{B}T$ [106, 107]. In the case of an ion within a hydrophobic pore, this energy barrier is reduced; however, for the ion crossing the bilayer within a 5 Å water-lined hydrophobic defect [106] w is still around 10 $k_\mathrm{B}T$ and therefore the hydrophobic pore is unlikely to allow significant passage of charged molecules. On the other hand, the headgroup-lined lumen of hydrophilic pores readily permits flow of electrolytes

[††]The Born equation, $\Delta_{\mathrm{solv.}} G^{\ominus} = -\frac{z^2 e_0^2 N_\mathrm{A}}{8\pi\epsilon_0 r_i}(1 - \frac{1}{\epsilon_\mathrm{r}})$, estimates the free energy of solvation of an ion of radius r_i using an electrostatic model that considers the transition of the ion from a vacuum to a continuous dielectric medium of relative permittivity ϵ_r [104].

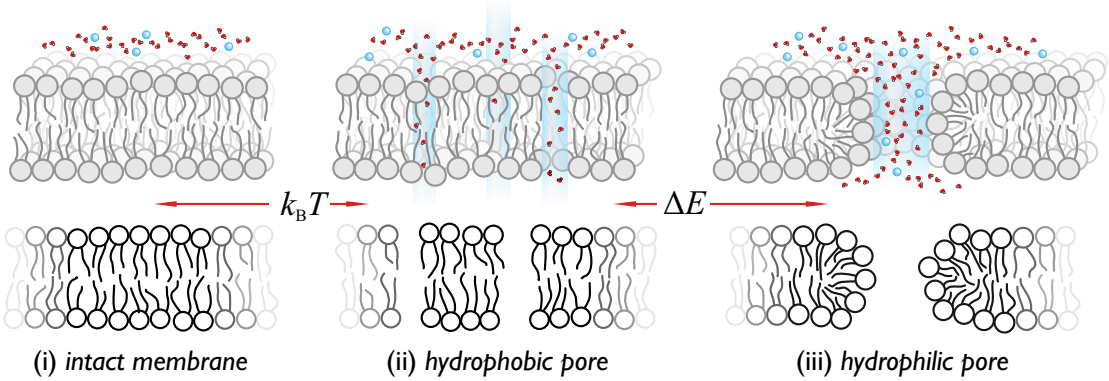


Figure 1.9: The transient, aqueous defects that form the basis of electroporation theory. An intact membrane (*i*) is subject to thermal fluctuations, that generate hydrophobic pores (*ii*). These permit translocation of water (*red/grey*), but limit the passage of ions (*blue*). At sufficiently large radii, the unfavourable interaction between the tailgroups and water encourage a lipid rearrangement to form a hydrophilic pore (*iii*). However, the barrier to this process must be overcome by an input of energy, ΔE. In electroporation, this is provided by the electric field. The energetics of this process shall be covered in Chapters 2–4.

across the membrane. For this reason, these hydrophobic and hydrophilic defects are sometimes referred to as non-conducting and conducting pores respectively.

Thermal fluctuations and the fluidity of the bilayer mean that lipid molecules are in constant lateral motion [34, 108]. Hydrophobic pores may arise therefore as a result of these thermal fluctuations [94, 109]. As discussed previously, lipid structures in aqueous environments arrange themselves to minimise contact between the tailgroups and water (see Section 1.2.1), and as such a cylindrical pore is not predicted to be long-lived, and can therefore proceed in one of two ways: (1) the parted lipids return and close the pore, or; (2) the phospholipids reorientate to line the pore with their headgroups [57]. Without the input of additional energy, however, the barrier to conversion to a hydrophilic pore is too large to be overcome by the thermal energy, estimated to be of the order of several tens of $k_B T$ [110, 111].

Under normal circumstances, then, hydrophilic pores do not spontaneously form within the membrane, as any hydrophobic defects generated quickly collapse, and the membrane retains its integrity [109]. However, with an external input of energy from an electric field, the barrier to hydrophobic pore inversion may be surmounted,

producing membrane-spanning, conductive defects characteristic of electroporation. Removal of the field results in pore closure, as the hydrophilic pore can no longer be sustained. Should the magnitude of the field be great enough, the theory also shows that this permits a pore to continue to expand until the bilayer is destroyed. The way in which this happens, along with how the electric field favours pore formation, will be covered in Chapter 2, where the theoretical treatment and the mathematical apparatus for describing electroporation shall also be considered in greater detail.

1.4.4 Applications & Protocols

The nature of the electroporation protocol that is applied and therefore outcome of permeabilisation depend on the cellular system being targeted: the electroporation protocol must induce the correct change in membrane permeability. There are many reviews that cover electroporation applications; for two broad surveys, the reader might see the reviews by Haberl *et al.* [112] and Yarmush and colleagues [113], however the most common applications and their general considerations are briefly outlined here.

Introducing genes or drugs requires that cells are only transiently porated (termed reversible electroporation), such that pores are open for a sufficient period and are of sufficient size to allow entry of the material [114], but this protocol must not come with any deleterious effects, namely: pores must not be too large or open too long so as to result in material loss from the cells; pores must not be too large to result in destruction of the membrane; they must seal over a sensible timeframe (milliseconds to at most a few minutes [115]); and there should be no (or limited) thermal effects of the transmembrane voltage. This applies to several applications including that of gene transfection discussed in the previous section. Electrochemotherapy involves local chemotherapeutic drug delivery of poorly-permeant drugs such as cisplatin or bleomycin to cancerous tissues [25, 116]. Protecting organisms against disease by introducing engineered DNA that elicits immunological responses (DNA vaccination) and gene therapy, the treatment of diseases (such as cancer) by transfecting cells with genetic material [113, 117] also have these requirements.

In the case of applications such as the degradation of tumour tissue [21, 118–120], large pores that render the cells non-viable, or complete rupture of membranes (generally termed irreversible electroporation in the literature) is required, however there needs to be minimal damage to surrounding connective tissue or blood vessels, either by thermal [121] or electrolytic effects [122]. Whilst more work needs to be done on assessing and controlling the secondary effects of ablation by electroporation, for example inducing cardiac arrhythmia [123, 124], it has been found to have advantage over thermal or radiation-based ablative techniques, in that it appears to result in reduced disruption of neighbouring vessels and nerves [118, 119], bioactive species such as antigens, or of the extracellular matrix in the porated region [125], allowing for more rapid tissue regeneration [112] (and references therein). That said, the thermal effects of electroporation are currently one of the majorly-contested areas in the field. Electroporation, in terms of its nature, is almost always cited as a non-thermal technique [21, 118, 119, 122], however, there is an inevitable temperature increase due to Joule heating [121]. In *in vivo* electroporation, this increase has been found to vary depending on the voltage protocol, placement of electrodes, and the nature of the targeted cells. Heating during ablation treatments of various tissues in porcine, canine and other mammalian tissues can show a range of temperature increases from as little as 1 °C to as large as 10–40 °C [126, 127]. In the case of the latter, however, the increases 1 cm away from the ablation zone are often less than 5 °C. Whilst tissues are clearly able to dissipate thermal increases, the degree to which thermal effects influence neighbouring healthy tissue, and the short- and long-term outcomes in terms of efficacy (especially in the context of medical treatment where thermal damage could negate the structure-maintaining benefits of irreversible electroporation) are still being assessed [126–128].

Such considerations will also be required in the newly-reported applications of wound disinfection [19] and reduction of scar tissue in murine models [129] by Golberg, Yarmush and co-workers. On the other hand, in sterilisation protocols [18], and in the food industry where electroporation is utilised to enhance the extraction of proteins, vitamins, fruity juices and colour from plant matter such as apples,

sugar beet or grapes [130], in preservation [131], and dehydration (amongst others) [20], alternative considerations regarding surrounding material damage must be made, again unique to the application in question.

A great many protocols therefore exist to account for these requirements, with the maintenance of cell viability or the minimisation of surrounding tissue damage often the most crucial considerations. These voltage protocols, across almost all electroporation uses, take the form of a sequence of square-wave pulses, which are between several hundred and several thousand volts per centimetre in amplitude, and nano- to milliseconds in duration [19, 21, 22, 88, 131, 132]. The number of pulses, pulse amplitude, pulse width and pulse spacing are all varied to suit the target membranes, with these parameters dictating the degree of poration.

With the idea of applying a short, high-voltage pulse in mind, one might consider the similarity between electroporation protocols and the pulses delivered during life-saving cardiac defibrillation. During this process, the shock depolarises the heart muscle, halting irregular electrical activity and allowing the heart to re-establish its natural rhythm. Defibrillation shocks are on the order of milliseconds, and for the pulse to be effective across the entire organ, the amplitude must be of the order of several hundred to a thousand volts [133]. It is unsurprising therefore that myocardial tissue has been found to undergo electroporation under such stimuli [134, 135]. As a result, questions have been raised as to whether electroporation is pro- or antiarrhythmic during the defibrillation mechanism, and its possible role in causing post-shock cell damage and impaired cardiac function [134, 136, 137].

1.4.5 Current Outlook

The sequence that leads to electroporation, proposed in 1979 by Abidor *et al.* and subsequently (mathematically) refined in the following decades [57, 109, 138, 139], has been borne out in molecular dynamics simulations, which have demonstrated the formation of hydrophilic channels from membrane-spanning hydrophobic pores (Figure 1.10, *right*) [77, 111, 140, 141], and along with experimental verification

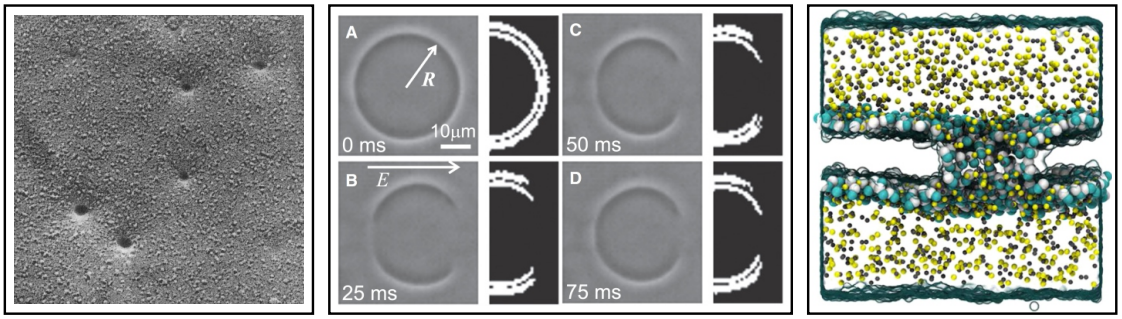


Figure 1.10: Electropore imaging studies. *Left*: Volcano-like depressions in the extracellular face of a red blood cell imaged at 60,000× magnification, 3 ms after the application of an electroporating pulse, as observed by rapid freezing of the cells followed by electron microscopy. Adapted from [144]. *Centre*: A vesicle subjected to a 5 ms pulse of 50 $kV \cdot m^{-1}$ shows large pore formation at the poles facing the electrodes. Adapted from [146]. *Right*: Cross-section of a toroidal pore of radius 1.8 nm formed in a POPC membrane, as modelled by a molecular dynamics simulation. Headgroups are green and white; sodium and chloride ions are yellow and grey, with water and the lipid tails transparent. Adapted from [76].

of pore formation [142, 143], the transient aqueous pore hypothesis continues as the accepted mechanism that underlies electroporation.

Nevertheless, studies have indicated a lack of complete understanding regarding the phenomenon. Chang and Reese imaged volcano-like structures on the surfaces of electropermeabilised red blood cells, Figure 1.10 (*left*) indicating structures on the scale of tens to hundreds of nanometres [144]; in GUVs, however, pores are observed to be micrometres across, Figure 1.10 (*centre*) [62, 145, 146]. Furthermore, resealing rates in cells are on the order of seconds to minutes [138, 143, 147], but milliseconds in GUVs [146, 148], and nanoseconds in MD simulations [111, 149].

In short, there is still much to be learned about the governing mechanisms of electroporation. Furthermore, a lack of visualisation methodologies means that predictions about pore behaviour remain unverified. By its very nature, electroporation is a difficult phenomenon to study experimentally. Pores are transient, opening and closing on very short timescales, and are on the most part too small be visualised. Despite the fact that its mechanism is still not fully understood, the wide range of applications that electroporation lends itself to broadens the case for improving our comprehension of electroporation mechanisms. Experimental studies such as this are therefore not solely academic, for refinement

of the existing theories will improve our models and in turn permit more effective use of electropermeabilisation to manipulate the biological cell membrane.

1.5 Bilayer Interrogation Techniques

The following outlines the basis of the experimental techniques that will be used in this work to investigate pore formation in DIBs. Whilst it gives an outline of the main principles, further information relevant to their application to droplet-interface bilayers may be found in the following chapters.

1.5.1 Electrophysiology

Electrophysiological methods are those that monitor the electrical properties of biological systems. They have been indispensable in studies involving the electrical behaviour of cardiac tissue, neuronal signalling, and the properties of membrane-bound voltage-gated ion channels, porins and transporters [150–153]. As these systems suggest, electrophysiology may be used to investigate individual proteins, single cells or entire organs. Ion channels are now understood to regulate the electrical properties of these larger tissues, but channel malfunction can also result in disease, such as cystic fibrosis, epilepsy, cardio-vascular and neuro-muscular diseases [151]. Such is the importance of understanding ion channels that Erwin Neher and Bert Sakmann were awarded a Nobel Prize in Medicine in 1991[‡‡] for developing single-channel electrophysiological techniques that showed for the first time the gating of single, isolated channels [154].

Electrophysiology usually involves either measurement of the current passing through membrane pores or channels under a fixed (applied) voltage, or monitoring the voltage response of the system after an injection of a current stimulus (more common in cardiac and neuron studies, where signal transduction is driven by changes in voltage known as action potentials) [153]. In the case of single proteins, they could be endogenous molecules, interrogated by monitoring or excising a

[‡‡]The Nobel Prizes for Chemistry in 1997 and 2003 were also awarded for work on ion channels.

patch of naturally occurring cell membrane (as in Neher and Sackmann's work), or channels reconstituted in artificial bilayers [155].

In the context of this work, electrophysiology is used to characterise the bulk electrical properties of DIBs (Chapter 2), used alongside optical measurements of calcium flux through electropores (Chapters 3 and 4) and to probe pore formation by antimicrobial peptides (Chapter 5). This work makes use of the voltage clamp, a methodology in which the membrane current is measured as a response to the applied transmembrane voltage. Although the physical setup shall be detailed in the relevant sections of the following chapters, it is useful to outline the principles of operation here.

1.5.1.1 The Voltage Clamp

The fundamental structure of the voltage clamp is shown in Figure 1.11. It is based around an analogue circuit element called an *operational amplifier*, or *op-amp*, in an elegant configuration termed a *current-to-voltage converter*.

The op-amp, Figure 1.11a, is a comparator: its output voltage V_{out} is equal to $A_{\text{v}}(V_{+} - V_{-})$, that is the difference between the inverting $(-)$ and the non-inverting $(+)$ inputs, amplified by a large factor A_{v}, called the gain. If, for example, the inverting input is raised to an input voltage V_{in} and the inverting input is grounded, shown in Figure 1.11b, V_{out} will simply be equal to V_{in} multiplied by the gain (so long as the supply voltage is large enough to produce an output of this magnitude).

Incorporating *negative feedback* into the system, Figure 1.11c, alters the op-amp behaviour. Feeding some of the output voltage back decreases the differential between the inputs. This reduces V_{out}, leading to a rise in the input differential, and the cycle begins again. An equilibrium is reached where the amplifier outputs a voltage that forces the inverting input to lie just below V_{in}, such that the right amount of (a very small) differential is amplified to generate the correct output voltage, hence maintaining the balance.

The utility of this is realised when the bilayer system to be interrogated is connected to the inverting input (Figure 1.11d). As discussed, the inverting input

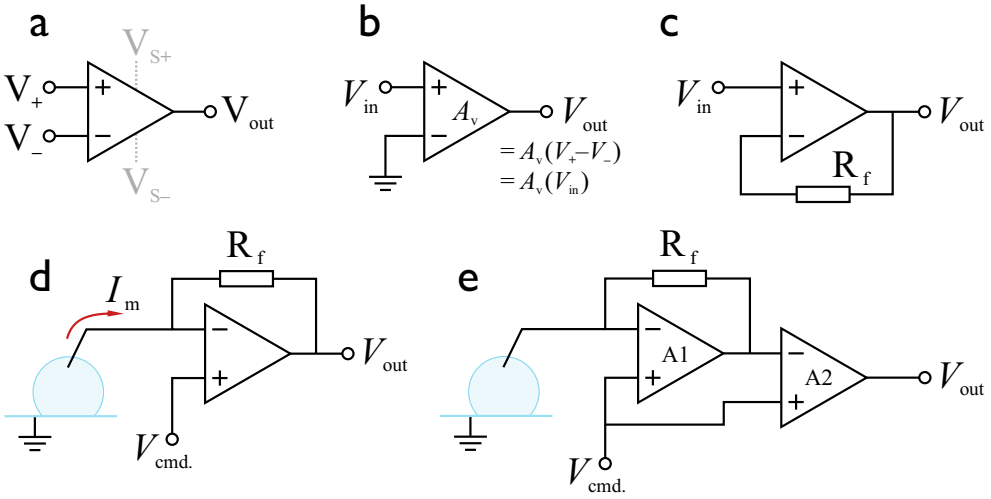


Figure 1.11: Voltage clamp and current measurement circuits. (a) Schematic of an operational amplifier (op-amp). The device amplifies the difference between the non-inverting (+) and inverting (−) inputs, limited to its supply voltages fed to V_{S+} and V_{S-} (these supplies have been omitted elsewhere in the figure for clarity). V_{out} is equal to $A_v(V_+ - V_-)$, where A_v is the amplifier gain. The example in (b) highlights this relationship, where grounding the inverting input causes V_{out} to follow V_{in}. (c) A negative feedback element, the resistor R_f, forces the op-amp to generate a voltage that keeps the inverting input at a potential just below the non-inverting input. (d) When applied to a measurement setup, this may be used to clamp the bilayer at a potential dictated by the command voltage $V_{cmd.}$. Membrane currents must travel through R_f, therefore this circuit is said to be a current-voltage converter, as (part of) the signal at V_{out} is proportional to I_m, with the constant of proportionality being R_f. (e) A differential amplifier A2 separates the command voltage from the bilayer signal coming from the I–V converter (A1).

will follow the voltage at the non-inverting input. This means that a command voltage $V_{cmd.}$ set at the non-inverting input will be applied to the membrane. Should the bilayer be electrically active, for example through ion channels or electropores, the membrane current, I_m, will vary at the inverting input. Vitally, the op-amp draws (essentially) no current [156], and therefore I_m can only travel through the feedback resistor R_f. A signal is therefore constantly fed to V_{out} that is directly proportional to the membrane current, that is $V_{out} = I_m R_f$ [157]. Figure 1.11e shows the (simplified) final setup, in which a second op-amp, wired as a differential amplifier, separates the applied voltage from the bilayer signal.

This simple configuration allows for the simultaneous injection of voltage and the monitoring of the resulting transmembrane current with a single pair of electrodes. Furthermore, and crucially for nanometre-sized channels or pores which have very

small conductances, appropriate choice of components within the I–V converter allows a sensitivity of down to picoamperes [156]. In practical terms, the current-to-voltage converter circuitry is housed within a *headstage*, which feeds I–V data back to a *patch-clamp amplifier*, which can correct for electrical artefacts and from where the command voltage is controlled. Such a setup shall be detailed in Chapter 2.

1.5.2 Total Internal Reflection Fluorescence Microscopy

Total internal reflection fluorescence (TIRF) microscopy is a sensitive optical technique commonly used to interrogate the interface between liquids and solids [158], by means of illuminating the boundary between them. In the experiments described, the effect is used to excite those fluorophores contained in the droplet that reside with a limited volume above the membrane, or labelled molecules within the bilayer. The ability to observe single molecules or localised, isolated fluorescence events is greatly advantageous in membrane studies, as it allows the behaviour of *individual* species or phenomena to be probed. This is in contrast to bulk measurements, which by their very nature produce an ensemble average, obscuring the behaviour and contributions of the system's individual components.

1.5.2.1 Fluorescence

The absorption of a photon by a molecule results in a concomitant increase in that molecule's energy. If the energy of the photon is sufficient, this increase can manifest itself as a promotion of an electron to a state of higher energy than that of the ground (resting) state of the molecule. Fluorescence, photon emission between states of the same spin multiplicity, is one of the processes by which such an excited molecule, typically containing an aromatic moiety, may relax from this electronically excited state.

Figure 1.12 shows a Jablonski diagram, a representation of the processes that may occur as a result of photon absorption, depicting the ground state, S_0, the first two excited singlet states, S_1 and S_2, and the first excited triplet state, T_1.

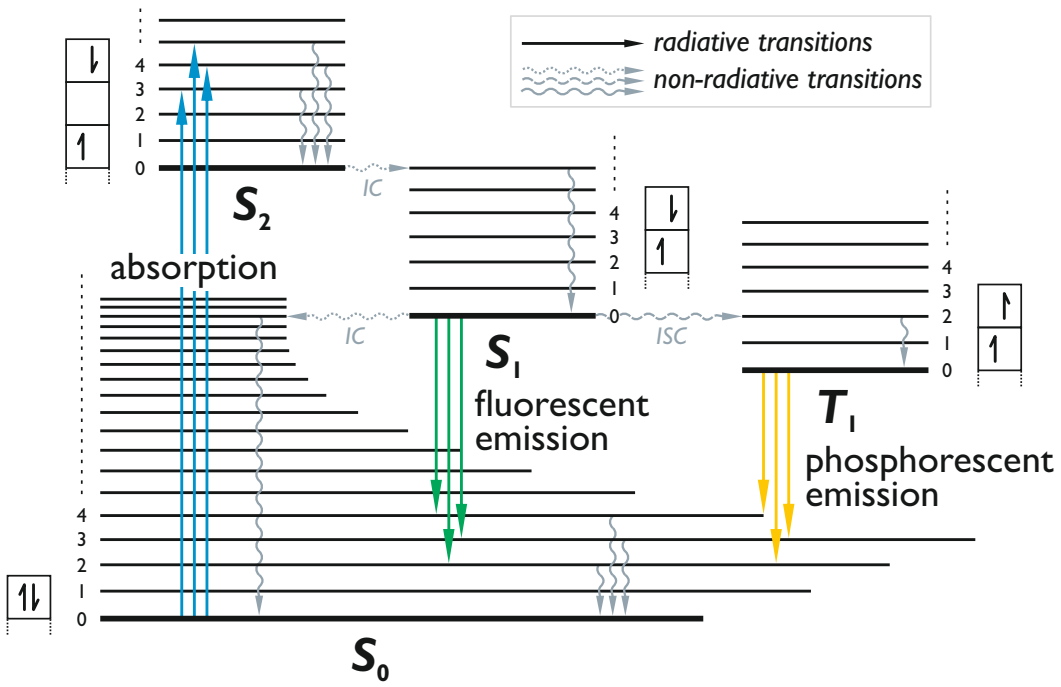


Figure 1.12: Jablonski diagram depicting the common decay routes of an excited fluorophore, along with simplified electron configurations. The vertical axis is indicative of the relative energies of these states, each of which may be in one of many vibrational levels (0, 1, 2, 3 etc.). Vertical wavy lines indicate vibrational relaxation; absorption and emission (vertical solid lines) usually take place from the configurations with the lowest vibrational energy. Horizontal wavy lines show some possible spin-allowed internal conversion (IC) and spin-forbidden intersystem crossing (ISC) pathways. *N.B.* Not all transitions and possible excitation levels of the molecule have been shown.

Each of these electronic configurations can exist in a number of vibrational energy levels, denoted $\nu = 0,\ 1,\ 2,\ 3$ etc.

Typically, the ground state of a molecule is a *singlet* state, in which all electrons are spin-paired (one 'up' and one 'down') in the molecular orbitals, and given the label S_0. Interaction between a photon of sufficient energy and an electron in this state will result in that electron's promotion to a configuration of higher energy, taking $\sim 10^{-15}$ s [159]. However, any promotion that involves the inversion of electron spin is forbidden by quantum laws, and so excitation produces an *excited singlet* state ($S_1,\ S_2,\ S_3\ \ldots$), with the electrons remaining spin-paired.

The energy input not only alters the electron configuration to a singlet state of higher energy, but it also raises the vibrational energy of the molecule. In solution, however, intermolecular collisional dissipation of this energy quickly brings the

excited singlet to its lowest vibrational level, $\nu = 0$. The system then rapidly ($\sim 10^{-12}$ s) converts to the lowest energy excited singlet state (in this scheme, S_2 becoming S_1). This is called internal conversion (IC), the interconversion of states with the same spin multiplicity, and takes place if there is sufficient overlap (similarity) between the wavefunctions of the singlet states. Vibrational relaxation causes the molecule to then relax to the lowest vibrational level of S_1.

From here, internal conversion to S_0 is possible but slow because there is poor overlap between the $\nu = 0$ S_1 state and the similar energy, high vibrational state of S_0. Relaxation to the ground state therefore takes place by the release of a photon, usually to an elevated vibrational level, which quickly ($\sim 10^{-12}$ s) relaxes. This cycle of photon absorption and release is known as fluorescence, and takes around 10^{-8} s [159]. Since the release of the photon occurs from a state of lower energy than that populated by the excitation, the emitted photon is of lower energy and hence the emission wavelength is always longer than the excitation wavelength.

The first excited singlet may also decay in other ways. The excitation energy may be removed by a quencher, a molecule that relaxes the fluorophore back to the ground state without photon emission. Another major pathway is that of phosphorescence, photon emission between states of differing spin multiplicity. Although forbidden, coupling between the electron spin and orbital angular momenta in S_1 allows a slow spin flip to take place by *intersystem crossing* (ISC), producing an excited *triplet* state (T_1), with unpaired spins (right hand side of Figure 1.12). This process is however slow, as is the spin-forbidden regeneration of the singlet ground state by phosphorescent photon emission, resulting in phosphorescence lifetimes of milliseconds to seconds. In the absence of a quenching molecule, then, fluorescence outcompetes phosphorescence, providing when illuminated a constant, rapid ($\sim 10^{8}$ s^{-1}) source of photons at wavelengths that may be separated from the excitation light.

1.5.2.2 TIRF Theory

Total internal reflection (TIR) occurs when light propagating through a medium of refractive index n_1, such as glass, meets the boundary with a medium having a lower index of refraction, n_2, for example an aqueous solution. The light will undergo TIR when the angle of incidence, θ_i, measured from the normal to the interface, exceeds the critical angle, θ_c, defined by [158]:

$$\theta_\mathrm{c} = sin^{-1}\frac{n_2}{n_1}. \tag{1.2}$$

When this is the case (*i.e.* when $\theta_\mathrm{i} > \theta_\mathrm{c}$), the beam is reflected back into the n_1 medium. At the same time however, an electromagnetic field is generated which propagates a small distance beyond the n_1/n_2 interface. This field, which oscillates parallel to the plane of incidence, is termed an evanescent wave. The intensity of the electric field component of the wave — the component that will interact with a fluorescent molecule — decays exponentially with increasing distance z from the surface along the normal axis:

$$I(z) = I_0 e^{-z/d} \tag{1.3}$$

where I_0 is the intensity at the interface ($z = 0$). The distance that the field travels into the second medium is given by:

$$d = \frac{\lambda_0}{4\pi}[n_1^2 sin^2\theta_\mathrm{i} - n_2^2]^{-\frac{1}{2}} \tag{1.4}$$

with λ_0 being the wavelength of the incident light in a vacuum. The depth d is on the order of λ_0 [158], decreasing with increasing θ_i.

In the setup used in this work, both the correct angle of incidence and observation of the sample are achieved using a specialised objective lens, in a setup shown in Figure 1.13. The n_1 and n_2 media are a glass coverslip and the hydrated agarose substrate respectively. For glass and pure water, these refractive indices are $n_1 \simeq 1.45$ and $n_2 \simeq 1.33$, with θ_c equal to 66.5°. For excitation with blue laser light, $\lambda_0 = 473$ nm, the most common wavelength used in the experiments described within this thesis, the evanescent wave is therefore expected to travel

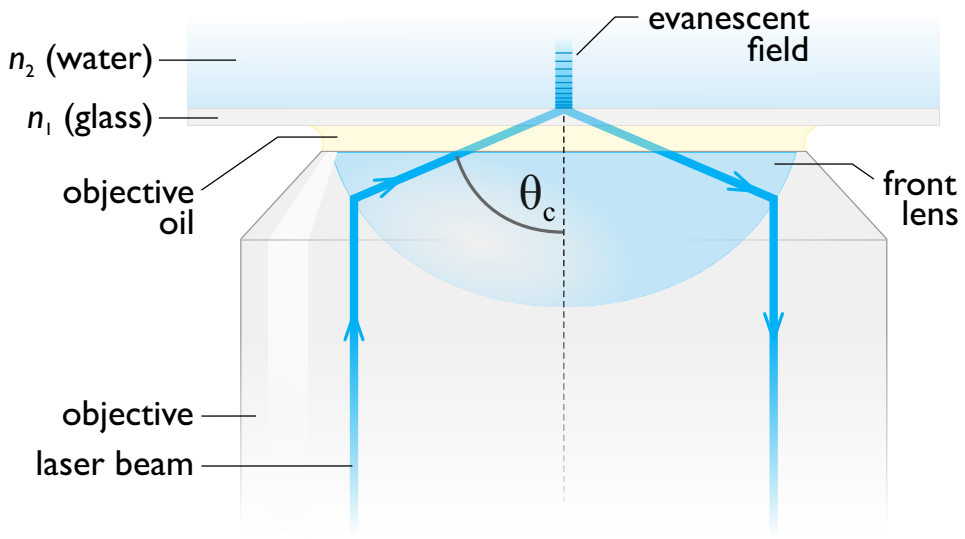


Figure 1.13: Objective-based total internal reflection. The cartoon depicts an aqueous sample with refractive index n_2 resting on a glass coverslip, which has refractive index n_1. The objective makes contact with the glass via index-matched oil (matched to n_1), which ensures that light continues to travel through media with refractive index n_1 between leaving the lens and entering the coverslip. An incident laser beam (*blue*) is aligned such that it is refracted through the front lens at just over the critical angle, θ_c; at the interface between n_1 and n_2, the light is totally internally reflected, generating an evanescent field that propagates into the sample.

$d = 335$ nm into the aqueous solution, decaying rapidly from the glass surface. This provides, then, a means of selectively illuminating those fluorophores localised to the bilayer. This is advantageous in increasing the signal-to-noise ratio (SNR) of fluorescent measurements: restricting the excitation to a limited volume reduces the amount of unwanted emitted light collected from fluorophores in the bulk solution. The specific application of TIRF microscopy to DIBs as used in the experiments presented in this work shall be covered in the introduction to Chapter 3, where its utilisation in optical single-channel recording shall be explained.

2

Electroporation in DIBs: Electrical Characterisation

In this chapter, the electrical characterisation of voltage-driven pore formation in lipid bilayers is presented, along with its underlying theory. The response of DIBs under various voltage protocols was investigated, in order to visualise the current response as a result of electropore formation, and to determine the factors that influence the electrical stability of the bilayer. These are the first in-depth electrical studies of electropore formation in DIBs.

2.1 Introduction

Electrophysiological measurements have been used to characterise electroporation in all applicable* membrane systems [57, 62, 142, 160], for the obvious reason that pores give rise to a passageway for conductive ions to flow. Although the resulting currents are small (10^{-12} A), this flux is detectable using the electrophysiological techniques discussed in Chapter 1. As a fundamentally electrical phenomenon, these types of investigations are therefore a sound starting point when studying electroporation.

Before presenting the findings of the electrical characterisation of electroporation in DIBs, however, in the following section the theoretical basis of the phenomenon

*Cell suspensions, individual cells or their membrane patches, BLMs, vesicles, DIBs may all be interrogated electrically, however SLBs formed directly on a support are often inaccessible to electrical measurements.

shall be outlined, in the interest of interpreting the results in this and the coming chapters in greater detail.

2.2 Theory of Electroporation

2.2.1 Formation of Transient Aqueous Pores

Membrane-spanning pores are thought to exist in one of two lipid configurations, as introduced in the previous chapter (Figure 2.1a). In the hydrophobic pore, the lipids are simply parted with respect to an intact membrane, as a result of thermal fluctuations [109]. However, the unfavourable interactions that result from internalisation of water into the bilayer core in the presence of such a defect encourages any expansion of the pore beyond a radius r^* to be accompanied by a lipid rearrangement. This rearrangement is such that the pore wall is lined with lipid headgroups, a configuration termed a toroidal or hydrophilic defect. The energy of this state is given by a function comprised of two competing terms:

$$E_{\text{hydrophilic, V=0}} = 2\pi r\gamma - \pi r^2\sigma \tag{2.1}$$

where r is the radius of the pore, γ is the line tension, and σ is the surface tension of the membrane [57, 109]. The two terms are competing since the line tension, the energy per unit length associated with the pore walls, works to contract the pore, whilst the surface tension attempts to expand it. The line tension and surface tension are of the order of 10^{-11} J·m^{-1} and 10^{-3} J·m^{-2} respectively [109, 146, 161]; for a pore of 1 nm, the line tension term in equation 2.1 is two orders of magnitude larger than that of the surface tension. Any pore formed will therefore reseal immediately.

Subjecting a bilayer membrane to an electric field will modify equation 2.1. In the presence of an electric field, the dielectric of a parallel plate capacitor experiences an electrocompressive stress perpendicular to the surface, proportional to the square of the voltage V across the dielectric [102, 162]:

$$p_{\text{elec.}} = \frac{1}{2}\epsilon_{\text{m}}\epsilon_0(\frac{V}{h_{\text{e}}})^2 \tag{2.2}$$

which has units of pressure, and in which ϵ_{m} is the relative permittivity of the membrane, ϵ_0 is the permittivity of free space and h_{e} is the dielectric (*i.e.* hydrocarbon tail) thickness of the membrane. Since the bilayer is almost incompressible, this stress is associated with an increase in membrane area, and thus an additional surface tension:

$$\sigma_{\mathrm{elec.}} = \frac{1}{2}\epsilon_{\mathrm{m}}\epsilon_0(\frac{d_{\mathrm{m}}}{h_{\mathrm{e}}^2})V^2 \tag{2.3}$$

where d_{m} is the total bilayer thickness. The application of a potential difference V across the bilayer modifies the expression for the hydrophilic pore thus:

$$E_{\mathrm{hydrophilic,\ V\neq 0}} = 2\pi r\gamma - \pi r^2\sigma - \pi r^2 a_p V^2 \tag{2.4}$$

where

$$\begin{aligned} a_p &= \frac{1}{2d_{\mathrm{m}}}(\epsilon_{\mathrm{w}} - \epsilon_{\mathrm{m}})\epsilon_0 \\ &= \frac{1}{2}(\frac{\epsilon_{\mathrm{w}}}{\epsilon_{\mathrm{m}}} - 1)C_0 \end{aligned} \tag{2.5}$$

with ϵ_{w} being the relative permittivity of water[†]. $C_0 = \frac{\epsilon_0\epsilon_{\mathrm{m}}}{d_{\mathrm{m}}}$ is the specific capacitance[‡] of the membrane. This additional term therefore describes the electrocompressive and capacitative changes as a result of the transmembrane voltage and of replacing low permittivity lipid with high permittivity water upon pore formation [163]. Put simply, this voltage-dependent term in the hydrophilic pore energy effectively augments the membrane surface tension.

Equation 2.4 is plotted in Figure 2.1b, for several values of V_{applied}, using the parameters from [109], which are those commonly used in the electroporation literature ($\gamma = 1.8\times10^{-11}$ J·m^{-1} and $\sigma = 1\times10^{-3}$ J·m^{-2}). The quadratic function behaves thus: any formation of a pore will result in a movement up the energy curve at low radii. Since this raises the free energy of the system, the pore returns to $r = 0$, so long as no fluctuation in radius can expand the pore beyond the turning point in the curve. This turning point, referred to as the critical point,

[†]Note that the difference between h_{e} and d_{m} is small, and so in approximating $h_{\mathrm{e}} \simeq d_{\mathrm{m}}$, equation 2.3 and the last term in equation 2.4 take the same form.

[‡]Capacitance per unit area, F·m^{-2}.

may be found by differentiating equation 2.1 with respect to r and setting the result equal to zero, which yields:

$$\Delta E_{\mathrm{c}} = \pi\gamma^2/\sigma \tag{2.6}$$

and

$$r_{\mathrm{c}} = \gamma/\sigma. \tag{2.7}$$

A pore with a radius larger than that at the turning point (the critical radius, r_{c}) will be in a position to continuously expand, since this will reduce the free energy of the system. In other words, beyond r_{c}, which according to equation 2.7 is of the order of a few tens of nanometres, the bilayer ruptures. However, the barrier to rupture, ΔE_{c}, is large on the scale of the thermal energy, and so any formed pores cannot fluctuate to such radii. However, the application of a potential reduces this energy barrier, and pulls r_{c} to smaller radii. At some value of V_{applied}, the barrier to unbounded pore expansion vanishes.

The form of the hydrophobic pore energy has been modelled by Glaser *et al.* as:

$$E_{\mathrm{hydrophobic,\ V=0}} = 2\pi r d_{\mathrm{m}} \sigma(r) \tag{2.8}$$

where $\sigma(r)$ is the interfacial tension between the lipid tails and water in terms of modified Bessel functions [110]. This interfacial tension rises steeply with increasing radius, but is slightly reduced at very small radii (see the dashed lines in Figure 2.1c). The hydrophobic pore walls necessarily order the water within the pore (see Chapter 1), and the larger the pore the greater the number of water molecules that are restricted, leading to the rise in energy. However, at small radii, the regions of ordered water overlap, decreasing the (expected) total ordering, thus leading to a small reduction in $\sigma(r)$ at small r. Nevertheless, the function rises sharply with the pore radius, making the spontaneous formation of large hydrophobic pores highly unlikely.

In order to construct the model of pore formation, one further consideration is required regarding the barrier to hydrophilic pore closure. Pore closure requires that the lipid headgroup-lined pore walls are brought in close proximity, and therefore repulsive interactions arise from the headgroups themselves and any

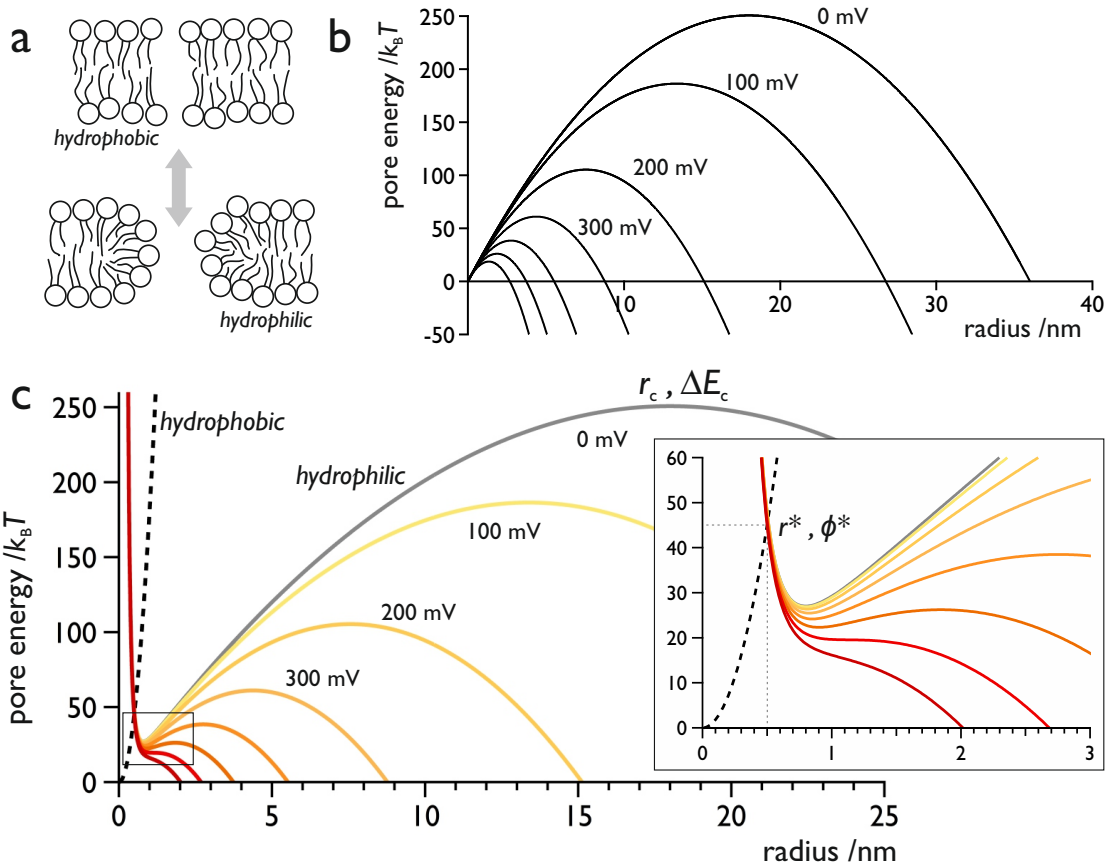


Figure 2.1: Electroporation theory. (a) Structures of the hydrophobic and hydrophilic pores around which the theory of electropermeabilisation is based. (b) Equation 2.4 plotted using common values [109] for the membrane parameters at various voltages. As the voltage increases, the barrier to membrane rupture diminishes. (c) Electroporation energy curves taking both the hydrophobic (*dashed*) and hydrophilic (*solid*) energies into account. *Inset*: At radii just beyond the crossover point r^* between the hydrophobic and hydrophilic energy curves there exists a a local minimum, which supports a population of toroidal pores. Increasing the voltage broadens this minimum; at higher voltages, the minimum vanishes and any toroidal pore formed will expand unhindered until the bilayer is destroyed.

bound ions, along with an energy barrier to removing the interfacial water from the headgroups. Neu and Krassowska approximated the pore wall interactions and lipid rearrangement contribution to equation 2.4 as $(\frac{C}{r})^4$, where C is a constant given as 9.67×10^{-15} J$^{\frac{1}{4}}\cdot$m [109][§]. In the same work, in which they built upon the original theory by Abidor and colleagues, they found that the Bessel functions Glaser *et al.*

[§]The power and the value of the constant were chosen to match the predictions made by Glaser *et al.*, such that the modified hydrophilic energy curves of Neu and Krassowska would intersect that of the hydrophobic pore at the values of r^* and ϕ^* experimentally estimated by Glaser and co-workers.

used to describe the hydrophobic pore could be approximated to a quadratic form. The commonly used pair of equations used to describe electroporation became:

$$E_{\text{hydrophilic, V}\neq 0} = 2\pi r\gamma - \pi r^2\sigma - \pi r^2 a_p V^2 + (\frac{C}{r})^4 \tag{2.9}$$

and

$$E_{\text{hydrophobic}} \simeq \phi^*(\frac{r}{r^*})^2 \tag{2.10}$$

with ϕ^* the local energy maximum at the intersection between the hydrophobic and hydrophilic curves, and r^* the corresponding radius [109]. ϕ^* is therefore the energy barrier to hydrophilic pore formation.

Equations 2.9 and 2.10 are plotted in Figure 2.1c. Based on the above theory, the sequence of electroporation events is as follows. In the absence of the electric field, thermal fluctuations generate hydrophobic pores, which seal rapidly due to the dominating line tension. Application of a voltage augments the surface tension, which encourages expansion of pores. Now, when hydrophobic pores open, they are converted to hydrophilic pores if their radius exceeds r^*. Once ϕ^* has been surmounted, the pore exists within a local (energy) minimum bounded by ϕ^* at low radii and the energy barrier at the critical radius at large radii. Thermal fluctuations modulate the size of the pore; any fluctuation that brings the radius beneath r^* closes the defect. As the potential is increased, the local hydrophilic minimum broadens and the critical barrier ΔE_c diminishes. Eventually, this barrier is removed altogether and application of a potential above a critical voltage V_c allows the immediate generation of a continually expanding pore from a hydrophobic one and the bilayer is destroyed. This is not to say however that there can be no rupture of the membrane by unbounded pore expansion if the applied voltage is below V_c. Sufficiently near the critical voltage, when the barrier ΔE_c is still present but has been greatly reduced, fluctuations in radius space can still form a critical pore, if such a fluctuation is able to expand the pore radius beyond r_c.

2.2.2 The Role of the Electric Field

The term containing voltage in equation 2.4 describes an effective change in surface tension as a response to the electric field, due to water (high permittivity) replacing the lipid tails (low permittivity) in the space occupied by the pore. That is, electroporation theory only considers the effect of the field *once a pore has been formed*. Whilst it is the case that in the presence of an electric field the dielectric of the membrane, as a parallel plate capacitor, experiences a pressure proportional to the square of the voltage across it, the electroporation theory does not tell us if the field interacts with the membrane in order to *form* pores, or how it might do so.

In fact, by the equations presented above, the field does not *need* to be pore forming. Thermal fluctuations are expected to create hydrophobic pores in the absence of a field; these brief hydrophobic pore openings are thought to be the cause basal rates of ion permeation through membranes [164, 165]. Any expansion of the pore results in a rearrangement of the lipids to form a toroidal pore, as discussed in the previous section, but this is hugely disfavoured by the line tension, which closes it. In the presence of an electric field, however, the appearance of the third term in equation 2.4 augments the intrinsic surface tension of the membrane which allows the line tension to be counteracted. The field in this model is therefore not pore *forming*, but pore *stabilising*.

However, the electric field has been predicted to aid in the pore formation process. The understanding of the interaction between the electric field and the membrane preceding electroporation has largely come from molecular dynamics simulations.

The force $\mathbf{F}$ on a molecule in an electric field gradient is given by:

$$\mathbf{F} = \boldsymbol{\mu} \cdot \nabla \mathbf{E} \tag{2.11}$$

where the vector quantites $\boldsymbol{\mu}$ and $\mathbf{E}$ are the dipole moment of the molecule and the local electric field respectively [164]. In the case of electroporation, where the field is usually normal to the bilayer surface (*i.e.* aligned along the z-axis), of interest is the component of the force normal to the membrane [77]:

$$F_z = \mu_z \frac{\partial \mathbf{E}}{\partial z}. \tag{2.12}$$

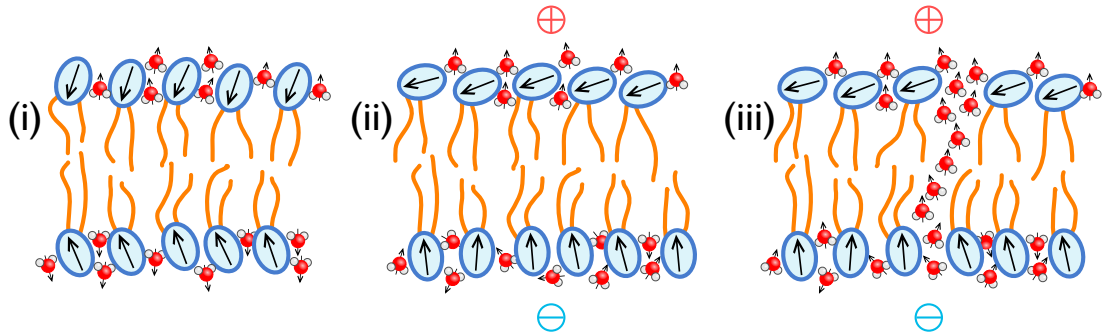


Figure 2.2: The alignment of interfacial water molecules during electropore initiation. (*i*) In the absence of an electric field, the water molecules at the lipid tail/headgroup interface have aligned dipoles (shown by black arrows) due to interaction with the dipoles of the lipid headgroups. (*ii*) An electric field reinforces the dipole alignment at the anodic side, but changes that water orientation at the cathodic leaflet. The headgroup dipoles also attempt to align with the field. (*iii*) Interfacial water realignment encourages deeper penetration into the hydrophobic core, leading to increased chance of water channel formation across the bilayer.

In the presence of an electric field, the dipole of water is subjected to a torque as the partial charges of the oxygen (δ^-) and hydrogen (δ^+) atoms align with the field. MD simulations indicate that alignment of the so-called interfacial water molecules (those that reside at the headgroup/lipid tail interface) aid in pore initiation [164, 166], which is shown schematically in Figure 2.2 for a bilayer containing a single species of zwitterionic phospholipid. For such a lipid, the headgroups also possesses a dipole due to the negatively charged phosphate moiety near the lipid tails and the positively charged terminal alcohol (for example choline or ethanolamine; see Chapter 1). In the absence of a field (Figure 2.2*i*), the interfacial water molecules are already partially aligned due to the interaction of the δ^+ and δ^- charges of water with the charges in the headgroup [141]. When an electric field is applied, the dipoles in the system attempt to align with it, as described above. The field therefore reinforces alignment of the water molecules on one face of the bilayer (in this case the anodic leaflet), and weakens the orientation of water at the other, depicted in Figure 2.2*ii* [77, 164]. The lipid headgroups are also subjected to this force, but their packing prevents large-scale dipole re-alignment, and the small alignment that takes place is not predicted to contribute directly to pore formation. In simulations of bilayers over 15–20 ns at minimum porating fields of $\sim$320 mV·nm^{-1}, the mean

$N^+ \rightarrow P^-$ (headgroup) dipole angle shifts less than 5° relative to the zero-field case for POPC, DPPC and DOPC [164, 167], and those lipids that become involved in the pore walls show no significant change in headgroup dipole angle until *after* the formation of the hydrophobic pore and the headgroups begin to associate with the growing water column [167]. Furthermore, removal of the (lipid) dipole by setting all headgroup charges to zero does not prevent the formation of water defects [164]; in an even more simplified system, 3.5 nm slabs of octane in water at similar field strengths formed water channels in the same way as lipid bilayers [77].

In the absence of an external field (in a perfectly *symmetric* membrane system), the alignment of water and the headgroups in opposing leaflets produces a local field at each leaflet, the two of which are of equal magnitude but opposing directions. The applied field has the effect of increasing the force F_z on the interfacial water molecules at the anodic side, which leads to deeper penetration of water into the bilayer core and increased likelihood of hydrophobic pore formation [77, 164]. However, some simulated membranes have been found to porate from the cathodic leaflet, such as DOPC, or form defects from both leaflets [164]. It appears that the balance of local electrostatics and the properties of the lipid, at least in these simulations, play an important role. In the case of DOPC, it was suggested that the unsaturated tails, leading to a larger area per lipid, allows more water into the interfacial region; when a potential is applied, re-alignment at the cathodic leaflet (see Figures 2.2*ii* and *iii*) points the electronegative oxygen of water towards the bilayer interior, exposing it to the positive field in the membrane and drawing it in.

2.2.3 The Stages of Pore Formation in MD Simulations

In general, *in silico* bilayer models are formed using several hundred molecules of a chosen lipid, which is equilibrated with several thousand water molecules either side of the bilayer, sometimes with the inclusion of simple electrolytes [140, 141, 149]. The volume under study is usually of the order of tens of nanometres across, so in order to mitigate effects that might result from the small system size, the model is subject to periodic boundary conditions. Once the system is stable, the

simulated application of an electric field can be affected most commonly by one of two methods. In the charge imbalance method, the transmembrane potential is set up through differing salt concentrations either side of the bilayer [76]. Alternatively, a force is applied to all atoms bearing a charge q_i such that $F = q_i E$, where E is the external electric field [140]. The applied fields are of the order of 0.1–1 V·nm^{-1}, with simulations running to 100s of nanoseconds.

Electroporation in MD studies under these conditions invariably takes place in three stages [140, 149, 166]. Firstly, as a result of water alignment, local depressions appear in the membrane surface. Next, these depressions deepen, allowing water to traverse the membrane. When this happens, there is a molecular rearrangement of the lipids in the vicinity of the water file, with the migration of the lipid headgroups finally generating a hydrophilic pore. The formation of the inital defects and water channels appear to be stochastic, as is predicted by the electroporation model: the time taken for pore initiation in simulations depends on the strength of the electric field, but in general takes 2–25 ns, with conversion to a hydrophilic pore taking place within under 5 ns thereafter [149, 164, 166, 167]. Similar timescales have been found in BLM and cellular studies either observing increases in conductivity or permeability to fluorescent dyes or other molecules, in which application of pulses as short as 4 ns could induce electroporation [168–171]. The final simulated hydrophilic pores are of the order of 1–5 nm in radius [76, 149, 166, 172], which are of the order of those generated in model and cellular membrane systems [143, 173].

Molecular dynamics is therefore a useful tool in predicting the early stages of electroporation, giving an indication as to the mechanisms of pore formation at a molecular level. However, at present, and likely due to constraints imposed by computing power, simulations have a limit with regard to making predictions about electroporation over longer timescales or in more complex systems, such as those with multiple pores or membrane environments with containing more than a handful components, as would be required to model the processes that take place *in vivo*. That said, some studies over the last few years have tackled these more complex environments. One such study modelled electroporation in *in silico* models of the

outer membranes of the Gram-positive and Gram-negative bacteria[¶] *Staphylococcus aureus* (modelled using a mixture composed of PG, (the unusual) lysyl-PG and cardiolipin) and *Escherichia coli* (the outer leaflet composed of lipopolysaccharide (LPS), and the inner a mixture of PE, PG and cardiolipin) [175]. The study found that electroporation in the Gram-positive membranes took place via the same stages outlined above for simpler bilayers (under similar electric fields and on similar timescales), with similar defect formation in one leaflet, followed by insertion of water into the membrane leading to the generation of a membrane spanning water column, and finally formation of hydrophilic pores with movement of the lipid headgroups into the pore walls. In the *E. coli* outer membrane model, however, defect formation always took place from the inner leaflet regardless of the direction of the applied field, and the large LPS molecules could not begin to move into the pore until phospholipid molecules from the inner leaflet had reached through to the outer leaflet and a full hydrophilic pore had formed. This meant that the Gram-negative membranes were more resistant to electroporation, with water penetration into the bilayer not always leading to pore formation; furthermore, whereas the Gram-positive pores was stable over 100 ns of simulation, the *E. coli* defects collapsed back to a pore-free membrane in 30 ns after pore formation. It is hoped that expansion of models such as these to even larger systems or the more complex geometries of a cell will continue, so that we may 'visualise' the processes taking place on the molecular scale, and support the experimental findings that come from investigating electroporation in real systems.

[¶]Bacteria are often classified as either Gram-positive or Gram-negative, depending on their appearance after a commonly used staining technique used to differentiate them, called the Gram stain. Gram-positive species possess a single bilayer outside of which there is a thick layer of peptidoglycan anchored to the bilayer [174]. Gram-negative bacteria have an inner and an outer membrane, with a thin layer of peptidoglycan in the periplasmic space. The inner membrane is made of phospholipids but the outer membrane is an asymmetric structure, the inner leaflet composed of phospholipids and the outer leaflet of lipopolysaccharides (LPS).

2.3 Materials & Methods

2.3.1 Materials

1,2-diphytanoyl-*sn*-glycero-3-phosphocholine (DPhPC) was purchased from Avanti Polar Lipids (Alabaster, Alabama, USA) or Lipoid (Ludwigshafen, Germany) and used without further purification. The majority of other materials were acquired from Sigma-Aldrich (Dorset, UK) and similiarly used as shipped, unless otherwise stated. Doubly deionised 18 MΩ·cm Milli-Q water (Direct-Q, Millipore Corporation, Massachusetts, USA) was used throughout. Electrolyte solutions containing potassium chloride were buffered with 10 mM HEPES (4-(2-hydroxyethyl)-1-piperazineethanesulfonic acid) and adjusted to pH 6.97–7.02 with potassium hydroxide, with the pH being monitored using a pH meter probe. Phosphate-buffered saline (PBS) solutions were prepared from standard tablets: one tablet was dissolved in 200 mL of deionized water, yielding a solution containing 10 mM phosphate buffer, 2.7 mM potassium chloride and 137 mM sodium chloride at pH 7.4. Potassium solutions were treated overnight with Chelex resin (200-400 mesh, Bio-Rad, UK) in order to remove divalent cations, with the resin subsequently removed using a 0.22 μm Steriflip disposable filter (Millipore Corporation). Glass coverslips measured 24 mm × 40 mm, thickness No.1 (Menzel-Gläzer, ThermoFisher Scientific, UK). Devices and incubation chambers were purpose-machined from polymethyl methacrylate (PMMA, RS Components, UK) on a Roland Modela MDX40 CNC (computer numerical control) machine using 0.5–3 mm square-end mills.

2.3.2 Conductivity Measurements

The conductivity of the electrolyte solutions was measured at a room temperature of 21.1 °C using a Mettler Toledo FG3 meter with LE703 probe (Mettler Toledo, Leicester, UK), calibrated with a standard reference solution of 12.88 mS·cm^{-1}. Three separate measurements were taken. For the 1.5 M KCl, 10 mM HEPES, pH 6.98 solution, the average of these three measurements was 143.9 ± 0.4 mS·cm^{-1}.

2.3.3 Lipid Stock Solutions

Lipid arrives from the supplier in lyophilised powder form. A small quantity (∼25 mg) was dissolved in chloroform and transferred to a pre-weighed glass vial (Supelco, Pennsylvania, USA). The solvent was evaporated-off using a nitrogen stream, and the vial left under vacuum for at least 30 minutes to remove any remaining chloroform. The mass of dry lipid was recorded, and the appropriate volume of chloroform was added so as to form a stock solution of between 10 and 50 mg·mL^{-1} lipids in chloroform. Stocks were kept at −20 °C. Fresh mixtures of lipid-in-hexadecane were made from the chloroform stock at the start of each experiment, since lipids are highly hydroscopic, and their viscosity and propensity to form bilayers varies with the age of the lipid-in-oil solution. When a device was to be prepared, the appropriate volume of (chloroform) stock ws transferred to a vial, the solvent evaporated by a nitrogen gas stream and the vial placed under vacuum as before, after which the corresponding volume of hexadecane was added to achieve a concentration of 8.7 mg·mL^{-1}.

2.3.4 Agarose Solutions

Aliquots of dry, powdered agarose were autoclaved and stored at room temperature. Two types were used: hydrogel substrates were formed from ultra-low gelling point agarose (gel point 8–17 °C) dissolved in Milli-Q water at 0.75 % (wt./vol.); the rehydrating agarose consisted of low gelling point agarose (gel point 26–30 °C) dissolved in the appropriate buffered electrolyte solution at 1.5 % (wt./vol.). These solutions were prepared in 1.5 mL microcentrifuge tubes and placed in an electric bath (both Eppendorf, UK) at 90 °C for 20 minutes in order for them to homogenise.

2.3.5 Ag/AgCl Electrodes

The ground electrode was made from 1.5 mm diameter silver wire, and the electrode for insertion into the droplet (the 'driving' electrode) was 100 µm diameter silver wire (both 99.9 % purity; Sigma-Aldrich). They were soldered onto polyvinyl chloride (PVC)-shielded copper wire (RS Components), at the other end of which

was soldered a connector for linking to the headstage of the patch-clamp amplifier. The silver portion of the electrodes were treated in 30 % (vol./vol.) aqueous solution of fresh sodium hypochlorite, the coating process taking ∼30 minutes for the 0.1 mm driving electrode and several hours for the ground.

2.3.6 Device Preparation

All droplet-hydrogel bilayer experiments were carried out using a small PMMA apparatus containing 16 wells, measuring 43 mm × 27 mm × 4.2 mm, designed and fabricated in the lab. This apparatus, termed a 'device', is shown in Figure 2.3. Devices were prepared in the following manner. Firstly, coverslips were subjected to an oxygen plasma for several minutes. This serves to clean the surface, and render the surface hydrophilic, encouraging spreading of the substrate agarose solution. (Furthermore, as will be relevant in the forthcoming chapters, this process also reduces background fluorescence by destroying any organic matter present.) A cleaned coverslip was placed inside a spin-coater (WS-650M2-23NPP/LITE, Laurell Technologies, USA), held in position by vacuum suction. 140 μL of the 0.75 % (wt./vol.) ultra-low gelling agarose solution, which had been kept at 90 °C, was pipetted onto the centre of the coverslip, which was subsequently spun at 4000 r.p.m. for 30 s. The resulting dried agarose layer has been estimated to be ∼100 nm in thickness [176]. Devices were cleaned vigorously with distilled water, ethanol and 10 % Decon 90 (Decon, UK) solution with the aid of a toothbrush and brief sonication (USC-TH bath sonicator; VWR, UK), then dried using a nitrogen gas stream.

The coated coverslip was placed on the underside of the device within a 0.2 mm recess (see Figure 2.3a and d) and affixed in place using adhesive tape. This served to seal the gap between the glass and PMMA surfaces, in order to prevent evaporation of water from the hydrating agarose, which was introduced subsequently. The purpose of the latter is to keep the substrate agarose hydrated (see Figure 2.3b). The device was inverted and placed glass-down on a clean surface. 165 μL of hydrating agarose solution, 1.5 % (wt./vol.) low gelling agarose in (typically) 1.5 M buffered KCl, was pipetted at 90 °C into the device via one of the filling holes

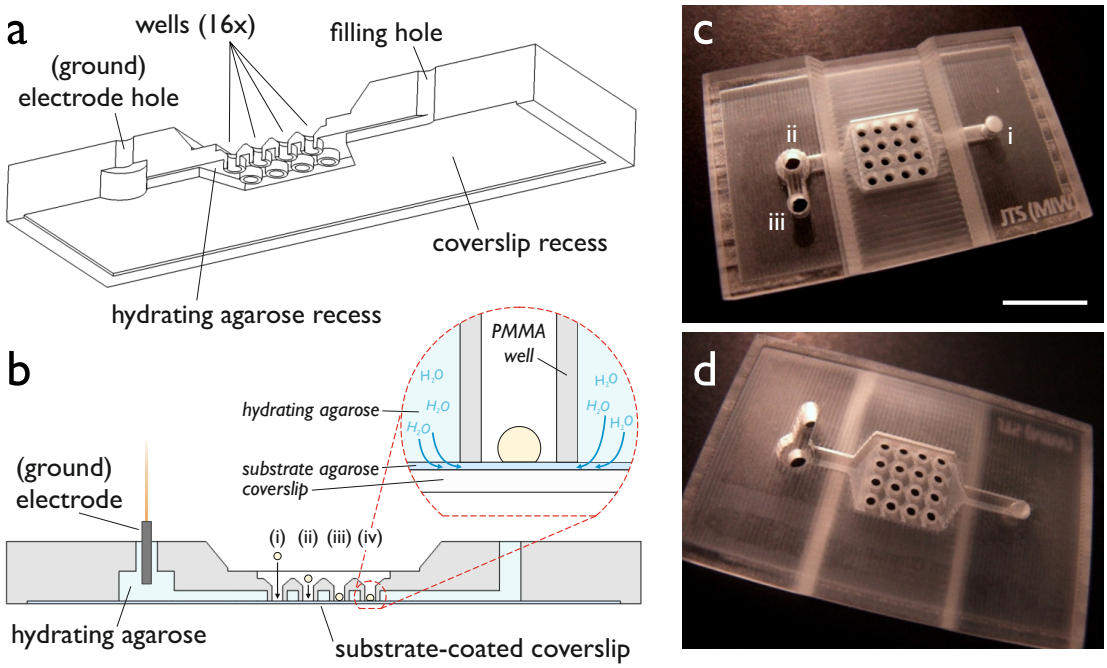


Figure 2.3: The PMMA device used to form DIBs. (a) Cut-through, as viewed from the underside. (b) Side-on cartoon of an assembled device, again as a cut-through. Once the substrate agarose (dark blue) has been spun onto a coverslip, this is then placed within the recess seen in (a). Hydrating agarose (light blue) is then flowed through the device, where it flows around the wells, but does not cover the substrate. Roman numerals represent placing a droplet (yellow) within a well (*i*–*ii*), its sinking towards the substrate under gravity (*ii*–*iii*) and formation of a bilayer (*iv*). *Inset*: Cartoon of a well containing a DIB. Dotted arrows indicate movement of water and electrolyte into the substrate from the hydrating agarose. (c) Photograph of a device from above; this side faces upwards during experiments and is the face from which the device is filled and that droplets are placed in the wells. The device is filled with the hydrating agarose from filling hole (*i*), flowing from right to left until it emerges from the filling holes on the opposite side. Opening *i* is covered, and the ground electrode inserted into *ii*. Opening *iii* serves as an overflow during electrode insertion, after which it is covered. See Figure 2.4 for a constructed device. Scale bar: 1 mm. (d) View of the underside, revealing the well 'pillars' and the 0.2 mm recess into which the coverslip sits.

(*i*, Figure 2.3c). This solution was introduced continuously until the liquid front emerged from the holes on the opposing side (from *ii* and *iii*, Figure 2.3c). Care was taken so as not to introduce air bubbles which would dry the surrounding hydrogel, causing an offset in electrolyte concentrations either side of the membrane. The ground electrode was coated in a small volume of hydrating agarose solution, which prevented incorporation of air when inserted into the device. The hole labelled *iii* in Figure 2.3c acts as an overflow when the electrode is inserted. The filling

and overflow holes were then covered using laboratory adhesive labels (Tough-Tags, Sigma-Aldrich). A prepared device is shown in Figure 2.4.

2.3.7 Experimental Setup

The prepared device was placed on the stage of an inverted microscope (Nikon Ti-U Eclipse, Nikon Instruments UK), which rested on a self-levelling vibration insulation table (Thorlabs, Ely, UK). The stage was mounted in the base of a steel Faraday cage fabricated specifically for use on the microscope, Figure 2.4b, whose purpose was to isolate the device, electrodes and headstage from stray electrical interference. Line outlets, lights and other electronic equipment produce 60 Hz signals that can interfere with current recording. The metal walls of the cage interact with the interference, dissipating the alternating field as a current which is removed via a grounded lead [157]. The lead was connected to the ground of a patch-clamp amplifier (Axopatch 200B, Axon Instruments, Molecular Devices, California, USA); in the centre of the cage lid a wire mesh permitted illumination of the device from the microscope lamp above. A layer of Parafilm M (Bemis Flexible Packaging, Wisconsin, USA) was sandwiched between the underside of the device and the stage in order to isolate the device electrically. A square hole was cut in the film to allow optical access via objectives beneath. The ground electrode was plugged into the headstage of the patch clamp amplifier, which was separate from the main unit and kept within the Faraday cage. The tip of the driving electrode was coated in the 0.75 % (wt./vol.) substrate agarose solution, by application with a micropipette tip dipped in the molten solution. This was done to aid wetting of the electrode by the droplet, however, only the smallest region possible was coated — achieved by the application of the agarose via a pipette tip and viewed using a stereoscope; a view of this is shown in Figure 2.5b — otherwise the aqueous interior of a droplet tended to creep up the electrode, altering the bilayer area and often removing the droplet from the surface altogether. The driving electrode was then affixed to an xyz-micromanipulator (Narishige, Japan), also mounted within the cage, with three dials protruding from cut-outs in the cage walls to allow x-, y-

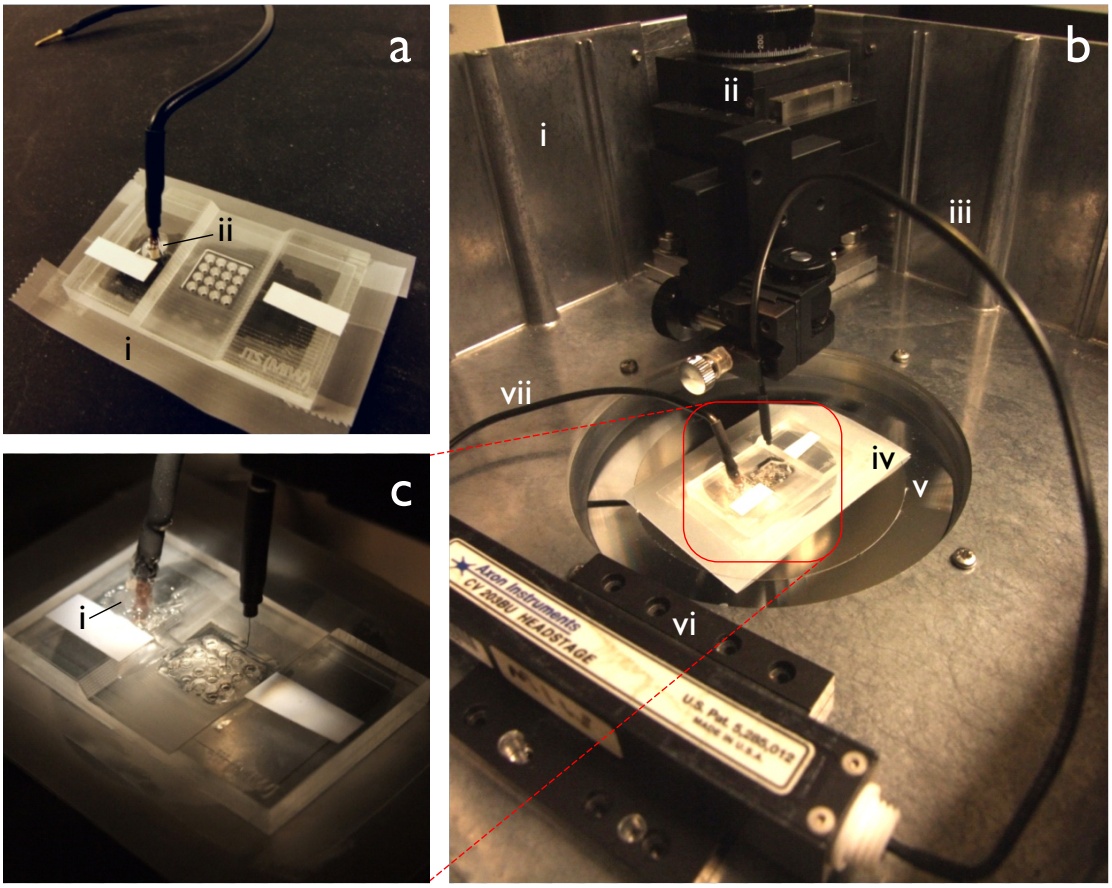


Figure 2.4: Electrical experiment setup. (a) Device ready for experiment. *i* indicates the adhesive tape used as a seal. The white strips close-off the overflow and filling holes (*i* and *iii* in Figure 2.3c). Excess agarose around the ground electrode entrance can be seen as a transparent mound, *ii*. The irregular darker region is hydrating agarose which seeps between the coverslip and the underside of the device during filling. (b) Setup for electrical recording, highlighting (clockwise): *i* the Faraday cage; *ii* three-axis micromanipulator; *iii* driving electrode and its attachment to *ii*; *iv* Parafilm isolating the device from the cage; *v* microscope stage insert, a central hole in which is just visible beneath the device and permits optical access; *vi* headstage, connected to the patch-clamp amplifier via leads which exit the cage through a small cut-out; *vii* ground electrode. (c) Close-up of the highlighted region in (b) showing the device during operation. The entrance made by the ground electrode has been sealed with vacuum grease, *i*.

and z-axis translation, and the other end connected to the headstage. Finally, the exposed agarose surrounding the ground electrode was covered in vacuum grease (Dow Corning, Michigan, USA), again to prevent drying-out (see Figure 2.4b).

2.3.8 Monolayer Formation

In order to form a bilayer, the aqueous surfaces to be brought together required that a lipid monolayer assemble upon them. 70 μL of the lipid-in-hexadecane solution earlier prepared was pipetted into the wells of a prepared device in two 35 μL applications. This was so that the travel on the pipette was not too great that control of solution egress was lost; the solution must be applied slowly to the top of the wells and the fluid allowed to flow down the sides, in order to prevent air bubbles being trapped at the agarose surface. The droplets were formed in a separate incubation 'tank', machined from PMMA containing parallel troughs approximately 2 mm wide (Figure 2.5a). Troughs were filled with 29 μL of the same lipid-in-oil mixture applied to the device, after which the aqueous component was then pipetted into the oil, with volumes in the range of 20–50 nL, either using a standard laboratory pipette, or a piezoelectric nanoinjector (Nanoliter 2000; World Precision Instruments, Sarasota, Florida, USA).

2.3.9 Bilayer Formation

After incubation, droplets were transferred individually to the centre of the 16 wells in the device via a pipette, care being taken to perform this action slowly so as to minimise disruption of the lipid monolayer. The droplets sink to the bottom of the device under the influence of gravity. Formation of a bilayer is evident as a visible circle concentric within the droplet diameter; focusing slightly above or below the surface of the interface improves contrast of the bilayer edge. A fully-formed bilayer is shown in Figure 2.5c.

The dependence of bilayer formation and their stability on the lipid concentration and the incubation time of both the device and the droplets was not investigated extensively, however it was found that increased incubation time led to an increase in the period of time taken for bilayer formation, as shown in Figure 2.6 for DPhPC. Lipid solutions became more viscous over time, decreasing the rate at which the droplet sank to the bottom of the well. Furthermore, it is possible that build-up of additional lipid layers around the aqueous structures retarded the apposition

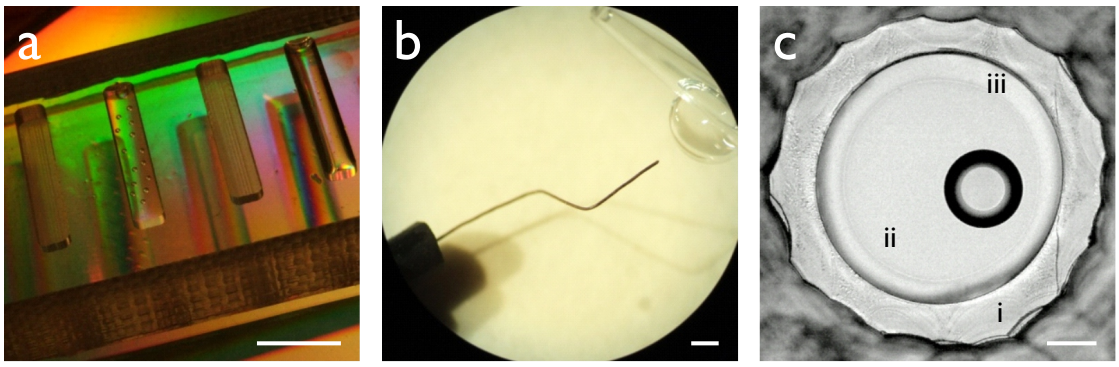


Figure 2.5: Monolayer and bilayer formation. (a) 18.4 nL droplets incubating in a tank. Scale bar: 5 mm. (b) View seen down a stereoscope when coating the tip of the 0.1 mm driving electrode in agarose, applied from a micropipette tip, seen top right. Scale bar: 1 mm. (c) Droplet with a fully-formed bilayer within a 1 mm well. Surface *i* is the wall of the well, or well 'pillar'. Within this can be seen a uniform grey circle on which the droplet sits, *ii*, surrounded by a lighter rim, *iii*. The former is the agarose substrate, the latter hydrating agarose that has seeped between the pillar and the coverslip. The bilayer can be seen as the bright ring in the centre of the droplet. Scale bar: 200 µm.

of the initial droplet and hydrogel monolayers. Too low a lipid concentration, or too short an incubation time, however, and droplets were found to rupture immediately on contact with the planar surface.

It was found that a concentration of ∼8.7 mg·mL^{-1} did not result in a significant proportion of contact rupture and formed bilayers quickly after the aqueous surfaces were incubated. Concentrations of 9.0 mg·mL^{-1} and above resulted in rapid accumulation of monolayers, but meant that older droplets took too long to form bilayers. After successive adjustments, incubation times of 30 minutes for droplets and 15 minutes for the device were used. As may be noted from the range of the x- and y-axes in Figure 2.6, bilayer formation time appeared to be slightly more sensitive to the incubation period allowed for the device than that for the droplets. 'Over-incubation' of the device may be more problematic than for the droplets since pipetting of the latter during transfer to the device is likely to disturb and deplete any lipid multilayers which have accumulated, whereas those associated with the agarose receive no such agitation.

Droplets that did form lasting bilayers were found to be incredibly stable when unperturbed; in one circumstance in which a device had been left without dismantling, all eight droplets with bilayers were present nine days after their formation.

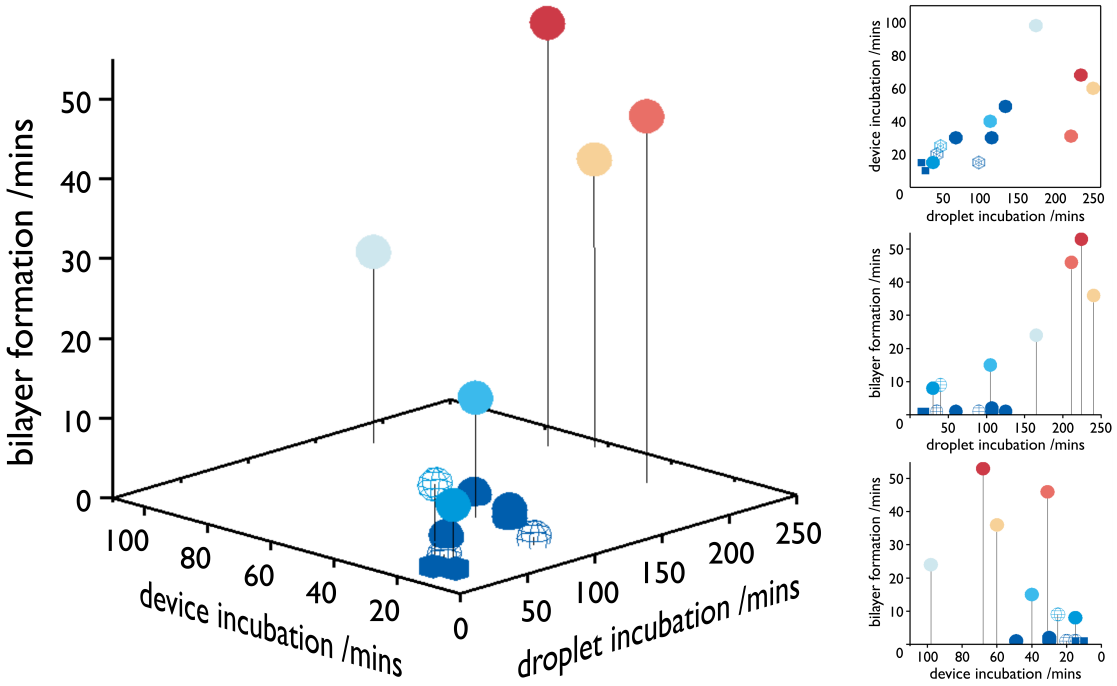


Figure 2.6: Dependence of bilayer formation on incubation time. Droplets tended to burst if either the device or the droplets were incubated for less than 15 minutes. Three lipid concentrations are presented: *open spheres*, 8.5 mg·mL^{-1}; *closed spheres*, 8.7 mg·mL^{-1}; *cubes*, 9.0 mg·mL^{-1}. Panels on the right-hand side show views along the principal axes.

2.3.10 Electrical Recording & Data Analysis

Once a bilayer had formed, the driving electrode was inserted from the top of the droplet. This process was aided by the presence of a small quantity of agarose applied to the tip (see Section 2.3.7 and Figure 2.5b).

Recordings were made through the Axopatch 200B amplifier which interfaced with a computer via a BNC-2090A rack-mountable connector block and an NI PCIe-6251 M-series data acquisition card (both National Instruments, Texas, USA). All unnecessary electrical equipment was switched off, including lights, to minimise noise. Measurements were filtered during acquisition at 1 kHz. Traces were recorded on WinEDR electrophysiology software (versions 3.2.6 to 3.7.2; John Dempster, Strathclyde University, UK) at 10.035 kHz. Voltage stimulus protocols were also designed and applied to the bilayer using this software. Alternatively, potentials of between 0 and ±1000 mV could be sent to the driving electrode using an interface

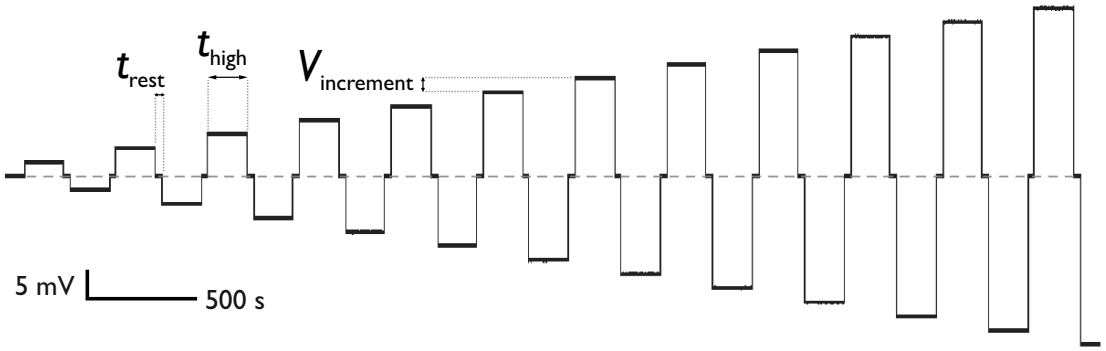


Figure 2.7: Example of a voltage protocol applied to characterise the electrical behaviour of DIBs, defined by the period that the potential is applied, t_{high}, the duration at 0 mV between voltage applications, t_{rest}, and the magnitude of the voltage increase at each step, $V_{increment}$. In this protocol the bilayer is subjected to between ±5 and ±300 mV, incremented in 5 mV intervals, for 180 s, with each potential separated by a 'rest' period of 30 s. The red dashed line indicates 0 mV.

on the patch-clamp amplifier.

Data for I–V curves were collected by exposing bilayers to voltage protocols designed within WinEDR. An example of such a protocol is depicted in Figure 2.7. It applies potentials in 5 mV increments for 180 s, with each step in voltage separated by a 30 s period at 0 mV. The purpose of this 'rest' period is to allow the bilayer to relax to its unperturbed state; GUV studies, including those in which the vesicles contain agarose, show pores reseal in 200 ms or less [146, 148]. Defects are therefore expected to close on similar timescales in agarose-based DIBs. As such, 30 s was considered ample for membrane recovery.

All experiments were conducted at a room temperature of around 21 °C. Electrical traces were analysed in WinEDR and IGOR Pro 6 or 7 (Wavemetrics, Oregon, USA). Errors are given as the standard deviation unless stated otherwise.

2.4 Results & Discussion

In order to investigate the electrical behaviour of DIBs, bilayers were subjected to voltage protocols that applied incrementally increasing voltage steps to the bilayer for many tens of seconds (Figure 2.7). These periods were chosen in order to observe at length the stochastic behaviour of electropores by means of their current fluctuations.

In cellular systems, application of voltages for extended periods is deleterious owing to material leakage or Joule heating, but in model membranes there exists no such requirement to preserve the integrity of the system. Interestingly, apart from the earliest studies where recording equipment was limited to chart recorders [82] or oscilloscope readouts [57], voltage-clamp conditions have not been used extensively in planar membrane models to investigate electroporation. Instead, current-clamp setups have been implemented in order to study longer-lived conductive pores [177, 178]. Under such a regime, clamping the current means that the transmembrane potential must vary in order to preserve Ohm's Law, and therefore a widening pore results in a drop in V_{m}. This negative feedback limits the size of V_{m}, preserving the membrane, and along with the tendency of BLMs to lack stability under long-lived (as opposed to pulsed) electric fields, there is an opening in the literature for extended voltage-clamp studies of electropores.

2.4.1 Ensemble Response

A representative current recording of a DIB in response to a voltage protocol (180 s 'high', 30 s rest, +5 mV increment) is shown in Figure 2.8a. Its features are common to every bilayer discussed in this work that was excited by a voltage.

The initial response of the membrane to a stepwise increase in V_{applied} is capacitative charging of the bilayer, Figure 2.8b. This is consistent with the double layer acting as a parallel-plate capacitor: a region of low relative permittivity material (the bilayer) within conductive electrolyte solution. Applying a voltage across a capacitor builds an equal and opposite charge across its plates, or in the case of a bilayer, across the leaflets of the membrane. The quantity relating dictating the magnitude of accumulated charge as a result of a voltage drop across a capacitor is termed its capacitance. During capacitor charging a displacement current flows as (opposing) charges build on the opposing leaflets, but exponentially decays rapidly to zero as the charge reaches its maximum value, since the diminishing accumulation leads to lesser and lesser movement of charge. The decay follows an exponential relationship, as detailed in Figure 2.9. The system may be modelled

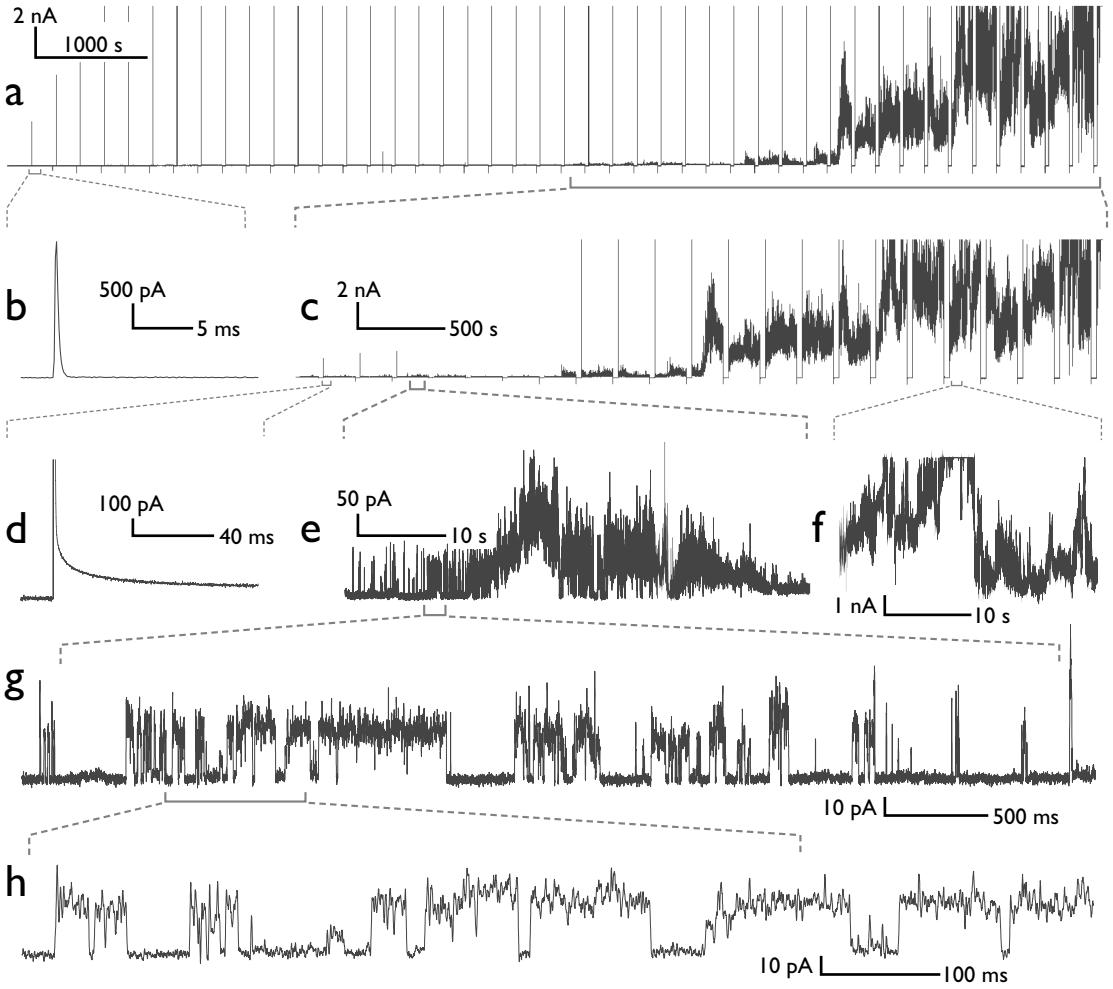


Figure 2.8: Current response of a DIB subjected to a voltage protocol with parameters $t_{\text{high}} = 180$ s, $t_{\text{rest}} = 30$ s, $V_{\text{increment}} = +5$ mV. (a) Complete current trace, up until bilayer rupture at 230 mV. (b–h) show expanded regions of (a), highlighting: (b) capacitative charging at 5 mV; (c) small fluctuations indicating electroporation onset at ∼120 mV; (d) capacitative charging at 120 mV; (e) fluctuations from the baseline conductance at 130 mV; (f) very large fluctuations with no constant baseline at 205 mV; (g) and (h) expansions of (e) showing small, discrete conductances. *N.B.* Traces at high voltages could only be recorded up to 10 nA, which was the upper recording limit of the Axopatch 200B amplifier.

by a simple circuit in which the voltage is supplied to the membrane (represented by a capacitor, C_{m}) via an external (*i.e.* non-membrane) series resistance ($R_{\mathrm{ext.}}$), which represents the resistance of the electrodes and the electrolyte [179]. In such a circuit, the voltage follows:

$$V_{\mathrm{applied}} = V_{\mathrm{R}} + V_{\mathrm{C}} = IR_{\mathrm{ext.}} + \frac{Q}{C_{\mathrm{m}}} \tag{2.13}$$

where V_{R} and V_{C} are the voltages across the resistor and capacitor in the circuit and Q is the charge on the capacitor. As mentioned, during charging, the charge on the capacitor increases and the current through the circuit diminishes. In other words, at t=0, there is no charge build-up on the capacitor and therefore $I = V_{\mathrm{applied}}/R_{\mathrm{ext.}}$, and as $t \to \infty$, $Q \to C_{\mathrm{m}}V_{\mathrm{applied}}$ and the current drops to zero. The current flow within the circuit follows:

$$I(t) = \frac{V_{\mathrm{applied}}}{R_{\mathrm{ext.}}} e^{-t/\tau_{\mathrm{cap.}}} \tag{2.14}$$

where $\tau_{\mathrm{cap.}}$, the charging constant, is characteristic of the circuit:

$$\tau_{\mathrm{cap.}} = R_{\mathrm{ext.}}C_{\mathrm{m}} \tag{2.15}$$

The charging constant represents the period of time taken for the capacitor to charge to ∼63.2 % of its maximum voltage[‖], or the displacement current to decay to ∼36.8 % of its value from a given time t. Fitting a single exponential to the decay in Figure 2.8b yields a time constant of 193.9 ± 1.3 µs. The value of the maximum current during the transitive spike, $I_{\mathrm{max.}}$, will occur at t=0; as can be seen from equation 2.14, $I_{\mathrm{max.}}$ can therefore be used to determine $R_{\mathrm{ext.}}$. This, along with the time constant, allows the membrane capacitance to be calculated. From the data in Figure 2.9, the membrane capacitance is found to be ∼107 pF. In this instance, the bilayer was approximately 140 µm in diameter, and therefore the specific capacitance was calculated to be ∼0.0069 F·m^{-2}. Although a rough estimate, this is in agreement with values previously calculated for DPhPC DIBs in

[‖]The capacitor charge follows a similar exponential relationship to that of the current in the circuit: $Q = C_{\mathrm{m}}V_{\mathrm{applied}}(1 - e^{-t/\tau_{\mathrm{cap.}}})$.

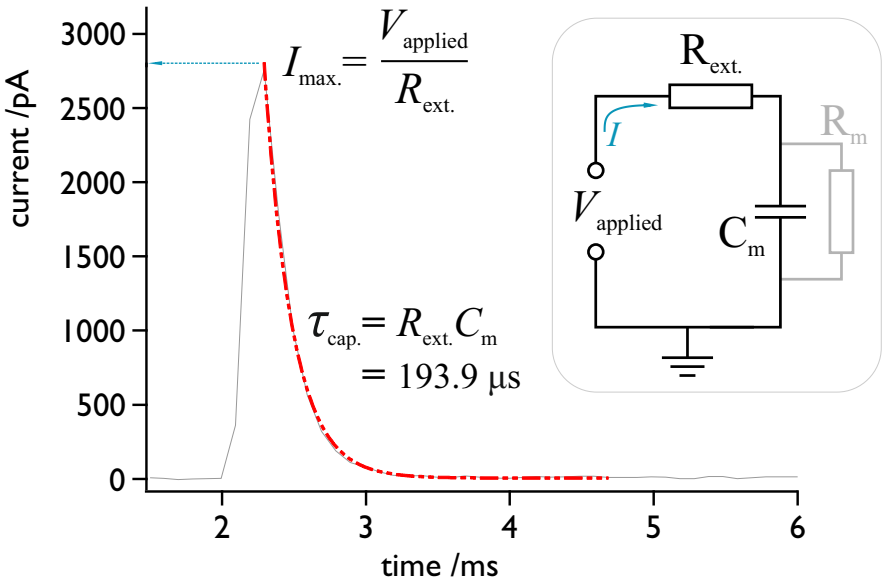


Figure 2.9: Capacitative charging of a bilayer in response to a 5 mV jump in V_{applied}. Grey line is the same trace as shown in Figure 2.8b; the red broken line is a single exponential fit to the data, which allowed the corresponding charging constant to be determined as $\tau_{\text{cap.}} = 193.9 \pm 1.3$ µs (standard deviation from fit). *Inset*: Simple circuit model of the bilayer. Strictly, the membrane has both a capacitance (C_{m}) and a resistance (R_{m}) associated with it, however at present the latter may be neglected.

hexadecane in our laboratory (∼0.0064 F·m^{-2}) [180] and in studies on polyethylene glycol-supported DPhPC bilayers (∼0.008 F·m^{-2}) [181]. The similarity of these values confirms the presence of a continuous membrane, and the applicability of this simple circuit model, a model which shall be returned to later. It is also of the correct order when compared to values found in *in vivo* systems, for example 0.0076 F·m^{-2} in nerve terminals [182] and 0.0102, 0.0078 and 0.0099 F·m^{-2} in mast, chromaffin and Chinese hamster ovary cells respectively [183]. It is desirable that the bilayer model mimics the biophysical properties of biological membranes; in the case of electroporation, as indicated by equation 2.4, it is important that the specific capacitance C_0 of the model membrane has a biologically appropriate value.

It may be noted that the charging time of the membrane elevates with the applied potential — compare Figures 2.8b and d, recorded at 5 mV and 120 mV respectively. This is expected, since the capacitance of lipid membranes increases with the transmembrane voltage [103, 180]. As outlined in Section 2.2 the potential, in driving a charge to accumulate across the membrane, generates a compressive

force. The pressure $p_{\text{elec.}}$ on the dielectric of a capacitor (as given in equation 2.2) is related to the capacitance by [102]:

$$p_{\text{elec.}} = \frac{1}{2}\epsilon_{\text{m}}\epsilon_0(\frac{V}{h_{\text{e}}})^2 = \frac{1}{2d_{\text{m}}}C_0V_{\text{m}}^2 \tag{2.16}$$

where the approximation $h_{\text{e}} \simeq d_{\text{m}}$ has been made. It should be noted that this is only valid if the specific capacitance is independent of the applied potential [102]. The relationship between the specific capacitance of DPhPC DIBs and the applied potential in the same setup as employed in this work has been investigated [180]. C_0 was found to vary quadratically with V_{applied}, following the empirical relationship:

$$C_{0,V\neq0} = C_{0,V=0}(1 + \beta V_{\text{applied}}^2) \tag{2.17}$$

where β was experimentally determined to be 0.64 V^{-2}. This means that C_0 for DPhPC DIBs increases by 0.64 % over 100 mV, and therefore equation 2.16 is applicable to the system. Since the bilayer is fluid, the compressive force as a result of the transmembrane voltage may therefore increase the membrane area (A) or reduce its thickness (d_{m}). Since C_{m} is proportional to the former and inversely proportional to the latter via $C_{\text{m}} = \epsilon_{\text{m}}(A/d_{\text{m}})$, the capacitance, and therefore $\tau_{\text{cap.}}$, increases. The relationship between the (total) membrane capacitance and V_{applied} follows a similar quadratic form to equation 2.17, with a 6.3 % increase in the total DIB capacitance over 100 mV [180]. This increase contributes to the increased capacitative decay lifetimes of the bilayer current observed at the point of voltage switching as V_{applied} is increased. That said, as can be seen in the two cases shown in Figure 2.8, charging is rapid, occurring in <50 ms.

Once the membrane has charged, the current returns to the background level, typically within a few picoamperes of 0 pA when V_{applied} is a few tens of millivolts, but increasing with increasing V_{applied}. The bilayer remains essentially non-conducting until ∼100 mV, where fluctuations in the current above the baseline begin to appear (Figure 2.8c and e). This is the onset of electroporation.

Initially, the conductive periods are transient, with the current returning to the baseline (Figure 2.8g, h), presumably as the pore or pores rapidly open and

reseal. These fluctuations are very rapid, with the shortest occurring over 1–2 ms, and shall be discussed further in Section 2.4.3. As the potential is increased, these fluctuations increase in magnitude, whereupon the current no longer returns to any stable baseline, as seen in Figure 2.8f. This could be the result of two scenarios: (1) a single, large pore that remains open, or (2) multiple pores that open and close, sufficient in number so as to keep the membrane in a constantly conductive state, so long as V_{applied} is maintained. By electrical recording alone, however, it is not possible to determine which of these caused the elevated currents preceding membrane breakdown.

2.4.2 I–V Characteristics

To enable the comparison between the electrical behaviour of bilayers containing different lipids, and (later) those with additional species such as pore-forming proteins, the current response of the bilayer was plotted against stimulating potential. Further, it was useful to parameterise the resulting I–V curves in some manner. This was done by defining the voltages at which electroporation was first observed, and that at which the bilayer ruptured. According to electroporation theory, the latter corresponds to the voltage at which unbounded pore expansion may take place (see Section 2.2), commonly termed in the literature the critical voltage, V_{c}. The value of V_{c} therefore provides an indication of the stability of the membrane under study with regards to its propensity to rupture. According to equation 2.9 and the curves in Figure 2.1, V_{c} is predicted to be of the order of a few hundred millivolts.

A typical I–V curve is shown in Figure 2.10, obtained from a bilayer experiencing a voltage protocol that explored both positive and negative potentials. The current level for each voltage step was obtained from the current recording using a procedure written in IGOR Pro (Wavemetrics, Oregon, USA). This procedure fragmented the trace into segments corresponding to the periods of applied voltage, removing the portions during which the bilayer was at 0 mV. It truncated the first 5 s from the beginning of each segment; the purpose of this was to ensure that the conductance spike and capacitive decay to the baseline conductance level were

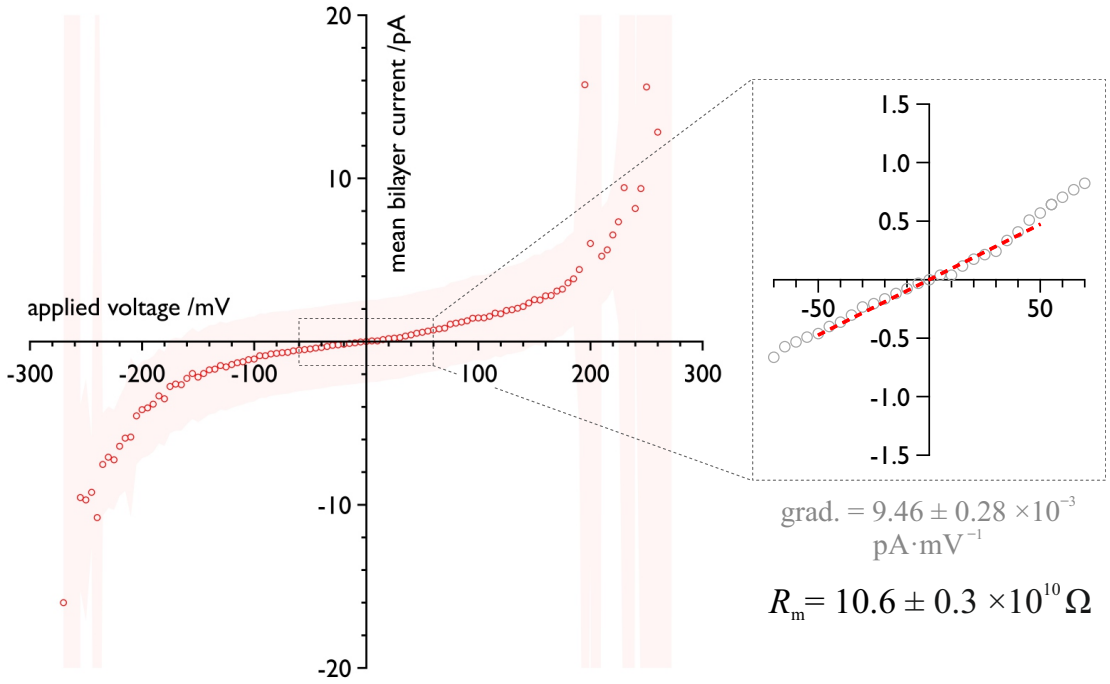


Figure 2.10: I–V curve for a DPhPC droplet-interface bilayer, obtained by plotting the mean bilayer current at each applied potential. The standard deviation of the means are displayed as the shaded region spanning the data markers; at higher voltages this band becomes larger as the currents display a greater variation in values. The expanded region details the linear portion of the curve; linear regression analysis of the data ($r^2 = 0.987$) over the range ±50 mV finds the membrane resistance to be $R_\mathrm{m} = 10.6 \pm 0.3 \times 10^{10}$ Ω.

not included in the data, such that the current changes only represented the contribution from electroporation. The program then calculated the arithmetic mean of the current across each (truncated) segment. Although this method is crude in terms of representing the true conductance behaviour (for example, a current value may imply a pore or pores being open for the entire duration, whereas in fact defects may have opened in brief bursts of high conductance, with the bilayer remaining sealed for the majority of the period; see Section 2.4.3), it serves as an indicator of the overall behaviour.

The I–V curve displays much of the information displayed in Figure 2.8a. At low voltages, the membrane is effectively non-conducting, showing a linear dependence of the (mean) bilayer current on the applied potential. The membrane resistance at this stage is of the order of gigaohms, $R_\mathrm{m} = 10.6 \times 10^{10}$ Ω (expanded region, Figure 2.10). Current fluctuations begin to appear in the region of 100–150 mV,

evidenced by the I–V characteristic becoming non-Ohmic, and hence non-linear. This continues until the bilayer ruptures. As expected, the bilayer displays the same behaviour at both positive and negative potentials.

Figure 2.11 displays I–V curves for a series of bilayers subjected to different protocols. All took the same form as in Figure 2.7, but t_{high}, t_{rest}, $V_{\text{increment}}$ were varied. This was done in order to ascertain whether these parameters had a strict bearing on the electroporation outcome, however, no discernible relationship between these parameters and the current response of the bilayer could be ascertained.

The initial bilayer resistance varies in the thirteen recordings presented in Figure 2.11 from 2.9 $\times 10^9$ Ω to 4.3 $\times 10^{10}$ Ω. This variation is most likely related to the size of the bilayer used to make the recording, and deficiencies in lipid packing. Although lipid membranes are commonly discussed as being impermeable to ions, they exhibit a small, non-zero permeability. For potassium this has been measured to be in the region of 10^{-13} m·s^{-1} [184] and 10^{-10} m·s^{-1} for halides [185] in bilayers comprised of monounsaturated phosphatidylcholine lipids. The mechanism of transport across the bilayer has been proposed to be via a solvation-diffusion route for both Cl^- and K^+, apart from in very thin bilayers (<20 Å) where potassium may use thermally generated hydrophobic pores [185]. Any defects in the membrane will therefore increase the permeability of these ions across it. Nevertheless, the variation in the (gigaohm) resistances of the DIBs in this study are consistent with the bilayer being essentially non-conducting.

In general, current fluctuations are evident in the I–V curves from 100 to 150 mV. Inspection of the individual traces revealed the smallest fluctuations tended to occur from ∼80 mV. This is the same potential at which DPhPC was found to porate in patches made at the end of glass pipettes [47].

The mean onset voltage had no dependence on the applied protocol, with $\bar{V}_{\text{onset}} = 101 \pm 68$ mV ($n = 4$) for the protocol applying a voltage for 180 s, and $\bar{V}_{\text{onset}} = 109 \pm 64$ mV ($n = 10$) when the membrane was excited for 300 s. Similarly, the rupture potential V_{c} was found to be in the range of 200–300 mV regardless of the protocol, with a mean of 224 ± 39 mV ($n = 17$).

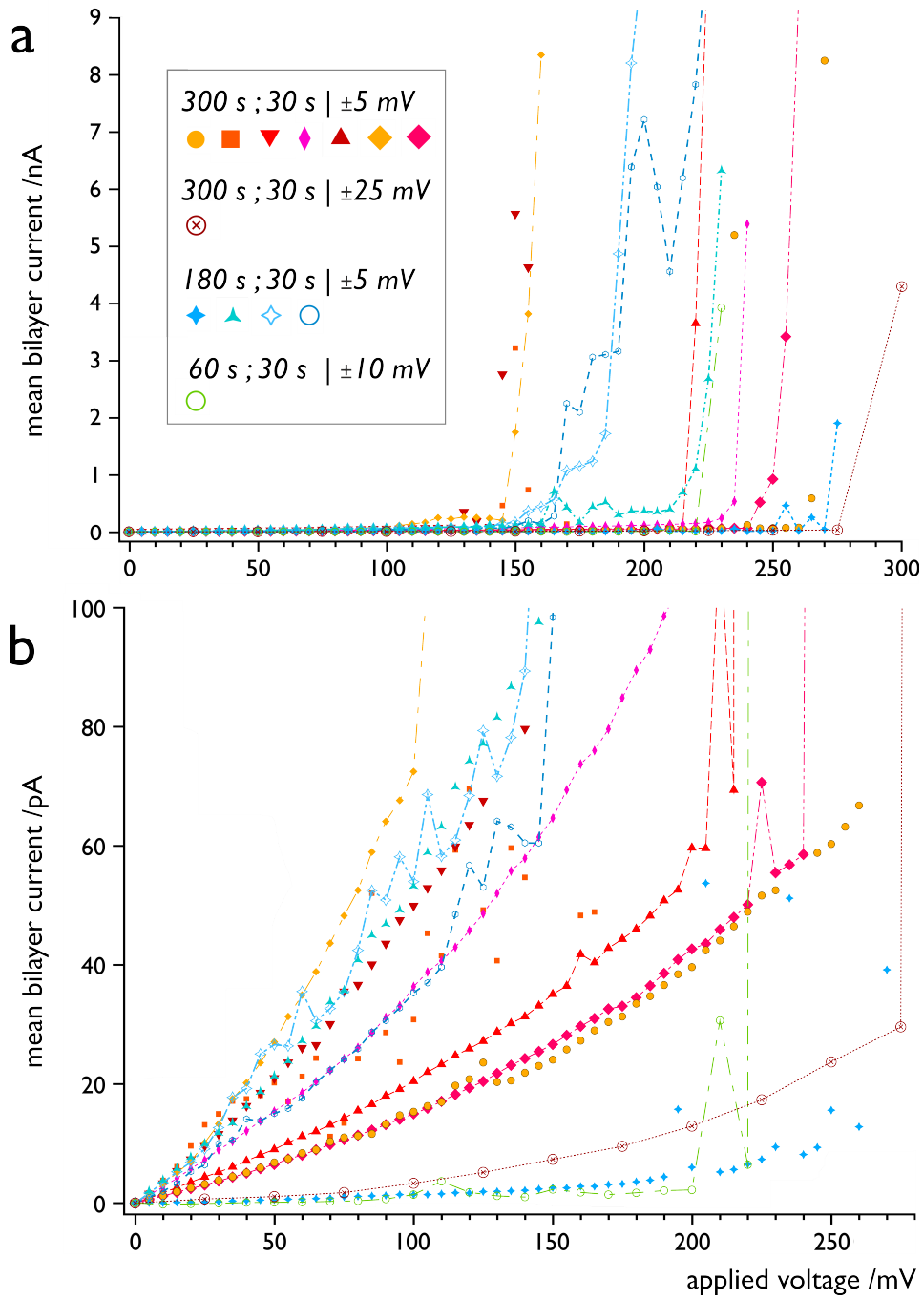


Figure 2.11: I–V curves for DPhPC bilayers under various voltage protocols. Ordinate axes are the mean bilayer current; abscissæ indicate the applied voltage. (a) The current response to different protocols across the full recording range of the patch-clamp amplifier (up to 10 nA). The three characteristic parameters of the protocol — the 'high' period, rest duration, and voltage increment — are notated next to the markers that represent the current response to these protocols in the I–V curves. (b) Expansion of the data displayed on in (a). Error bars have been omitted for clarity, but followed the same trend as those in Figure 2.10.

These observations are consistent with the model of electroporation. Pore formation is not directly predicted to be dependent on the duration of the applied field, only on its magnitude (unless the duration that the field is applied is insufficient to allow the membrane to experience the full potential difference; see footnote, Section 1.4.2). As discussed in Section 2.2, the field serves to lower the barriers to pore formation and expansion, processes which are then governed by fluctuations in the pore radius (unless the potential is so large as to immediately destroy the membrane). The appearance of pores is therefore stochastic, and a small pore may reseal or a large defect expand uncontrollably at any point during the application of a sufficient potential, regardless of its duration, so long as the pore has time to vary in radius. In practical electroporation applications, the reasons for applying fields for periods of nano- to milliseconds are several-fold. The field must be large in order for all membranes in a multi-cellular environment to attain a sufficient V_{m} for permeabilisation, however, these high fields at extended periods might lead to rupture, permit excessive material efflux, or result in other damage. Pulsing of the field reduces the time period that the pores are able to remain open, but furthermore, matching the pulse duration to the timescale of the radius fluctuations lessens the period that the radius is able to vary, in turn reducing the likelihood that a near-critical pore leads to rupture [139]. In the experiments presented here, where the intent was to investigate the nature of the electropore, the durations of non-zero V_{applied} were orders of magnitude longer than the pore fluctuations, giving electropores ample time to explore their surrounding radius space, generating conductance traces of stochastic pore opening, closure, and bilayer rupture.

Whilst I–V curves characterise the ensemble current response, it is difficult to ascertain a great deal about individual pore behaviour from traces that depict timescales spanning many hundreds of seconds. The following section therefore considers the various behaviours at shorter periods which contribute to the total current fluctuations.

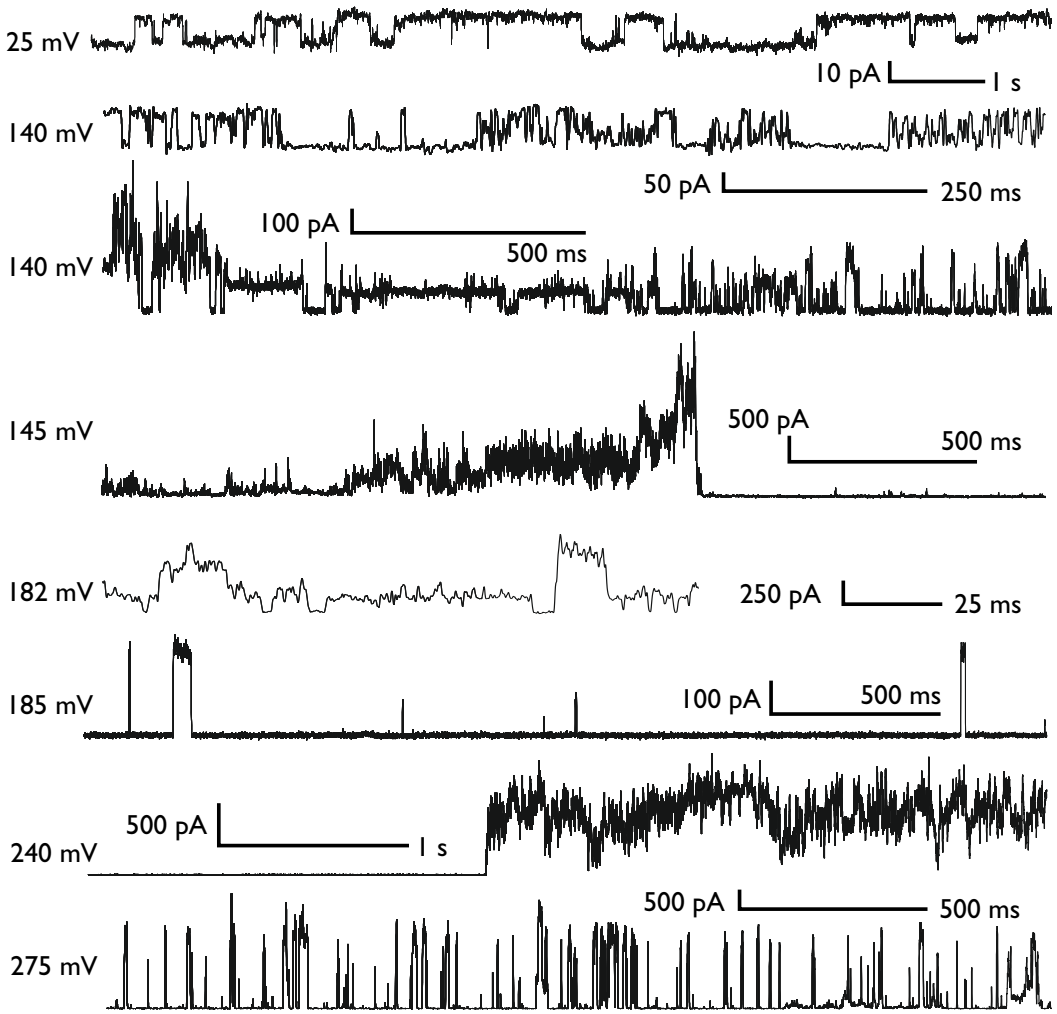


Figure 2.12: Variations in ensemble electropore conductance. Examples taken from different bilayers at various applied potentials. A wide range of conductance behaviours were observed, however it was not possible to determine how many defects contributed to each trace. Some traces have been filtered with a 21-point Savitsky-Golay filter in order to make visualisation clearer.

2.4.3 Specific Behaviours

The current traces, when observed at shorter timescales, revealed a range of conductance behaviours, as shown in Figure 2.12. Although $\bar{V}_{\text{onset}}$ was found to be in the region of 100 mV, occasionally current fluctuations were observed at voltages as low as 25 mV. At these low potentials, discrete changes in the membrane current were observed; however they were not limited to low voltages, and were seen up to ∼140 mV. Occasionally, it appeared that the stepwise behaviour was occurring simultaneously with other electrical activity (third trace, Figure 2.12).

At low potentials, it is not unreasonable to assume that the number of pores in the membrane is small, and in the case of the discrete fluctuations, such behaviour might be representative of the first stable hydrophilic pore formation. The energy curves for electroporation (Figure 2.1) imply that the local minimum that supports hydrophilic pores broadens with the applied potential. In the opposite case, low potentials should exhibit a narrow energy well for pores to reside in. We might expect therefore that pores formed in this regime have limited radius space in which to explore, and that only a small decrease in radius is required to close the pore again. This would have the effect of restricting the conductance to a narrow range. As such, the discrete conductances observed here may represent these smallest defects. If for now it is assumed that this is the case, that there is a single pore in the membrane fluctuating between a closed state and an open state of relatively fixed size, an estimate may be made of the pore radius, using $G = \pi r^2 \cdot g/d_{\mathrm{m}}$, where G is the conductance of the pore (800 pS and 710 pS for the two uppermost traces in Figure 2.12), and g is the electrolyte conductivity [177, 186] (*N.B.* This equation and its approximations are discussed in greater detail later in this chapter, in Section 2.4.4.2.) Although this equation will produce and underestimate of the pore radius as it does not account for the voltage drop across the pore (see Section 2.4.4.2), using $d_{\mathrm{m}} = 4.8$ nm [187] and the measured value of $g = 14.39$ S·m^{-1} for the conductance of the electrolyte (see Materials & Methods), the radii derived from these discrete conductances are around 0.2–0.4 nm. This is of the order of the smallest predicted electropores [110, 143, 149, 172, 173], and is consistent with the notion that the smallest conductive pores must be able to support at least a single column of ions, whose radii are on the order of these calculated pore sizes.

At higher potentials, the stepwise conductance is no longer visible, as the increased field generates a greater number of pores at different radii. At this stage it is not possible to be certain about the number of pores present in the membrane. However, pore fluctuations were observed to be stochastic: large conductances could diminish within milliseconds, or apparently very large pores could appear from a

previously 'silent' membrane. In all cases, fluctuations were rapid, with changes of several hundred picoamperes occurring within a millisecond.

2.4.4 Physiological Electrolyte Solutions

In the majority of the measurements undertaken for this work, relatively high salt concentrations were used in the electrolyte solutions. Droplets almost always contained 1.5 M potassium chloride, and the agarose electrolyte was osmotically balanced with the droplet interior, depending on the experiment. These concentrations are around ten-fold higher than those found in the cytoplasm of biological cells [188]. High concentrations were used for two reasons. Firstly, it improved the longevity of the membranes: ion association with the lipid headgroups is known to modulate the bilayer properties. For example, a ten-fold increase in sodium chloride concentration has been shown to cause a 35 % reduction in the lateral diffusion of zwitterionic POPC lipids [189]. Divalent cations exhibit binding constants of between 10 and 100 M^{-1} [190], and calcium ions have been found to raise the lipid melting temperature** [191]. These effects are thought to be the result of increased electrostatic bridging interactions between lipid headgroups mediated by the ions associated with the leaflet, generating tight lipid-ion complexes [192]. Secondly, in experiments measuring the calcium flux through electropores (Chapters 3–5), it was advantageous to use higher ion concentrations in order to maximise the detected signal.

2.4.4.1 Lowering of V_c

In order to assess the influence of elevated ionic strengths on the electroporation outcome, DIBs were constructed with aqueous components containing electrolytes at biologically-relevant concentrations. Phosphate-buffered saline (PBS) is a commonly-used buffer solution designed to mimic the content, osmolarity and concentrations of the ions within human cytosol. DIBs were prepared with this solution, which

**Below the melting temperature (T_m), lipids exist in the gel phase, with tight, ordered packing; above T_m the lipids are in the fluid or liquid phase, where the molecules are free to laterally diffuse. DPhPC is in the fluid phase between −120 and +120 °C [46], owing to the branching of its aliphatic chains which preclude close packing of the individual lipid molecules.

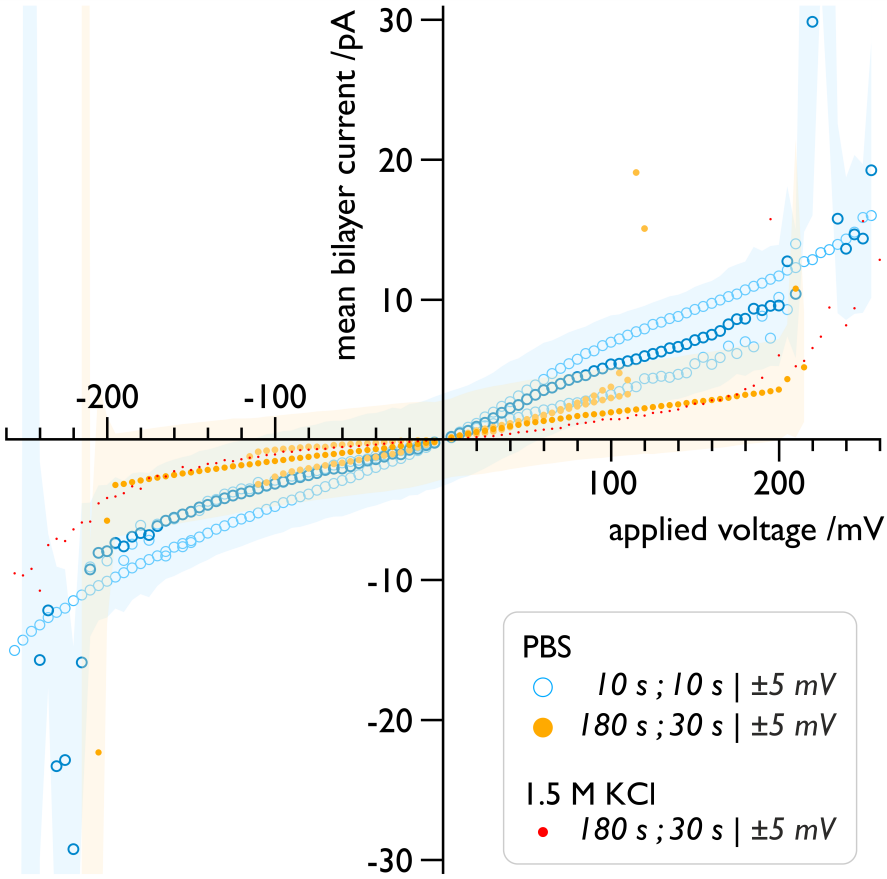


Figure 2.13: I–V curves at physiologically-relevant electrolyte concentrations, obtained using two different voltage protocols. Error bars have been indicated by coloured bands; these errors correspond to the I–V curve with the darker markers of the same colour. The red data points are from a run made with a high-salt (KCl) buffer for comparison.

contained 137 mM NaCl, 2.7 mM KCl and 10 mM sodium phosphate(s)[††]. Representative I–V curves for these bilayers are shown in Figure 2.13.

These curves show the same overall behaviour as their high-salt counterparts (those containing 1.5 M KCl, Figures 2.10 and 2.11), with a linear phase preceding a non-linear increase in conductance before bilayer breakdown. Inspection of V_{onset} and V_{c} however indicates a modulation of the bilayer properties as a result of the drop in ionic strength. For the 180 s high, 30 s rest protocol (yellow markers, Figure 2.13), these values were $\bar{V}_{\text{onset, PBS}} = 128 \pm 43$ mV ($n = 4$; the early stages of recording of a fifth bilayer were obscured by severe interference from an unknown source, but V_{onset} was not greater than 95 mV as fluctuations larger than the noise

[††]For proprietary reasons, the exact phosphate composition is not usually reported by the manufacturer.

became visible at this voltage) and $\bar{V}_{\mathrm{c,\ PBS}} = 145 \pm 44$ mV ($n = 5$). Comparing these parameters with those obtained from experiments using buffered 1.5 M KCl, $\bar{V}_{\mathrm{onset,\ KCl}} \simeq 110$ mV and $\bar{V}_{\mathrm{c,\ KCl}} \simeq 224$ mV, there appears to have been little change in the onset potential, but a decrease in the breakdown voltage. It is easy to imagine that the reduction in ionic strength overall reduces the number of attractive, bridging interactions between headgroups and ions. These associations would work against parting of the membrane to form pores, an effect that could be considered an increase in the effective line tension (γ) of the membrane.

It is however more difficult to rationalise as to why the onset voltage appeared to remain of the same order, since presumably the factors that favour pore widening and irreversible expansion (rupture) at lower voltages should also favour the opening of pores at reduced potentials. This might therefore imply that higher ionic strengths do not, at least to an appreciable degree, stabilise the membrane against pore formation, but rather stabilise against pore expansion that leads to rupture. It is important to note at this stage that NaCl and KCl do not interact in the same way with lipid headgroups. Whereas the Na^+ ion is predicted to penetrate into the headgroup region and bind tightly to three lipid molecules near the phosphate or carbonyl carbons, K^+ interacts less strongly, and further away from the phosphate towards the headgroup-water interface, due to its larger radius and smaller charge density [172, 193, 194]. Binding constants for K^+ to PC membranes have been experimentally measured to be up to 0.1 M^{-1}, but up to 0.9 M^{-1} for Na^+ [190] (and references therein). This would support the perhaps surprising experimental observations by others that have indicated the ionic strength of KCl has little influence on the electroporation breakdown voltage [186, 195]. Although within error, $\bar{V}_{\mathrm{onset,\ PBS}}$ was 15 % higher than that for KCl, which might be explained by the stabilising effect of sodium seen in other bilayer systems: experimentally, increasing the concentration of sodium ions in the presence of bilayers has been found to reduce lateral diffusion in multilamellar POPC membranes [189], and to increase the force required to puncture DMPC (dimyristoyl phosphocholine) SLBs [196], supporting the predictions that Na^+ binds strongly to lipids.

The origin of the reduction in V_c observed here may also be aided by the sodium ions. In the case of pore closure, as discussed in Section 2.2, the coming together of the hydrophilic pore walls in order to collapse a pore requires sufficient proximity of the two aqueous surfaces. Strong Na^+ association with the headgroups, in contrast to weaker binding by potassium, might be expected to heighten the barrier to pore closure, as the higher charge density of Na^+ holds itself and water to the membrane surface more tightly, not only introducing a further (repulsive) electrostatic cost [197] but raising the energy input required to remove the interfacial water. This may give more time for the radius of a near-critical pore to fluctuate beyond r_c. Unfortunately, little data on electroporation in the presence of sodium solutions exists, however MD simulations in which hydrophilic pore-containing membranes were allowed to equilibrate for 20 ns in the absence of an electric field have indicated that Na^+ ions can impede pore sealing in DPPC [198]. Furthermore, strong interactions with the hydrophilic pore walls were found to result in a large reduction in the conductance in sodium (chloride) filled pores relative to those simulated to contain potassium [172]. At a field of around 235 mV, pores with a radius of around 0.7 nm exhibited a Na^+ conductance of $G_{Na^+} = 0.95$ nS·M^{-1}; with K^+ electrolyte the cations had a conductance of $G_{K^+} = 5.28$ nS·M^{-1}. As the field is increased and the pores grow, the more sodium ions within the pore lumen experience bulk-like electrolyte and do not bind to the walls, so G_{K^+}/G_{Na^+} falls, but is still ∼2.4 at 500 mV. The interaction between ions and bilayers is clearly complex and is a topic of continued discussion in the literature, particularly in the case of computer simulations which can exaggerate or misrepresent ion behaviour near the headgroups depending on the choice of force field implemented [193, 199, 200].

2.4.4.2 Pore Conductance Considerations

The reduction in conductance of the pore is relevant here when considering the nature of the electric field in the pore's presence. In terms of the circuit model introduced in Section 2.4.1, the formation of a conductive pore is equivalent to placing a resistor in parallel with the membrane capacitance, as represented in

Figure 2.14. This equivalent circuit is commonly used to describe the permeabilised membrane [92, 114, 179, 201].

The current through this pore resistance will depend on the pore radius and the conductivity of the electrolyte that fills it. To a simple approximation, the conductance of a pore of radius r will be:

$$G_{\text{lumen}} = \frac{\pi r^2 \cdot g}{d_{\text{m}}} \tag{2.18}$$

where g is the conductivity of the solution and d_{m} is the membrane thickness, as already presented in Section 2.4.3. However, the *measured* conductance will be lower than G_{lumen}, owing to a further resistance associated with the current paths that converge from the bulk electrolyte at the entrance of the pore [202]. This additional contribution is known as the access or spreading resistance, and has been approximated by [197]:

$$R_{\text{access}} = \frac{1}{2rg}. \tag{2.19}$$

This resistance is the dominating factor in large pores [203]. The equation for the pore conductance then becomes:

$$G_{\text{pore}} = \frac{1}{R_{\text{access}} + R_{\text{lumen}}} = \frac{2\pi r^2 \cdot g}{\pi r + 2d_{\text{m}}}. \tag{2.20}$$

These equations represent an approximation as the pore is assumed to be cylindrical. The toroidal pore geometry complicates any calculation of the defect conductance owing to its shape. In addition, any interactions between the ions and the pore walls have been neglected. Fortuitously, simulations have shown that equation 2.18 follows calculations made for toroidal pores up to 50 nm very well (albeit somewhat underestimating the conductance), and for small pores in the range $0<r<2.5$ nm it matches both more complex models and MD calculations [197]. These equations are therefore commonly used to estimate pore radii from conductance data [177, 178, 197]. In this regard, it is worth noting that since the access resistance only dominates at large radii, for small pores, equations 2.18 and 2.18 yield similar values when used to calculate small radii; a conductance of 750 pS (the mean of

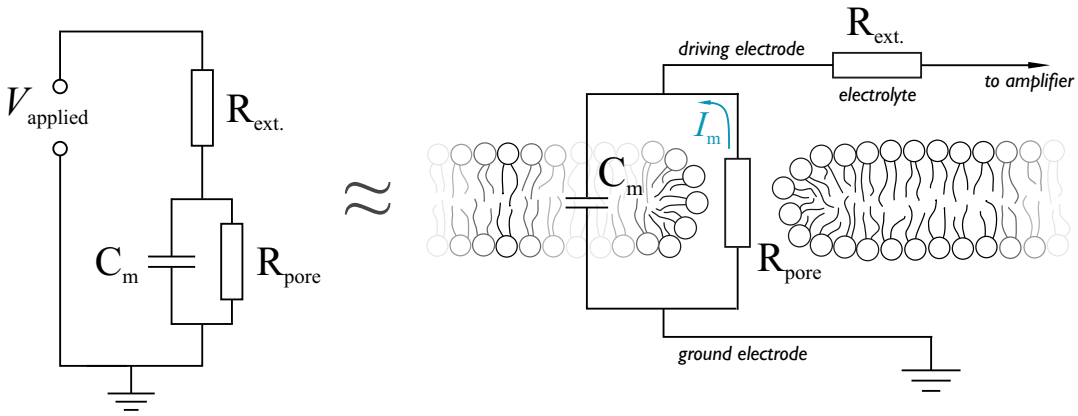


Figure 2.14: Equivalent circuit for electroporation. Pore formation opens a conductive route through R_{pore}, giving rise to measurable current fluctuations as the pore radius varies.

the conductance values derived from the discrete fluctuations discussed in Section 2.4.3) gives a pore radius of 0.31 nm when using equation 2.18, whereas the simpler equation 2.18 yields a slight underestimation at 0.29 nm. Equation 2.18 is therefore very commonly employed in such calculations in the literature.

Figure 2.15 shows crudely how the conductance of the pore, variable either by its size or the conductivity of the solution filling it, affects the local transmembrane voltage. The circuit is the same as that in Figure 2.14, with the component values representing estimates in a bilayer system. $R_{\text{ext.}}$ and C_{m} were estimated from the capacitative spikes at low step changes in the applied potential (see Section 2.4.1), whilst R_{pore} was estimated using equation 2.18. In this model the membrane is considered to be intact (panel *i*), or containing a single pore of 1 nm or 50 nm radius (panels *ii* and *iii*). Assuming the bilayer capacitor is fully charged, the voltage across the membrane V_{m} is given by:

$$V_{\text{m}} = V_{\text{applied}}(1 - \frac{R_{\text{ext.}}}{R_{\text{ext.}} + R_{\text{pore}}}) = V_{\text{applied}}(\frac{R_{\text{pore}}}{R_{\text{ext.}} + R_{\text{pore}}}) \tag{2.21}$$

a full derivation of which may be found in Appendix B. In the absense of a pore[‡‡], the bilayer experiences the full magnitude of V_{applied}. However, in the presence of a conductive pathway, the voltage drop across the membrane is reduced. This pathway — the pore — therefore reduces the potential experienced by the membrane.

[‡‡]Strictly the membrane should also have its resistance $R_{\text{m}} \simeq$ 1–100 GΩ associated with it, however its large magnitude will result in the full voltage drop across the bilayer.

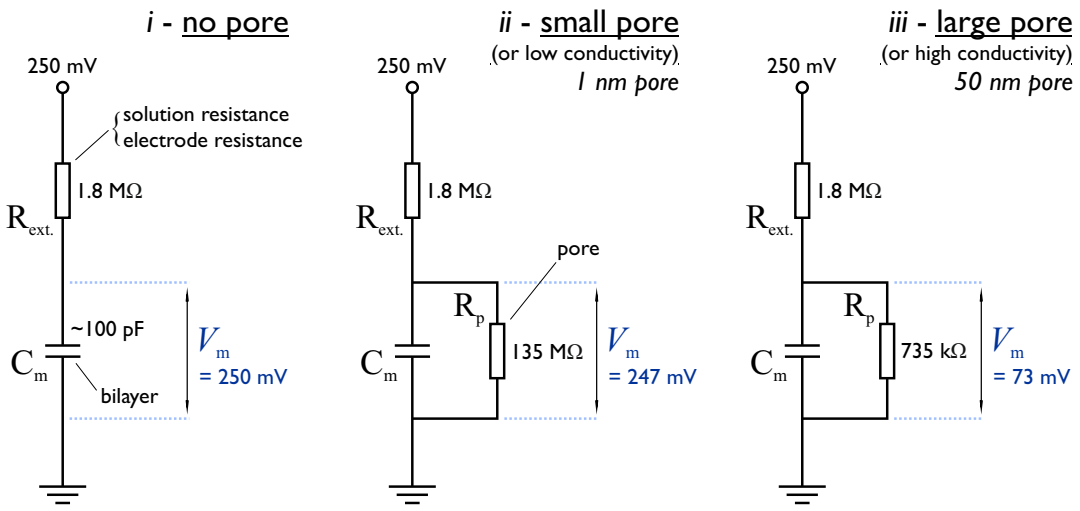


Figure 2.15: Model of voltage drop across the membrane. In *i*, in the absence of a pore, the membrane experiences the full applied voltage. The membrane resistance has been omitted for clarity since its large value will not result in a reduction of V_{m}. Introducing a conductive defect lowers V_{m} (*ii* and *iii*).

The effect of lowering the electrolyte concentration on V_{onset} and V_{rupture} may therefore be understood in terms of the reduction of conductance of the pores. The KCl solutions used were measured to have a conductivity of 143.9 ± 0.4 mS·cm^{-1}, whereas PBS solutions made to the concentrations used in this work have conductivities of 14–20 mS·cm^{-1} (manufacturer's information). Using equation 2.21, a 5 nm pore under an applied potential of 100 mV experiences a local field of 85 mV in the KCl buffer, but in PBS, V_{m} is only reduced to 98 mV. The more conductive KCl solutions therefore produce electropores with lower resistances, thereby reducing the local transmembrane potential. This, akin to negative feedback, increases the voltage at which a critical pore is able to form. Conversely, PBS electropores, with lower conductances, could not relax the field in the region of the pore as effectively, resulting in larger experienced transmembrane voltages, and hence lowering $\bar{V}_{\mathrm{c}}$ whilst keeping the onset voltage constant.

Despite these discussions, it is not possible to firmly pinpoint the origin of the effects observed in altering the electrolyte. Indeed, it is likely to be a combination of factors that with further experimentation with the concentration and nature of the electrolyte might be elucidated. However, despite these variations

between electrolytes, DIBs closer to physiological conditions display the same electrical behaviour as their high-salt counterparts, with V_{onset} and V_{c} of the same magnitude and varying by less than 100 mV. This would suggest that the high ionic strength conditions utilised in the following chapters do not significantly distort electroporation behaviour.

2.4.5 Influence of the Protocol

A final set of remarks shall be made on a second series of experiments run in PBS buffer, some of which are shown in Figure 2.13 (blue). Interest at that time was to reduce the period of recording (the 180 s 'high' protocol with a 5 mV increment spanning ±300 mV for example lasts seven hours) and so a protocol of 10 s 'high', 10 s rest was applied to the bilayers. It was found that V_{onset} and V_{c} were elevated relative to their respective values under a longer, 180 s 'high', 10 s rest protocol, with $V_{\text{onset; 10s,10s}} = 194 \pm 36$ mV (compared with $V_{\text{onset; 180s,30s}} = 128$ mV) and $V_{\text{c; 10s,10s}} = 251 \pm 22$ mV (with $V_{\text{c; 180s,30s}} = 145$ mV). The jump in both parameters suggests that the duration of the protocol was the dominant factor.

This is of interest as these results imply that there is some time dependence of electropore formation. At around 80–100 mV, where under longer protocols the membrane would begin to porate, these membranes remained electrically silent. This returns the question as to how exactly the electric field interacts with the membrane and the stochastic nature of electroporation as a whole. Under shorter timescales (<10 s), it appears that there is insufficient time for pores to form before the voltage is removed. Similarly at high voltages, the pores have less time to fluctuate in radius, delaying the rupture process. Furthermore, some of this period will be consumed by the bilayer charging; at potentials near 200 mV, charging times in DIBs encroach on the order of seconds. Since the bilayer only experiences the full V_{applied} after the charging time, this additionally limits the period available for fluctuations.

2.5 Summary & Limitations

The electrical response of DIBs was examined under a range of conditions. This is the first such characterisation of electroporation in membranes formed by the contact of an aqueous droplet and a hydrogel substrate each bearing a lipid monolayer. The ensemble current response to the electric field shows the same fluctuations observed in other membrane systems, consistent with the formation of membrane-spanning, conductive defects in a voltage-dependent manner. Initially, the membrane is essentially electrically insulating, but with increasing potential, conductive fluctuations begin, which increase in magnitude until the bilayer ruptures. The onset of these fluctuations, their behaviour over time, and the voltage at which the bilayer ruptures all appear to be stochastic: there is a range of these behaviours and voltages, supporting a model based on fluctuations of the lipid molecules that are predicted to be the basis of hydrophilic electropores.

The toroidal pore model set out at the beginning of this chapter takes account of (some of) the lipid properties through physical parameters such as the line tension γ and the surface tension σ, and bilayers composed of different lipids should show modified I–V curves, reflecting variations in their physical properties. In this chapter, only DPhPC was used to form DIBs. Unfortunately, the measurement of the line and surface tensions of lipid membranes is a difficult task, and these are parameters that will vary between membrane systems of different compositions. At present, this precludes the ability to correlate the values of γ and σ with the ensemble electrical behaviour of the bilayer, and parameters such as the rupture voltage. It also restricts use of the equations that describe electroporation, set out at the beginning of the chapter, to making loose predictions regarding, for example, the rupture potential or the critical radius.

Furthermore, the influence of the properties of the surrounding system are not explicitly taken into account. This leads to difficulty in accurately assessing the effect of, for example, electrolytes on electroporation. Moving from 1.5 M KCl solution to PBS containing 2.7 mM KCl and 137 mM NaCl lead to similar values of $\bar{V}_{\text{onset}}$ (if not a slight increase) and a large decrease in $\bar{V}_{\text{c}}$. The latter might be explained

by loss of attractive lipid-ion-lipid bridging interactions at lower ionic strengths, and lower conductivity pores leading to less relaxation of the local transmembrane voltage. Despite the quantity of monovalent cations in solution being order of magnitude less when comparing the PBS to the 1.5 M KCl electrolytes, strong Na^+-lipid interactions may have a stabilising effect on the membrane and lead to the slightly increased $\bar{V}_{\text{onset}}$; similar stabilising interactions may have assisted in lowering $\bar{V}_{\text{c}}$ by impeding pore closure. Exploring the behaviour of electroporation at a range of KCl and NaCl concentrations would aid in clarifying the effects that these ions have on DIBs. Nevertheless, the same conductance fluctuation behaviours and similar magnitudes of the extracted parameters $\bar{V}_{\text{onset}}$ and $\bar{V}_{\text{c}}$ in both electrolytes indicates that electroporation in 1.5 M KCl does not deviate heavily from that observed under more biologically relevant electrolyte conditions.

With regard to the techniques employed in this chapter, electrophysiological recordings of bilayers have an inherent limitation, in that they can only report of the total conductance of the membrane. This technique alone cannot therefore provide information on the individuals within the ensemble, an ensemble that may consist of a distribution of pore sizes. Naturally, questions have been raised in the literature about the number of pores the exist in the membrane. Early works sometimes assumed that only one pore is present — the same assumption made in this work when estimating the radius of the pore at low potentials (Section 2.4.3). Others base their models on the existence of multiple pores. These two cases cannot be definitively distinguished using electrophysiological recording. Furthermore, pores are dynamic in their size, and hence their conductance. Therefore, in order to better understand their behaviour, the ability to resolve the individual contributions to the bulk current signal is necessary. In the next chapter, a methodology is developed in order to achieve this.

3

Electroporation in DIBs: Optical Characterisation

This chapter takes a first look at electroporation using optical single-channel recording in droplet-interface bilayers. It presents a broad range of observations on the dynamic and interactive properties of electropores, many of which have only until now been predicted by simulations or numerical models.

3.1 Introduction

As discussed in Chapter 2, electrical recordings are one of the two standard ways of investigating the formation of electropores experimentally. The alternative method is to optically monitor the transport across the membrane of some detectable molecule, be it glucose, which might cause a change of local refractive index in white light microscopy, or a fluorophore, detectable by its emission upon excitation by a laser. In essence however, these methodologies are the same: the detection of the *presence* of a pore by way of the material that flows through it. The reason for the lack of experimental apparatus to detect electropores is a fundamental one — they are simply too small to be observed directly by current optical methods.

3.1.1 Previous Imaging Studies

Direct observation studies of electropores are rare. Chang and Reese observed '*volcano-like openings*' 20–120 nm across in red blood cell membranes that were frozen 3 ms after a poration pulse [144]. Whilst it is generally not contested that these defects were caused by the pulse, the structures that they imaged by electron microscopy have been disputed by some of their peers as artefacts of material efflux from the cell and cellular swelling, enlargening the pores [92, 204]. Some numerical models catering for the geometries and parameters of cells have on the other hand been able to support Chang and Reese's observations [205, 206]. Regardless of whether the defects are of their true size or of exaggerated dimensions, their images show pores existing on the nanoscale. Similar defects were observed in hepatocytes excised from rabbit tissues 15–30 minutes after *in vivo* electroporation [207]. In this study, pulses designed to irreversibly* porate the membrane were used, the probable cause of the longevity of these pores. These, however, are static images of electroporation, revealing little about their dynamic behaviour.

Far larger, macro-scale pores ($\geqslant$10 μm in diameter) have been observed in GUVs [62, 145, 146]. These studies have been able to investigate dynamic properties, such as pore sealing. However, there tends to be only a single pore observed in the membrane at a time (numerical studies predict the formation of tens to hundreds of thousands of pores in cellular membranes [205, 206]), and these studies have been limited to observation of pores no smaller than a few micrometres. These are much larger than the nanoscopic pores observed in cell systems (20–490 nm) [144, 207], predicted by simulations [76, 77, 149, 205, 206] and implied by cellular uptake assays [143].

Moreover, it is very rare that the advantages of both electrical and optical techniques can be combined in a single electroporation experiment. Electrophysiological measurements can achieve high time resolutions, with modern patch-clamp

*In *in vivo* applications, the term 'irreversible' is used to mean the formation of pores so as to render the affected cells non-viable. Such pulses would destroy model membranes, however total membrane rupture does not occur in cells, as the underlying support structures of the membrane are thought to act as anchoring points for small portions of membrane, limiting 'rupture' to small regions [208].

amplifiers able to make current readings on the microsecond timescale, but lack the ability to deconvolute the multiple, simultaneous conductances that produce the current traces and give no spatial information on conductive channels. Visualisation of pores could improve our understanding of their dynamic properties, rupture behaviour and inter-pore interactions, but real-time observational methodologies are inadequate at present. In certain configurations, BLMs can offer optical access, for example in the work of Chandler *et al.*, where confocal imaging[†] was used to monitor fluorescently-labelled polynucleotides that were electrophoretically driven into α-hemolysin channels embedded in the membrane [211]. However, electroporation as yet has not received the same interrogative treatment, presumably because of the lack of stability of BLMs under electroporative fields and the additional complexities introduced by the confocal setup. The nature of GUVs has evidently made the imaging of small pores highly challenging, along with the fact that recording currents from a single vesicle is difficult. The work in this chapter attempts to address these limitations, presenting a means to combine the advantages of both optical and electrical techniques in DIBs in order to study the rarely observed facets of electroporation.

3.1.2 Optical Single-Channel Recording

In 2003 Demuro and Parker presented work that addressed the limitations of optical and electrical recording of transmembrane currents [212]. Their interest was to improve optical techniques for detecting ion channels whilst maintaining the ability to monitor their conductance. They achieved this by imaging the flux of calcium ions through voltage-gated Ca^{2+} channels in oocyte membranes. The cells were injected with a calcium-sensitive dye, which exhibits >15-fold increase in its fluorescent emission upon binding the ion. It was demonstrated that the typical electrical signals from ion channels could be reproduced by confocally imaging the bursts of fluorescent signal that resulted from calcium passing through the protein pores.

[†]Confocal imaging limits the imaging volume in order to interrogate a sample with a highly restricted depth of focus. By eliminating out of focus light, high spatial resolution is achieved, and three-dimensional images can be built-up from images taken at different depths [209, 210].

Demuro and Parker extended the applicability of this technique from confocal imaging, which can be limited by the speed at which the focused laser spot can be scanned in order to create an image, to TIRF microscopy (see Chapter 1), allowing a large area to be illuminated at once, with the optical sectioning that TIRF affords restricting the detected signal response volume, and thus improving the signal-to-noise ratio and resolution of the experiments [213].

This technique, termed optical single-channel recording (oSCR), presents itself as a candidate for studying electroporation in DIBs. Rather than image the ion flux through a protein-based pore, Ca^{2+} motion through electropores could be observed, giving an indication of the location, size and dynamic properties of the pores. This idea led to the work presented in this and the following chapters.

3.2 Materials & Methods

3.2.1 Materials

DPhPC stored as stock solutions in chloroform at −20 °C were used as described in Chapter 2. Quest Fluo-8H (AAT Bioquest, Sunnyvale, California, USA) and ethylenediaminetetraacetic acid (EDTA) tetrasodium salt (Sigma-Aldrich) were used without further purification in addition to those substances and materials reported in Chapter 2. All other substances were purchased from Sigma-Aldrich, unless stated otherwise.

3.2.2 Conductivity Measurements

The conductivity of the electrolyte solutions was measured at a room temperature of 21.1 °C as before, using a Mettler Toledo FG3 meter with LE703 probe (Mettler Toledo, Leicester, UK), calibrated with a standard reference solution of 12.88 mS·cm^{-1}. Three separate measurements were taken. For the 750 mM $CaCl_2$, 10 mM HEPES, pH 7.00 solution, the average of these three measurements was 97.2 ± 2.0 mS·cm^{-1}, and 143.9 ± 0.4 mS·cm^{-1} for 1.5 M KCl, 10 mM HEPES, pH 6.98. A 1:1 mixture of solutions was made in order to simulate the contents of a hydrophilic

pore and thus estimate the pore electrolyte conductivity. The solution (750 mM KCl, 375 mM $CaCl_2$, 10 mM HEPES) was measured to be 121.1 ± 0.6 mS·cm^{-1}.

3.2.3 Fluo-8H Solutions

The fluorescent dye was stored at −20 °C as a 1 mg·mL^{-1} stock solution dissolved in Milli-Q water. From this, solutions suitable for imaging experiments were prepared using component proportions previously determined in the laboratory [214]. 15 μL of aqueous 1.5 M KCl solution containing 10 mM HEPES buffer at pH 6.98–7.02, treated with Chelex resin to remove any divalent cations that would otherwise bind to Fluo-8H in the droplet and increase background fluorescence levels, was pipetted into a 1.5 mL Eppendorf centrifuge tube (Eppendorf, UK). 0.6 μL of 10 mM aqueous EDTA was added in order to chelate any remaining divalent ions. This also serves to 'sharpen' the edges of the imaged calcium fluxes by chelating diffuse ions at the edge of the detected transients. This was followed by 0.6 μL of the 1 mg·mL^{-1} Fluo-8H stock (dye concentration ∼46 μM). This was vortexed briefly to ensure a homogenous solution and stored at −20 °C. When required, the tube was warmed until the solid had melted and was vortexed again. The tube was wrapped in aluminium foil at all times to reduce exposure of the fluorophore to ambient light. Droplets were made in the same way as those for electrical-only experiments by pipetting a volume of the solution into an incubation tank containing lipid dissolved in hexadecane. Whilst the monolayer was assembling, the tank was covered in a black enclosure, again to reduce light exposure.

3.2.4 Device Preparation

Devices were constructed in the same way as described previously, the only difference being that the 1.5 % (wt./vol.) hydrating agarose gel was made with 750 mM $CaCl_2$; the concentration was set to half that of the KCl in the droplet to ensure a balance of charge either side of the membrane, despite the difference in osmotic pressure.

3.2.5 Simultaneous Imaging & Electrical Recording

The practical setup for imaging DIBs was the same as that described in Chapter 1. Briefly, prepared devices were mounted inside a Faraday cage along with the patch-clamp amplifier headstage. The earthed Faraday cage rested on the stage of an inverted microscope (Eclipse Ti-E, Nikon). White light illumination from above was permitted via a grille in the lid of the Faraday cage; fluorescent illumination was from beneath. Bilayers were imaged using a 60× TIRF objective oil-immersion lens (Plan Apo TIRF ×60, 1.45 NA; Nikon UK, Surrey, UK) under white light for the purposes of inserting the driving electrode. The fluorophore was excited by a 473 nm continuous wave laser beam (Shanghai Dream Lasers Technology Co., Shanghai, China, or Vortran Laser Technology, Sacramento, California, USA) which was coupled to the inverted microscope by an optical fibre or launched directly via a periscope. The power at the back focal plane of the objective was 1–4 mW. Fluo-8H emits in the green portion of the visible spectrum, with $\lambda_{\text{emission max.}} = 514$ nm (see Appendix C for emission and excitation spectra). The fluorescence and excitation signals were separated by means of a dichroic mirror (C67196; Nikon, or XF2037; Omega Optical, Brattleboro, Vermont, USA), and the collected signal from the bilayer transmitted through an emission (bandpass) filter (XF3080, bandwidth 510/23 nm; Omega Optical, or Brightline bandpass 525/39 nm; Semrock, Rochester, New York, USA) in order to eliminate stray excitation wavelengths. Images were recorded using an electron-multiplying charged-coupled device (CCD)[‡] camera (either iXon3 897 EMCCD, 512×512 pixels, imaging area ∼136×136 μm^2 or iXon+, 128×128 pixels, imaging area ∼50×50 μm^2; both Andor Technology, Belfast, UK). A schematic of the optical setup is shown in Figure 3.1. All experiments were conducted at room temperature of around 21 °C unless stated otherwise.

[‡]Charged-coupled devices consist of an array of light-sensitive elements, which each generate a charge proportional to the number of photons that strike them. By adjusting the potential of the adjacent element, this accumulated charge may be be shifted from one element to another. For a two-dimensional image, the first column of charges is converted into a voltage, row by row. The grid of remaining charges is then shifted, and the next column read. In this way, the photon information that landed on the sensor is converted into a sequence of voltages. The invention of the CCD in 1969 [215] lead to the 2009 Nobel Prize in Physics for its creators, Willard Boyle and George E. Smith. For a text on the principles of operation, see [216].

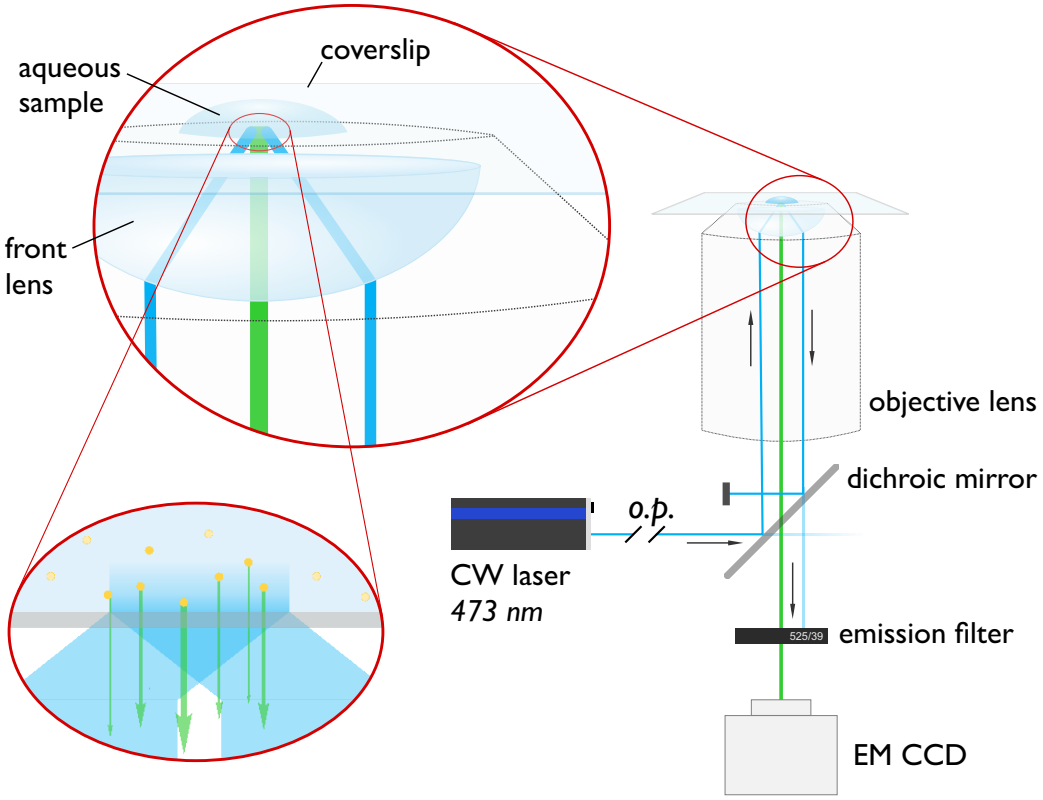


Figure 3.1: Excitation and emission pathways for oSCR imaging. Blue laser light from a continuous wave (CW) laser source passes along an optical path (*o.p.*) that collimates and focuses the beam. A dichroic mirror that has a near-zero transmittance for light below a threshold wavelength, but passes wavelengths longer than the threshold, reflects the laser into the TIRF objective lens, where it undergoes total internal reflection at the coverslip-water interface, exciting fluorophores within the evanescent field created (see Chapter 1). The laser beam returns along the input path, however a small proportion of light may be transmitted through the dichroic. An emission filter cuts out these unwanted wavelengths en route to the detector. The desired fluorescent emission signal travels down the centre of the objective and passes through the dichroic and the emission filter to the electron-multiplying charge-coupled device (EM CCD).

Negative potentials were applied to the droplet to induce poration in order to ensure calcium flow took place from the agarose into the droplet. When a pore opened this could be detected as a bright circular spot in the bilayer, which for convenience is termed a SCCaFT (single-channel calcium flux transient) [217].

3.2.6 Phase-Separated Bilayers

1,2-dipalmitoyl-*sn*-glycero-3-phospho-(1'-rac-glycerol) (DPPG) and porcine brain-sphingomyelin (bSM) were obtained from Avanti Polar Lipids and used with-

out further purification. Cholesterol was obtained from Affymetrix UK (High Wycombe, UK). Lipid stock solutions in chloroform were prepared from lyophilised lipid powder and stored at −20 °C. The lipophilic dye DiI (1,1'-dioctadecyl-3,3,3',3'-tetramethylindocarbocyanine perchlorate) was purchased from Life Technologies (Paisley, Scotland, UK). Mixtures of either DPhPC/DPPG/cholesterol or DPhPC/bSM/cholesterol were formed as 1:1:1 molar solutions in hexadecane, with a total lipid concentration of 8.7 mg·mL^{-1}. The lipid-in-oil mixture also contained 1 mol% DiI. Both the droplets and the device were incubated in this solution, and after the droplets were added to the device wells, the device was incubated at 45 °C for 20 minutes to ensure lipid mixing. Both Fluo-8H and DiI were excited by the 473 nm laser. DiI exhibits strongest absorption in the green portion of the visible spectrum, however here it was excited with a blue laser in order to simultaneously observe phase separation and SCCaFTs. Since the excitation wavelength (473 nm) was well separated from $\lambda_{\text{absorption max. DiI}} = 549$ nm (see Appendix C for excitation and emission spectra), the DiI emission intensity was low enough so as not to obscure the signal from any SCCaFTs, thus permitting the simultaneous imaging of phase-separated lipid regions and the calcium flux through pores within them. Emission signals were passed through a 542/50 nm bandpass filter (Semrock).

3.2.7 Bilayers at Elevated Temperatures

When required, DIBs were warmed by placing them on a heated microscope stage (PE94; Linkam Scientific Instruments, Tadworth, UK) within the Faraday cage. The temperature of the stage was regulated by an external unit. Bilayers were given time to equilibrate before recordings were made; the temperature of the device was monitored using a thermocouple temperature probe in a well adjacent to that containing the droplet to be imaged.

3.2.8 Image Processing

3.2.8.1 Background Correction

Some images showed signs of uneven illumination by the TIRF spot generated by the optical setup. In other cases, images were found to subtly 'flicker' from frame to frame, due to slight variations in the laser power, or image rescaling during recording. In order to correct for this, a simple procedure was written in the image processing software ImageJ (W. S. Rasband, U.S. National Institutes of Health, Bethesda, MD, 1997-2011). The steps are highlighted in Figure 3.2, using a 1000 frame recording at -160 mV as an example. Beneath each stack of images is a plot of the mean intensity of a 60×60 pixel^2 (15.9×15.9 μm^2) region of interest drawn over an area of the bilayer that contained no electropores during the recording, which shows the background fluctuations for each stack. A fast Fourier transform (FFT) bandpass filter was applied to each image within the raw image stack. The FFT filtered out structures larger than a user-defined threshold, which was set to be $\sim$15 % above the diameter of the largest SCCaFT in the stack. Variations in the TIRF profile were far bigger than this, so were removed during the FFT. However, this transformation cannot remove the frame-to-frame variation in overall intensity (see Figure 3.2, centre), and so a process that is termed here *mean-of-patch correction* was applied. In mean-of-patch correction, a region of the bilayer that contained no SCCaFTs throughout the duration of the stack was highlighted. The patches used were always $\geqslant$100 pixel^2. For each FFT filtered image in the stack, the mean value of the intensity in of patch was computed. The intensity values of every pixel of the frame was then divided by this number, with the process repeated for all frames. In taking a value for the background intensity for each individual image, frame-to-frame variations in the overall intensity could be eliminated (Figure 3.2, right).

A common alternative background correction method is to calculate the median pixel intensity across the stack for all pixels. Division of the raw stack by this median image results in removal of the background. However, this method of background removal was rarely used, for two reasons. Firstly, it cannot remove frame-to-frame ensemble intensity variations. Secondly, electropores were found to

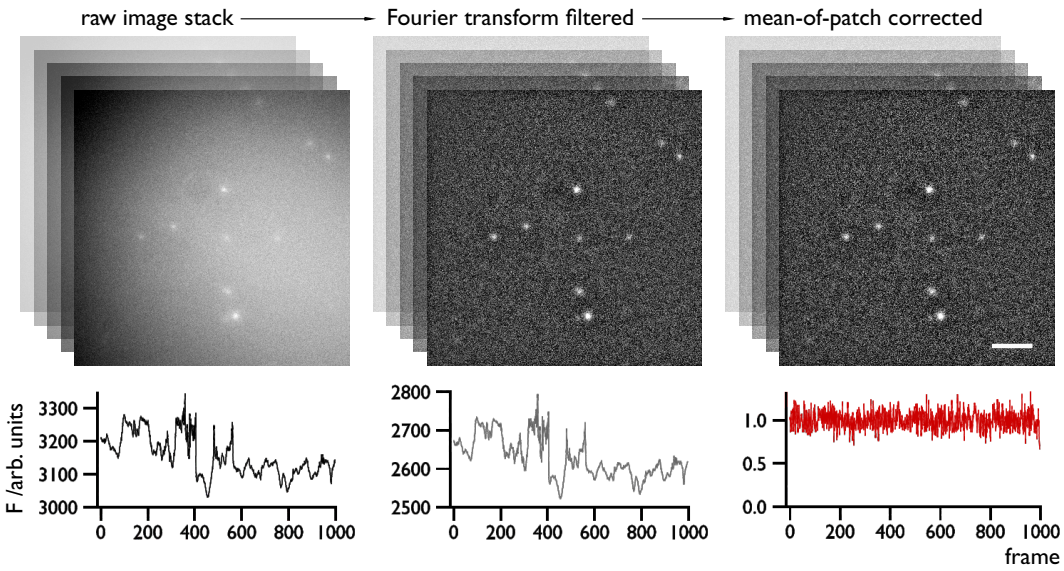


Figure 3.2: Background correction procedure. *Left*: A raw image stack showing uneven TIRF illumination, recorded at −160 mV. *Centre*: The result of a fast Fourier transform bandpass filter on the raw images. In this case the filter removed structures larger than 30 pixels (7.95 µm) across. *Right*: Mean-of-patch correction removes the intensity fluctuations across the image. Beneath each stack is a plot of the mean background intensity (ordinate axes) versus frame number (abscissæ). See the main text for a full explanation of this procedure. Scale bar: 20 µm.

diffuse relatively slowly, and many remained stationary or diffused within a small area (for example, see pore 3, yellow box in Figure 3.12), which meant that the median image contained bright regions where these slow-moving SCCaFTs were present. Dividing or subtracting this image from the stack would therefore result in unwanted removal of the more sluggish pores.

3.2.8.2 Further Image Processing

Tracking of diffusing pores and initial image processing was carried out using the Trackmate plugin in Fiji [218]. Spots were detected by Trackmate using its Laplacian of Gaussian algorithm and tracked with the Linear Assignment Problem tracker, allowing for gap closing over a maximum distance of ∼5 pixels over 10 frames. Detected spots and their associated tracks were then manually checked and filtered for quality. Other image processing was conducted in ImageJ.

3.2.9 Data Analysis

Analyses were carried out in Igor Pro 6 or 7 using custom-written procedures. Spot fluorescence was analysed by examining a circular region of interest around each spot. The mean pixel intensity of this region versus time was then calculated. Errors are given as the standard deviation unless stated otherwise.

3.3 Results & Discussion

A schematic of the oSCR setup for imaging electroporation is shown in Figure 3.3. Bilayers were formed as DIBs on agarose, but with asymmetric electrolytes either side of the membrane. The droplet contained 1.5 M buffered KCl, 10 mM EDTA and 46 μM of the calcium-sensitive dye Fluo-8H. The fluorescence of this dye, which is based on fluorescein, increases more than 200-fold upon binding Ca^{2+} (manufacturer's information); the dissociation constant K_d for binding is estimated to be 232 nM, making the dye highly sensitive to very small concentrations of calcium ions.

In order to prevent a charge imbalance existing across the membrane, which would alter the experienced transmembrane potential, the hydrating agarose contained 750 mM buffered $CaCl_2$. Whilst this osmolarity mismatch results in an osmotic pressure difference across the membrane ($\Pi_{\text{droplet}}/\Pi_{\text{agarose}} \simeq 1.2$)[§], droplets were allowed to equilibrate before imaging, and no observable changes in the droplet (hence bilayer) diameter were seen once bilayers had formed.

3.3.1 Effect of Calcium

In order to assess the influence of calcium ions on electroporation behaviour, voltage protocols were run for the generation of I–V curves, as detailed in Chapter 2. The curves followed the same form as those from KCl-only experiments, however, the

[§]The osmolarity of a solution is given by $\sum_i = \varphi_i n_i C_i$, where n_i is the number of particles that the solute dissociates into, C_i is the concentration, φ_i is the osmotic coefficient, which accounts for non-ideality of the solution, and the index i represents a particular solute. Using $\varphi_{\text{KCl}} = 0.9$ [219] and $\varphi_{\text{CaCl}_2} = 1.0$ [220], with KCl and $CaCl_2$ ideally dissociating into two and three species respectively, the osmolarities of these solutions may be calculated.

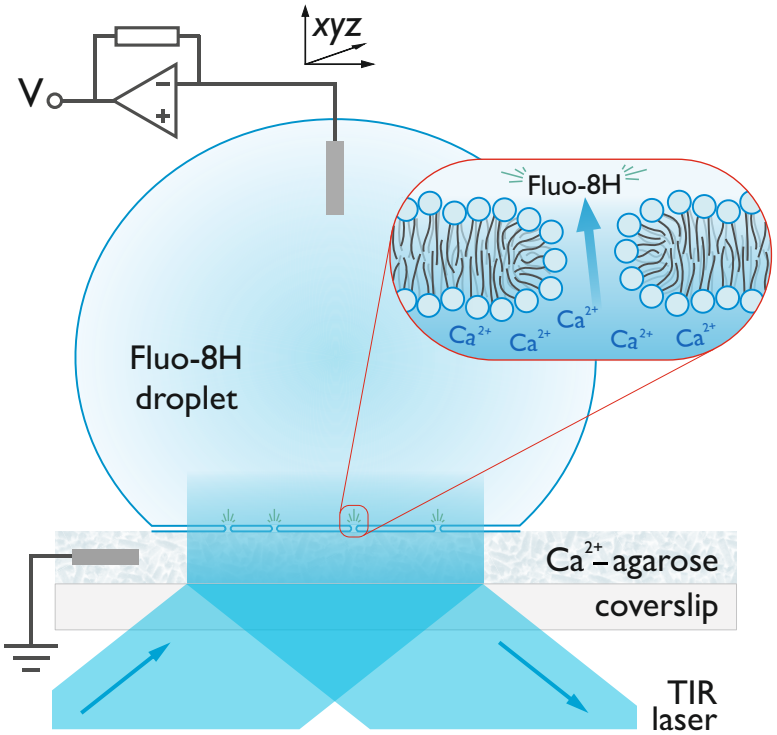


Figure 3.3: Setup for oSCR imaging of electropores. Expanded region highlights the motion of Ca^{2+} from the agarose into the droplet, where it binds to Fluo-8H, enabling visualization of the flux through individual electropores by TIRF microscopy.

presence of calcium was found to have a stabilising effect. Protocols with different t_{high} and t_{rest} values were run, but little difference in the electrical behaviour could be discerned when comparing the resultant I–V characteristics. Figure 3.4 highlights typical curves for these protocols. The non-linear portion of the curves end at generally larger potentials than in experiments with KCl electrolyte (see Figure 2.11), indicating that rupture instability was initiated at higher voltages in the presence of Ca^{2+}. This is borne out in the value of $\bar{V}_{\text{c, CaCl}_2}$, which was 269 ± 34 mV ($n = 12$). Protocols with short t_{high} showed the same rupture potentials as those with longer voltage application periods: $\bar{V}_{\text{c}}$ for protocols with t_{high} of 180 or 300 s was 270 ± 17 mV ($n = 3$), whilst for t_{high} of 60 or 75 s, the critical voltage was 268 ± 17 mV ($n = 9$). Similarly, the onset potential was found to be elevated, with 122 ± 31 mV ($n = 10$) across all protocols. Both of these values represent a 20 % increase over the values obtained in potassium-only bilayers. As discussed in the previous chapter, certain ions associate strongly with the charged moieties

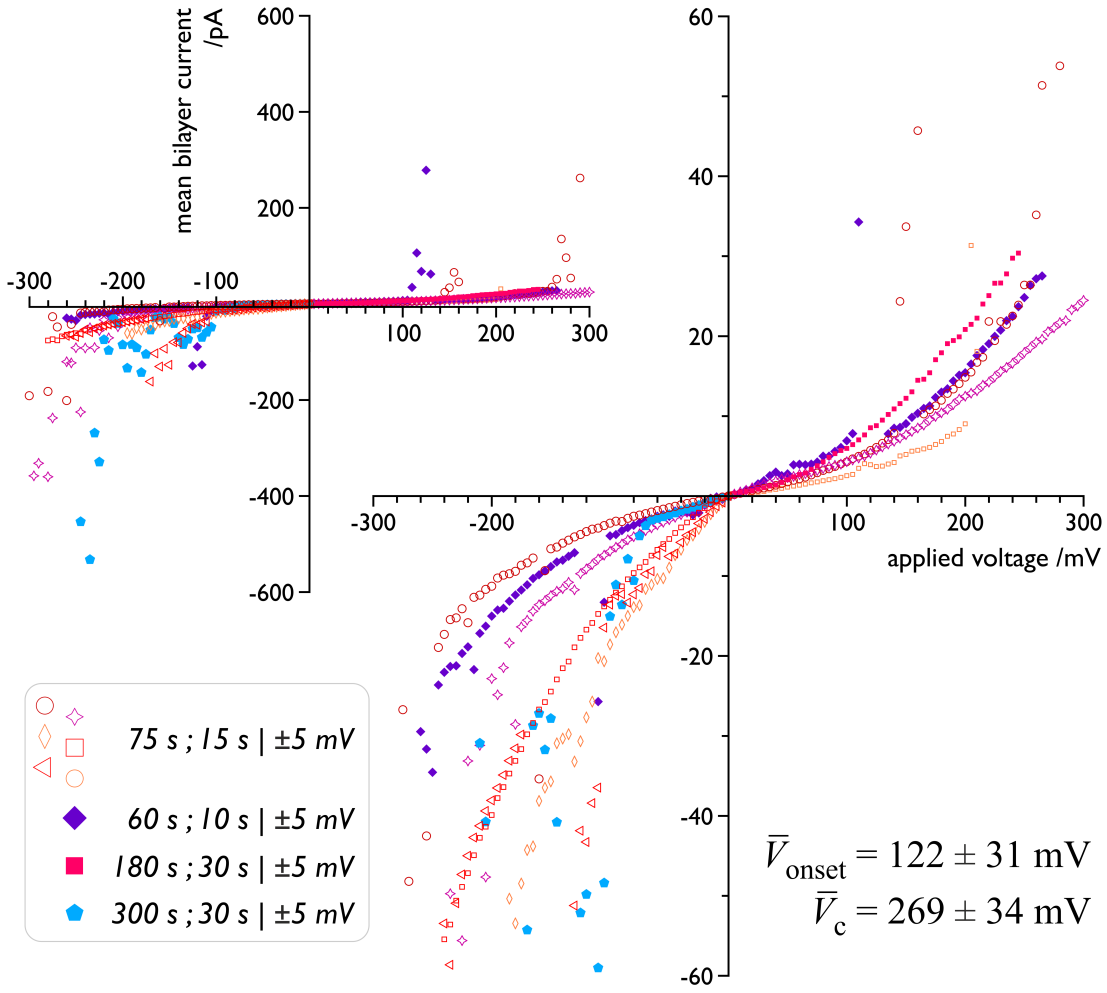


Figure 3.4: Ensemble electrical behaviour in the presence of asymmetric electrolytes; 1.5 M KCl was in the droplets, and 750 mM $CaCl_2$ in the agarose. Bilayers exposed to several different protocols demonstrated the same elevated onset and rupture potentials, consistent with lipid-lipid stabilisation interactions mediated by Ca^{2+} ions. Protocols were run at negative and positive potentials to ensure no bias in the electrical behaviour, since by their configuration oSCR experiments required negative voltages to be applied to the membrane.

of the lipid headgroups. Calcium is known to associate particularly strongly [190, 221], having been shown to inhibit electroporation-like gating at the lipid transition temperature[¶] of 2:1 (wt./wt.) brain phosphatidylserine/cholesterol bilayers [222],

[¶]Lipids at their phase transition temperature have been shown to exhibit the type of conductance fluctuations observed in this work and other electroporation studies. A review by Thomas Heimburg demonstrates many examples of this phenomenon [191]. Channel formation occurs at lower voltages at the transition temperature, and although the exact reason for this has yet to be determined, it is probably linked to the disruption of the lipid ordering during the phase change, which allows aqueous pores to form more easily.

and to induce gating in DPPC bilayers heated to above their melting temperature [223]. Both of these observations are the result of Ca^{2+} stabilising the bilayer and in doing so, raising T_m. The increase in the values of V_{onset} and V_c in DIBs are consistent with the same mechanism of stabilisation. Despite the modulation in bilayer stability against poration, the voltages at which pores appeared and bilayers ruptured were appropriate for studying electropores optically. Bilayers were electrically active over a wide range of voltages spanning around 200 mV, allowing for the study of pore behaviour in relation to its driving force.

3.3.2 Optical Detection of Electropores

Upon the application of a potential difference of sufficient magnitude across the bilayer (usually $\geqslant$90 mV; the droplet was negative with respect to the substrate), and under TIRF illumination, electropores were observed as bright spots against a dark background, as calcium was driven from the substrate into the droplet and bound to the dye. These SCCaFTs — single-channel calcium flux (or fluorescence) transients — allowed the localisation of individual pores within the bilayer, and the investigation of their properties.

Figure 3.5 displays several images of DIBs during electroporation under TIRF illumination. It is interesting to note the variation in the distribution of apparent pore sizes in the images. As shown in these examples, the potential may induce the formation of a single pore (Figure 3.5a), multiple pores of a range of diameters (Figure 3.5b) or a population of small pores may exist alongside very large ones (Figure 3.5c). The radii of all of these pores were constantly fluctuating, with some pores remaining open for many seconds, and some transiently opening and closing. The range of behaviours that electropores imaged in this way demonstrated shall be discussed in the subsequent sections.

The systematic application of larger potentials resulted in the formation of *both* a greater number of pores and larger pores, Figure 3.6. As already alluded to, however, this did not mean that all pores increased in size when the potential was raised, nor that newly formed pores were larger than at lower potentials. Further

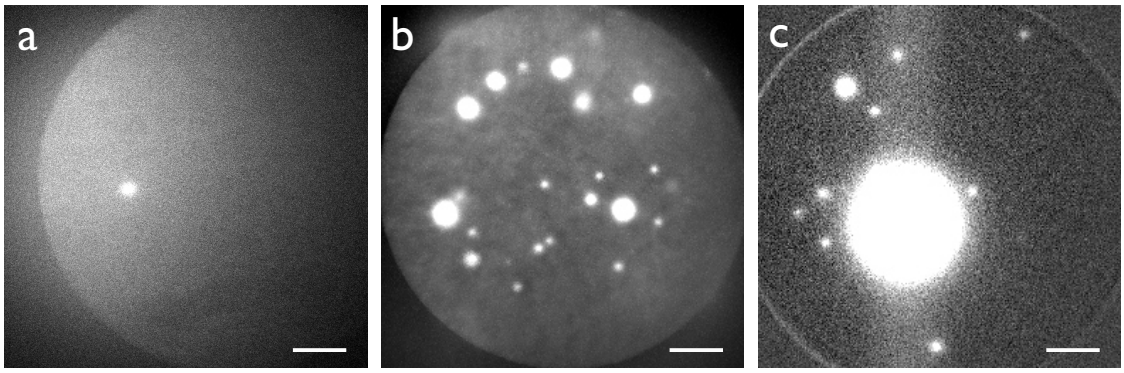


Figure 3.5: Visualising electropores in DIBs. (a) A single electropore in a bilayer held at −200 mV. Image is the raw data, recorded at 9.91 Hz. (b) Multiple electropores at −485 mV. Image is the maximum pixel intensity of 40 frames recorded at 61.69 Hz. (c) A very large pore at −260 mV. Single, background-corrected frame, recorded at 61.69 Hz. All scale bars: 20 µm.

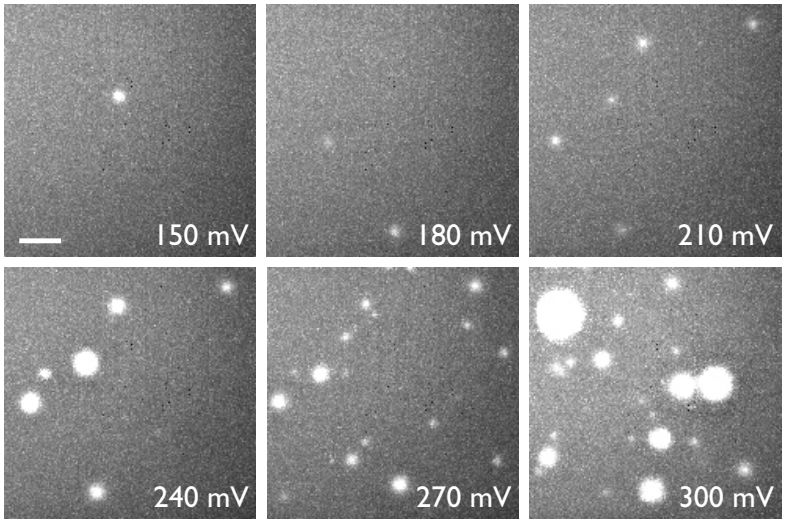


Figure 3.6: Increasing pore formation with voltage. Images are maximum intensity projections of >1000 frames recorded at 29.94 Hz on the same bilayer at successively elevated potentials. Scale bar: 20 µm.

discussion regarding these particular observations shall be left for now and returned to in Chapter 4, where a more detailed investigation and its implications for the electropore energy landscape shall be discussed.

3.3.3 Correlating Electrical & Optical Measurements

The detection of SCCaFTs was intended as an optical complement to the concurrent electrophysiological measurements made during electroporation. In order to assess the effectiveness of oSCR recordings in reporting pore fluctuations, the

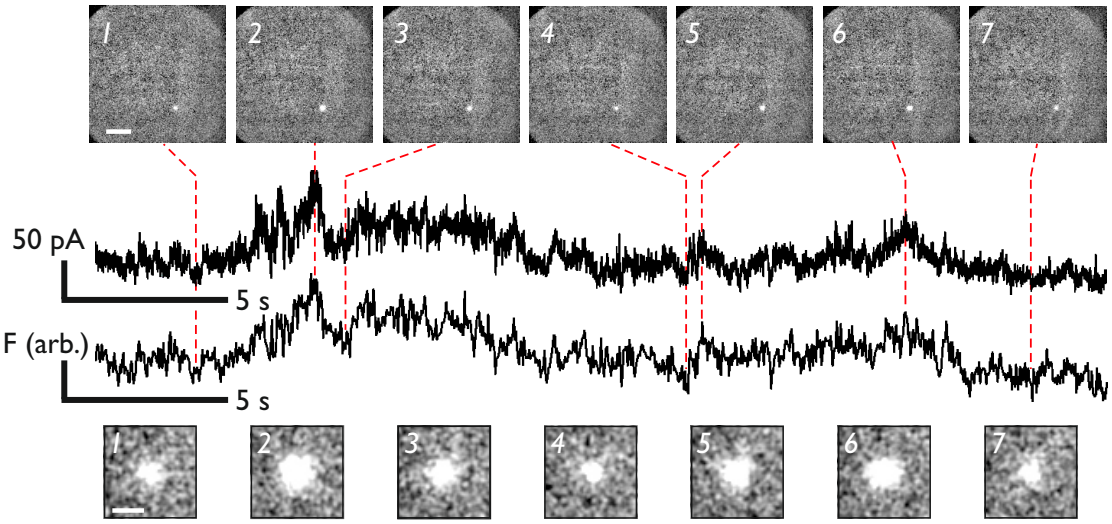


Figure 3.7: Correlating electrical and optical signals. A single pore is present in a DIB membrane held at −160 mV. The upper black trace is the total bilayer current, which has been inverted along the horizontal axis to aid comparison with the intensity data. The mean fluorescence intensity from a circular region of interest ascribing the maximum diameter of the SCCaFT is plotted beneath. The oSCR recording shows excellent reproduction of the electrical signal. *Upper images*: frames at 32.9 Hz demonstrating only a single pore is within the entire bilayer. The bilayer edge is visible in the top corners of the images. Scale bar: 25 µm. *Lower images*: expanded views of the pores showing the fluctuation in SCCaFT radius. Scale bar: 5 µm.

correlation between the electrical behaviour of the membrane and the fluorescence signal was sought.

Figure 3.7 demonstrates such correlation between signals. The current flow from a single pore was accurately mirrored by the simultaneous visual readout. This additionally confirmed that the conductance fluctuations were solely due to this lone defect, and that ionic flux across the membrane was not mediated by any other route. The ability of oSCR to report on the behaviour of individual pores is further highlighted in Figure 3.8, wherein the separate contributions to the electrical signal from multiple pores within a bilayer, which were indistinguishable in the electrical recording, are clearly revealed by the optical method. The membrane, held at −200 mV, contained three conductive defects; individual fluorescence traces of three of these pores (F_A, F_B and F_C) allow their relative influence on the total conductance (E_{A+B+C}) to be assessed. It demonstrates that a consideration of the electrical information alone is insufficient to reveal what is happening across

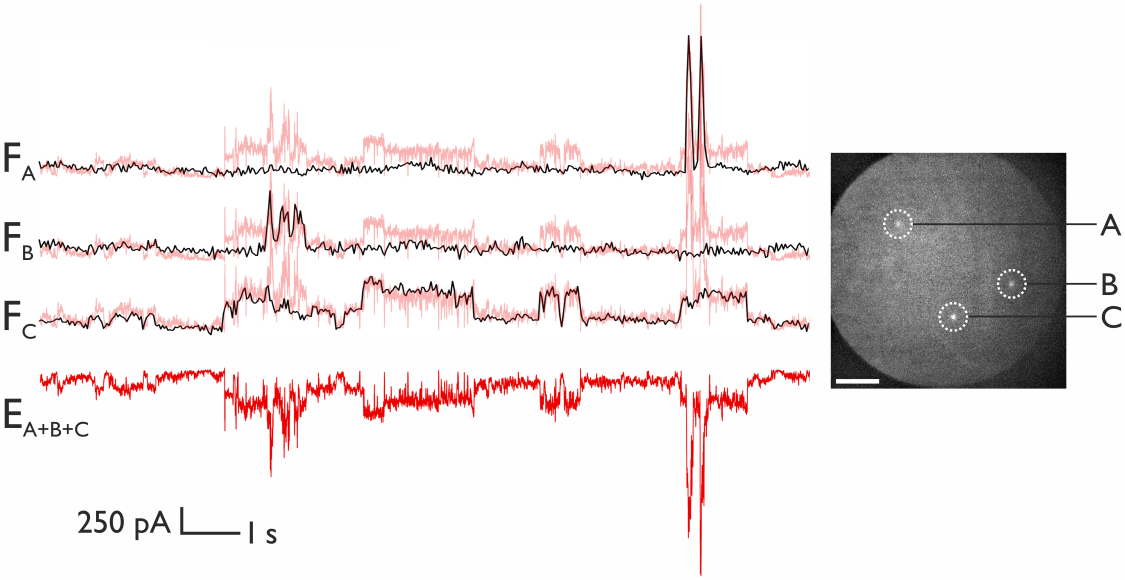


Figure 3.8: Deconvoluting multiple electrical signals. Three pores in a membrane at −200 mV contribute to the bilayer current signal, E_{A+B+C} (*red*). Deflections are downwards due to a negative potential being applied. Black traces are the mean recorded intensities from the pores marked A, B and C. The image is the maximum intensity over 200 frames recorded at 32.9 Hz. Scale bar: 25 µm.

the entire membrane surface.

In addition, it can be seen that V_{applied} is able to support a range of pore sizes: the large conductance near the end of the recording (pore C) indicates a much larger pore, opening twice in quick succession, compared with the pores at less than half its current, which often had longer lifetimes. This begins to provide information on the stochastic formation of pores: defects do not all form at the same size, and not all radii are stable for long periods.

3.3.4 Individual Pore Behaviours

Electropores demonstrated a variety of fluctuating behaviours, which are summarised in Figure 3.9. At low potentials, the discrete, step-wise changes in conductance observed in the electrical-only recordings (Chapter 2) were reproduced. This confirms the hypothesis that the similar electrical events were the result of a single pore in the membrane. It further implies that the barrier to pore closure must be relatively small, since otherwise, after pore formation, the pore would be trapped open. The line tension must therefore be sufficiently large in this system (that is,

comparable to the surface tension and voltage terms in equation 2.9) so as to (a) to encourage collapse of the pore, and (b) overcome the repulsive headgroup-headgroup interactions as the hydrophilic pore walls come together.

Higher potentials showed that pores did not have one single fluctuation regime. In reference to the traces in Figure 3.9, some showed switching between quiescent and noisy states, which could manifest itself as very rapid openings (−237 mV) or gradual increases in conductance (−165 mV). Sudden rises to very high intensities were observed (−263 mV), alongside long periods at stable radii (−243 mV). In some cases, a pore at a relatively low potential would continue to grow (−142 mV); in others, heavy fluctuations terminated suddenly with collapse of a pore (−263 mV). All of these modes could occur at elevated potentials, with no apparent favour of one mode over another.

It was also noted that the event of pore closure took place very rapidly, with the oSCR signal dropping back to the background intensity often within a single frame of imaging. This is evident in the recordings at −127, −151, −237 and −263 mV, indicating that pore closure is independent of the applied potential. In the fastest imaging experiments conducted, pores closed within 8 ms. The instantaneous nature of the closing transitions implies that electropores exhibit a propensity to close; that is, should the transmembrane potential drop or surface tension ease momentarily, the line tension will instantly work to close the pore.

3.3.5 Electropore Diffusion

The lipid molecules forming the bilayer are in constant thermal motion. An electropore therefore, as an entirely lipid-based structure, should be expected to show two-dimensional diffusion within the bilayer. Scott Freeman, Michele Wang and James Weaver implied that they believed electropores should diffuse when they discussed pore-pore interactions based on numerical studies in 1994 [201], however there is very little material in the literature that covers the topic. This is very likely due to the lack of imaging capability being able to verify or contradict such predictions.

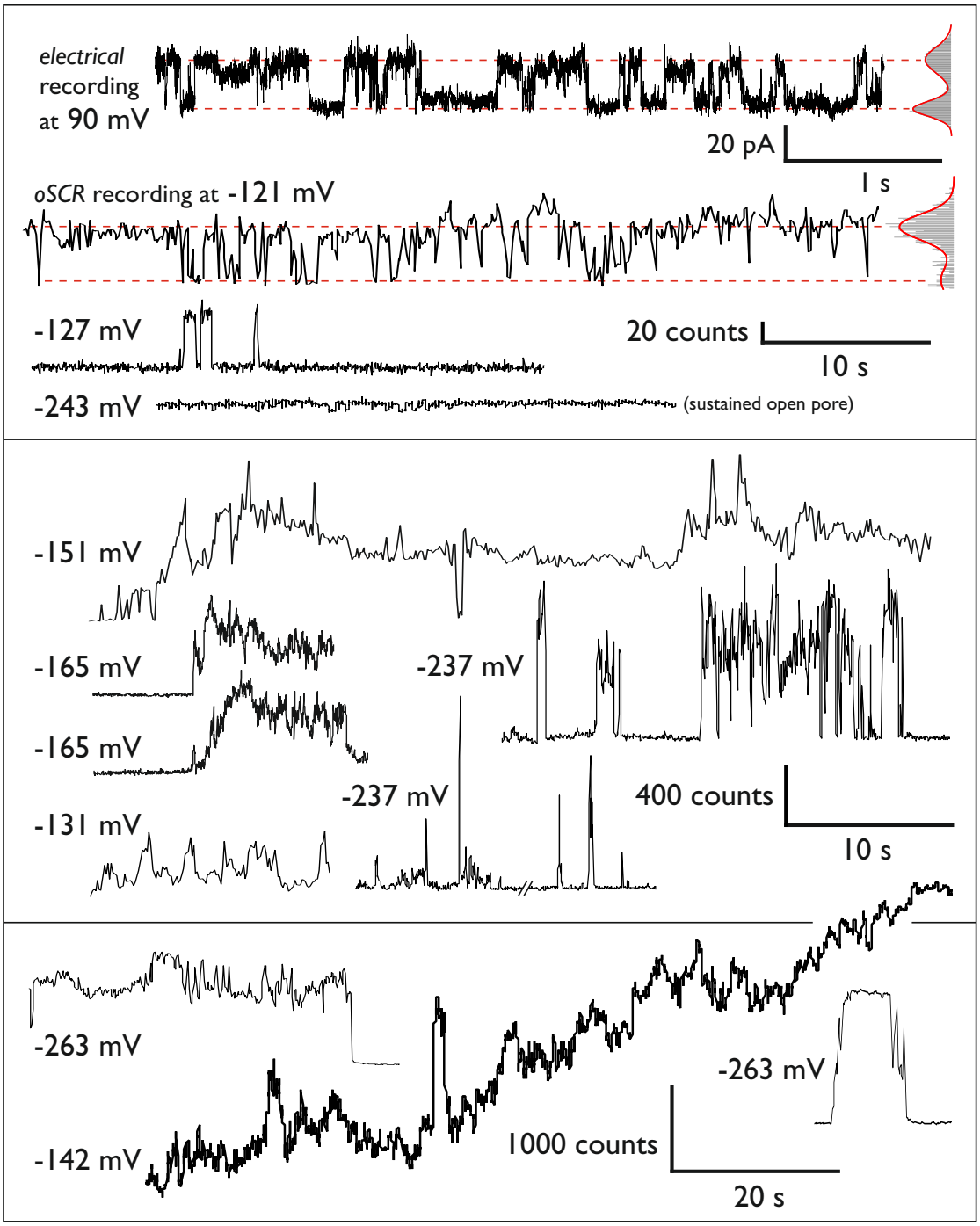


Figure 3.9: Individual electropore gating behaviour, as revealed by oSCR fluctuations. At low potentials, discrete electropore gating may be detected, resembling electrophysiology data. As the potential is increased, a large variety of gating regimes can exist. The three sections delimit traces that have the same scaling in intensity and time; these scales extend down the figure.

Electropores in DIBs were observed to diffuse. However, whilst in initial experiments some electropores were seen to exhibit this behaviour, around 80 % of the SCCaFTs observed in DIBs were stationary. This was of concern, as it implied interactions between the agarose and the bilayer. These may have been mediated in different ways. Agarose is a polymeric gel of two subunits based on D- and L-galactose [224]. Atomic force microscopy (AFM) shows that the surface undulates with the depressions of the order of a few hundred nanometres (300 ± 200 nm) [225]. Curvature of the membrane to accommodate these depressions, encouraged by the pressure imposed by the electrical field, may result in a 'pit' which could restrict the motion of a pore formed within it. Alternatively, it may be that a branch of the interwoven gel structure protrudes from the surface far enough to push into the lower monolayer, nucleating a pore at this location.

3.3.5.1 Encouraging Diffusion via Hydration

These two scenarios rely on the water cushion between the lower leaflet and the upper surface of the agarose gel being relatively small. Varying the concentration of the substrate agarose solution appeared to have little effect on the diffusion of electropores, and so attempts were made to ensure adequate hydration of the substrate. This was achieved by the fusion of small droplets of buffer to the substrate after the addition of the lipid-in-oil solution to the device wells. Droplets of between 2 and 6 nL were used, which were formed using a piezoelectric nanoinjector. Small volumes were used as larger droplets tended to produce a water cushion that raised the bilayers beyond the TIRF illumination field.

With careful hydration, SCCaFTs demonstrated that electropores are able to move through the lipid matrix. The data derived from electropore diffusion is shown in Figure 3.10. Diffusing pores were tracked using the Trackmate plugin in Fiji [218], which uses Gaussian fitting to locate bright spots within an image, and forms the most likely trajectory between the spot and those detected in the subsequent frames (for a description of the algorithm's operation, see [218]). Gaussian fitting allowed sub-pixel resolution of pore locations. 2D Gaussian curves were fitted

to single oSCR readouts of electropores, and the error of the fit in terms of its x- and y-locus was noted. From five pores, the average of these ten errors was 0.08501 pixels, corresponding to a localisation error of 23 nm.

SCCaFTs from electropores flickered on and off as pores opened and closed, even whilst they were diffusing. This meant that some pore trajectories included frames where the oSCR signal was absent, resulting in separate trajectories in the Trackmate output. In these cases, Trackmate was set to join likely trajectories using its 'gap closing' function; trajectories were linked if the pore reappeared within 10 frames (in the data presented in Figure 3.10, this corresponds to 162.1 ms) over ∼5 pixels. An example of such a trajectory is shown in Figure 3.10a.

From the x- and y-coordinates, the mean squared displacement versus time (MSD vs. Δt) was computed. This was done by a custom procedure in Igor Pro, which calculated the square of the Pythagorean distances between coordinate pairs separated by a given time lag Δt. That is, for a trajectory along (x_1, y_1), (x_2, y_2), (x_3, y_3), ..., (x_N, y_N), the square displacement was defined as:

$$[\Delta r_i(\Delta t)]^2 = [x_i(t + \Delta t) - x_i(t)]^2 + [y_i(t + \Delta t) - x_i(y)]^2 \tag{3.1}$$

for pairs of coordinates separated by time increment Δt, where i represents one of n specific pairs of coordinates separated by Δt. For example, a trajectory of ten steps (N = 10) would have $n = 8$ pairs of coordinates separated by a Δt of two steps: (x_1, y_1) and (x_3, y_3), (x_2, y_2) and (x_4, y_4), (x_3, y_3) and (x_5, y_5) and so on until (x_8, y_8) and (x_{10}, y_{10}). The square displacement was averaged over the number of coordinate pairs that existed for a given time step:

$$\langle[\Delta r(\Delta t)]^2\rangle = \frac{1}{n}([\Delta r_i(\Delta t)]^2 + [\Delta r_j(\Delta t)]^2 + [\Delta r_k(\Delta t)]^2 + ...) = \frac{1}{n}\sum_{i=1}^{n}[\Delta r_i(\Delta t)]^2. \tag{3.2}$$

Plotting these average displacement values against the time lag Δt that each one was calculated for produces an MSD vs. Δt characteristic of the diffusing electropore in question. In two dimensions, the gradient of the MSD vs. Δt plot is equal to $4D_{\mathrm{lat}}$, the lateral diffusion coefficient [226]. Its value allows the quantification of the mobility of a particle, protein or in this case a pore, by way of the region of

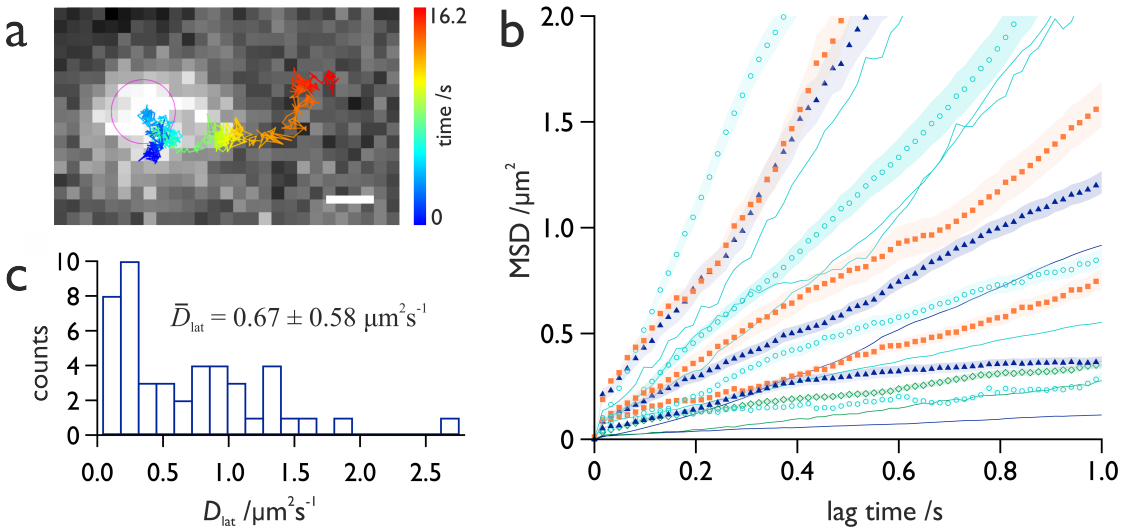


Figure 3.10: Diffusional behaviour of electropores. (a) Trackmate output shown as a single frame from an oSCR stack (61.7 Hz) of a diffusing electropore, recorded at −200 mV, overlaid with the tracking trajectory (blue, 0 s, to red, 16.2 s). The pink circle indicates the detected location of the spot in this frame. Scale bar: 2 μm. (b) MSD vs. Δt plots for 18 electropore trajectories obtained at −180 mV (aquamarine), −200 mV (orange), −260 mV (green) and −330 mV (dark blue) and recorded at a frame rate of 61.7 Hz. The gradient of the curves at $\Delta t < 1$ s were used to calculate the lateral diffusion coefficient, D_{lat}. The magnitude of V_{applied} appeared to have no influence on D_{lat}, with a wide range of diffusion coefficients displayed at all voltages. Errors (±1 standard deviation of the average squared displacement at each Δt) are displayed as a coloured band on some plots. (c) Histogram of the 46 analysed trajectories, highlighting the spread of D_{lat} values. The mean lateral diffusion coefficient was 0.67 ± 0.58 $\mu m^2 \cdot s^{-1}$.

space that it may explore in a given time period. MSD vs. Δt plots for electropores at different voltages are shown in Figure 3.10b.

MSD vs. Δt curves obtained from electropores showed little dependence on the magnitude of the applied potential (Figure 3.10b). Trajectories obtained from 180 to 330 mV demonstrated a broad range of diffusion coefficients, ranging from 0.037 to 2.74 $\mu m^2 \cdot s^{-1}$, with a mean of 0.67 ± 0.58 $\mu m^2 \cdot s^{-1}$ ($n = 46$). The values at the upper end of this range match those of pores formed by the antimicrobial peptide alamethicin (see also Chapter 5) in DIBs [227]. The low-end diffusivity values suggest that in some cases there may have been agarose-lipid interactions reducing the mobility of the lipids in the substrate-facing side of the bilayer.

The lack of correlation between diffusivity and V_{applied} may be expected. Mathematical modelling of the electric field within an electropore predicts an inhomo-

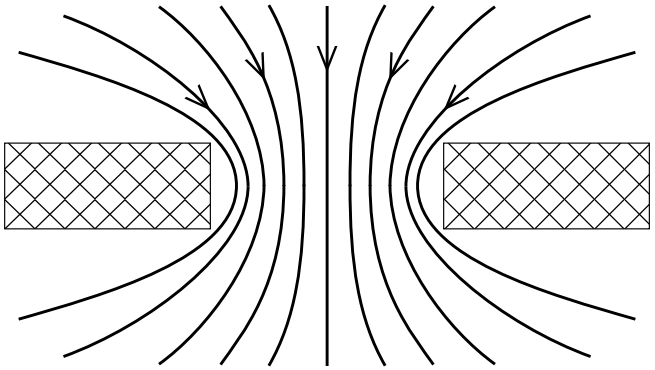


Figure 3.11: Electric field lines in an electropore, as predicted by mathematical modelling by Neu, Smith and Krassowska [228]. Shown is a cross-section through the centre of a cylindrical pore within the bilayer (hatched region). The field lines are found to concentrate at the pore walls. *N.B.* The solutions for the electric fields within cylindrical and toroidal pores were very similar.

geneous field [228], as depicted in Figure 3.11, in which the field lines (and hence the magnitude of the field) concentrate at the pore walls. Whilst the field produces a force on the pore walls, this applies equally around the circumference of the pore. Therefore, an increase in the potential difference is unlikely to result in an anisotropic alteration of the field in the plane of the membrane, such that motion of the pore in one direction would be favoured over another. However it may be expected that a larger voltage would produce larger pores. The theory of Saffman and Delbrück shows that the diffusivity of objects within a bilayer is inversely proportional to their radius [108]. In the case of a toroidal pore, the 'object' in the bilayer might conceivably be the plug of electrolyte filling it. However, elevated potentials were found to produce a distribution of pore sizes (see Section 3.3.2 and Chapter 4), rather than only expand pores found at lower voltages, and many of the tracked pores were of a similar size. Furthermore, any presumed relationship between V_{applied} (hence pore size) and D_{lat} may be additionally complicated by the rapidly fluctuating pore radius.

3.3.5.2 Encouraging Diffusion via Heating

Electropores were also found to diffuse more readily when the bilayer was heated. DIBs were heated to 30 °C using an electronically controlled microscope stage.

Again, pores showed no discernible dependence on the applied voltage in the range 100–170 mV, with the spread of MSD vs. Δt (Figure 3.12) plots appearing similar to those for hydrated bilayers (Figure 3.10). Recordings were made at lower voltages owing to bilayers being more unstable with respect to rupture at 30 °C. Elevated temperatures have been shown in other systems to increase the likelihood of electropore formation [179, 229–231]. This is consistent with the greater thermal energy increasing the probability of hydrophilic pore formation through greater (thermal) lateral lipid fluctuations.

The distribution of D_{lat} values, Figure 3.12a and b, is again broad, but pores generally exhibited larger diffusion coefficients than in additionally-hydrated bilayers, by around one order of magnitude, on account of the increased temperature raising the bilayer fluidity. These values, with a mean of 6.22 ± 4.44 $\mu m^2 \cdot s^{-1}$, near those of individual lipids seen in macroscopically aligned DOPC bilayers at the same temperature [232, 233].

Despite this increase for many pores, some (albeit mobile) defects were still found to be restricted in their motion. An example of this is depicted in Figures 3.12c and d. The images highlight three pores in the same bilayer, which were all mobile to varying degrees, as demonstrated by their overall trajectories (Figure 3.12c), but their overall displacements were quite different. This is especially true in the case of pore *3*, which was only able to move within a few pixels of its starting point. Observation of restricted diffusion despite an apparent increase in membrane fluidity would suggest that substrate-bilayer interactions may still have been playing a rôle. From AFM measurements, the depressions in an agarose gel of 0.75 % should be around 500 nm across [225]. Whilst in the images discussed here this corresponds to the width of one pixel, should the agarose pits be larger in DIBs than in the gel slabs reported in [225], for example due to spinning the agarose onto the coverslip, or the surface structure being dictated by the underlying glass, this might give rise to such restricted diffusion of nanoscale electropores.

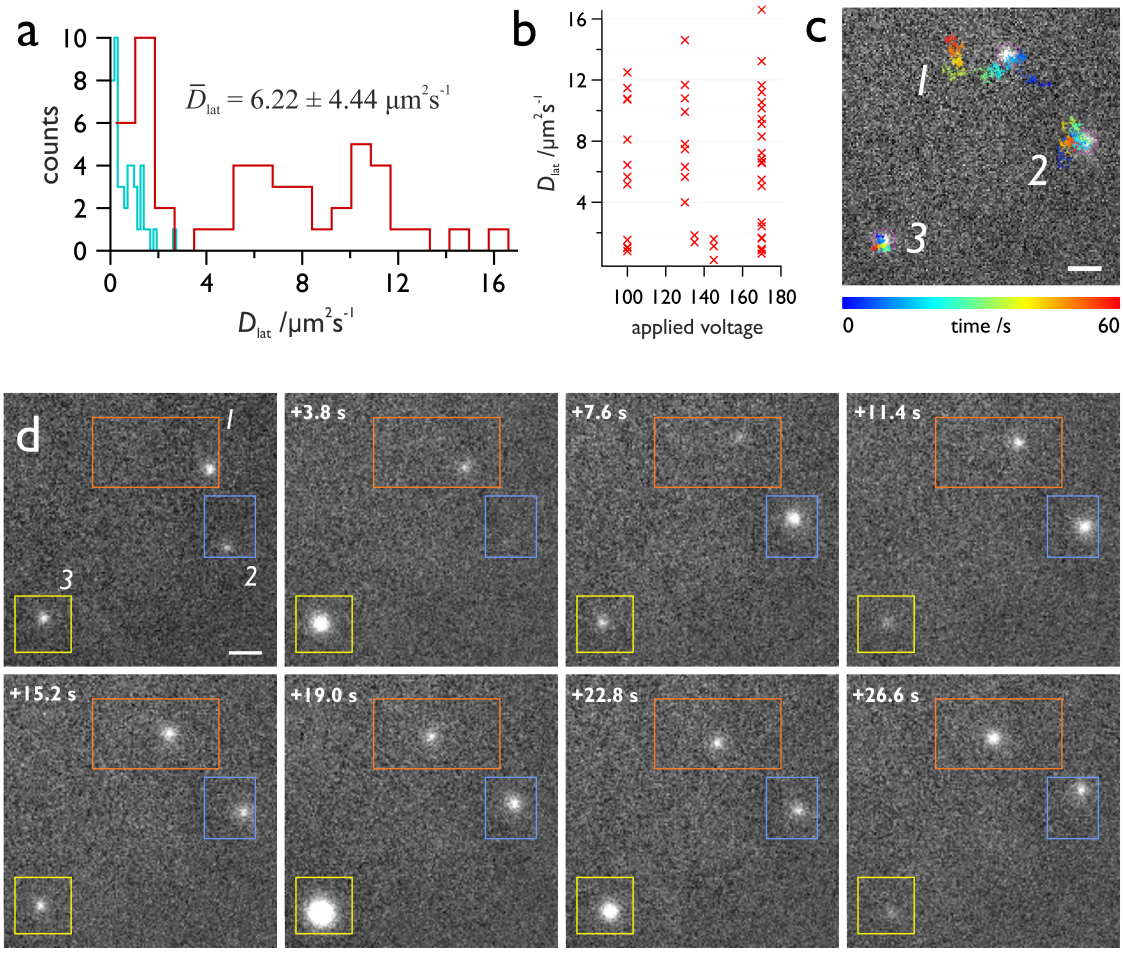


Figure 3.12: Diffusion at elevated temperatures. (a) Histogram of the 50 analysed trajectories at 30 °C. Pores were found to generally diffuse faster under heated conditions, with $\bar{D}_{\text{lat}} = 6.22 \pm 4.44\ \mu\text{m}^2 \cdot \text{s}^{-1}$. *Red*: diffusion coefficients for heated bilayers; *aquamarine*: diffusion coefficients for hydrated bilayers for comparison. (b) D_{lat} values show little voltage dependence. (c) and (d) 30 ms frames from an image stack containing three diffusing SCCaFTs. In (c) trajectories lasting the full 60 s of the recording are shown as coloured overlays, running from 0 s, blue, to 60 s, red. The area explored by the pores is represented in (d) by a coloured box; frames cover the first 27 s of the trajectories, with each of the 30 ms snapshots 3.8 s apart. Under the same bilayer conditions, these three SCCaFTs exhibit quite different displacements, despite all three being mobile. Scale bars: 10 μm.

3.3.6 Electropores in Phase-Separated Bilayers

Molecular dynamics simulations have predicted that electroporation is favoured in lipid regions of greater disorder [234]. In these simulations, ternary lipid mixtures were modelled — mixtures in which the lipid partitions into separate phases with different membrane fluidities. In their model, simulated bilayers of unsaturated DOPC, saturated DSPC (1,2-distearoyl-*sn*-glycero-3-phosphocholine) and cholesterol were formed. DSPC and cholesterol packed together to form a more ordered phase, called the liquid-ordered (L_o) phase, whilst the reduced lipid-lipid interactions as a result of poorer chain packing in DOPC (see Chapter 1) forced it to remain in a more fluid, liquid-disorded (L_d) phase. These systems were allowed to equilibrate for 50 ns, after which a voltage of the order of 350 $mV \cdot nm^{-1}$ was applied, and the simulation run for 20 ns. When these membranes were exposed to a potential difference, electropore formation was found to occur in exclusively the L_d phase within $\sim$8 ns.

Until now, there has not been a simple means to investigate these predictions experimentally. In order to do this in DIBs, phase-separated bilayers were prepared using two ternary mixtures, DPhPC/DPPG/cholesterol and DPhPC/brain sphingomyelin (bSM)/cholesterol, both as 1:1:1 molar ratios. These bilayers exhibited L_o and L_d phases, which were visualised by incorporating 1 mol% of the lipophilic dye DiI into the lipid mixture. This fluorescent marker partitions into the L_d phase, resulting in images of bright L_d regions and dark L_o areas, Figure 3.13.

In both lipid mixtures, electropores were found to form exclusively in the L_d phase, and in all observed cases diffused freely within the L_d regions. They were able to move close to the L_o patches, with their paths following the L_o contours (Figure 3.13a *orange*; b; c *red*) but were never observed to move into them. Nor was pore formation observed to take place within any L_o phase with subsequent expulsion into the L_d region. A slight exception to this is shown in Figure 3.13d. On the right edge of this bilayer, a third region in addition to the clear dark L_o and bright L_d phases was visible. Its intensity was approximately halfway between that of the L_o and L_d phases. It is proposed that this is the result of two 'unregistered' leaflets,

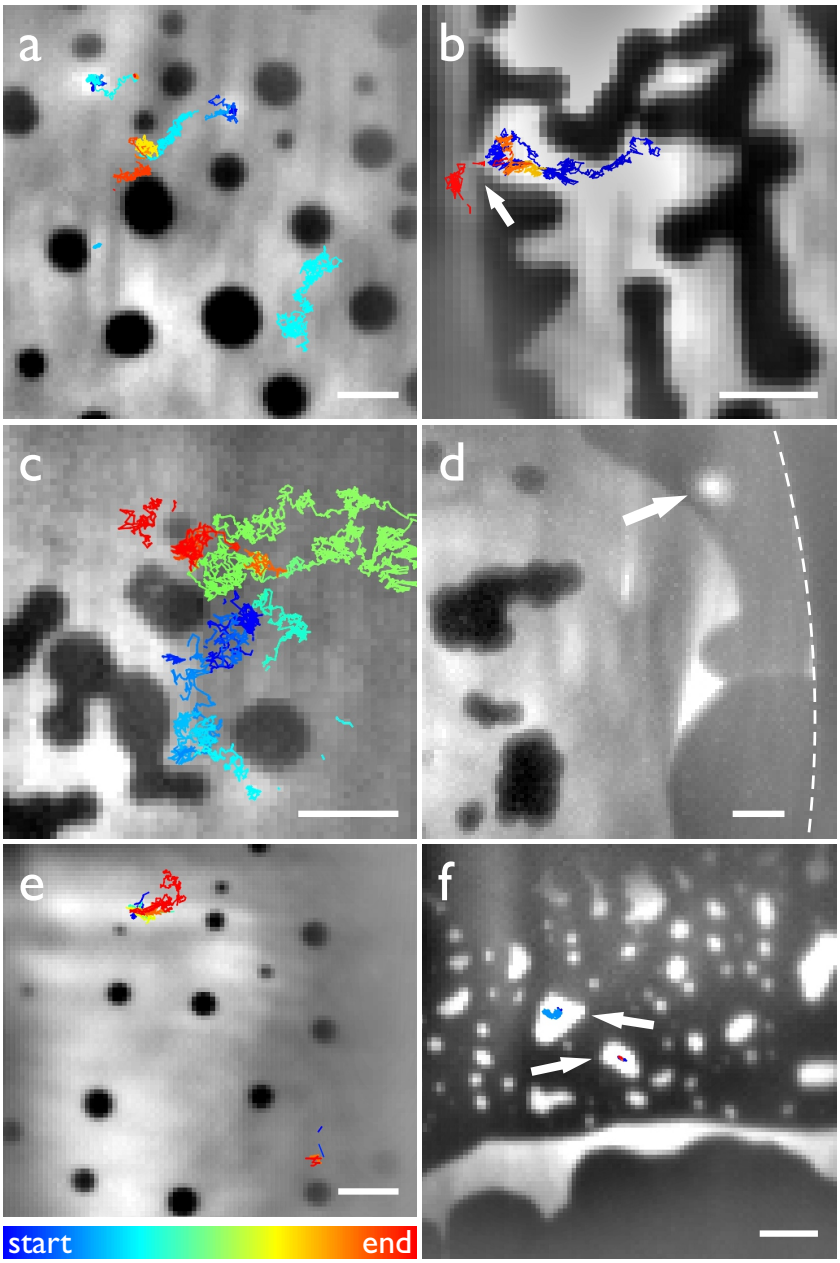


Figure 3.13: Electropore formation in phase-separated bilayers. Images are frames or median stacks (between 500 and 7000 frames), overlaid with electropore trajectories. The trajectory colour represents the timepoint in the recording. Bilayers were composed of (a-c) DPhPC/DPPG/chol, 1:1:1 mol%; (d-f) DPhPC/b-SM/chol, 1:1:1 mol%. Absence of DiI in the L_o phases rendered them dark under TIRF illumination. (a), (c) and (e): Electropores diffuse between mobile L_o regions, but never within them. (b), (d) and (f): Electropores explore L_d areas of the membrane around largely stationary L_o zones. In (b) the pore passes through a small constriction in the L_o phase, marked by an arrow. (d) An electropore forms in a region suspected to consist of unregistered bilayers, however it did not diffuse. The bilayer edge is indicated by the dashed line. (f) Pores are formed and trapped in small pools of L_d membrane in a largely L_o surface. *Recording parameters*: (a) −130 mV, 99.4 Hz; (b) −90 mV, 99.4 Hz; (c) −100 mV, 99.4 Hz; (d) −95 mV, 49.9 Hz; (e) −95 mV, 49.9 Hz; (f) −130 mV, 49.9 Hz. All scale bars represent 5 µm.

each of which possess L_o and L_d phases. Overlap of an L_o phase in one leaflet and an L_d region in the other results in the areas of intermediate darkness. The electropore that was generated here did not diffuse, unlike those in pure disordered areas. Whilst there was enough flexibility in one leaflet to allow the pore to form, both leaflets would need to be fluid in order for the membrane-spanning pore to be mobile.

3.3.7 Pore-Pore Interactions

The electroporation literature contains questions about electropore behaviour that, in the absence of visualisation, can only be addressed theoretically. One such raised is whether electropores are able to coalesce [146, 201]. In recording the data presented here over a number of years, no pores were ever seen to coalesce, although the phenomenon cannot be ruled out entirely. Pores smaller than several hundred nanometres across are within the Abbe diffraction limit, and furthermore, the plume of Ca^{2+} that enters the droplet from the agarose is not restricted to the radius of the defect through which it travels, since these ions may diffuse out in three dimensions once beyond the mouth of the pore. In other words, the observed SCCaFT is larger than the pore that produces it. This means that there is the possibility that pore coalescence within a single SCCaFT could take place unobserved. In addition, the planar geometry of DIBs differs from those of cellular and GUV-based membranes, which exhibit curvature. The electric field experienced by the membrane is at its maximum where the field lines are normal to the bilayer surface, and as such pores form at the 'poles' facing the electrodes in spherical bilayers [146]. One might predict therefore that under large voltages, pores localised in this way might coalesce [201].

Although no coalescence was observed, pores did show other interactive behaviour. When there were few pores in the membrane, defects in close proximity, showed anticorrelation in their oSCR signals. Two examples are shown in Figure 3.14. In both cases, the pores were within less than 15 μm of one another. This influence between electropores is evidence that local changes in surface tension or V_m modulate the radii of other pores. Over larger distances, pores of this size showed no anticorrelation, suggesting that over longer length scales, the dampening

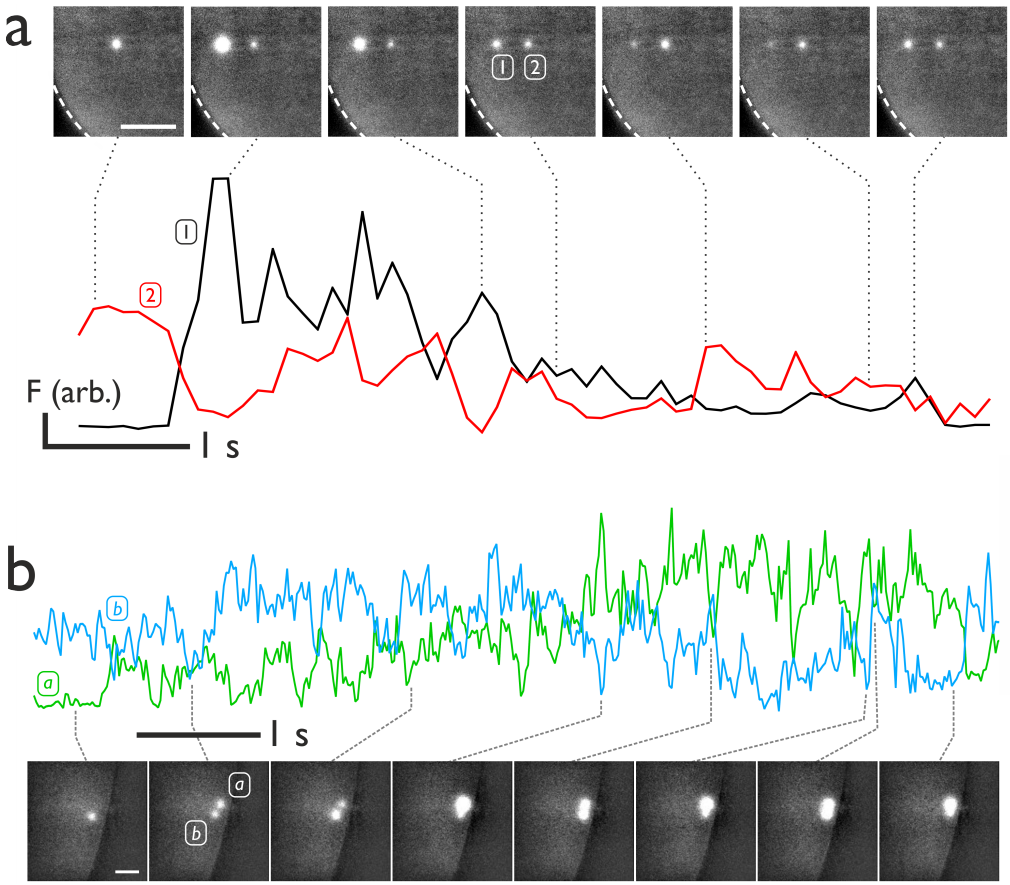


Figure 3.14: Anticorrelation in oSCR signals. Pores in close proximity were observed to gate in a contrary fashion. (a) A pair of pores separated by ∼12 µm, with single frames recorded at 9.91 Hz. Scale bar: 20 µm. (b) Pores ∼6 µm apart; frames recorded at 49.9 Hz show anticorrelation at improved time resolution. Scale bar: 10 µm. Both recordings were made under $V_{\text{applied}} = -130$ mV.

of modulations in surface tension or the electric field is more efficient. The necessity for there to be few pores in the membrane in order to observe anticorrelation is presumably due to the increase in complexity of the system when a greater number of pores are present; when a pore is responding to small changes in tension and voltage driven by many neighbouring defects, the relationship between them will be harder to discern.

Freeman *et al.*, in one of the few works that deal with the motion of electropores, predicted that pores should form away from one another, and moreover, in a planar membrane they should migrate away from one another [201]. They further considered if there might be a magnetic interaction between adjacent pores due to current flow, and deemed any potential interaction negligible. Whilst the origins

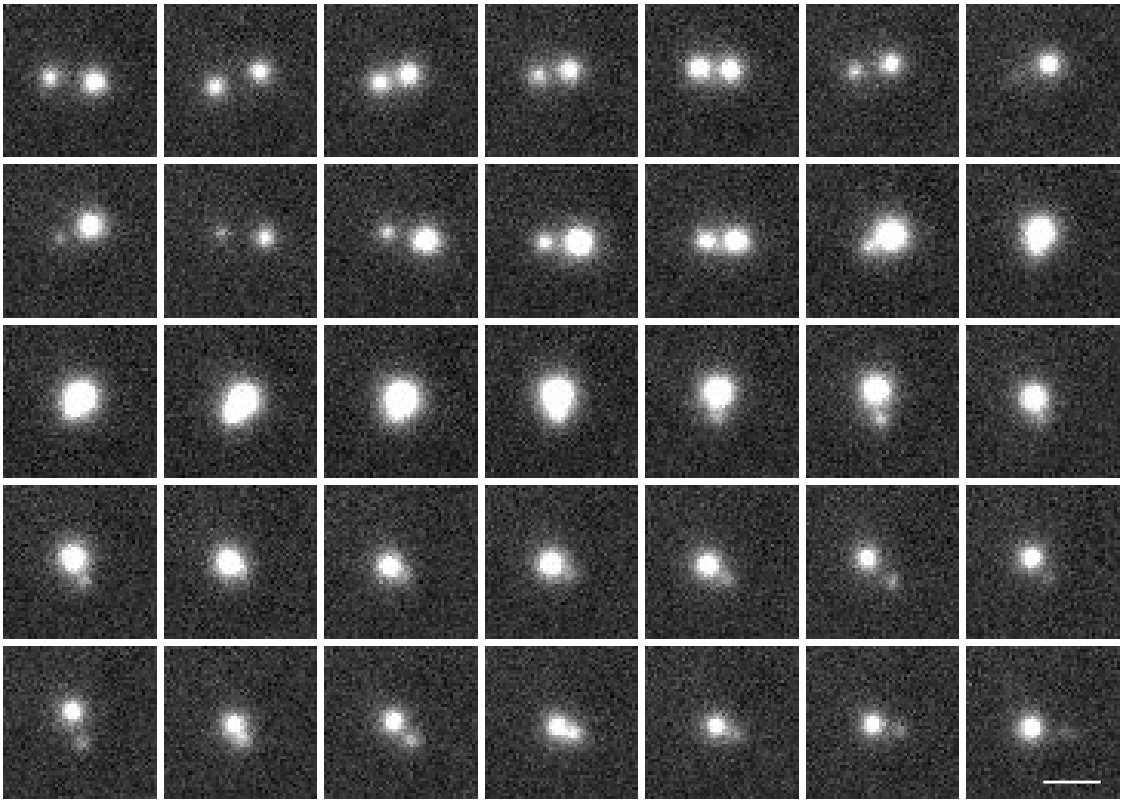


Figure 3.15: Tandem diffusion of an electropore pair. Images recorded at 33.0 Hz of electropores at −100 mV. Each frame marks a time step of 304 ms from the previous image, starting top left. Rather than diffuse apart as predicted, this pair remained together, following one another about the membrane surface. Scale bar: 10 μm.

are not clear, interactions of this type were observed in DIBs. An example is shown in Figure 3.15. These mobile, diffusing pores diffused in tandem, with the motion of the (typically) larger pore (on the right-hand side in the first frame, top left) being followed by its smaller neighbour.

3.3.8 Bilayer Rupture

Further queries have been raised in the literature as to whether bilayer rupture is a result of a single expanding pore, or a collection of smaller defects [146, 203]. Figure 3.16 shows consecutive frames during two instances of DIB breakdown, demonstrating the observation that bilayers in DIBs always rupture via a single electropore. During the growth of the critical defect, other pores within the membrane shrink and seal, and the bilayer visibly decreases in radius. Both of these are the result of a relaxation of the field as a large current flows through the

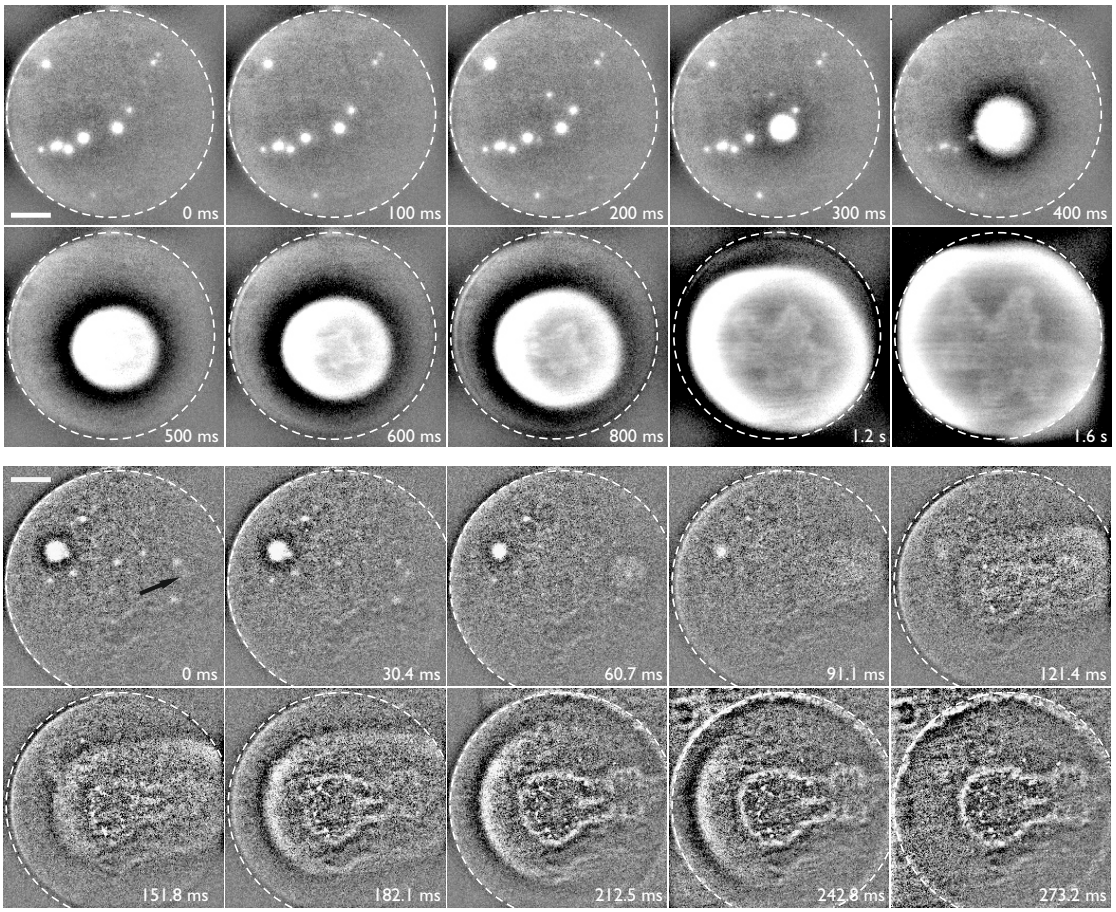


Figure 3.16: Imaging bilayer rupture. *Upper*: Breakdown occurs at −200 mV from a pore in the centre of the bilayer. The bilayer shrinks (starting size is indicated by the dashed circle) and the other pores within the DIB diminish during rupture. *Lower*: Sequence of rupture at −193 mV. Despite the bilayer initially containing an apparently larger pore, the membrane ruptures from the pore indicated by the arrow in the first frame. Scale bars: 20 μm.

critical pore. In the presence of a large pore the local transmembrane potential is reduced (see Section 2.4.4.2), which diminishes the ability of the field to support multiple pores, and the other pores in the membrane therefore seal. As discussed in Chapter 2 (Section 2.4.1), the transmembrane potential exerts a pressure on the membrane; the influence of this can be observed in DIBs, as the bilayer area is seen to expand when the voltage is applied. During bilayer rupture, reduction of the transmembrane voltage also reduces this electrostatic pressure on the membrane, causing it to relax back to a smaller total area (Figure 3.16).

Once started, in no case could the rupture process be arrested, even by the

removal of the applied potential, and it always resulted in complete destruction of the bilayer and its host droplet. The patterns that the membrane forms during rupture are similar to the floral instability patterns seen in rupturing multilamellar vesicles [235]. In phase-separated bilayers, and in the case where a larger proportion of the membrane was in the liquid-ordered phase (see Figure 3.13), the liquid-ordered boundary delimiting the disordered regions in which electropores could form did not restrict the expansion of the pore at elevated potentials: rupture occurred from one disordered region and proceeded to destroy the whole bilayer.

The observation of membrane breakdown by a single pore goes some way to support the current mechanistic model of electroporation: it is expected that once a defect above the critical radius is formed, minimisation of free energy will take place rapidly by continued increase of pore size. This is indeed what is observed in DIBs.

3.4 Summary

The work in this chapter presents the first known visualisations of a dynamic ensemble of electropores. Whereas electrical recording alone can only report on the total membrane current, revealing little about the contribution from individual defects, optical single-channel recording relays in real time a signal from each component pore. These signals are found to correlate very well with the electrical data, therefore providing an optical readout of the contribution to the total bilayer conductance. This optical complement to electrical recording reveals spatial and dynamic information unavailable in the current traces.

The diffusion of electropores, along with their rapid fluctuation in conductance, reveals them to be highly dynamic structures. Their fluctuation regimes are various, with some remaining stable for many tens of seconds, and others having lifetimes of milliseconds. Presumably this variety is a result of local variations in transmembrane potential, local surface tension, or defect-prone regions of the membrane. Pore closure, however, dominated by the line tension, is a rapidly occurring process: large pores may reseal suddenly of their own accord, and the removal of the electric field results in the immediate collapse of all SCCaFTs.

These experiments continue to support the outline theory of electroporation and to inform us about it. First and foremost, electropermeabilisation is an effect mediated by pores. An increased electric field serves to increase the probability of pore formation. Through oSCR it has been demonstrated that the increase in conductance at higher potentials observed in electrophysiology measurements are the result of both an increase in the size and number of pores. A dynamic range of pore radii exists, with stochastic changes in radius. Rupture takes place when the radius of one pore exceeds a critical value, after which unbounded expansion of the pore may occur leading to destruction of the membrane.

The unique ability to monitor electropore motion has resulted in observations of pore-pore interactions and behaviour that until now could only be predicted by numerical and computer simulations. These point towards a complex interplay between the local fields and forces governing electroporation. In particular, pores respond to other defects around them, especially large or proximal ones. It is proposed that these interactions are mediated either by the local transmembrane voltage or the bilayer tension; the sensitivity of pores to the variations in the local membrane stresses is likely the cause of the range of fluctuation regimes we observe. The response of the local transmembrane field in the presence of a pore, and the implication for the formation of further pores has already been considered in Chapter 2, but what of variations in surface tension? In a work that introduced further detail to the basic model of electroporation, Smith, Neu and Krassowska incorporated tension coupling between pores, substituting the constant surface tension parameter σ in equation 2.9 for an effective surface tension, σ_{eff}, which is a function of the area of the membrane that is occupied by pores, A_{p} [114]:

$$\sigma_{\text{eff}}(A_{\text{p}}) = 2\sigma' - \frac{2\sigma' - \sigma}{(1 - A_{\text{p}}/A)^2} \tag{3.3}$$

where σ is the tension of the membrane in the absence of pores (when there are no pores, A_{p} is equal to zero, and σ_{eff} equals σ), σ' is the energy per area (the tension) of the hydrocarbon-water interface, estimated to be 2 $\times 10^{-2}$ J·m^{-2} [236], and A is the total area of the bilayer. According to this equation, as pores are created

and expand, the total pore area A_p increases, decreasing the effective membrane tension experienced by each pore. This decrease in σ_{eff} can halt the expansion of further pores, or those already present in the membrane. This presents another means, along with local variations in V_m, by which the presence of a pores may influence the existence and behaviour of other defects.

3.4.1 Sensitivity & Limitations

Although the locations of individual pores can be resolved to within a few tens of nanometres, their nanometre structures cannot be imaged directly. Instead, their presence is inferred by way of the calcium ions that pass across the membrane at the pore locus. Optical detection of electropores is unavoidably constrained by the diffraction limit, and if multiple pores exist within the diffraction-limited point-spread function (PSF) of the microscope, they will be unresolved. For the imaging system used in this work, Gaussian-fitting to the fluorescence signals from single dye molecules allowed the PSF to be determined, with a full-width half-maximum of 0.59 μm. Multiple pores within a region of this width cannot not therefore be resolved.

A further limitation of oSCR recording of electropores is that obtaining a direct measurement of pore size from the fluorescent events is challenging [213]. It is complicated by several factors, such as the rate at which calcium is drawn through the pore by electrophoresis, and the rate of the lateral diffusion of the Ca^{2+} 'cloud' once it enters the droplet, and for these reasons the SCCaFTs produced by electropores are far larger than the true size of the defects that generate them. One conceivable means to estimate the pore size from the fluorescence intensity would be to calibrate the SCCaFT signal with a pore of known radius. For example, α-hemolysin is a pore-forming channel of defined radius [237], and therefore at a given voltage (*i.e.* under the same electrophoretic conditions), the quantity of calcium drawn through its pore in a given period of time will be relatively constant. The intensity of the resulting SCCaFTs intensities would therefore be representative of pores of the same size as the lumen of α-hemolysin. If several pores of different

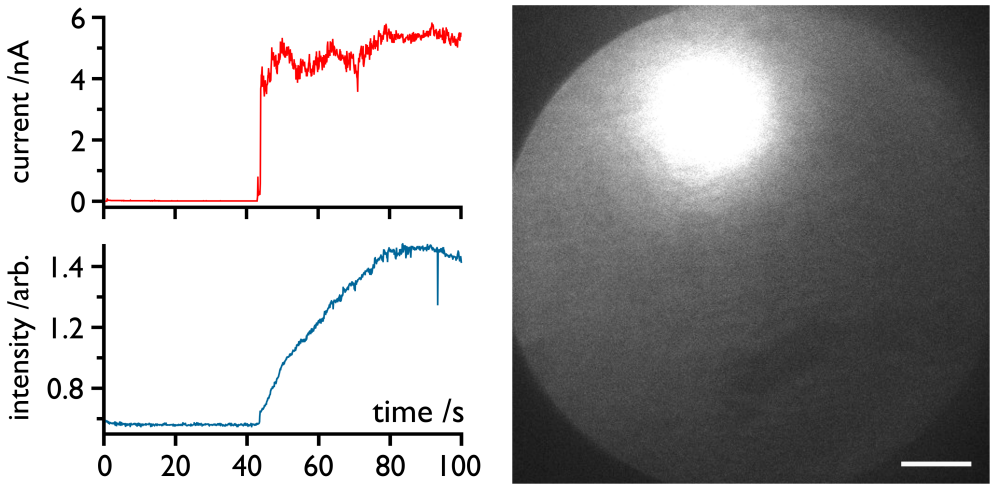


Figure 3.17: oSCR signal lag in the case of large pores. A sizeable defect generates rapidly around 40 s into an oSCR recording. From the current trace (red), it can be seen that this takes place very suddenly, however the corresponding SCCaFT intensity has a delay of ∼50 s before it begins to reproduce the current recording (last 10 s). Image is a 100 ms frame from the recording, demonstrating the large SCCaFT signal. Scale bar: 20 µm.

sizes could be inserted into DIBs, their respective SCCaFT intensities could be used to calibrate the oSCR recordings of electroporation. In the same manner, pores of known conductance could be used to correlate SCCaFT intensities with individual electropore conductances.

Electroporation was seen to begin at around 80–120 mV in bilayers set up for oSCR characterisation. Under the conditions used, electropores generated at the lower end of this bracket were visible as SCCaFTs. Assuming that the discrete conductance step traces in Figure 3.9 are the result of the opening of the smallest possible pore, this represents an optical detection limit, in terms of conductance, of around 400 pS.

At low voltages, there was no detectable delay between the reduction or increase in electrical signal and the change in its corresponding SCCaFT readout. This was also true when the voltage was removed: pores were observed to close immediately. In the presence of a very large pore, however, SCCaFTs deviated from the approximately proportional relationship between the pore current and oSCR intensity. An example of this is shown in Figure 3.17, where the SCCaFT signal

takes ∼50 s to 'catch up' with the instantaneous change in conductivity.

Similarly, upon pore closure, large pores left a visibly dissipating 'cloud' behind, the intensity of which dropped with increasing time. Slow response of the Fluo-8H signal after pore collapse was however more often than not observed in droplets that had seen a greater period under electroporative stress. In these cases, the EDTA present in order to chelate and remove the diffuse cloud by preventing any further binding of Fluo-8H was likely becoming saturated. Otherwise, the binding of Ca^{2+} to the dye was found to be rapid, reporting reliably the same fluctuations seen in the current response, as seen in Figures 3.7 and 3.8. The millisecond time resolution of these experiments was therefore largely dictated by the speed of the imaging CCD.

The usually rapid dye response can be put to further use. As the oSCR recordings are able to follow the millisecond conductance fluctuations (which were recorded on a faster timescale of 100 μs), oSCR has the potential to be used to report on the kinetic aspects of electropores. This shall be considered in the following chapter.

4

Electroporation in DIBs: Investigating the Energy Landscape

The work in this chapter constitutes a series of efforts to derive quantitative electroporation parameters from oSCR recordings, with an emphasis on understanding the mechanistic basis of electroporation. These measurements exemplify the unique ability of this imaging technique to observe the gating of individual electropores within the ensemble created by the transmembrane voltage.

4.1 Introduction

Experimental studies in the past have been used to glean a variety of information about electroporation and its contributing factors. Having demonstrated the applicability of droplet-interface bilayers to the real-time observation of electropores and their qualitative behaviour, attempts were made to extract more quantitative information about the process. In particular, the ability to observe the gating of individual electropores for the first time raised the question as to whether any information about the underlying pore-forming mechanisms could be gained. Understanding the energy landscape of electroporation, the forces governing it and the influence of the system's parameters are the key to better predicting electroporation outcomes in protocols for real-life applications.

4.2 Materials & Methods

The analyses presented in this chapter were carried out on data from bilayers prepared as described previously, with any variations set out below.

4.2.1 Gaussian Fitting of SCCaFTs

After background subtraction of the image stack (see Chapter 3), Gaussian fitting was performed in a custom-written procedure in Igor Pro. The code found the brightest pixel within an image stack, which was presumed to be part of the brightest SCCaFT. A 2D Gaussian was fitted at this locus, and then a patch containing the fit subtracted from the original image stack. This process was repeated until no SCCaFTs remained with intensities three standard deviations (3σ) above the standard deviation of the background, the latter being a measure of the background noise. This idea is based on an algorithm used to detect dim stars in astronomy, known as the CLEAN algorithm [238], and has been utilised to perform super-resolution imaging of single, fluorescently-labelled proteins in live cells [239].

4.2.2 Counting Electropore Lifetimes

oSCR recordings were made of bilayers at a range of potentials, with a time resolution of 16.21 ms. The open and closed times were obtained using a simple procedure that first located the brightest pixel in the image stack, and extracted a patch around it dictated by a user-defined radius. The procedure ran through the substack, counting the period that the brightest pixel in each frame of the substack was above or below a user-set threshold, chosen to be 3σ of the background fluctuations. The patch was removed from its host stack and the process repeated again.

4.2.3 Controlling Bilayer Temperature

The heated stage used to encourage diffusion of electropores (as described in Chapter 3) did not alone present an easy method for altering the bilayer temperature. The oil immersion lens in contact with the coverslip on the underside of the device acted as a particularly effective but unwanted heatsink, meaning that temperatures

far greater than that desired in the device needed to be applied, and that it took extended periods of time for the device to equilibrate. To combat this, the objective was heated via a custom-built resistance heater. This and the heated stage were set together in order to regulate the temperature of the device. The temperature was continuously monitored using a thermocouple placed in the well adjacent to that containing the imaged DIB.

4.2.4 Imaging Super-Hydrated Bilayers

For experiments where additional hydration was used to raise the bilayer (25–90 μm) relative to the substrate, a 60× 1.20 NA (numerical aperture) water-immersion objective was used, and the laser was incident on the bilayer at a glancing angle, rather than totally internally reflected. A lower NA objective was selected in order to increase the working distance. The coverslip was marked with pen before spin-coating the substrate agarose. This reference was used to measure the axial (z) position of the bilayer above the substrate using the electronic readout of the vertical position of the stage on the microscope.

4.3 Results & Discussion

4.3.1 The Distribution of Pore Sizes

Increasing the transmembrane voltage was found to increase both the size and the number of pores observed within the bilayer (Figure 3.6). However, small pores were found to exist at both low and high values of V_{applied}, rather than there being a constant increase in pore size. Investigation of such a parameter, crucial to the instantaneous stability of the membrane system and indicative of the magnitude of the local and global electric fields, may yield further insight into the mechanistic details.

As discussed in Chapter 3, the radius of a spot cannot be used as a precise measure of the pore radius. However, with a certain degree of approximation the intensity of a SCCaFT may be utilised as an approximate readout for the size of the

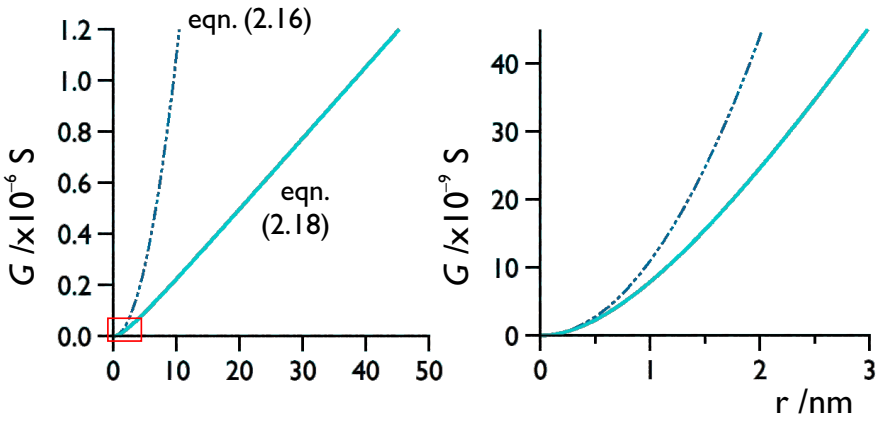


Figure 4.1: Variation of pore conductance with radius. Equation 2.18 is plotted (*solid line*) for a bilayer 4 nm thick, with electrolyte conductance g equal to 14 S·m^{-1}. The right-hand panel shows an expansion of the region indicated by the red box. Only at very small radii (*right panel*) does the conductance scale non-linearly with increasing radius. The dashed line plots equation 2.18, which does not take the pore access resistance into account (see Chapter 2).

underlying pore. From equation 2.18 the conductance of an electropore is predicted to be approximately linearly proportional to the pore radius [197].

$$G_{\text{pore}} = \frac{2\pi r^2 \cdot g}{\pi r + 2d_{\text{m}}}. \tag{2.18}$$

G_{pore} is plotted in Figure 4.1 for a bilayer 4 nm thick, with electrolyte conductance g equal to 14 S·m^{-1}, which demonstrates that the conductance is largely linear, only becoming non-linear at very small radii ($r < 2$ nm), when $\pi r < 2d_{\text{m}}$ and the access resistance no longer dominates*.

To a good approximation then, the pore current, proportional to the conductance, is therefore proportional to the pore radius. Since current by definition is the number of charge carriers in motion per unit time, then the quantity of Ca^{2+} passing through a pore per unit time will also be proportional to its radius. The relationship between the quantity of calcium ΔCa^{2+} and the resultant increase in fluorescent signal ΔF for the Fluo-8H analogue Fluo-3 has been estimated to follow $\Delta Ca^{2+} = k \cdot \Delta F$ for small (a few pA) calcium currents [240]. Presuming a similar relationship between Ca^{2+} and Fluo-8H, then we may make the approximation that the intensity of a SCCaFT is proportional to the pore radius. This is complicated by the fact that

*In this case equation 2.18 can be approximated to equation 2.18; see also Section 2.4.4.2.

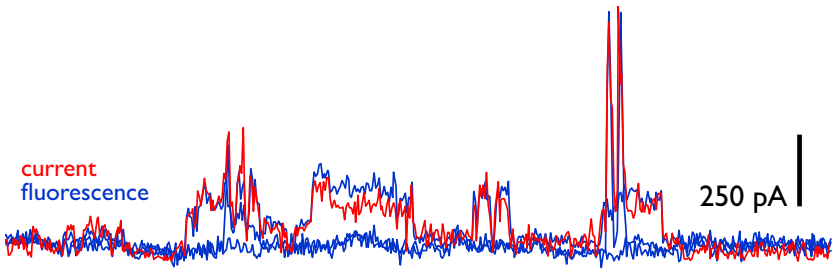


Figure 4.2: Current vs. intensity relationship for large pores.

the currents through electropores are most often greater than a few picoamps, and furthermore that the detected signal mass ΔF is collected from a volume of Fluo-8H solution above the pore, even with the optical sectioning that TIRF illumination affords. That is, at any one moment the signal is a combination of free dye molecules binding Ca^{2+} emanating from the pore, and those already bound to ions that came through the pore previously. This will increase the detected pore intensity above the expected value for a given radius. However, the comparison between oSCR and current signals for individual electropores, as reported in the previous chapter, would indicate that SCCaFT intensity is proportional to the pore radius to a reasonable approximation. This is true of currents even on the nanoampere scale. To show this, the data from the triplet of pores shown in the previous chapter, Figure 3.8, has been reproduced in Figure 4.2. Here, the raw fluorescence intensities from the three pores (*blue*) are displayed, aligned by their baseline intensities. Overlaying the corresponding bilayer current (*red*) demonstrates a reasonable agreement between the relative currents of the three pores and their relative SCCaFT intensities. SCCaFT intensity was therefore used as a proxy measurement to investigate the pore size distribution dependence on the applied potential.

To probe this, 2D Gaussian curves were fitted to all spots within oSCR image stacks recorded over incrementally increased applied potentials in the range of 160 to 250 mV. A further complication to the use of fluorescent intensity as a measure of pore radius is that the Ca^{2+} ions are driven electrophoretically through the pore; at higher voltages a greater flux (and hence SCCaFT signal) would be expected for a

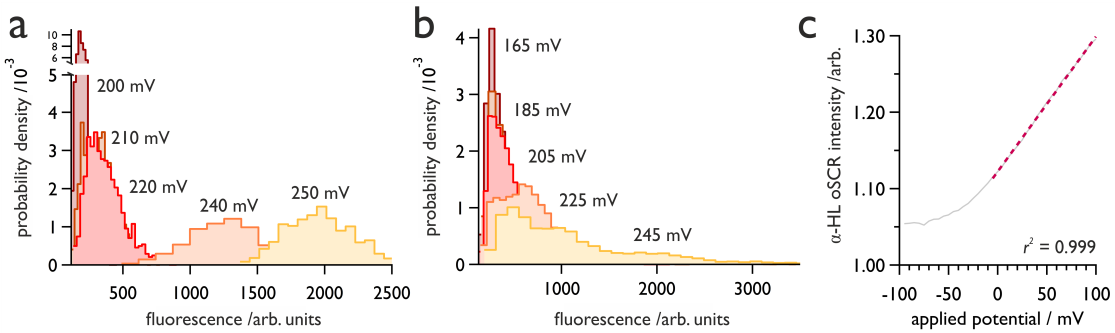


Figure 4.3: Pore size distributions. (a) Histograms of pore intensities for a single pore across a range of voltages in the same DIB. This pore was chosen as one that showed an increase in radius with voltage. (b) Data for the full ensemble of pores in a DIB. The number of detected spots was 2424, 3137, 5641, 8411 and 9428. (c) Dependence on SCCaFT intensity on the applied voltage for a pore of fixed radius. Linear regression to the data ($r^2 = 0.999$) at positive potentials, for which the protein exhibits a preference, showed an intensity increase of ∼1.6% every 10 mV. This was used to correct the Gaussian-derived intensities used in plotting (a) and (b). *α-hemolysin data was collected by Dr. Shuo Huang. Present address: Nanjing University, China.*

given pore size. This was corrected for by imaging Ca^{2+} ion flux through the pores of α-hemolysin, a heptameric, β-barrel pore-forming bacterial protein [237]. Its fixed conductance allowed the estimation of the increase in SCCaFT intensity associated with an increased V_{applied}. The intensity was found to have a linear relationship with the applied potential, as shown in Figure 4.3c. The amplitudes of the Gaussian fits to electropore SCCaFTs were corrected based on these measurements.

Histograms of the corrected amplitudes of these Gaussians are plotted in Figure 4.3 against the voltage at which the experiments were conducted. Figure 4.3a represents the change in pore size distribution for a single pore. It should be noted that this pore was deliberately selected as one that showed an increase in radius with V_{applied} — other pores do not necessarily show this behaviour. The bilayer was imaged for the same period of time at each potential, with the SCCaFT intensity recorded for all frames. It can be seen that the size distribution broadens and shifts to higher radii with an increase in the applied voltage.

Other pores did not show an increase in size as the potential was raised, with some increasing only to return to small pore sizes at higher voltages, or remaining small at all potentials. In addition, some pores did not re-open when the voltage was raised.

These variations again represent the pores' dependence on their local environment.

Therefore, the same analysis was applied to all pores formed in a DIB, Figure 4.3b. The main features are as follows: (1) the peak of the histograms shift to greater intensities with increasing voltage; (2) the distributions broaden as the voltage rises; (3) the whole distribution does not move towards higher intensities with increasing voltage, rather the tail becomes extended with a population of the smallest pores remaining present.

These points are of interest as they allow consideration of the shift in the electroporation energy curves as the voltage is varied. Firstly, and expectedly, we note that an increased field is able to support pores of a greater radius: as the energy input rises, pores become larger as the right-hand term in equation 2.4

$$E_{\text{hydrophilic, V}\neq 0} = 2\pi r\gamma - \pi r^2\sigma - \pi r^2 a_p V^2 \tag{2.4}$$

is better able to combat the contractile effects of the line tension. Secondly, the broadening of the distribution suggests that the width of the local energy minimum in which the pore radius fluctuates on the hydrophilic energy curve broadens at higher potentials. The population of smaller pores is retained as the potential is raised, and although the distribution becomes less dominated by them at elevated voltages, the smallest observable defects remain across the full range of V_{applied}. It is not the case that a larger field leads to exclusively larger pores, instead the field has the capacity to generate more sizeable defects should they be supported by the local environment. This is demonstrated in Figure 3.6, where larger pores exist alongside defects of radii that would be observed at far lower potentials. To a very crude approximation, if the smallest pores generate SCCaFTs of ∼200 counts (arbitrary intensity units) and are of the order of 1–2 nm, then the SCCaFTs of 2000–3000 counts in the same bilayer are of the order of 10–30 nm; that said, very large pores might generate a sufficient volume of Ca^{2+} so as to locally saturate the Fluo-8H dye and any further size increase would lead to no further increase in intensity, meaning that these larger pore sizes may be an underestimate.

It could be argued that since the histograms contain intensities for all spots within a fluorescence recording, the data indicating the presence of the smallest pores arises from detection of defects just after their generation, before they expand. This is true, however, we may simply note that inspection of oSCR traces reveals the presence of these smallest pores at all voltages. We may infer from this that the crossing point between the hydrophobic and hydrophilic energy surfaces is not susceptible to a change in radius with V_{applied}, *i.e.* the crossing radius r^* does not shift to higher values with the voltage, since the size of the smallest pores is maintained.

4.3.2 Gating Kinetics

The nature of this crossing point was further investigated by considering two lifetimes that are characteristic of an electropore: the period that pores remained open, and the duration taken for a pore to reappear. In this discussion these are termed the 'open' and 'closed' times respectively. These were obtained using a simple procedure that counted the number of frames within an image stack that a pore was open or closed for. 'Open' was defined as having an intensity above a threshold set at 3σ of the background fluctuations, chosen to ensure no erroneous pixels were considered to be pores. Since using oSCR the smallest pores can be detected (see the detection of discrete gating events, Chapter 3), the intensity dropping to the background was considered to be the result of full pore closure, rather than a decrease to a radius that did not permit sufficient Ca^{2+} flux to allow observation of a SCCaFT. An example of open/closed time gating detection is shown in Figure 4.4a, along with the results from the timescale analysis.

The probability density histograms for both times (Figure 4.4b) were best fitted with double exponentials. Single exponentials yielded very poor fits and were clearly inappropriate. The characteristic lifetimes for these fits are plotted against the applied voltage in Figure 4.4c. The striking feature is that both the open and the closed lifetimes of a pore are almost invariant with the electric field.

This analysis only considers those pores that open and close within the duration of the oSCR recording (just over 30 s). Electropores can, especially at high voltages,

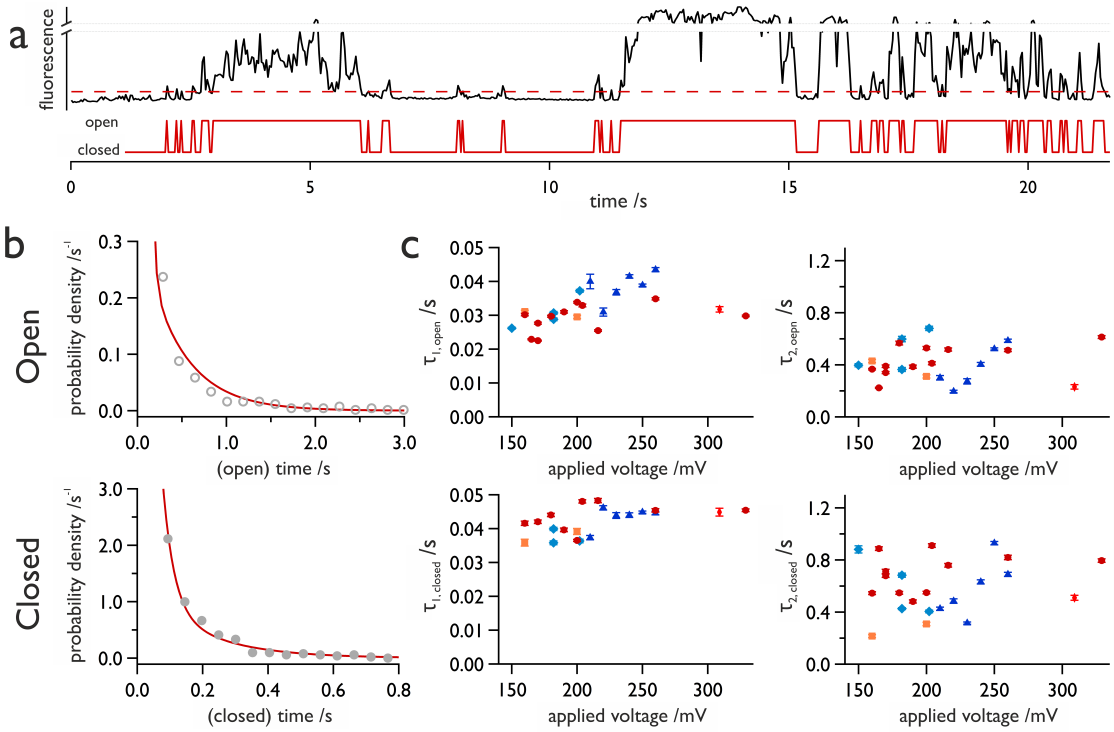


Figure 4.4: Electropore lifetimes. (a) Fluctuating intensity of an isolated electropore (black trace) with detected open and closed states (red). The red dashed line is the threshold that defines the open and closed states, equal to 3σ of the background fluctuations. (b) Representative histograms at both extremes of V_{applied} showing exponential fits to the open and closed time distributions that exhibit two decay constants. The applied potential was 260 mV for the open lifetime and 160 mV for the closed lifetime histogram. (c) The dependence of electropore lifetimes on V_{applied}. Different markers represent data from experiments carried out on different bilayers on different days, but under identical experimental conditions. The number of pores analysed was >1,900. Temporal resolution: 16.21 ms. Error bars are the errors ($\pm 1\sigma$) in τ from the bi-exponential fits to cumulative histograms of the open or closed times.

remain open for tens (or in some cases hundreds) of seconds, however the proportion of these instances relative to the rapidly fluctuating electropores is low; by eye, observing oSCR recordings, most of the pores in the membrane fluctuate on the order of a second or so. These data therefore report on those pores rapidly transitioning over the hydrophilic-hydrophobic barrier. Considering this, the open time then, represents the depth of the energy well in which an electropore might reside, with the closed time indicating the height of the barrier to hydrophilic pore formation. The independence of the former would imply therefore that there is very little deepening of the electropore energy well with increasing voltage. In the previous

section it was seen that a rise in potential broadens this local minimum, granting access to a greater range of pore radii, and so it must be that the potential has a greater influence at larger r; the tail of the energy curve moves downwards, until surmounting the barrier to critical pore formation at r_c is no longer impossible — the bilayer ruptures — but it is proposed that pores at these higher potentials are no more stable than those at lower voltages.

The variation of oSCR spot intensities suggested that the crossing radius does not vary with V_{applied}. The fact that the closed time similarly does not vary with increasing potential must mean then that the height of the energy barrier to hydrophilic pore formation is also fairly constant, *i.e.* the point (r^*, ϕ^*) is fixed. This makes physical sense in line with the proposed mechanism for the transition between a hydrophobic and a hydrophilic pore: the lipid rearrangement is predominantly driven not by the external field, but by the minimisation of the unfavourable interaction between water and the tail groups. Similarly, collapse of a conducting defect will always require the coming together of the water-lined toroidal pore walls, and the physical forces associated with this, along with those governing the transition of lipids back to a parallel, unperturbed bilayer arrangement, are unlikely to be greatly modulated by the potential. The idea that the crossing point exists at a fixed location in terms of energy and radius has been hypothesised in the literature [110, 241]. These results point towards this being the case.

The reason for the open and closed times exhibiting two components is not clear. Analysis of individual pores showed that single pores (both diffusing and stationary) also exhibited double exponential behaviour. Examples are shown in Figure 4.5. The distributions in Figure 4.4 are therefore the result of each defect being able to exist in either a short- or long-lived open or closed state, rather than there being two separate populations of pores. The individual analysis would also suggest that the differing lifetimes are not related to the spatial location of the pore; the fact that diffusing pores also demonstrate a pair of lifetimes largely precludes interaction with substrate as being the source of these bimodal kinetics.

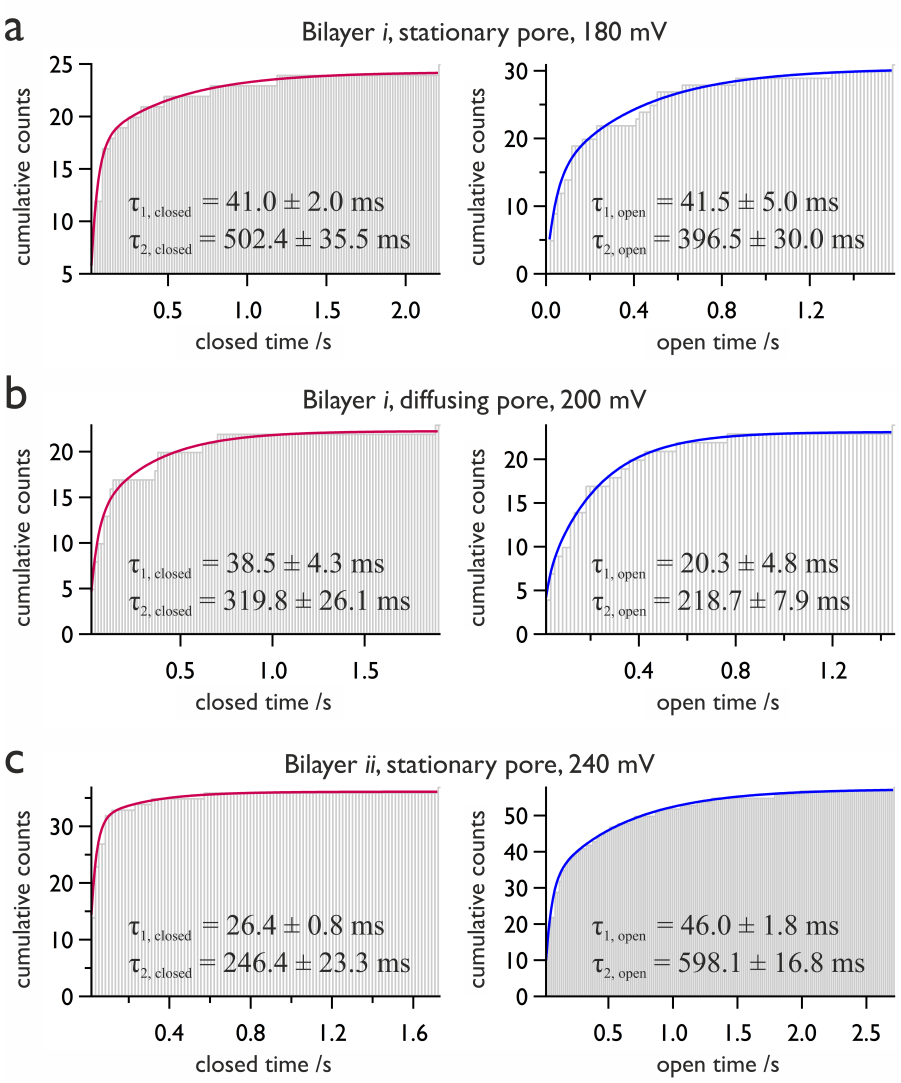


Figure 4.5: Lifetimes of individual pores. Cumulative histograms and bi-exponential fits to the data show that the individual defects exhibit two lifetimes. This analysis of isolated pores indicates that the double-exponential fits are appropriate for the ensemble histograms in Figure 4.4, and that the two lifetimes are not a result of two distinct populations of pore. All three pores exemplified here exhibited different mobilities, demonstrating that the double-lifetime behaviour is independent of the experiment and pore diffusion properties.

The longer timescales, $\tau_{2,\text{ open}} \simeq 400$ ms, and $\tau_{2,\text{ closed}} \simeq 600$ ms, most likely bear a link to the depth of the energy well and the barrier ϕ^* respectively. Their relative values ($\tau_{2,\text{ closed}} > \tau_{2,\text{ open}}$) points towards the barrier to conductive pore formation being larger than the barrier that must be overcome in order to collapse the pore. This is consistent with the current depiction of electroporation energy curves.

The shorter times ($\tau_{1,\text{ open}}$ and $\tau_{1,\text{ closed}}$, on the order of 30–40 ms) have a less obvious origin, and imply a smaller energy barrier to pore formation and closure. Non-ideal collapse of a hydrophilic pore may result in a membrane structure of higher free energy than an unperturbed bilayer; the energy barrier to pore re-formation would thus be reduced and a pore may quickly appear again, giving rise to the short closed lifetime, $\tau_{1,\text{ closed}}$. What this structure could be is not clear. It could be a packing defect generated during pore closure, or perhaps the entrapment of a pocket of water in the bilayer. Kamran Melikov and colleagues proposed the idea of a non-conductive, pre-pore state in 2001, after analysing conductance traces in DPhPC BLMs and showing that the after inducing poration, the current level upon reapplication of the potential depended on the interval after the first voltage step [242]. Interestingly, they also found bimodal gating that had lifetimes (on the order milliseconds) independent of the voltage, although they acknowledged that their electrical data could be the result of multiple pores. Recent simulations have suggested that DPhPC can form conductive hydrophobic pores, that is an ion-permeable defect that has a cylindrical geometry [243, 244]. These are predicted to be high-energy structures [106] and so their formation may be rapidly followed by collapse. Alternatively, and more likely, $\tau_{1,\text{ open}}$ and $\tau_{1,\text{ closed}}$ could be the result of the briefest pore openings as the local transmembrane potential only just overcomes ϕ^*, forming a pore that relaxes the field once again, closing it. As yet, however, the above can only be speculative in nature.

4.3.3 Temperature Dependence of Electroporation

The independence of the gating kinetics data on the applied voltage presented a means to calculate the barrier to electropore formation. Such a parameter is clearly

crucial to the description of electropore formation, and so its determination in DIBs was sought. (In this section, two barriers shall be discussed. The hydrophilic-hydrophobic intersection barrier ϕ^* can be approached from two directions: from large radii during pore sealing or from small radii in toroidal pore formation. The distinction shall be made between the two by denoting them $\phi_{o\to c}$ and $\phi_{c\to o}$, where o and c denote 'open' and 'closed' respectively.)

The rate at which hydrophilic pores are formed (that is, transition over the energy barrier $\phi_{c\to o}$; see Figure 4.7b) is described by:

$$k = \frac{vA}{a_0} \cdot \exp\left(- \frac{\phi_{c\to o}}{k_B T} \right) \tag{4.1}$$

where v is the frequency of lateral lipid fluctuations, A the area of the membrane and a_0 the area per lipid [110]. This rate will be proportional to the inverse of the closed lifetime, with an expression of the same form for open lifetimes. Taking logarithms:

$$\ln \tau_c = \frac{\phi_{c\to o}}{k_B T} - \ln \frac{vA}{a_0 C} \tag{4.2}$$

where C is the constant of proportionality linking k to τ. $\phi_{c\to o}$ has been experimentally estimated to be $\sim$45 $k_B T$ in asolectin black lipid membranes [110]. Equations 4.1 and 4.2 apply to a bilayer experiencing zero transmembrane potential. When a voltage is applied:

$$\ln \tau_c = \frac{\phi_{c\to o}(V=0)}{k_B T} - \ln \frac{vA}{a_0 C} - \frac{\pi r^{*2} (\epsilon_w - \epsilon_m) \epsilon_0 V^2}{2 d_m k_B T} \tag{4.3}$$

where as before d_m is the membrane thickness, r^* the radius at which a hydrophobic pore converts to a hydrophilic pore, ϵ_w and ϵ_m the relative permittivities of water and the membrane respectively, and ϵ_0 the permittivity of free space. However, with a bilayer thickness of 4.8 nm [187] and r^* given a value of 0.5 nm [110, 143, 149], the term $\frac{\pi}{2d_m} r^{*2} (\epsilon_w - \epsilon_m) \epsilon_0 V^2$ only becomes comparable to tens of $k_B T$ (the predicted value of $\phi_{c\to o}$) when $V > 500$ mV. This is far above the mean rupture potential for DPhPC DIBs. Furthermore, the fact that electropore lifetimes do not vary significantly with the applied potential implies that the energy barrier is relatively constant in this voltage range (further supported by the results of

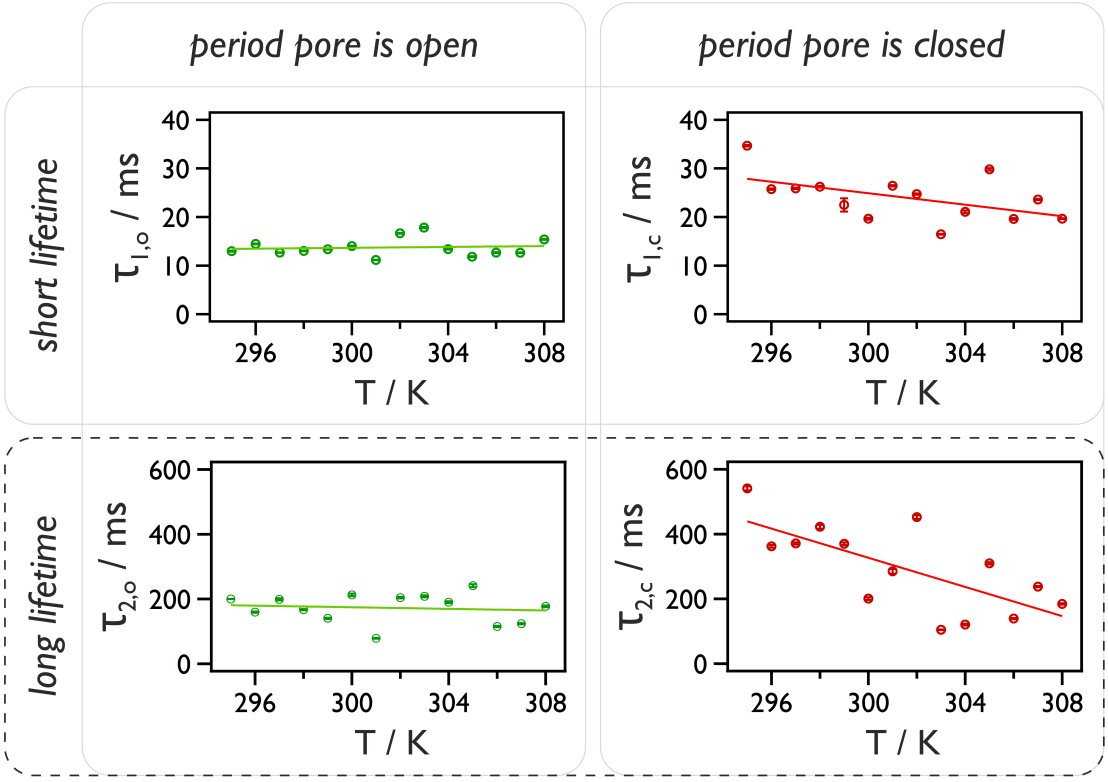


Figure 4.6: Temperature dependence of the open and closed pore times. Double exponentials fitted to histograms of these periods again yielded a pair of τ values characteristic of those functions, for both the open ($\tau_{1/2,o}$) and closed periods ($\tau_{1/2,c}$) at each temperature. The open lifetimes appeared to vary only slightly with increasing temperature, whereas there was a clear temperature dependence of the closed lifetimes. The error bars, which are the standard deviation of the tau values derived from the histogram fits, are largely obscured by the data points; straight lines are linear regression fits to the data points. The data presented within the black dotted area is the same as that in Figure 4.7.

numerical modelling of electroporation [110, 241], and under these conditions equation 4.3 reduces back to equation 4.2.

The barrier ϕ could therefore be estimated by examining electropore gating as a function of temperature. Increasing the temperature would be predicted to make electropore formation more likely due to the increased mobility of lipids increasing the likelihood of hydrophobic pore formation and the size of the fluctuations in radius space of the pores [179, 191, 229–231]. Electroporation and bilayer rupture were more likely as the temperature was elevated in DIBs; experiments were therefore carried out at 100 mV, a balance between a potential sufficient to observe electropores near room temperature, but one low enough to prevent rupture at elevated temperatures.

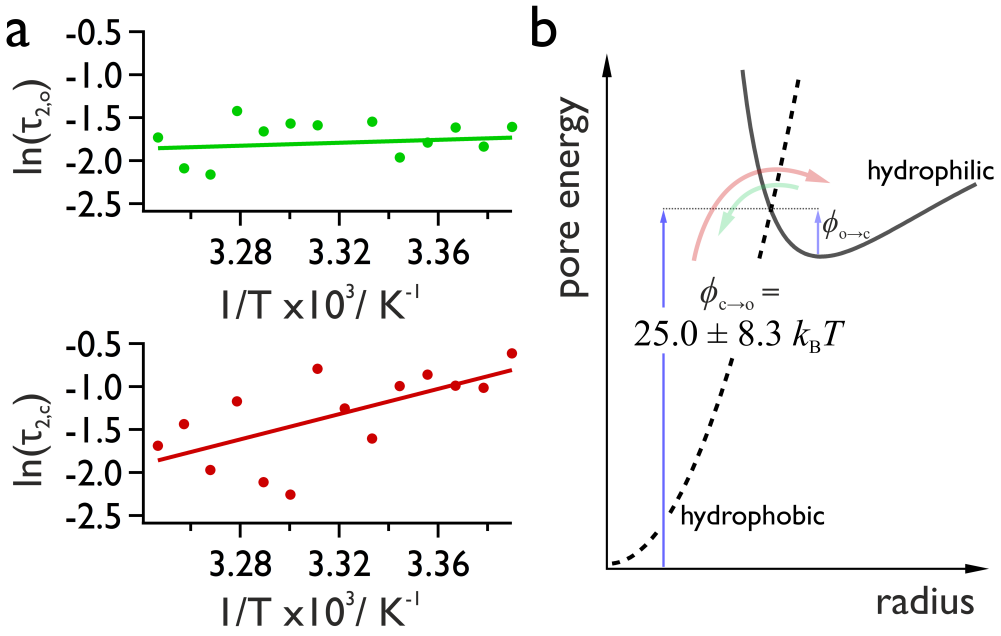


Figure 4.7: Estimating the barrier to electroporation. (a) Arrhenius-type plots for electropore open (*upper*) and closed (*lower*) lifetimes. The data shown here are for the τ_2 lifetimes; $\tau_{1,\,\mathrm{open}}$ and $\tau_{1,\,\mathrm{closed}}$ showed the same trend as their longer counterparts (see Figure 4.6). Each data point is derived from at least 5 pores (maximum 337, mean 54). Error bars, derived from the standard deviation of the fits that revealed the lifetimes, are obscured by the data points. (b) Detail of the hydrophobic-hydrophilic energy curves. The colour of the arrows correspond to the data in (a): $\tau_{2,\,\mathrm{closed}}$ is the period a pore spends attempting to overcome $\phi_{\mathrm{c}\to\mathrm{o}}$ (*red*); $\tau_{2,\,\mathrm{open}}$ is the average time a pore resides in the hydrophilic regime before returning to a closed state via $\phi_{\mathrm{o}\to\mathrm{c}}$ (*green*).

The results from the analysis of 754 pores (34 bilayers) are presented in Figure 4.6. Measurements were made between 22 and 35 °C. Whereas both τ_{closed} lifetimes were found to decrease with increasing temperature, both τ_{open} values had no strong temperature dependence. Arrhenius-type plots were generated from this data for the τ_2 lifetimes, Figure 4.7. A linear fit to the $\tau_{2,\mathrm{closed}}$ data found the estimated barrier to pore opening in DPhPC to be $\phi_{\mathrm{c}\to\mathrm{o}} = 25.0 \pm 8.3\ k_{\mathrm{B}}T$, which is in agreement with the estimate made by Glaser *et al.* [110] and in more recent numerical models [241], and in very good agreement with the barriers calculated from MD simulations of phosphatidylcholine bilayers by Majhi *et al.* [245], who based their calculations on pore initiation times and similar Arrhenius kinetics. Although within error, the estimate of the barrier to pore collapse from a hydrophilic pore from these experiments was, as expected, smaller than that of $\phi_{\mathrm{c}\to\mathrm{o}}$, with $\phi_{\mathrm{o}\to\mathrm{c}} = 2.9 \pm 6.4\ k_{\mathrm{B}}T$.

The observed temperature dependence of electroporation lifetimes are consistent with a toroidal pore model where the formation of hydrophilic pores takes place via a hydrophobic intermediate. This intermediate is simply a parting of lipids within the membrane with no molecular reorientation, a transient state generated by the thermal energy. In raising the bilayer temperature, the probability of surmounting this barrier to hydrophobic pore formation is increased. This is what we observe: $\tau_{2,\mathrm{closed}}$ decreases with increasing temperature. The open lifetime, however, appears to vary less strongly with temperature. This implies that the increased lipid fluctuations as a result of increased $k_{\mathrm{B}}T$ do not greatly aid in surmounting $\phi_{\mathrm{o}\rightarrow\mathrm{c}}$. More likely, the lipid rearrangement that is required to close the pore — overcoming forces such as double layer repulsion between the headgroups and the removal of the interfacial water as the toroidal walls come together [109, 236] — dominates the energetics of this return process.

4.4 Influence of the Agarose Substrate

Significantly perturbing hydrogel-bilayer interactions would be a severe disadvantage of DIBs in the study of electroporation and other bilayer properties. The ability to assess the kinetic features of electropores encouraged further exploration as to whether they were affected by the agarose substrate. To do this, DIBs were generated on an agarose substrate that was 'super-hydrated': following addition of the lipid-in-oil solution to form a monolayer at the agarose-oil interface, large ($\sim$200 nL) droplets of buffer solution were fused with the interface, in the same manner as the experiments designed to encourage electropore diffusion described in Chapter 3. In the present case, the droplets were much larger, increasing the volume of buffer present on the agarose-facing side of the DIB, and raising the bilayer away from the substrate by between 25 and 90 μm.

Data obtained from electropores formed on these 'super-hydrated' DIBs produced a few observations of interest. As with the fusion of smaller droplets, the additional hydration brought about the diffusion of electropores. $\bar{D}_{\mathrm{lat}}$ was found to be 1.94 $\pm$ 0.87 $\mu\mathrm{m}^2\cdot\mathrm{s}^{-1}$ ($n = 8$), which is of the order of the largest lateral diffusion coefficients

seen for standard substrate. The measurements displayed a tighter distribution of values, although the sample size was much smaller (n was 46 for standard bilayers). This slightly increased diffusivity, and lack of very slowly diffusing pores compared with the standard preparation suggests an improved membrane fluidity, which might be expected for larger aqueous separations between the bilayer and the agarose [246]. In addition, over-hydrated bilayers were found to rupture at lower potentials compared with standard bilayers exposed to the 180 s 'high', 30 s rest protocol, with $\bar{V}_c = 97 \pm 38$ mV ($n = 5$). This would suggest that the presence of an agarose substrate serves to stabilise the bilayer against rupture when the two are in close proximity. For a membrane separated from a substrate by a thin layer of fluid of thickness h, the surface frictional coefficient b is given by:

$$b = \frac{\eta_w}{h} \tag{4.4}$$

where η_w is the viscosity of the fluid [246]. At small separations, we might expect the frictional coupling between the substrate and the bilayer to reduce the membrane fluidity, and that this restricts larger-scale fluctuations in the pore radius that might lead to pore expansion and bilayer rupture.

Although the I–V characteristic and rupture potential informs about the stability of the entire bilayer, there was particular interest in determining whether the dynamic behaviour of the pores had changed upon an additional hydration cushion. It might be expected that if the agarose were influencing individual pore properties, there would be a difference in gating kinetics when the bilayer is raised away from it. However, the characteristic lifetimes for pores in super-hydrated bilayers were essentially identical to those for standard DIBs. The pore gating lifetimes, derived from 8 pores, were $\tau_{1,\text{open}} = 61.2 \pm 0.5$, $\tau_{1,\text{closed}} = 42.9 \pm 1.7$, $\tau_{2,\text{open}} = 748.5 \pm 11.1$, $\tau_{2,\text{closed}} = 328.1 \pm 22.6$ ms. Further, the fact that these distributions were again best fit with double exponentials suggested that the short time components observed in standard DIBs (Section 4.3.2) do not result from any bilayer interaction with the substrate.

4.5 Summary & Limitations

The quantitative and qualitative observations made in this chapter have enabled a further look at the electropore energy landscape and support the current theoretical model. The ability to probe the underlying energetics of pore formation continues to build on our current understanding of the process.

The broadening of the distribution of SCCaFT intensities derived from electropores in response to increasing the transmembrane voltage supports the notion of a broadening potential energy well. In an ensemble of defects, the distribution maintains its smallest pores, regardless of the potential. The radius of transition over the hydrophobic-hydrophilic barrier must therefore remain relatively constant. Whilst this point on the energy curve appears to be fixed, the tail of the size distribution extends to larger and larger radii; only one of these pores need fluctuate past the critical radius to rupture the membrane [109].

Although broadly informative, using the SCCaFT intensity as a readout of pore size is an approximate measure. The signal mass of a Fluo-8H SCCaFT depends on several factors that make turning intensity data from oSCR recordings into measurements of channel size or conductance problematic. These include a dependence on the period that a pore is open, since a pore open for a longer period will generate a greater fluorescence 'cloud'; the amount of out-of-focus light (coming from the Ca^2-Fluo-8H cloud) augmenting the detected signal; and the spread of Ca^{2+} radially from the pore [247]. Determining the relationship between of each of these and the true pore size is a worthwhile but challenging pursuit.

Timescale analysis was conducted on the basis that whilst the intensity or radius of a SCCaFT were not direct measures of the underlying pore properties, the time response of oSCR had been shown to match that of the electropore current fluctuations. The resolution in these experiments was limited therefore by the frame rate of recording, which was nearing 62 Hz (16.2 ms per frame) in the data in Figure 4.4. In order to improve kinetic resolution, the experiments conducted at a range of temperatures were recorded at 8.3 ms per frame. This was achieved by in-camera 'binning' of the signal from four pixels into a single value, which reduces optical

(spatial) but improves temporal resolution. In counting the electropore lifetimes, loss of some optical resolution did not affect the detection of their gating, and resulted in timescales of similar magnitude. Comparisons are difficult, however, owing to the small errors attributed to these timescale measurements, which could only be derived from the errors in the parameters of the exponential fit to the lifetime histograms. This makes it difficult to assess as to how variable these timescales are, which results in the large errors in the estimation of the pore opening and pore sealing barriers. It is worth noting that spread of the values of $\tau_{2,\text{closed}}$ (Figure 4.6) relative to the other lifetimes, especially $\tau_{1,\text{closed}}$ and $\tau_{2,\text{open}}$, which show a narrower range over the varying temperature. Inspection of $\tau_{2,\text{closed}}$ in experiments conducted at room temperature under varying applied voltage shows the same behaviour. The origin of the larger spread of $\tau_{2,\text{c}}$ values has yet to be determined. One way to improve these measurements would be to repeat the experiments but on multiple bilayers, averaging together the pore lifetimes from each of these membranes.

Despite these variations, the results presented are in general supportive of the current electroporation model, although such a model does not immediately suggest a pair of lifetimes for the opening and closing processes. Diagrams in the literature are inconsistent in showing whether the hydrophobic-hydrophilic crossover point varies with the applied voltage. The investigations in this chapter would point to this barrier being fixed, and therefore, unlike the surface tension, the line tension does not have a significant voltage dependence.

In the super-hydration setup, the bilayer was beyond the evanescent TIRF field, and although with a glancing incident angle oSCR recordings could be achieved, this is not a viable configuration for sensitive bilayer imaging with high-magnification, low-numerical aperture lenses. They could conceivably be used however in epifluorescence configurations under lower magnifications should investigators be concerned about agarose-bilayer interplay. Nevertheless, 'super-hydrated' bilayers in this case enabled the validation of the data collected in other oSCR experiments as not a result of agarose effects.

That said, membrane-substrate effects such as these may not be entirely misrepresentative of biological systems. The cytosol is far from a dilute, watery volume — it is packed densely with proteins, macromolecules, organelles and support structures [248]. Indeed, the way in which the interaction between the actin cortex and the membrane alters electroporation has been considered, for example [208]. In order to mimic the effect of the cortex and its anchoring proteins on electroporation, the local surface tension was constrained (in a mathematical model) in triangular areas with dimensions equivalent to those found on the cytosolic face of erythrocyte membranes. This work indicated that such anchoring could stabilise pores on the order of 20–50 nm formed within these regions. A hydrated meshwork beneath the DIB may in fact serve as a more appropriate mimic of the cytosolic leaflet than a cushion of water, albeit still a highly simplified one.

5

The Interaction of Antimicrobial Peptides with DIBs

This chapter presents preliminary data into investigations concerning the mode of action of four antimicrobial peptides (AMPs). oSCR detection of electropores was extended to incorporate single-molecule imaging of labelled AMPs diffusing in the bilayer. This methodology allows the real-time imaging of individual peptides and thus the determination of their location; this is the first known combination these two fluorescence techniques to study AMP modes of action in lipid bilayers. Results of analysing the radial distribution function of the peptides in the pore region are presented, supporting the currently accepted modes of action of the four peptides, and further suggesting that pores formed by these AMPs are dynamic.

5.1 Introduction

5.1.1 Antimicrobial Peptides

The ability of optical single-channel recording to provide spatial information about channels and pores within the membrane makes it a valuable tool for the study of pore-forming processes. It was therefore utilised in the preliminary study of the mechanism of pore formation by antimicrobial peptides.

Antimicrobial peptides (AMPs) are a broad class of short, gene-encoded amphipathic peptides largely possessed by organisms for the purpose of defence against invading organisms [1, 2, 5, 6, 249–251]. They are produced by every class of life, and show selective activity against bacteria, viruses and fungi. From jellyfish to birds, plants and fungi to arachnids, frogs to humans: all organisms must deal with the constant threat of invasion from microbes, and have in place mechanisms to defend themselves against predators or parasites. Most significantly, the release of antimicrobial peptides forms part of an organism's innate immune response as an initial defence against invading pathogens [1, 252]. However, AMPs have also been found in the venoms of wasps and scorpions, and in the defensive skin secretions of frogs [7, 9, 249, 253].

AMPs often exhibit broad-spectrum activity through a variety of modalities. Some attack the outer membrane of the target cells directly, forming transmembrane pores that result in loss of cytosolic material [2] or mediating other membrane effects, such as depolarisation or lipid clustering [6]. Others translocate this barrier (which may or may not be by pore formation) in order to enter the cell. Once internalised, they interfere with intracellular biochemistries, causing flocculation of intracellular contents, binding to nucleic acids, inhibiting cell wall or protein syntheses, or interrupting enzyme activity or mitochondrial function [2, 5].

The targeting of a physical structure rather than (or alongside) a biochemical pathway also makes it more difficult for a pathogen to rapidly develop resistance to attack: altering the architecture of the membrane could be a significant undertaking, given the great number of interdependent components that it contains and the biological pathways that rely on it [250, 254]. In light of increasing resistance to drug-based antibiotics, this is an attractive property of AMPs. Whilst their haemolytic ability precludes some of them from immediate therapeutic use [8, 255], the ability of AMPs to selectively target pathogenic membranes, along with their range of antimicrobial modes of action make them a starting point for the design of novel alternatives to drug-based antibiotics and other therapeutics [5, 250, 253, 256]. That said, some organisms have built mechanisms to mitigate the deleterious

effects of AMPs [2, 3, 257], and the full modes of action of these peptides are often unclear, warranting further study.

5.1.2 AMP-Bilayer Interactions

The common feature of the modes of action of AMPs is the interaction with a lipid bilayer. Whether the peptide disrupts the outer membrane or traverses it, an AMP must be able to selectively interact with the membranes of the pathogen over those of its host. Furthermore, since AMPs form part of the non-adaptive immune response, they must be able to selectively target the foreign species automatically. Arguably the simplest way to do this is to in some way recognise a property of the invader that the host cells do not possess, and the most available structure that an AMP has access to is the cell membrane. For example, human defensins and cathelicidins target bacterial membranes [258], which are rich in anionic phosphatidylglycerol and cardiolipin lipids as opposed to the zwitterionic-dominated outer leaflets of eukaryotes [3, 51], whereas in order for pore-forming bacterial toxins such as perfringolysin to bind they require the presence of membrane cholesterol [259, 260], a component absent in prokaryotic bilayers but abundant in those of their eukaryotic targets [254].

This selectivity for lipid bilayer interaction is mediated heavily by AMP structure. Two highly dominant features in this regard are amphipathicity and charge. AMPs variously adopt α-helical, β-sheet or extended forms, with many only adopting their secondary structure upon associating with the target membrane, but in all cases AMPs exhibit amphipathic features akin to the phospholipid molecules with which they interact [5]. The percentage of hydrophobic residues within an AMP is commonly around 50% [3, 249], a level of hydrophobicity that allows for partitioning into the lipid bilayer from an aqueous environment. Alongside, many of the pathogens that organisms must defend themselves against are bacteria, and for this reason, the majority of AMPs have evolved to target one specific property of bacterial membranes that easily isolates them from others: their charge. Bacterial membranes tend to possess a large proportion of negatively charged lipids [51], in contrast to

eukaryotic phosphatidylcholine-rich membranes [250], and this has resulted in the majority of AMPs developing as multi-charge cationic species with multiple charges often localised within the same region of the peptide [2, 3]. This feature confers a preferential electrostatic affinity for the negatively charged membranes of bacteria.

For α-helical AMPs, these features of amphipathicity and charge are combined through their secondary structure, allowing the molecule to associate parallel to the membrane surface during initial peptide-lipid interactions: the neutral polar and charged residues form one side of the helix and face the lipid headgroups, whilst the other side comprising the hydrophobic side-groups is embedded into the hydrophobic bilayer centre [6, 249].

5.1.3 Pore-Forming AMPs

Pore-forming AMPs generally fall into one of three categories based on the type of permeabilisation that they are thought to enact. These are shown in Figure 5.1, and bear a resemblance to the pores already discussed in this work. The barrel-stave model involves the formation of a pore by peptides without any lipid rearrangement. In the toroidal model, peptides induce the lipid to bend into the pore lumen, resulting in a pore lined with headgroups and the inserted peptides. In these two regimes, configurationally similar to those of hydrophobic and hydrophilic electropores, pore formation can result in irreparable material leakage from the target cell. The carpet model is the third mechanism, whereby the AMPs disrupt the membrane by extensively covering its surface, in some cases acting to solubilise portions of the membrane in a detergent-like manner.

It should be emphasised at this point that the above models are just that: proposed mechanisms for the translocation and disruption modalities of these small molecules. For some AMPs, their membrane-active mechanisms are known. For many others, however, their means of action remains to be determined. Much of the information about the mechanisms of AMP-mediated pore formation has been acquired from X-ray, nuclear magnetic resonance (NMR), circular dichroism (CD) and molecular dynamics studies, however imaging studies, although some exist

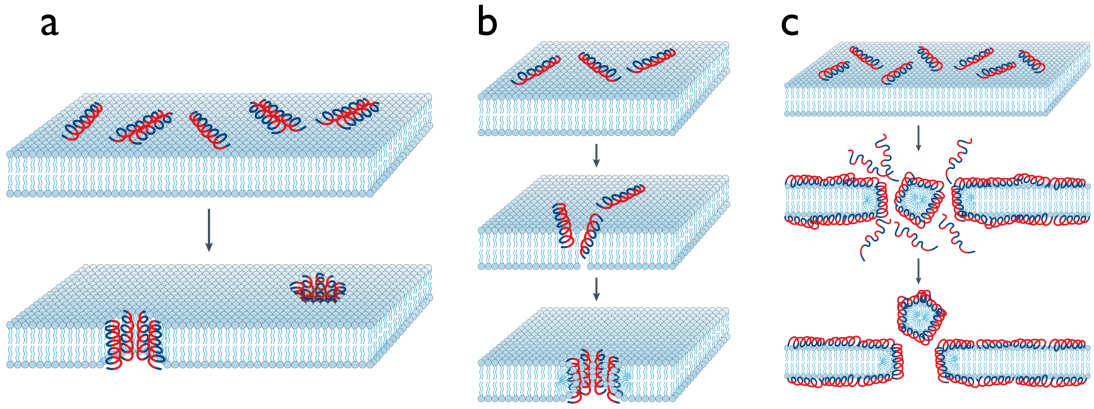


Figure 5.1: Models of antimicrobial peptide pore formation. (a) The barrel-stave model, in which insertion of the peptides generates a protein-lined pore with no lipid reorientation. (b) The toroidal mechanism, involving the stabilisation of a toroidal pore by the AMP monomers. (c) The carpet model, in which extensive association with the bilayer causes disruption. Hydrophilic portions of the AMPs are shown in red, and the hydrophobic residues are coloured blue. Adapted from [2].

[261, 262], are yet to be commonplace. Furthermore, many studies rely on bulk techniques that are unable to monitor the dynamic properties of the individual peptides. The ability to image the locations of AMPs and the pores that they form is therefore a complementary tool that can be used alongside already existing methods to improve our understanding of AMP action. The work presented here are preliminary steps in developing such a tool.

5.1.4 oSCR of AMP-Mediated Pores

Optical single-channel recording in DIBs lends itself to the study of AMP pores: a calcium-flux signal through the pores can be monitored, and the pores may therefore be localised within the membrane. Combining this with a visualisation of the peptide locations would render such an experiment highly useful for AMP investigations. DIBs allow such a setup to be constructed: peptides with an appropriate fluorescent marker can be added to the aqueous droplet used to form a bilayer, which after bilayer formation can be imaged sensitively using TIRF.

In order to investigate the applicability of oSCR and single-molecule imaging to AMP studies, four commonly-studied peptides were chosen: alamethicin, magainin-II, melittin and indolicidin. The structure of these peptides, along with a schematic

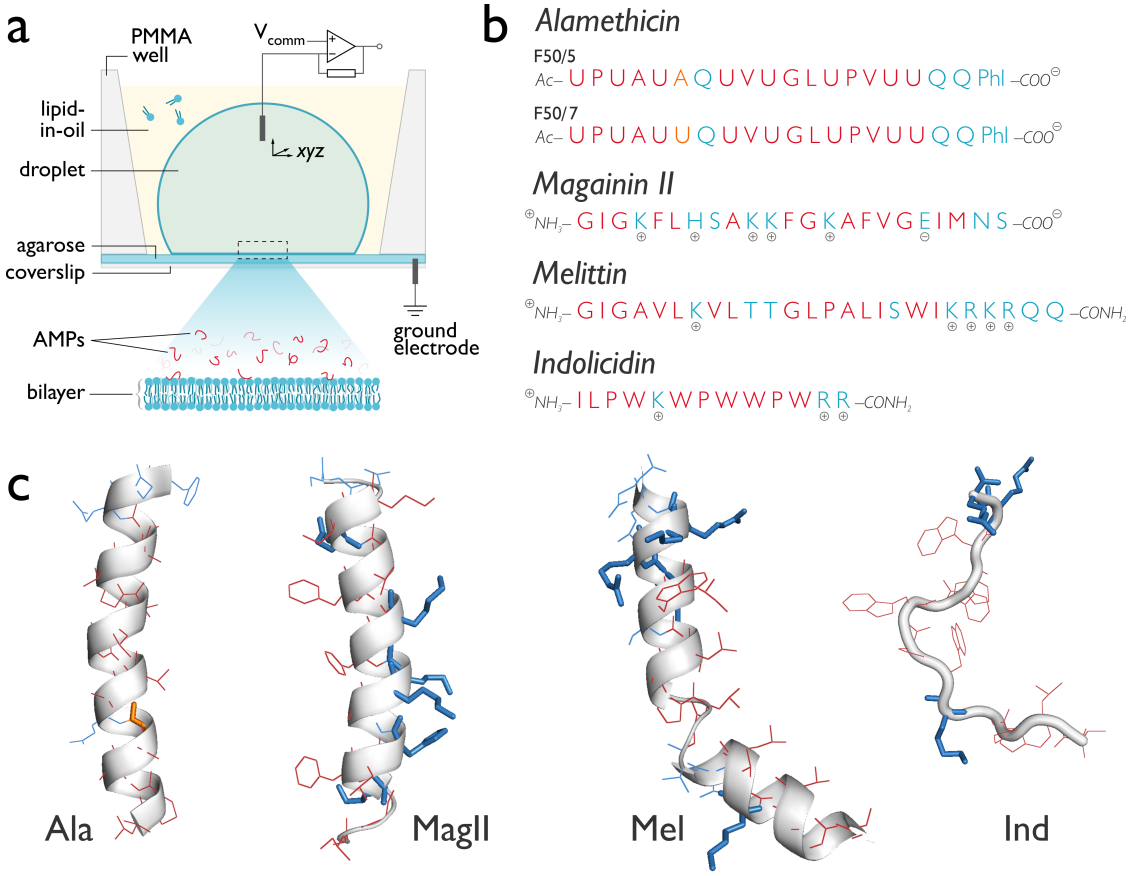


Figure 5.2: AMP structures and DIB setup. (a) Cartoon of the setup. AMPs present in the droplet can insert into the bilayer from above. (b) Peptide sequences of the AMPs used in this work. Colour coding: *blue*, hydrophilic side chains; *red*, hydrophobic residues; *orange*, the differing residues in the alamethicin homologues. U = Aib, α-aminoisobutyric acid (α-methylalanine); *Phl* = phenylalaninol. (c) AMP secondary structures (PDB structures, from left to right: 1AMT, 2MAG, 2MLT and 1G89). The C-terminus is shown uppermost. Colour coding is the same as in (b); residues with thicker side chains are those that bear a charge.

of the experimental setup, are shown in Figure 5.2.

5.1.4.1 Alamethicin

Alamethicin is a 20-residue peptide extracted from the fungus *Trichoderma viride* [263], and perhaps the best-studied of all antimicrobial peptides [255]. It forms an α-helical structure (with a slight kink at Pro^{14}), which is encouraged by the presence of α-aminoisobutyric acid (Aib) residues [264, 265], a non-proteinogenic amino acid that favours 3_{10}- and α-helices [266, 267]; circular dichroism, Raman and infra-red spectroscopies have indicated that the peptide is predominantly α-

helical in methanol and fluid membrane environments [255]. There exists a range of natural alamethicins, the two largest groups denoted (based on their mobility in thin-layer chromatography) F30 (∼85 % abundance) and F50 (∼12 %), which differ by either possessing a Gln or Glu residue at position 18 [265]. Alamethicin demonstrates broad-spectrum antibacterial activity at micromolar concentrations, as well as cytolytic activity against mammalian cells [255].

The most widely accepted mechanism of this toxicity is the barrel-stave model, in which several alamethicin molecules insert perpendicular to the membrane surface to line a water-filled pore [264]. In model membranes, orientated-CD, in-plane neutron scattering and X-ray diffraction of hydrated parallel bilayers show that at low concentrations alamethicin associates parallel to the membrane surface, leading to thinning of the membrane with increasing amount of peptide [187, 268]. At higher peptide-to-lipid ratios (P/L), above 1:40, monomers reorientate perpendicular to the bilayer plane [269–271]; the pores formed by this insertion were determined to have 3–12 monomers [264, 272, 273]. Electrical studies revealed that alamethicin disrupts planar bilayers of various lipids, with increased membrane conductivity manifesting as multiple, discrete conductance states [274–276]. This suggested the generation of conductive, transmembrane pores with the discrete steps resulting from a dynamic variation in the number of alamethicin units forming the pore, although electrical recordings could not provide direct evidence that this behaviour was the result of a single alamethicin pore. However, monitoring of the calcium flux through individual pores using oSCR demonstrated that multiple conductance states could be associated with a single point in the membrane [227], strongly supporting the idea that the discrete conductance steps are due to fluctuating numbers of monomers in the same pore.

5.1.4.2 Magainin-II

Magainin-II, present in the skin excretions of frogs of the *Xenopus* genus, is a cationic (+4–5 at physiological pH), 23-residue peptide that demonstrates antibacterial activity against a range of Gram-negative and Gram-positive species at micromolar

concentrations [9, 277]. CD measurements and solid-state NMR of aligned bilayers indicates that whilst magainin-II is unstructured in solution [277, 278], it adopts an α-helical structure when associated with 3:1 POPE/POPG bilayers, orientating parallel to the bilayer surface [277, 279–281], whilst X-ray diffraction and NMR studies of similar aligned systems reveal that magainin-II encourages thinning of the membrane [268, 282, 283]. Like alamethicin, orientated-CD [282] and IR and vibrational spectroscopies [284] indicate that an increase in P/L ratio results in a greater proportion of magainin-II adopting a transmembrane orientation.

The peptide has been shown to dissipate the transmembrane potential in cytochrome oxidase vesicles [285], induce leakage of calcein from anionic liposomes [279], and in PE/PS bilayers formed at the end of a glass pipette, micromolar concentrations of magainin-II were found to cause channel-like disruption, with a large variability in the amplitude of the current fluctuations [155]. These findings and other studies [286] indicate a preference for negatively charged lipids, and suggest a pore-forming mode of action. This was further supported by evidence that magainin-II accelerated the half-life of lipid flip-flop from hours or days to just minutes in asymmetric vesicles [287], and along with neutron in-plane scattering data that indicated only 4–7 magainin-II monomers were present in pores larger than those formed by alamethicin [282], this lead to the suggestion that the defects were toroidal in geometry, thus presenting a route for rapid inter-leaflet lipid motion via the curved pore walls [287].

5.1.4.3 Melittin

Melittin, a major component of honey bee (*Apis mellifera*) venom, is another well-studied AMP [288]. It is unstructured in dilute aqueous solution [289, 290], but when crystallised, the 26-residue peptide forms a bent α-helical rod, the bend occurring due to a non-helical portion at Thr^{11} and Gly^{12} [291, 292]. This structure was also found for melittin bound to dodecylphosphocholine micelles by 2D NMR [293]; Raman and CD studies have similarly found that melittin is α-helical when interacting with phosphocholine membranes at micromolar concentrations [294, 295].

Similar to magainin-II, this helical conformation results in the molecule presenting its hydrophilic residues (mostly) along one face, with the hydrophobic side chains along the other (Figure 5.2c). Using ^{13}C-NMR [296] and IR [297] spectroscopies, membrane-associated melittin was found to lie parallel to the bilayer surface. The segregation of hydrophilic and hydrophobic residues to opposing faces of the peptide permits the polar face to associate with the lipid headgroups, and the hydrophobic side to sit amongst the lipid tails; studies using electron paramagnetic resonance (EPR) to look at the quenching of different nitroxide-labelled side-groups around the helix of melittin in PC vesicles [298], and ^{1}H-NMR of PC/PS membranes showing suppression of amide hydrogen-deuterium exchange on the hydrophobic face of the peptide [299] support this orientation. A reorientation appears to take place when the P/L is raised: at 300 μM melittin was found to be 85 % parallel in POPC bilayers, but became 68 % perpendicular (*i.e.* inserted into the membrane) at 870 μM [300]; similar results of perpendicular melittin have been observed at 80 μM peptide in 7:3 DMPC/DMPS vesicles [301].

In planar bilayers made from asolectin, PC/PE or oxidised cholesterol, melittin induces current fluctuations in response to an applied potential, with increasing conductances at higher peptide concentrations but with little evidence of a well-defined pore, again similar to magainin-II [302–304]. In PC or PC/PG vesicles, melittin was shown to induce calcein leakage and through bulk fluorescence measurements that melittin translocated the bilayer [305]. Neutron scattering indicated pores of comparable size to magainin-II in aligned bilayers; these and other evidences suggest toroidal-like pores as opposed to the barrel-stave defects formed by alamethicin [300, 306].

When interacting with biological membranes, melittin inhibits Gram-positive and Gram-negative bacteria and fungal growth, displaying micromolar minimum inhibitory concentrations (MICs) [7, 277]. In addition, melittin also shows strong haemolytic ability [7, 286, 307]. It is interesting to note that despite melittin having a similar α-helical structure and charge (+6 at physiological pH) to magainin-II, melittin shows a lytic activity towards zwitterionic PC bilayers two orders of

magnitude stronger than magainin-II [286]. This ability to disrupt zwitterionic bilayers is consistent with the protein's mainly eukaryotic targets. Despite the peptide interacting more strongly with anionic (over zwitterionic) lipids [308], the incorporation of negatively charged lipids into PC vesicles in fact reduces melittin's disruptive propensity (but without loss of membrane-peptide association), likely due to strong peptide-headgroup electrostatic interactions [309, 310]. However, melittin is still active against anionic membranes, but the effect appears to be different to that in zwitterionic bilayers. In PC vesicles co-encapsulating markers of different sizes, micromolar melittin has been shown to induce size-specific leakage, with larger molecules released with increased peptide concentrations, but in PG vesicles it induced fusion and non-selective leakage of the markers [311, 312]. In planar supported PG and PS membranes, patches of bilayer were lost when incubated with 10 μM peptide [313]. PC and 9:1 PC/PG membranes on mica have shown similar, initially nanometre-sized defects that grow with incubation time [314]. As a result, and along with evidence that melittin can induce fragmentation of artificial bilayers into discs and micelles at high micro- and millimolar concentrations [315] (and references therein) melittin appears to be able to act in both a pore-forming and detergent-like manner, depending on the membrane.

5.1.4.4 Indolicidin

Indolicidin is a short, cationic (+4) peptide produced by bovine neutrophils. It has a unique structure amongst antimicrobial peptides: only 13 residues in length, it contains the highest proportion of tryptophan of any known peptide, with three proline residues interspersing the primary structure [316]. Three-quarters of its residues are hydrophobic; the three polar residues that it does possess are all positively charged. Indolicidin is active at concentrations of tens of micromolar against bacteria (both Gram-positive and -negative) and fungi, whilst also displaying haemolytic activity [316–319]. Analogues in which either the proline residues were substituted for alanine, or the tryptophan residues for phenylalanine, had comparable antibacterial and antifungal activities to the unaltered AMP, however

the Phe analogue had limited haemolytic ability, perhaps indicating the importance of the presence of Trp for interaction with zwitterionic membranes [317]. CD of indolicidin in buffer solution and in the presence of POPC or POPG vesicles indicates a largely disordered structure [320, 321], which was also found in CD measurements of indolicidin bound to POPC and POPG vesicles [320], and further supported by 2D NMR of the peptide in the presence of dodecylphosphocholine micelles (which showed similar CD spectra to lipid vesicles) [321]. The latter study revealed an extended structure for indolicidin on micelles, with the hydrophobic centre flanked by the positively charged regions at the termini; the use of spin-labels at various depths into the micelle suggested that indolicidin does not penetrate deeply into the lipid core. Despite the lack of well-defined secondary structure, further CD evidence suggests that the indole rings of the tryptophan residues stack, forming β-turns [319].

In egg PC vesicles, 1–10 μM indolicidin was found to instigate the release of negatively charged carboxyfluorescein but could not liberate the far smaller glucose molecule, nor the dye doxorubicin [322]. Further, the peptide was able to release other negatively charged markers, but this activity was reduced by the presence of organic anions. These results imply that indolicidin is able to facilitate organic anion transport across the zwitterionic membranes, but without pore formation. In a similar study, 30 μM indolicidin was only able to release 50 % of the anionic dye 8-aminonapthalene-1,3,6 trisulfonic acid (ANTS) contained within PC vesicles after more than 30 hours, whereas pore-forming melittin at 1.7 μM released all the dye within one-tenth of that time [320]. The incorporation of PG into bilayers, however, induced release of markers unselectively from vesicles, and with more effective release than in PC membranes [320, 322]. Whilst probably too short to span the entire lipid bilayer [323], BLMs made from DOPC/DOPS (5:1) were disrupted by indolicidin, with channel-like fluctuations [318]. However, DPhPC/DPhPG (4:1) BLMs were stable in the presence of indolicidin up to −330 mV, 50 mV above other membrane-active peptides [324].

Indolicidin inhibits bacterial growth at micromolar concentrations [316]. Despite the ability of the peptide to disrupt some model bacterial membranes, it was

found not to lyse *E. coli* membranes at up to 16 μM, but instead to induce filamentation, which is often indicative of the inhibition of DNA synthesis [325]. Further investigation found that 26 μM indolicidin resulted in 84–90 % inhibition of DNA production. High concentrations of the order of 100 μM were also found to slow protein synthesis. The evidences of organic ion transport across membranes, and of inhibition of internal cellular processes in bacteria, suggest that unlike the other three AMPs, indolicidin has a mainly non-pore forming mode of toxicity [324].

5.1.5 Contributions to This Work

The experiments presented here were conducted as a collaboration with Marc Szabo, who performed the initial electrical characterisation of the AMPs. Analysis of these data, followed by imaging experiments and subsequent analyses were devised and conducted solely by JTS.

5.2 Materials & Methods

5.2.1 Materials

1-palmitoyl-2-oleoyl-*sn*-glycero-3-phospho-(1'-rac-glycerol) (POPG), 1-palmitoyl-2-oleoyl-*sn*-glycero-3-phosphoethanolamine (POPE) and cardiolipin (CL) were purchased from Avanti Polar Lipids and used without further purification. POPE and CL were stored as chloroform stocks between 10 and 25 mg·mL^{-1}; POPG was stored as a 25 mg·mL^{-1} stock in 2:1 chloroform/methanol, in which it is more soluble than pure chloroform. TRITC-DPPE (1,2-dipalmitoyl-*sn*-glycero-3-phosphoethanolamine) and Atto590-DOPE (1,2-dioleoyl-*sn*-glycero-3- phosphoethanolamine) were stored as stock solutions in chloroform; an appropriate volume of these stocks were dried with the PE/PG/CL lipid mixture when single-molecule concentrations of labelled lipid were required.

Unlabelled melittin, magainin II and indolicidin were purchased from Bachem (Bubendorf, Switzerland). Unlabelled alamethicin was obtained from Sigma-Aldrich. The peptides were stored in powder form at −20 °C, and dissolved in Milli-Q water to appropriate stock concentrations when required. Labelled peptides were

covalently bound to a tetramethylrhodamine dye (TRITC; $\lambda_{\text{emission max.}} = 577$ nm), and were synthesised by Lifetein (Somerset, New Jersey, USA) in the case of melittin, magainin II and indolicidin. Labelled alamethicin was a gift from the group of Prof. Darren Dixon (University of Oxford, UK). The dye was conjugated to the C-terminus of the peptides, in order to minimise perturbation of the peptide behaviour. The C-terminus in all four AMPs is more hydrophilic than the N-terminus and is therefore more likely to remain at the lipid headgroup/solution interface when the protein inserts into the membrane. Conjugation of the dye to this end of the molecule should therefore minimise steric interactions that perturb the lipid-peptide dynamics. The same rationale has been employed in other labelling studies of AMPs [326].

5.2.2 Bilayer formation

In order to better mimic the bacterial membranes against which these peptides show activity, the AMPs were investigated in DIBs composed of POPE, POPG and cardiolipin in the ratio 69:29:2 (mol%). High concentrations of POPG were found to cause the formation of aggregates when dissolved in hexadecane; lipid solutions of 3.5 mg·mL^{-1} (total lipid) in hexadecane were therefore used, with the incubation times increased to around 1 hour accordingly.

Bilayers were prepared as described previously, with droplets containing the solution for SCCaFT imaging (1.39 M KCl, 9.3 mM HEPES, 370 μM EDTA, Fluo-8H) and various concentrations of AMP. In dual-colour experiments, it was found that there was signal bleed from Fluo-8H into the TRITC imaging channel (see Appendix C for excitation and emission spectra) when the calcium indicator dye was at the previously-used concentration of 46 μM. This was therefore reduced to around 7 μM, a reduction which lead to no apparent loss of sensitivity in detecting SCCaFTs. As before for oSCR recording, the agarose contained 750 mM $CaCl_2$.

5.2.3 Imaging Setup

Both dyes were excited by TIRF illumination: Fluo-8H was excited by a 473 nm laser beam, and TRITC by a laser at 532 nm. The imaging setup is shown in Figure

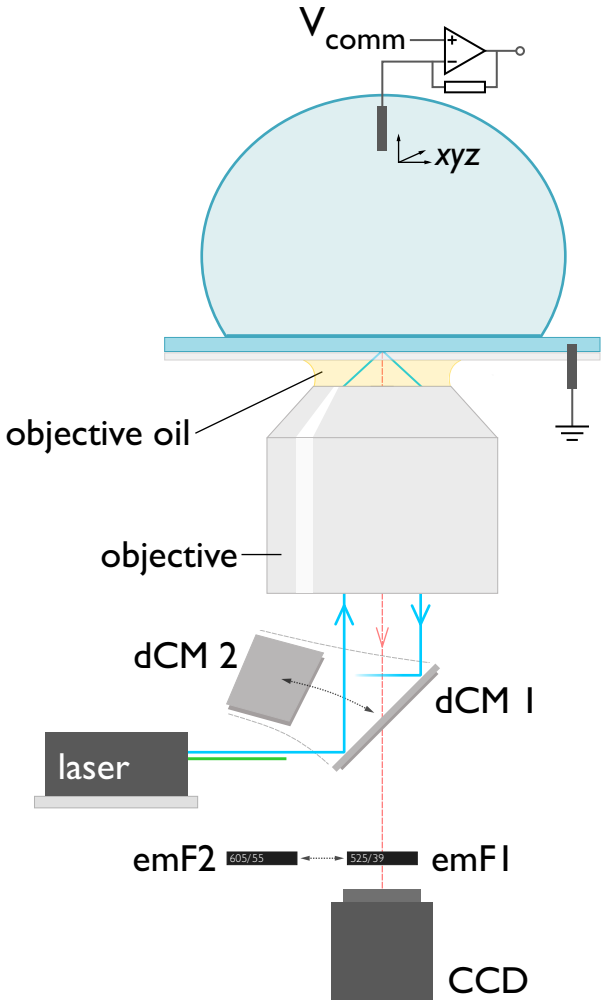


Figure 5.3: Dual-colour setup for oSCR and single-molecule imaging. A blue (473 nm) laser was used along with a dichroic mirror (dCM1) and emission filter (emF1) suitable for SCCaFT imaging in order to locate pores within the bilayer. Once a pore was located, a green laser (532 nm) was used to excite the TRITC-labelled AMPs; this required the dichroic mirror and emission filters to be changed to a pair appropriate for imaging at higher wavelengths (dCM2 and emF2).

5.3. After a pore (or pores) had been generated in the membrane, their resulting SCCaFTs were located under blue laser excitation, and imaged on the CCD, with a 525/39 nm emission filter in the optical path (identical to oSCR imaging of electropores; for full details, see Chapter 3). The excitation beam was then switched to a green laser in order to observe the labelled peptides in the same location as the SCCaFT. Fluo-8H still absorbs at 532 nm, and due to its emission spectrum being particularly broad (see Appendix C) and its emission intense, imaging of labelled peptides required the use of an emission filter that was shifted to longer wavelengths

and away from the peak emission of TRITC, in order to eliminate Fluo-8H signal bleed into the single-molecule channel. A 605/55 nm bandpass filter (Semrock) was therefore used for TRITC signals, despite the emission maximum for TRITC being at 576 nm. The dichroic mirrors and the emission filters were mounted on movable carousels or sliders to enable quick changing from the blue to green optical paths.

5.2.4 Radial Distribution Function Analysis

The radial distribution functions for single AMP molecules were computed using a custom-written procedure in Igor Pro. First, single-particle tracking analysis was performed by the Trackmate plugin in Fiji (see Materials & Methods, Chapter 3) in order to obtain sub-pixel localised positions of each molecule in each frame. Using these locations, the Igor procedure counted the number of spots within a circular shell of thickness dr at a distance r away from the pore locus. The pore locus was determined by fitting a 2D Gaussian to a z-projected stack of the SCCaFT recording. The spot count was normalised by the total shell area and the number density of particles (particles per unit area) within the frame; plotting the normalised count versus the distance r generated the radial distribution function, $g(r)$.

5.3 Results & Discussion

5.3.1 Electrical Behaviour of AMPs in DIBs

In order to determine whether the AMPs interacted with DIBs, micromolar quantities of the peptides were incorporated into the droplet solution. Concentrations in the micromolar range are akin to the local concentrations of AMP experienced by an invading pathogen, and those used in previous studies with these AMPs (see Sections 5.1.4.1–5.1.4.4). DIBs were formed from a ternary mixture of POPE/POPG/cardiolipin in a molar ratio of 69:29:2. This lipid mixture, containing ∼30 % anionic lipids (PG, anionic, and cardiolipin, doubly anionic), was chosen to mimic the plasma membrane of bacteria, which is the common target for these AMPs. Bilayers containing increasing concentrations of AMP were exposed to

the same voltage protocol used to characterise other bilayers in this work: 180 s 'high', 30 s rest, with a ±5 mV increment.

Figures 5.4 and 5.5 show the current response of bilayers exposed to this protocol in the absence and presence of the four AMPs. In the absence of peptide (grey markers), the curves are characterised by the same behaviour observed in DPhPC bilayers: a very shallow, linear current response at low voltages, followed by increasing non-linearity at higher voltages (>100 mV) as the electric field causes the formation of electropores in the membrane, increasing the membrane conductance. As the number and size of pores increases, the curve becomes steeper until the bilayer ruptures. The rupture potential V_c tended to be below that for DPhPC. This is consistent with a destabilisation of the bilayer due to the large quantity of anionic lipids. Electrostatic repulsion between the headgroups likely makes pore formation (energetically) easier by contributing to the effective tension in the plane of the bilayer. Furthermore, toroidal pores formed from charged lipid headgroups will face greater repulsion between the pore walls than hydrophilic pores in zwitterionic membranes, thereby potentially slowing pore closure.

Bilayers in the presence of low concentrations of AMP (darker colours in Figures 5.4 and 5.5) showed similar I–V curves to peptide-free bilayers, however, the curves became non-linear at increasingly lower voltages for alamethicin, magainin-II and melittin as the concentration of the peptide was increased. In contrast, the I–V curves for indolicidin showed little change from 500 nM to 50 μM peptide. This consistent with BLM studies using 4:1 DPhPC/DPhPG [324]. In fact, closer inspection of these curves and the electrical traces that were used to generate them demonstrated that in the presence of indolicidin, the increased bilayer current fluctuations (the onset of non-linearity, due to pore formation) and bilayer rupture on average appeared at *higher* voltages than in peptide-free bilayers. This would support the notion that indolicidin does not form pores in the bilayer, instead having a stabilising effect, as association of any cationic peptide with the negatively charged membrane will help screen the anionic headgroups from one another. In the

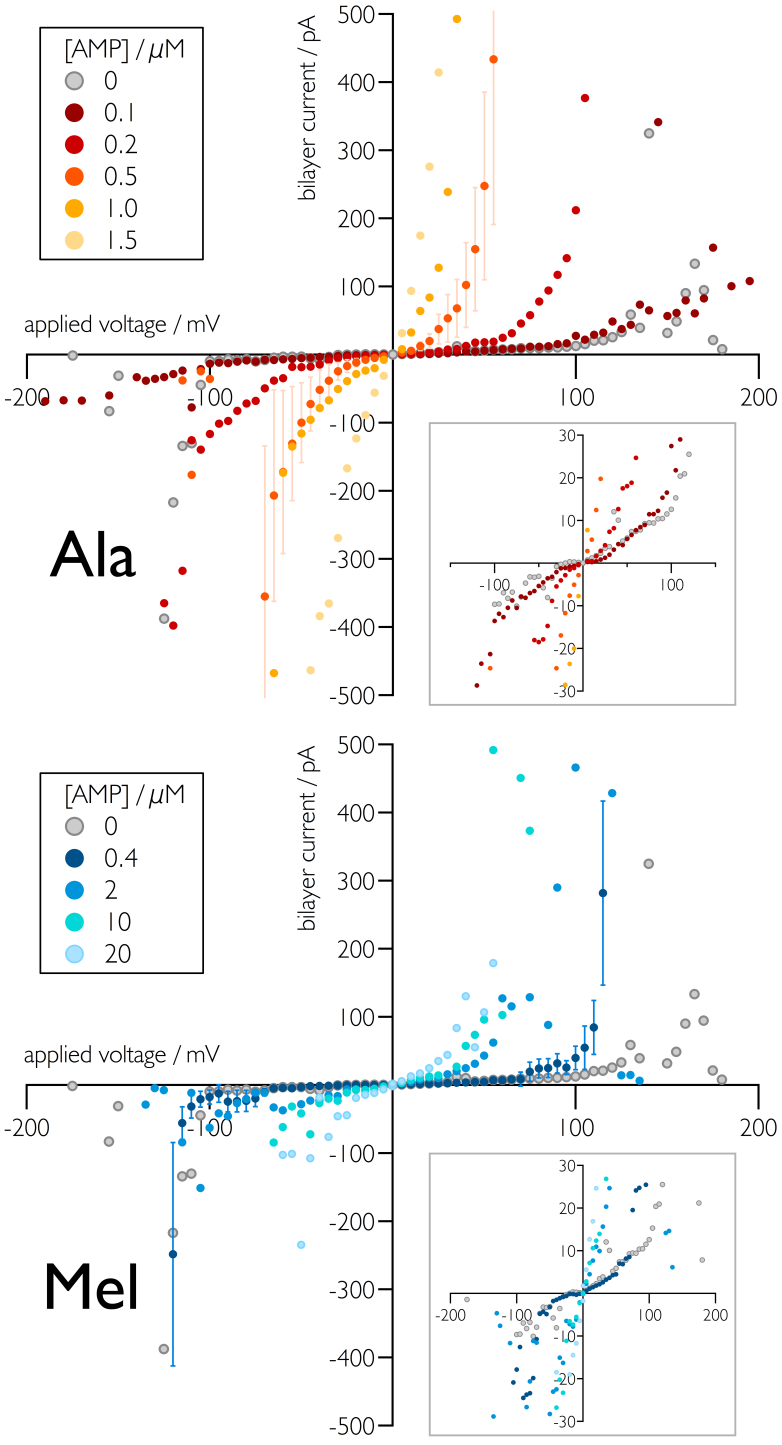


Figure 5.4: I–V curves for alamethicin and melittin in DIB bacterial mimics. The colour coding here is used throughout this chapter: *red*, alamethicin; *blue*, melittin; *grey*, bilayer with no AMP. The mean bilayer current was determined at each applied potential; the data points are the average of at least three independent bilayers. Alamethicin and melittin induced increased electrical conductivity with increasing AMP concentration. Error bars, which have been shown for just one concentration in each set of curves for clarity, are the standard deviation. *Insets*: Expanded regions about the origin.

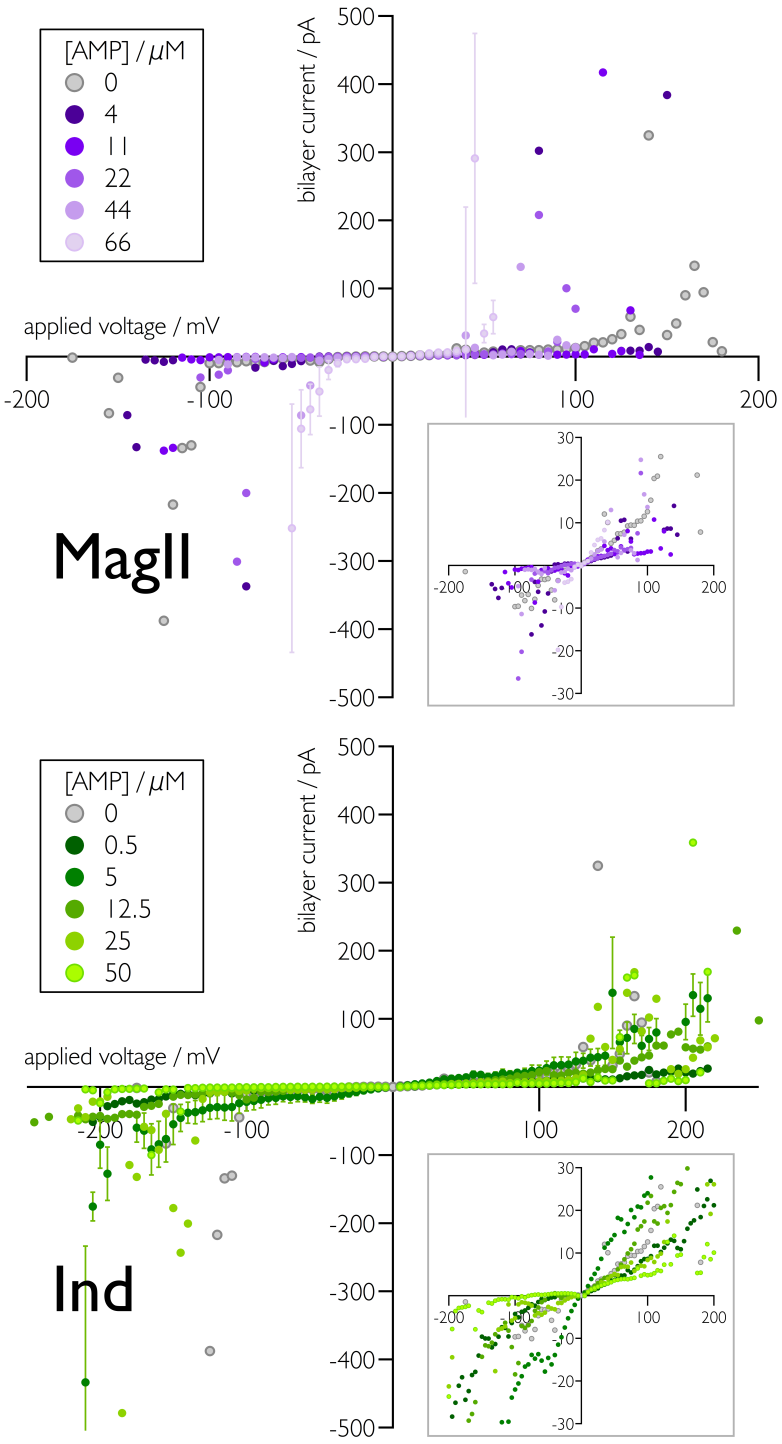


Figure 5.5: I–V curves for magainin-II and indolicidin in DIB bacterial mimics. The colour coding here is used throughout this chapter: *purple*, magainin-II; *green*, indolicidin; *grey*, bilayer with no AMP. The mean bilayer current was determined at each applied potential; the data points are the average of at least three independent bilayers. Magainin-II induced increased electrical conductivity with increasing AMP concentration, whilst indolicidin had little effect on the I–V curve. Error bars, which have been shown for just one concentration in each set of curves for clarity, are the standard deviation. *Insets*: Expanded regions about the origin.

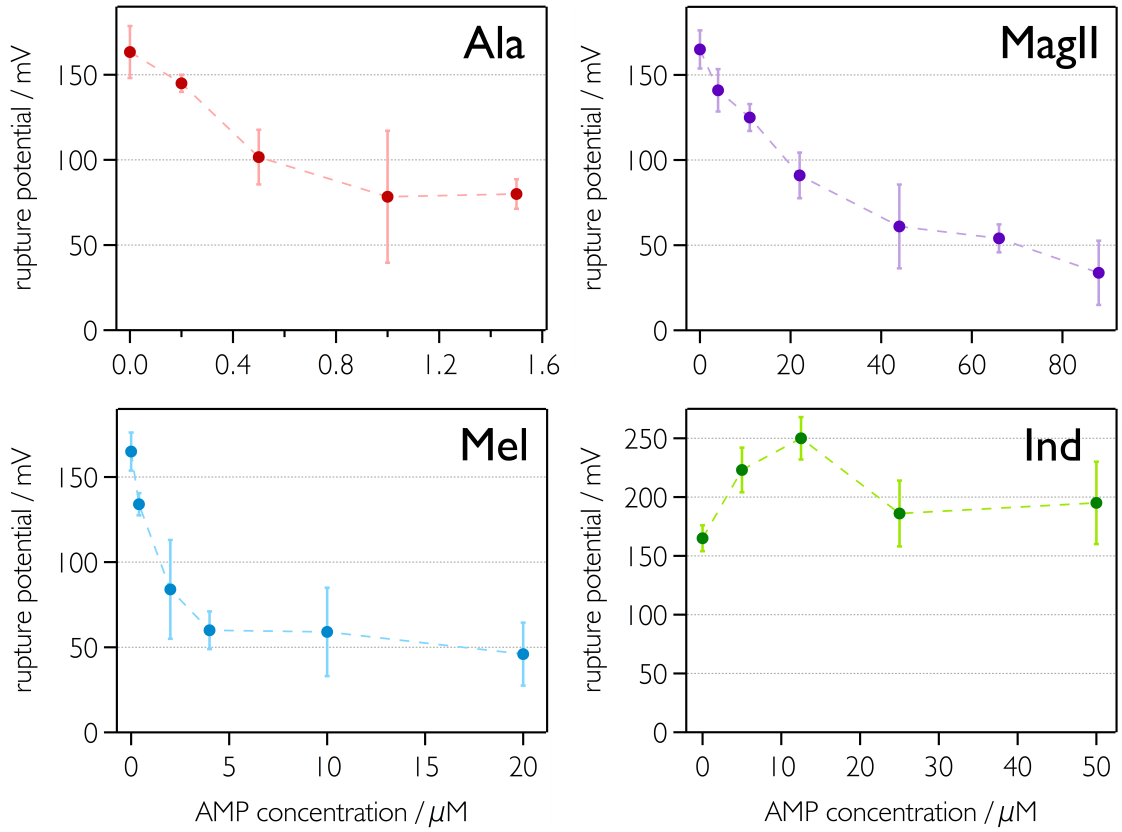


Figure 5.6: Dependence of the rupture potential, V_c, on peptide concentration. Points are mean values of V_c from at least three bilayer recordings; error bars show the standard deviation of the mean. The stabilising effect of indolicidin is clearly seen here.

absence of a pore-forming propensity in the case of indolicidin, this screening will reduce in-plane electrostatic lipid-lipid repulsion, thereby stabilising the membrane.

In order to better parameterise the I–V curves, the relationship between peptide concentration and the rupture voltage was investigated. These relationships, plotted in Figure 5.6, highlight the main findings from the I–V curves. Increasing peptide concentration leads to a reduction in V_c for all but indolicidin. For the latter, the stabilising effect of the peptide on the bilayer is clear: at all concentrations the bilayer ruptured at larger voltages than in the absence of peptide.

For the other peptides, V_c begins to level out with increasing quantity of AMP, presumably as the membrane environment becomes increasing saturated with peptide. It is interesting to note that alamethicin showed destabilising activities at far lower concentrations than magainin-II and melittin, despite the former being electrically neutral, indicating that the overall peptide charge is not necessarily

the dominating factor in the interaction between the peptide and the membrane. Also of note is that the minimum inhibitory concentrations of melittin have been found to be between around 1/5 and 1/10 of those of magainin-II, depending on the bacterial species that the AMPs are interacting with [277]; in the experiments presented here, the concentration at which melittin's influence on V_c begins to plateau is 1/5 to 1/10 of that of magainin-II.

Figure 5.7 presents examples of the electrical fluctuations of DIBs in the presence of AMPs. At low concentrations, alamethicin gated with discrete steps between conductance levels of differing heights. This behaviour is consistent with previous bilayer studies [274–276], and is believed to be the result of individual peptide monomers joining and leaving the barrel-stave pore structure. The conductance steps recorded in DIBs, ∼1.6 nS, also match the values of around 1.4 nS recorded previously in BLMs [272]. At concentrations above 500 nM, however, this behaviour is lost: the first signs of electrical activity are fluctuations with no defined conductance, akin to the fluctuations of electropores. These fluctuations occur at voltages well below those that generate electropores in the absence of peptide (see Figures 5.4 and 5.5), which might suggest that the peptide is no longer forming barrel-stave pores, but nucleating electropores. This idea shall be discussed in greater detail later.

The electrical activities of magainin-II and melittin do not show discrete conductances. This is expected for toroidal pore-forming peptides, for the pore wall structure consists of peptide *and* lipid headgroups, and therefore, as with toroidal electropores, the radius of the defect may fluctuate more freely than that of a barrel-stave pore. Occasionally, step-like changes in conductance were observed at low peptide concentrations (see *MagII, i* and *ii*, and *Mel, i–iii* in Figure 5.7). This could be due to the formation of small pores, in which, due to their small circumference, they might accommodate a few peptides and a limited amount of lipid in the pore wall. In this case, loss or gain of a peptide from the wall might give a step-like change in current. Larger pores with a greater proportion of lipid forming the walls however, do not show these discrete-like changes in current, since loss or gain of a peptide can be easily accommodated by a change in the number of lipids

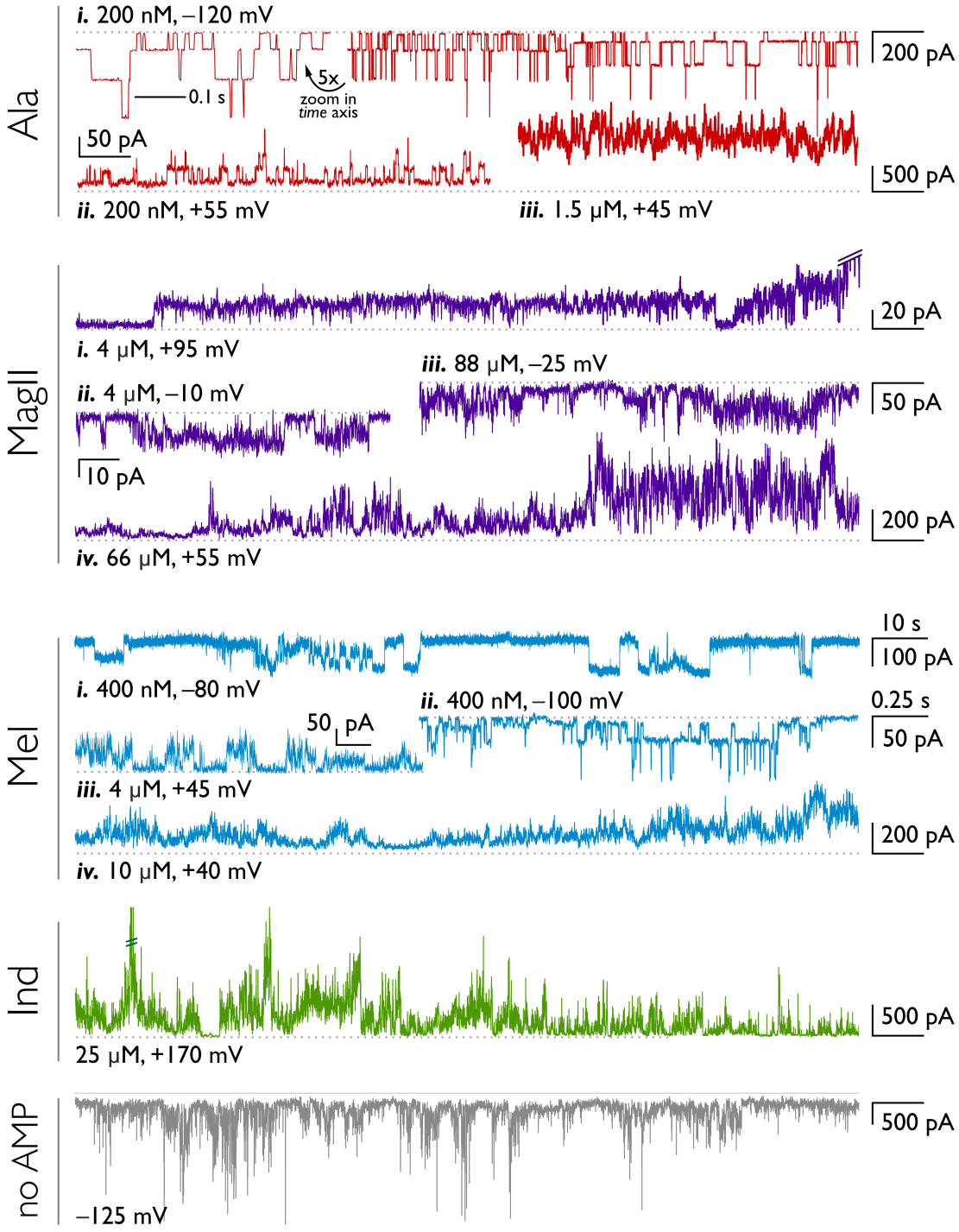


Figure 5.7: Electrical behaviour of AMP-containing DIBs. Alamethicin (*red*) at low concentrations gates with discrete conductance steps, but at higher concentrations of peptide, the discrete fluctuations are lost. Magainin-II (*purple*) and melittin (*blue*) show electropore-like gating, with occasional but ill-defined discrete-like events. The character of the fluctuations in the presence of indolicidin (*green*) were indistinguishable from those in pure bilayers (*grey*).

forming the toroid, rather than the ratchet-like changes in pore radius observed for alamethicin. Again, as with alamethicin, step-changes in bilayer current were not observed in DIBs containing higher concentrations of peptide.

Finally, the traces produced by indolicidin-containing bilayers were indistinguishable from pure electroporation, which suggests that the pores are similar toroids of variable radius. Like for magainin-II and melittin, these could be peptide-stabilised pores. However, the increase in V_c in the presence of indolicidin, along with other evidence that indolicidin does not permeabilise bilayer membranes [325], suggests that the fluctuations observed for this peptide are most likely those of electropores.

5.3.2 oSCR Imaging of AMP Pores

Calcium-flux imaging allowed the conductance contributions of individual pores to be isolated — as demonstrated previously with electropores. To image the pores formed by AMPs, the droplet solution contained an appropriate concentration of AMP so as to induce frequent and long-lived pore formation, but not render the bilayer too unstable. These concentrations were around 500 nM for alamethicin, 25 μM for magainin-II, 10 μM for melittin and 15 μM for indolicidin. Location of Fluo-8H SCCaFT(s) under blue-excited TIRF imaging, as used in the oSCR experiments of previous chapters, allowed the AMP pores to be indirectly observed. Monitoring the dynamic behaviour of single pores via their calcium flux signals allowed a closer look at their gating behaviour, beyond what could be gained by inspection of the electrical current data alone.

Typical fluorescence vs. time traces for the four AMPs are shown in Figure 5.8. As expected, the individual barrel-stave pores of alamethicin gated with discrete steps in intensity; the flux through a pore monitored in this manner (*i.e.* optically) could be correlated to the ensemble current being simultaneously recorded (as seen in the electrical and optical alamethicin traces in Figure 5.8). The oSCR signals in the presence of magainin-II, melittin and indolicidin however did not reveal consistent, discrete changes in fluorescence intensity, indicating ill-defined pore diameters in the case of all the isolated pores observed.

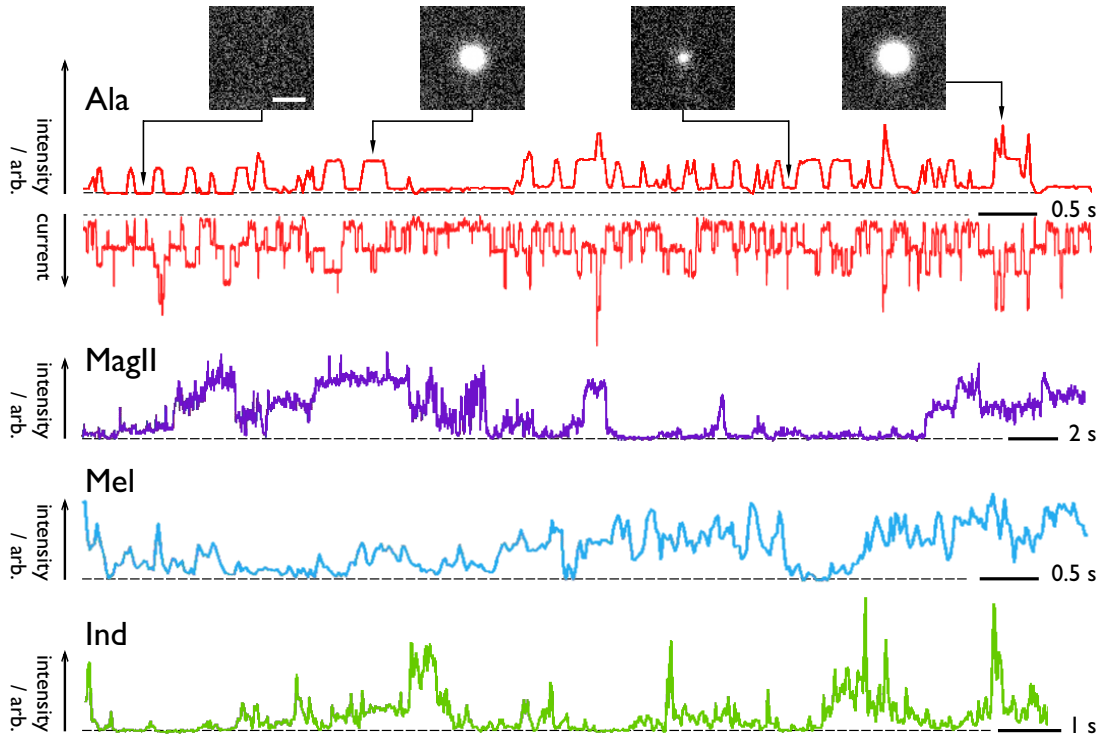


Figure 5.8: oSCR traces for AMPs. Fluorescence vs. time traces were obtained by extracting the mean intensity from a region of interest around the oSCR signal. Simultaneous electrical and optical signals are shown for alamethicin, with oSCR fluorescence as upward deflections and the total bilayer current as downward deflections, showing the contribution to the electrical activity of the selected pore. Images show single 20 ms frames. Scale bar: 10 µm. Dashed grey lines indicate the background fluorescence intensity or 0 pA level.

5.3.3 Single-Molecule and oSCR Imaging

In order to better understand the interactions between the AMPs and the membrane, combined single-molecule fluorescence and oSCR imaging experiments were carried out. In addition to unlabelled AMP (of the approximate concentrations detailed in the previous section), around 3 nM of TRITC-labelled peptide was present. During the experiment, electrical activity was established in the bilayer, followed by location of the resulting Fluo-8H SCCaFT(s) under blue-excited TIRF imaging. The excitation wavelength was then switched to green light, in order visualise the labelled peptides present at the bilayer (a schematic of this setup is shown in the Materials & Methods section). Figure 5.9a shows typical oSCR and single-molecule fluorescence readouts from these experiments, showing the same membrane patch

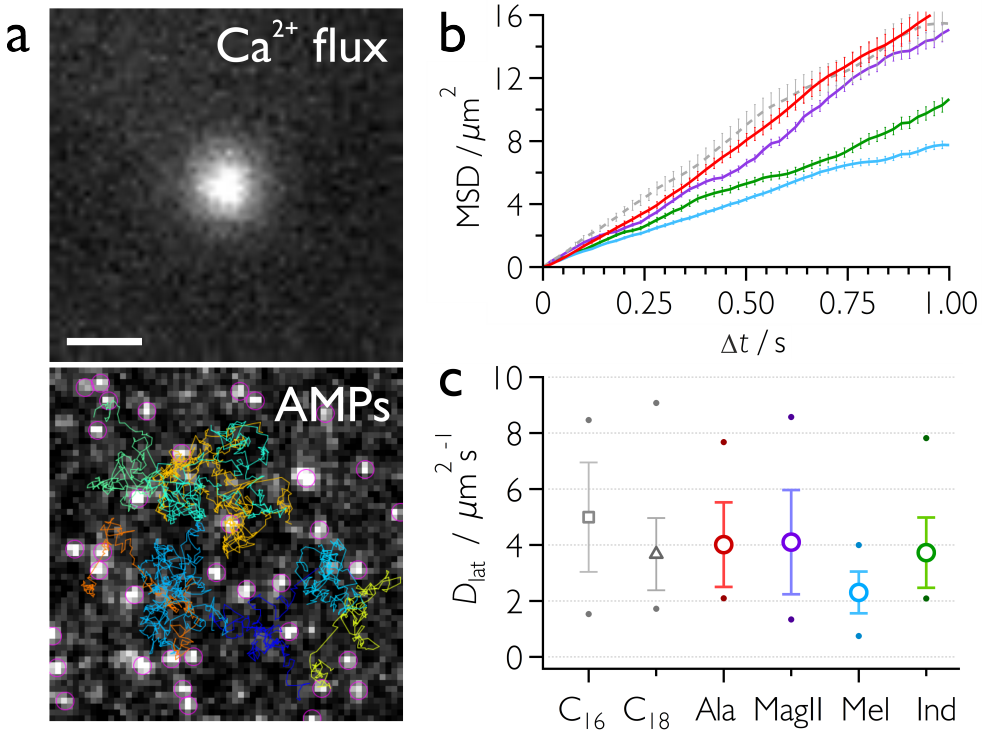


Figure 5.9: Dual-colour fluorescence imaging of AMP pore formation. (a) Ca^{2+} flux image under blue excitation (*upper*) of a SCCaFT in the membrane, and green excitation image (*lower*) showing single AMP molecules (in this case melittin) as bright spots in the same field of view. Pink circles are the spots detected by single-particle tracking, with the coloured lines showing the trajectories of some of the peptides. Images are single 20 ms exposures. Scale bar: 5 μm. (b) Example MSD vs. Δt plots for the four labelled peptides, along with that for dye-labelled lipid molecules for comparison (*grey*). (c) Mean lateral diffusion coefficients for the peptides and labelled lipids with two different chain lengths (TRITC-DPPE, 16 carbons and Atto590-DOPE, 18 carbons). Error bars show the standard deviation of the mean; points above and below indicate the maximum and minimum D_{lat} values.

under blue (for Fluo-8H) and green (for labelled peptide) excitation. The labelled peptides are seen as bright, spots in the bilayer, and were observed to diffuse laterally within the membrane. The lateral diffusion coefficients, Figure 5.9c, were computed from MSD vs. Δt plots. In order to compare the dynamic behaviour of the peptides to that of the surrounding lipids, analogous imaging experiments were carried out in the absence of peptide, but with the lipid mixture containing a small amount of dye-labelled lipid, either TRITC-DPPE or Atto590-DOPE (also excited by green laser light), to a final concentration of around 3 nM. Tracking of lipids in these DIBs yielded D_{lat} values of 4–5 $\mu m^2 \cdot s^{-1}$. The mean diffusivity of

the AMPs were of the same order, with means of ∼4 $\mu m^2 \cdot s^{-1}$, apart from melittin, which was ∼2.5 $\mu m^2 \cdot s^{-1}$. Whilst the reason for melittin showing a slower D_{lat} than the other AMPs was not investigated, the variation between peptides could be a result of the depth of penetration into the headgroup region of the membrane, as discussed in the introductory sections at the beginning of this chapter.

In general, however, these diffusion coefficients are around the same speeds as those of labelled lipids. Observation of two-dimensional diffusion of the peptides indicates that they are largely surface associated, however their orientation in the membrane cannot be determined. Whilst penetration into the bilayer, as seen for transmembrane proteins, leads to reduced diffusion coefficients with respect to the surrounding lipid molecules [327], the smaller size of AMPs may mean that there is a lesser difference in the diffusive properties whether the protein lies parallel to the membrane surface or is inserted into it. However, bulk FRAP (fluorescence recovery after photobleaching) data on BLMs containing labelled alamethicin showed that at voltages where typical discrete conductance steps were observed (*i.e.* at voltages where the protein was known to be inserted), the lateral diffusion coefficient was reduced by a factor of approximately 1.5 compared with bilayers at 0 mV [326]. In the experiments presented here, more complex analysis of the single-particle tracking data might uncover distinct populations of diffusion coefficients, possibly corresponding to a (faster) membrane-parallel and a (slower) membrane-perpendicular state, although further work would be needed to confirm the peptide orientation.

5.3.3.1 Radial Distribution Function Analysis

Despite the presence of a pore within the observed membrane patch, no variation in AMP surface distribution could be readily seen. All single-molecule recordings of AMPs resembled that shown in Figure 5.9a: an even distribution of freely-moving molecules across the membrane. AMPs were not seen to cluster in the region of the pore, nor did they aggregate elsewhere on the bilayer surface. If the proteins are associating with the pore walls, it might be expected that there should be

some localisation of peptides at the SCCaFT locus. By eye, there appeared to be no enhancement about the pore location.

In order to investigate this more rigorously, radial distribution functions (RDFs) were computed. The radial distribution function, $g(r)$, gives the probability of finding a particle at a distance r away from a given point. At $r \to \infty$, $g(r) \to 1$, as at infinite distance the system in question loses all order, and there is an equal probability of finding a particle at all r. The procedure used to determine this is schematically shown in Figure 5.10. Firstly, the location of the pore centre was determined by 2D Gaussian fitting to the oSCR image. This was the locus about which the RDF was calculated. Next, the image stack of diffusing peptides recorded in the same membrane area was tracked to generate AMP location coordinates for each frame. Using this information, the RDF procedure then counted the number of particles within a shell of $r + \mathrm{d}r$ at a distance r away from the pore locus. The value of r was incremented in steps of 40 nm, which is equal to the average localisation error of 2D Gaussian fitting of single molecules. The shell thickness $\mathrm{d}r$ was set to the same value. If $\mathrm{d}r$ is too small, the RDF may not find any spots within the shell, and $g(r)$ would be zero at a given r. The number of spots found within the shell was then divided by $2\pi r\mathrm{d}r + \pi\mathrm{d}r^2$, to normalise for the area of the shell, since in a larger shell more particles are likely to be found. Finally, to ensure $g(r)$ tended to unity, the count was normalised by dividing it by the number density, *i.e.* the average number of spots per frame. This counting procedure was repeated for the entirety of the single-molecule fluorescence stack, ∼2000 frames.

The results of this analysis are presented in Figure 5.11. The AMPs thought to induce pore formation in lipid membranes all demonstrate an enhancement in $g(r)$ near the pore, within a radius of around 500 nm. The increased likelihood of finding peptide near the pore for these AMPs is further supporting evidence that they form — or at least are able to associate with — membrane pores. Indolicidin on the other hand, thought not to primarily operate by forming transmembrane pores, shows no such enhancement of peptide at the SCCaFT locus. In bilayers containing no

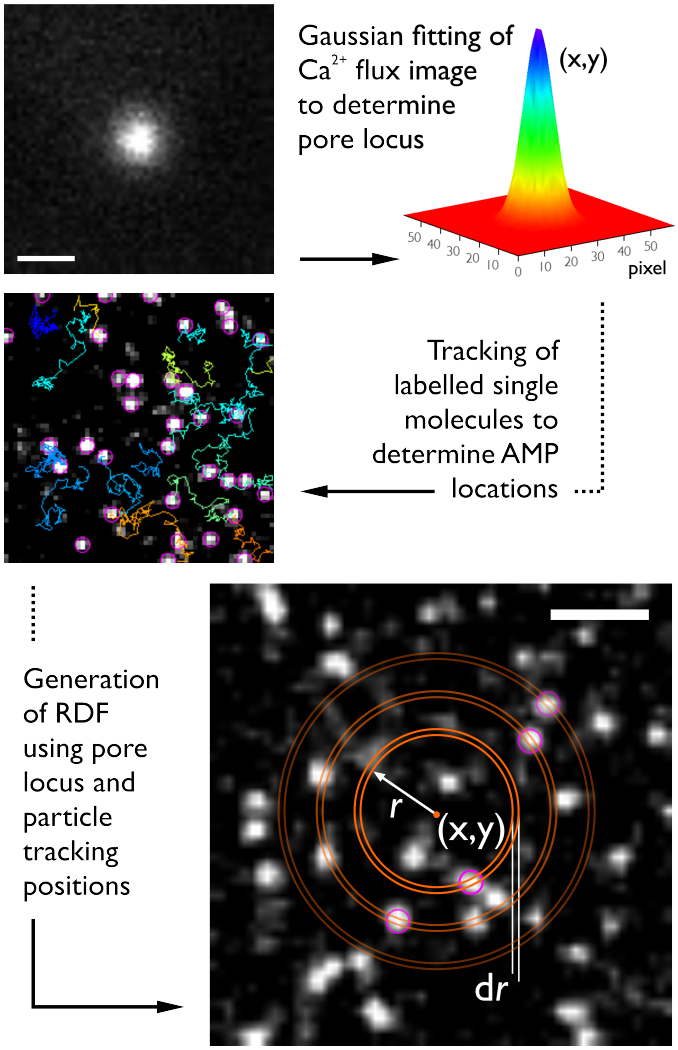


Figure 5.10: Radial distribution function analysis procedure. Coordinates of the pore location, obtained from the oSCR readout, and the position of the peptide molecules over time were determined by Gaussian fitting. These were used to calculate the RDF, the probability of finding a particle within a shell of thickness $r + \mathrm{d}r$ drawn a distance r away from the pore locus. See the main text for a full description of the procedure. Scale bars: 5 µm.

peptide but single-molecule concentrations of labelled lipid (either TRITC-DPPE or Atto590-DOPE), the RDFs for also show no localisation around the pore.

Since $g(r)$ is a normalised count of the number of particles at a given distance, the relative values near $r = 0$ give information about the quantity of peptide in the pore. It is interesting to note that magainin-II and melittin, both thought to operate through the same mechanism of forming toroidal pores, both give $g(r) \simeq 3.5$ as the pore is approached. On the other hand, alamethicin shows a $g(r)$ of double

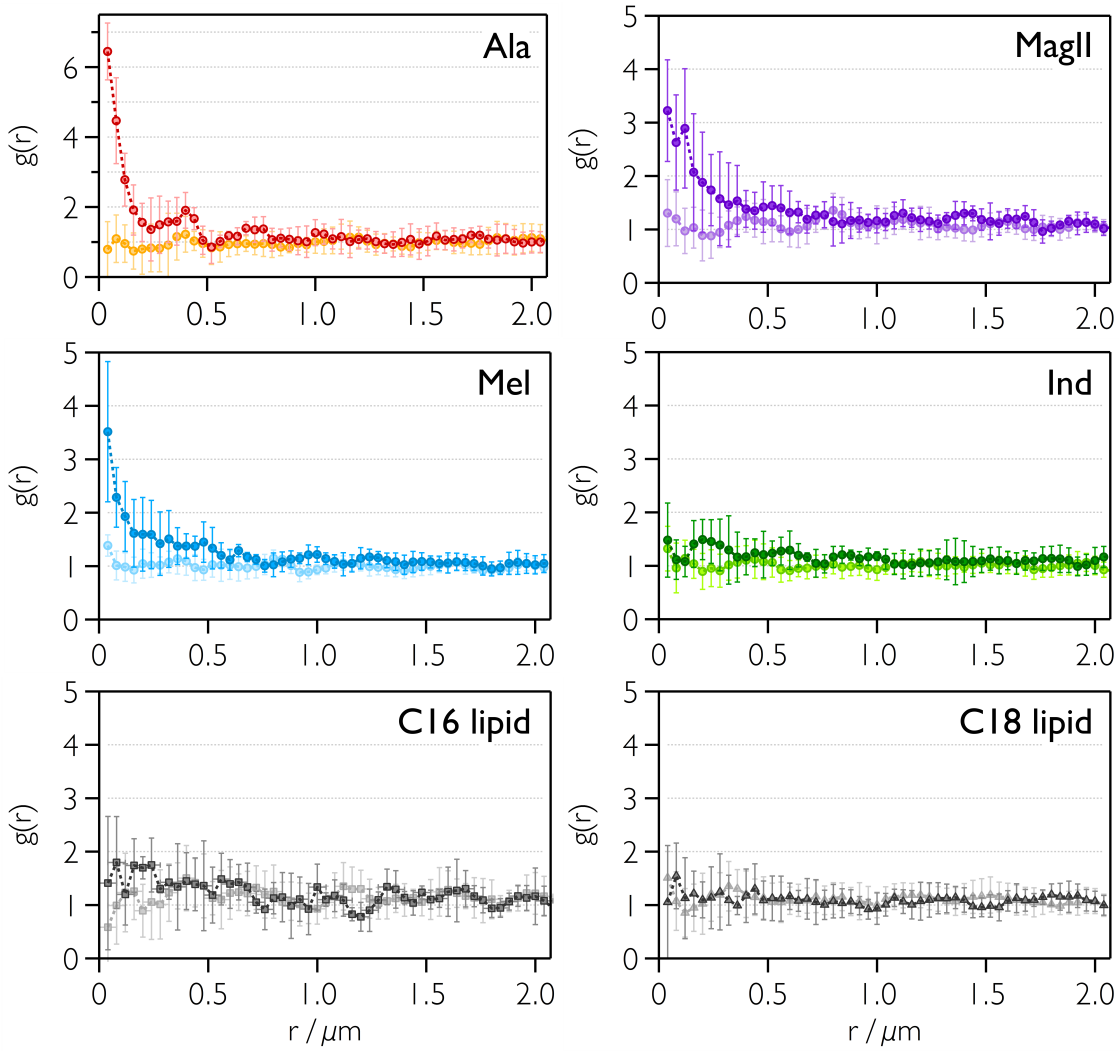


Figure 5.11: Radial distribution functions for AMPs. Each RDF is the mean of at least three separate pores. The dark coloured plots show the RDF computed about the pore locus; light coloured traces are those computed at a random location away from the pore. The pore-forming AMPs alamethicin, magainin-II and melittin show enhanced probability of finding peptide near the pore locus; indolicidin and the control lipids show no enhancement. The number of RDFs about the pore and non-pore locations that contributed to each plot are: *alamethicin* pore = 3, non-pore = 8; *magainin-II* pore = 6, non-pore = 17; *melittin* pore = 4, non-pore = 12; *indolicidin* pore = 5, non-pore = 16; C_{16} *lipid* pore = 3, non-pore = 8; C_{18} *lipid* pore = 7, non-pore = 18. Note that $g(r)$ is plotted on a different scale for alamethicin. Error bars are the standard deviation of the mean.

this value near the pore, indicating the twice the probability of finding peptide in the region. This is consistent with alamethicin forming barrel-stave pores in which the entire circumference of the pore must be lined with peptide, in order to prevent exposure of the bilayer core to the electrolyte, and magainin-II and melittin forming toroidal pores, which do not need to be fully lined as the pore wall can also be formed from the lipid headgroups.

Inspection of the single-molecule fluorescence recordings indicates that (in the case of alamethicin, magainin-II and melittin) very few AMPs that travel to the locus of a pore remain there until the fluorophore photobleaches. Instead, they pass through the region of the pore, the peaks in the respective RDFs indicating that these AMPs are more likely to spend more time around the pore than elsewhere in the bilayer. This is consistent then with idea of a *dynamic* pore structure, one in which the AMPs are free to enter and leave, as opposed to a structure with a constant number of constituent peptides. Indeed, if the pores were not dynamic, once the pore circumference was 'full' of peptide, no more would leave or enter it. Since the TRITC fluorophores were found to bleach within a few seconds of entering the TIRF field, a non-dynamic pore would therefore quickly become (and remain) dark for the majority of the recording, and we would observe little enhancement in $g(r)$ around the pore. The fact that short-lived fluorophores resulted in a peak in the RDF suggests that the pores formed by these peptides are in fact dynamic. In the case of alamethicin, this further validates the notion that individual peptide monomers are able to enter and leave a dynamic, multimeric pore structure. For magainin-II and melittin, a similar notion applies, in that peptides on the membrane surface exchange with those within the toroidal wall of the pore.

Considering the electrical data collected in AMP-containing DIBs thus far, we may speculate a little about the relationship between AMP-mediated pores and electropores. In the electrical recordings of alamethicin, the discrete conductance fluctuations betray the presence of barrel-stave pores, and not electropores. However, in the case of the toroidal pores thought to be formed by magainin-II and melittin, the fluctuations should be, and are, largely indistinguishable from electropores, at

least in their electrical behaviour. A toroidal pore supported by AMP molecules does not need to have its full circumference covered in peptide, as the lipid headgroups may form the majority of the defect. In this sense, the AMPs are simply stabilising the toroidal pore, rather than defining it. Since the electrical behaviour of these peptides did resemble that of electroporation, it raises the question as to whether the fluctuations were due to an AMP-mediated pore, or an electropore that was subsequently stabilised by peptide. The same question might be raised for alamethicin: at high peptide concentrations, no discrete steps were observed, suggesting pores of fluctuating, rather than well-defined radius. In this case the alamethicin could be thinning the membrane [187, 268], thus lowering the barrier to electropore formation.

Similarly, I–V curves for the lowest peptide concentrations show little change in the curve for the first (electrically silent) 100 mV when compared with the curves in the absence of the peptide. This linear portion implies that, like in pure electroporation, no pores are formed in the membrane. However, the rupture potential for these low concentrations (apart from indolicidin) is lower than that for pure electroporation (see Figure 5.6). It is likely that pore-forming peptides are able to associate with an electropore *once* it has formed. This would lead to a stabilisation of the pore [328], and perhaps encourage further association from other peptides, increasing the barrier to pore closure.

Indeed, it has been argued that membrane-active peptides that permeabilise membranes do so through mechanisms that all share the same energy landscape [328]. The starting point is identical to the physical formulation of electroporation (as laid out in Chapter 2): emergence of a pore in a membrane has an energy cost, proportional to the line tension and the radius, and at the same time there is a concomitant loss of surface tension energy, again proportional to the radius of the defect. Usually, the line tension dominates to close any transient pores of small radii generated stochastically. However, peptide association with the membrane may act to stabilise the pore rim and reduce the effective line tension [329]. Furthermore, adsorption of the peptide parallel to the bilayer causes thinning of the membrane

in some systems and an expansion in the membrane area, which in turn results in an increase in surface tension [4, 330]. This increase in surface energy is partially relieved when the peptides reorientate to associate with the pore walls. It is very possible that, despite differences in the means by which they are manipulated, altering the delicate balance between the line and surface tensions plays a major rôle in dictating pore formation in both AMP attack and electroporation.

5.4 Summary & Limitations

The experiments presented in this chapter demonstrate the utility of DIBs to study AMP-membrane interactions. The results indicate that membrane-bound AMPs suspected to operate by the formation of pores have enhanced densities around the locus of transmembrane conductive pores. Indolicidin, which is not believed to use pore formation as its primary mode of action, stabilised membranes against rupture and showed no enhancement of protein around the pore. Inspection of the single-molecule images also showed that these peptides readily cover the whole membrane, which has been implied in the literature, but seldom visualised in a dynamic system at the single-molecule level.

The ternary lipid system utilised in these experiments, whilst mimicking the anionic nature of bacterial membranes, is a simple one. AMP affinities and the way in which they interact with the membrane have both been shown to be composition-dependent, and bacterial membranes naturally vary in their composition. Nonetheless, these AMPs were found to behave in a manner consistent with bacterial and model membrane studies. The flexibility of the DIB system is such that increasing the complexity of the model membrane would be relatively simple. Mimicking the thick peptidoglycan layer of Gram-positive bacteria or the lipopolysaccharide-covered outer membrane of Gram-negative bacteria through which AMPs must pass would pose a greater challenge.

Optically, the current setup does not allow for constant monitoring of both the AMP molecules and the transmembrane pore. Whilst switching between laser excitation wavelengths could be performed quickly ($\sim$15 s), and electrical current

fluctuations indicative of an open pore (or pores) were maintained throughout the recordings, there was the chance that the pore in the region of interest could vanish. Closure of a pore during the single-molecule imaging would result in a false-negative when the RDF is analysed. A device such as an OptoSplit, which can simultaneously display on a single CCD the emitted light coming from the blue and green excitation channels side-by-side, would allow for simultaneous imaging.

A further limitation was the crossover between the Fluo-8H and TRITC emission spectra. Large pores resulted in a diffuse, SCCaFT-like signal appearing in the single-molecule channel, presumably due to excitation of Fluo-8H by the green laser. This was largely removed during the background subtraction procedure, after which it was usually easy to distinguish single molecules around the pore from SCCaFT bleed; the output of the spot detection process also went through a manual check to ensure that the correct signals were detected for RDF analysis. However there is a chance that without careful monitoring, false positives could be generated during the detection of labelled AMPs due to this decrease in signal-to-noise ratio, especially if such an analysis were to be conducted on a larger data set for which manual checks would render the process overly time-consuming. Using a dye at the red end of the spectrum, where the tail of Fluo-8H does not extend, would resolve this problem.

6 Conclusions & Further Work

This work has presented investigations into pore-forming processes in droplet-interface bilayers. Formed on hydrogel substrates, the ability to interrogate these membranes both electrically and optically has been utilised as a means to observe the formation of pores as generated by electric fields during the process of electroporation, and those that result from the interaction between antimicrobial peptides and the bilayer.

6.1 Electroporation in DIBs

6.1.1 The Electroporation Model

The work on electroporation presents the first known in-depth optical characterisation of individual pore behaviours within the ensemble of electropores generated by a transmembrane voltage. This is a significant step forward in the techniques available to study electroporation, as it allows the real-time imaging of small pores to be monitored. Using simultaneous oSCR and electrical recordings, both qualitative inferences and quantitative parameters could be derived. Parameters such as the diffusion coefficient for electropores have never been measured directly before. Analysis of the individual gating kinetics is also unique, for no study before this has been able to directly observe them.

The behaviour observed suggests that the curves for electroporation represent only a simplistic model of the process. For example, it appears that variations in the local surface tension and electric field are able to modulate pores in the vicinity: pores may respond to one another in an anticorrelated manner, and large pores can shrink defects elsewhere in the membrane. The way in which biological membranes dissipate or augment these local tensile or electrical stresses during electroporation is therefore of great interest if we are to further understand this phenomenon in vivo.

The simplicity of the electroporation model presented here is evident in several aspects. Firstly, it does not account for the complex properties of the bilayer, be it a model membrane or a real biological system. For example, incorporation of cholesterol into DPhPC BLMs was found to increase the electroporation onset potential due to improving lipid-lipid packing, but at high cholesterol contents, the onset potential decreased again, as cholesterol began to disrupt packing in the membrane once all the initial interstices had been filled [161]. Along with chain packing, the influence of headgroup interactions is similarly neglected. Charged headgroups would be expected to alter the interactions between the pore walls upon closure. (On this note, the value of the constant and the power in the $(\frac{C}{r})^4$ term in the electroporation equations, which represents the repulsion between the hydrophilic pore walls at small radii, were chosen to match the predictions made by Glaser *et al.* in the late 1980s, and have no real physical basis.) Higher proportions of charged lipids would likely increase the effective surface tension of the membrane by introducing in-plane repulsive interactions, and similarly increase the barrier to hydrophilic pore closure. Electroporation thresholds would therefore be expected to drop in highly charged membranes.

Charged headgroups also modify the electric field across the membrane. The interplay between the dielectric properties of headgroups, the differences in anion and cation concentrations either side of biological membranes, and the resulting nature of the electric double layer at the membrane surface all combine to result in a local electric field (the transmembrane potential) that exists even in the absence of an externally applied voltage [331]. This inherent transmembrane potential may

augment or counteract that of the applied voltage. Further, by the nature of the geometry of the curved walls of hydrophilic pores, lipid molecules at the apex of the curvature would have their headgroup dipoles orientated perpendicular to the applied electric field. The nature of those dipoles, dictated by the charged moieties within the headgroup, will dictate the interaction with the electric field and hence the forces on the pore walls. In the case of the intact membrane, whilst a headgroup dipole is not necessarily required for the generation of the initial water files that eventually lead to full electropores [164], once lipids begin to rearrange to form hydrophilic defects, the strength of the interaction between charged lipids and the electric field will have a bearing on the evolution of the pore [166, 167]. This is also true of the electrolyte that fills the pore: stabilising lipid-ion-lipid interactions, and the effect of these ions on the field within the pore are important considerations that are ignored in the transient aqueous pore hypothesis.

Given these omissions from the electroporation model, it is unsurprising then that its quantitative predictions are often only approximate ones. For example, plugging in standard physical parameters for lipid membranes predicts that the barrier to unbounded pore expansion E_c disappears at around 600–700 mV. Experimentally, this study found that voltage to be lower, around 250 mV. Further development of electroporation theory, in order to better match experimental observations quantitatively as well as qualitatively, will require the incorporation of the factors here mentioned.

6.1.2 Electroporation in Biological Membranes

In real membranes, bilayer complexity is far greater than most model membrane systems. Bilayers are inhomogeneous, asymmetric, charged, anchored or tethered, and contain a huge array of membrane proteins. The presence of cholesterol is known to influence electroporation. It may be reasonable to assume that lipids which associate with regions of high curvature by nature of their shape, such as singly-tailed lysolipids, may participate in hydrophilic pore formation. As has been shown in this work, electroporation also depends on lipid phase behaviour. In

biological membranes, lipid organisation could play a role in assisting or hindering pore expansion, as can the anchoring of the actin cortex [208]. It is possible that membrane proteins could also have the similar influences. Moreover, could these membrane species act as points of nucleation for electropores?

The droplet-interface bilayer platform does however lend the flexibility to study some of these influences. Very many lipid species can be incorporated into the membrane, either as better biological mimics, or to test the effect of a single parameter on the electroporation outcome. For example, the introduction of lysolipids into bilayers might be expected to lower the electroporation barriers, since their conical structure would promote the curvature of the membrane required to form toroidal pores. Similarly, systematic variation of the surrounding electrolytes is easily undertaken in DIBs. Whilst transmembrane proteins can be difficult to reconstitute into DIBs (often they must be stabilised in solution by detergent, which solubilises the membrane), the super-hydrated bilayers formed in Chapter 4 might be useful in the incorporation of transmembrane proteins, in providing a space beneath the bilayer in which the cytoplasmic domains could reside. Alternatively, in normally-hydrated DIBs (with a water cushion on the order of nanometres) these cytoplasmic domains would protrude through the bilayer and stick to the agarose substrate; this could be useful for mimicking pinning sites such as those of the cytoskeleton.

One question raised within this work is the importance of the bilayer surface tension, and how it might vary in the presence of electropores: coupling of local surface tensions might be the reason for the anticorrelated oSCR intensities observed for neighbouring pores, and for the large variation in radius fluctuation behaviours. The ability to mechanically manipulate a DIB through the electrode in the droplet might be a way to investigate this. Upon formation of electropores within the membrane, as visualised by oSCR, the electrode could be raised so as to shrink the bilayer until a single pore remained. In this case, if the fluctuations in pore radius were being modulated or augmented by adjacent defects, these perturbations would be removed and it might be expected that the pore radius fluctuations become more stable. Similarly, applying pressure on the top of the droplet would

be expected to reduce the membrane surface tension, as has been shown in the activation of the mechanosensitive channel MscL in droplet-droplet bilayers [67]. The ability to modulate the surface tension of DIBs whilst observing the effect on electropores by oSCR should aid in elucidating how dynamic changes in this parameter affect pore formation.

6.2 AMP Interactions with DIBs

Although the work on antimicrobial peptides is preliminary, it demonstrates the applicability of oSCR to the study of protein-mediated pores. The ability to localise both a pore and the peptides that generate it is a powerful tool, and one not yet reported elsewhere in the literature. To further this work, distinguishing between the toroidal and barrel-stave mechanisms may be facilitated by exploiting the fact the toroidal wall bridges the two membrane leaflets: translocation from one environment to another could be used to modulate a signal. For example, a lipid bearing a reactive moiety on the headgroup could translocate into a droplet containing a dye of complimentary reactivity, thus localising it to the bilayer. Alternatively the dye could be conjugated directly to the headgroup and present at a self-quenching concentration (or be in the presence of a quencher) that is relieved as the lipid moves to the opposite leaflet. Similar methods may allow indirect experimental evidence that the hydrophilic pores formed during electroporation are toroidal themselves.

oSCR can be further used to improve our understanding of AMP-mediated pore formation. For example, if a setup in which a large excess of calcium on one side of the bilayer is able diffuse through a transmembrane pore rather than be driven through it by a potential difference, this would allow the observation of AMP pore formation in the absence of a voltage. This is useful if we are to separate true AMP-generated pores from electropores simply stabilised by the peptides. In addition, oSCR and single-molecule imaging might be used to investigate AMP stoichiometry. The concentration of labelled peptides in the work presented in Chapter 5 was chosen to give resolvable, isolated spots. The ratio of labelled to unlabelled peptide was therefore around 1:250 for alamethicin. Increasing the

proportion of labelled protein might allow the number of alamethicin monomers within a pore to be deduced by counting the photobleaching steps within a single diffraction-limited spot, a technique that has been used previously in DIBs to determine the stoichiometry of heptameric transmembrane pores [332].

6.3 Closing Remarks

Understanding the cell membrane is a challenging task. It is a nanoscale environment of great complexity in its composition, geometry, and interactions with its surroundings. The aims of this thesis were to investigate the disruption of this vital cellular barrier. In doing so, the first steps were made in understanding electroporation in a relatively new model membrane system, droplet-interface bilayers. It is hoped that DIBs will continue to be used as an effective biomimetic platform for studying this often-used process, and the factors that govern it. Better understanding and modelling of electroporation will undoubtedly lead to more effective use of the phenomenon, especially in the context of its medical and therapeutic applications.

In addition, peptide-mediated pores were studied, with DIBs showing promising scope for probing membrane-AMP interactions in the future. Understanding the mechanisms of AMP pore formation is a fruitful goal. They have persisted through evolution, being found in the most basic to the most complex organisms, and have developed to target and disrupt specific cell membranes, especially those of bacteria. Learning from these naturally occurring peptides and designing *de novo* sequences that exploit their capabilities is a worthwhile pursuit; in an age where widespread antibiotic resistance becomes an increasing threat, new methods of keeping bacteria at bay will soon be needed.

To these ends, and many others, attempts to understand the cell membrane shall certainly continue apace.

Appendices

A
Publications

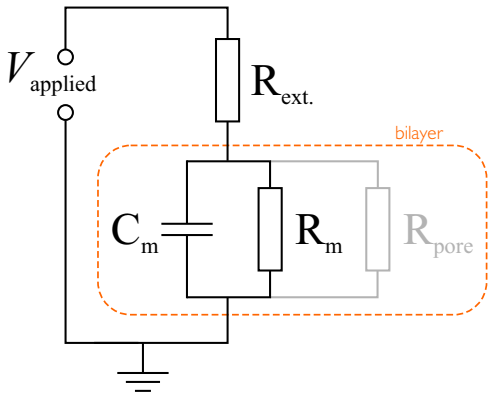
[1] Sengel, J.T. & Wallace, M.I. Imaging the dynamics of individual electropores. *Proc. Natl. Acad. Sci. U.S.A.* 113 (19). 2016.

[2] Sengel, J.T. & Wallace, M.I. Measuring the potential energy barrier to lipid bilayer electroporation. *Phil. Trans. R. Soc. B.* 372 (1726). 2017.

[3] Jones J.E., Diemer V., Adam C., Raftery J., Ruscoe R.E., Sengel J.T., Wallace M.I., Bader A., Cockroft S.L., Clayden J., Webb S.J. Length-dependent formation of transmembrane pores by 3_{10}-helical α-aminoisobutyric acid foldamers. *J. Am. Chem. Soc.* 138 (2). 2016.

B

Modelling Membrane Voltage Drop



The electrical properties of a lipid bilayer may be simply modelled by capacitor C_{m} in parallel with the (intact) membrane resistance, R_{m}. Transmembrane pores contribute as resistance R_{pore}. To complete the circuit description, $R_{\mathrm{ext.}}$ represents the resistance of the solution and the electrodes in the measurement circuit.

The total voltage in the model circuit will be:

$$V_{\mathrm{applied}} = V_{\mathrm{ext.}} + V_{\mathrm{bilayer}} \tag{B.1}$$

that is, the sum of the voltages across the measurement circuitry and bilayer respectively. Assuming V_{applied} is constant and that the capacitor is fully charged

(*i.e.* it is passing no current) the current will follow:

$$I = I_{\text{ext.}} = I_{\text{bilayer}}. \tag{B.2}$$

In other words, the current flowing through the measurement circuitry will be the same as that flowing across the bilayer. Applying Ohm's law to equation B.1, and noting the equivalence of the currents described by equation B.2,

$$\begin{aligned} V_{\text{applied}} &= I_{\text{ext.}} R_{\text{ext.}} + I_{\text{bilayer}} R_{\text{bilayer}} \\ &= I \cdot (R_{\text{ext.}} + R_{\text{bilayer}}) \end{aligned}$$

and rearranging:

$$I = \frac{V_{\text{applied}}}{R_{\text{ext.}} + R_{\text{bilayer}}}. \tag{B.3}$$

The voltage across the membrane is given by:

$$\begin{aligned} V_{\text{bilayer}} &= V_{\text{applied}} - V_{\text{ext.}} \\ &= V_{\text{applied}} - I R_{\text{ext.}}. \end{aligned}$$

Substituting in equation B.3:

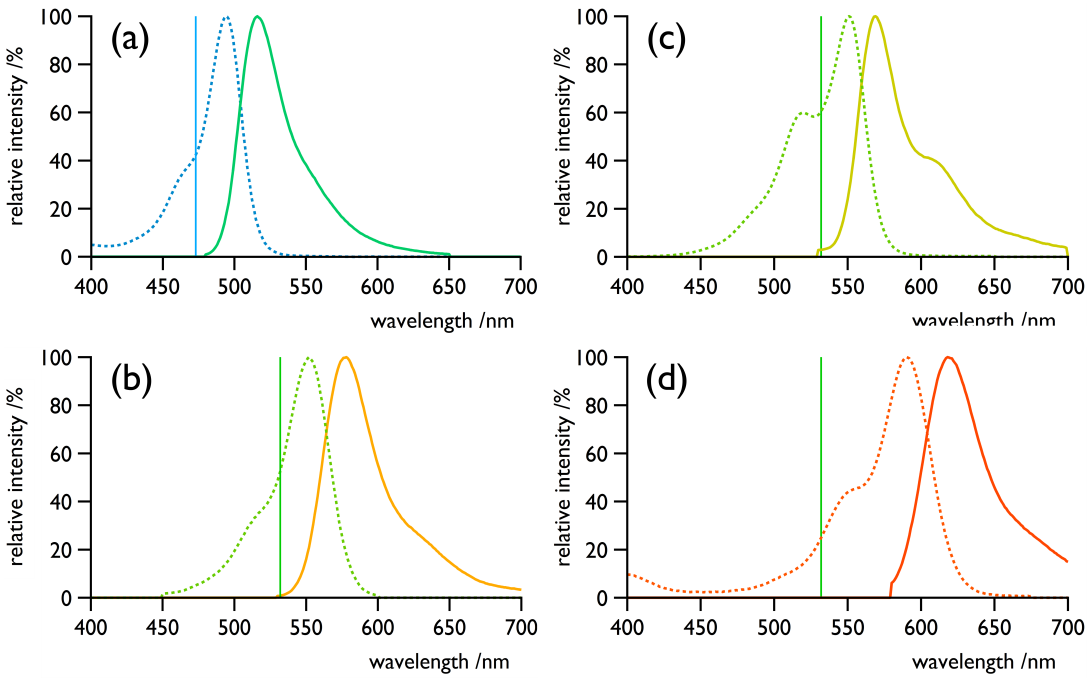
$$\begin{aligned} V_{\text{bilayer}} &= V_{\text{applied}} - \frac{V_{\text{applied}}}{R_{\text{ext.}} + R_{\text{bilayer}}} \cdot R_{\text{ext.}} \\ &= V_{\text{applied}}\left(1 - \frac{R_{\text{ext.}}}{R_{\text{ext.}} + R_{\text{bilayer}}}\right) \\ &= V_{\text{applied}}\left(\frac{R_{\text{bilayer}}}{R_{\text{ext.}} + R_{\text{bilayer}}}\right) \\ &= \frac{V_{\text{applied}}}{1 + R_{\text{ext.}}/R_{\text{bilayer}}}. \end{aligned} \tag{B.4}$$

Note that R_{bilayer} is the combined (parallel) resistance of the membrane and any transmembrane pores:

$$\frac{1}{R_{\text{bilayer}}} = \frac{1}{R_{\text{m}}} + \frac{1}{R_{\text{pore}}}.$$

However, since the membrane resistance is of the order of 1–100 GΩ, $R_{\text{bilayer}} \simeq R_{\text{pore}}$, and so the pore resistance R_{pore} may be used instead of R_{bilayer} in equation B.4. (Equation B.4 may be more quickly arrived at by simply noting that $R_{\text{ext.}}$ and R_{bilayer} form a voltage divider.)

C
Spectra



Excitation (*dotted lines*) and emission (*solid lines*) spectra for the fluorescent dyes used in this work. The vertical lines represent the excitation wavelengths of the blue (λ = 473 nm) and green (λ = 532 nm) lasers. (a) Fluo-8H. (b) TRITC (tetramethylrhodamine isothiocyanate). (c) DiI (1,1'-dioctadecyl-3,3,3',3'-tetramethylindocarbocyanine iodide). (d) Atto590.

Source: *Fluorescence SpectraViewer, www.thermofisher.com*

References

[1] K. V. R. Reddy, R. D. Yedery, and C. Aranha. "Antimicrobial peptides: premises and promises". *International Journal of Antimicrobial Agents* 24.6 (2004), pp. 536–547.

[2] Kim A. Brogden. "Antimicrobial peptides: pore formers or metabolic inhibitors in bacteria?" *Nature Reviews Microbiology* 3.3 (2005), pp. 238–250.

[3] Michael R. Yeaman and Nannette Y. Yount. "Mechanisms of Antimicrobial Peptide Action and Resistance". *Pharmacological Reviews* 55.1 (2003), pp. 27–55.

[4] Hiromi Sato and Jimmy B. Feix. "Peptide-membrane interactions and mechanisms of membrane destruction by amphipathic α-helical antimicrobial peptides". *Biochimica et Biophysica Acta (BBA) - Biomembranes* 1758.9 (2006), pp. 1245–1256.

[5] Vitor Teixeira, Maria J. Feio, and Margarida Bastos. "Role of lipids in the interaction of antimicrobial peptides with membranes". *Progress in Lipid Research* 51.2 (2012), pp. 149–177.

[6] Leonard T. Nguyen, Evan F. Haney, and Hans J. Vogel. "The expanding scope of antimicrobial peptide structures and their modes of action". *Trends in Biotechnology* 29.9 (2011), pp. 464–472.

[7] Leentje Moerman et al. "Antibacterial and antifungal properties of α-helical, cationic peptides in the venom of scorpions from southern Africa". *European Journal of Biochemistry* 269.19 (2002), pp. 4799–4810.

[8] Marc-Antoine Sani and Frances Separovic. "How Membrane-Active Peptides Get into Lipid Membranes". *Accounts of Chemical Research* 49.6 (2016), pp. 1130–1138.

[9] M Zasloff. "Magainins, a class of antimicrobial peptides from Xenopus skin: isolation, characterization of two active forms, and partial cDNA sequence of a precursor." *Proceedings of the National Academy of Sciences of the United States of America* 84.15 (1987), pp. 5449–5453.

[10] M. Simmaco, G. Mignogna, and D. Barra. "Antimicrobial peptides from amphibian skin: what do they tell us?" *Biopolymers* 47.6 (1998), pp. 435–450.

[11] Sascha Martens and Harvey T. McMahon. "Mechanisms of membrane fusion: disparate players and common principles". *Nature Reviews Molecular Cell Biology* 9.7 (2008), pp. 543–556.

[12] James E. Rothman. "Mechanisms of intracellular protein transport". *Nature* 372.6501 (1994), pp. 55–63.

[13] Nina Vardjan, Jernej Jorgačevski, and Robert Zorec. "Fusion Pores, SNAREs, and Exocytosis". *The Neuroscientist* 19.2 (2013), pp. 160–174.

[14] Oliver F. Brandenberg et al. “The HIV-1 Entry Process: A Stoichiometric View”. *Trends in Microbiology* 23.12 (2015), pp. 763–774.

[15] Sarah A. Connolly et al. “Fusing structure and function: a structural view of the herpesvirus entry machinery”. *Nature Reviews Microbiology* 9.5 (2011), pp. 369–381.

[16] Thomas C. Südhof. “The Synaptic Vesicle Cycle”. *Annual Review of Neuroscience* 27 (2004), pp. 509–547.

[17] William Wickner and Randy Schekman. “Membrane fusion”. *Nature Structural & Molecular Biology* 15.n7 (2008), pp. 658–664.

[18] Chong Liu et al. “Static Electricity Powered Copper Oxide Nanowire Microbicidal Electroporation for Water Disinfection”. *Nano Letters* 14.10 (2014), pp. 5603–5608.

[19] Alexander Golberg et al. “Pulsed Electric Fields for Burn Wound Disinfection in a Murine Model”. *Journal of Burn Care & Research* 36.1 (2015), pp. 7–13.

[20] Samo Mahnič-Kalamiza, Eugène Vorobiev, and Damijan Miklavčič. “Electroporation in Food Processing and Biorefinery”. *The Journal of Membrane Biology* 247.12 (2014), pp. 1279–1304.

[21] Chunlan Jiang, Rafael V. Davalos, and John C. Bischof. “A review of basic to clinical studies of irreversible electroporation therapy”. *IEEE Transactions on Biomedical Engineering* 62.1 (2015), pp. 4–20.

[22] E Neumann et al. “Gene transfer into mouse lyoma cells by electroporation in high electric fields.” *The EMBO Journal* 1.7 (1982), pp. 841–845.

[23] William J. Dower, Jeff F. Miller, and Charles W. Ragsdale. “High efficiency transformation of E. coli by high voltage electroporation”. *Nucleic Acids Research* 16.13 (1988), pp. 6127–6145.

[24] Anita Gothelf and Julie Gehl. “What you always needed to know about electroporation based DNA vaccines”. *Human Vaccines & Immunotherapeutics* 8.11 (2012), pp. 1694–1702.

[25] B. Mali et al. “Antitumor effectiveness of electrochemotherapy: a systematic review and meta-analysis”. *European Journal of Surgical Oncology* 39.1 (2013), pp. 4–16.

[26] Gerrit van Meer, Dennis R. Voelker, and Gerald W. Feigenson. “Membrane lipids: where they are and how they behave”. *Nature Reviews Molecular Cell Biology* 9.2 (2008), pp. 112–124.

[27] Christian Sohlenkamp and Otto Geiger. “Bacterial membrane lipids: diversity in structures and pathways”. *FEMS Microbiology Reviews* 40.1 (2016), pp. 133–159.

[28] Georg Pabst et al. “Rigidification of Neutral Lipid Bilayers in the Presence of Salts”. *Biophysical Journal* 93.8 (2007), pp. 2688–2696.

[29] Stephanie Tristram-Nagle et al. “Structure and Water Permeability of Fully Hydrated DiphytanoylPC”. *Chemistry and physics of lipids* 163.6 (2010), pp. 630–637.

[30] Peter H. Raven and George B. Johnson. *Biology*. 2nd Edition. Missouri: Times Mirror/Mosby College Publishing, 1989.

[31] Volker Endeward et al. “How does carbon dioxide permeate cell membranes? A discussion of concepts, results and methods”. *Frontiers in Physiology* 4 (2014).

[32] Jeremy M. Berg, John L. Tymoczko, and Lubert Stryer. *Biochemistry*. 6th Edition. New York: W.H. Freeman & Company, 2007.

[33] Erich Sackmann. “Biological Membranes - Architecture and Function”. *Structure and Dynamics of Membranes - From Cells to Vesicles*. Ed. by R Lipkowski, Erich Sackmann, and A. J. Hoff. Vol. 1. Elsevier Press, 1995.

[34] G. Vereb et al. “Dynamic, yet structured: The cell membrane three decades after the Singer–Nicolson model”. *Proceedings of the National Academy of Sciences* 100.14 (2003), pp. 8053–8058.

[35] Arthur Laganowsky et al. “Membrane proteins bind lipids selectively to modulate their structure and function”. *Nature* 510.7503 (2014), pp. 172–175.

[36] Saziye Yorulmaz et al. “Influence of membrane surface charge on adsorption of complement proteins onto supported lipid bilayers”. *Colloids and Surfaces B: Biointerfaces* 148 (2016), pp. 270–277.

[37] Allen G. Marr and John L. Ingraham. “Effect of Temperature on the Composition of Fatty Acids in Escherichia Coli”. *Journal of Bacteriology* 84.6 (1962), pp. 1260–1267.

[38] M. G. Kleinschmidt and Vern A. McMahon. “Effect of Growth Temperature on the Lipid Composition of Cyanidium caldarium. I. Class Separation of Lipids”. *Plant Physiology* 46.2 (1970), pp. 286–289.

[39] Ruthven N. A. H. Lewis and Ronald N. McElhaney. “Membrane lipid phase transitions and phase organization studied by Fourier transform infrared spectroscopy”. *Biochimica et Biophysica Acta (BBA) - Biomembranes* 1828.10 (2013), pp. 2347–2358.

[40] D Needham and R S Nunn. “Elastic deformation and failure of lipid bilayer membranes containing cholesterol.” *Biophysical Journal* 58.4 (1990), pp. 997–1009.

[41] Henna Ohvo-Rekilä et al. “Cholesterol interactions with phospholipids in membranes”. *Progress in Lipid Research* 41.1 (2002), pp. 66–97.

[42] Linda J. Pike. “Lipid rafts bringing order to chaos”. *Journal of Lipid Research* 44.4 (2003), pp. 655–667.

[43] Daniel Lingwood and Kai Simons. “Lipid Rafts As a Membrane-Organizing Principle”. *Science* 327.5961 (2010), pp. 46–50.

[44] Michael F. Brown. “Curvature Forces in Membrane Lipid-Protein Interactions”. *Biochemistry* 51.49 (2012), pp. 9782–9795.

[45] Todd P. Silverstein. “The Real Reason Why Oil and Water Don’t Mix”. *Journal of Chemical Education* 75.1 (1998), p. 116.

[46] H. Lindsey, N. O. Petersen, and Sunney I. Chan. “Physicochemical characterization of 1,2-diphytanoyl-sn-glycero-3-phosphocholine in model membrane systems”. *Biochimica et Biophysica Acta (BBA) - Biomembranes* 555.1 (1979), pp. 147–167.

[47] Martin Andersson et al. “Vesicle and bilayer formation of diphytanoyl phosphatidylcholine (DPhPC) and diphytanoyl phosphatidylethanolamine (DPhPE) mixtures and their bilayers’ electrical stability”. *Colloids and Surfaces B: Biointerfaces* 82.2 (2011), pp. 550–561.

[48] Peter J. Milianta et al. “Water Permeability across Symmetric and Asymmetric Droplet Interface Bilayers: Interaction of Cholesterol Sulfate with DPhPC”. *Langmuir* 31.44 (2015), pp. 12187–12196.

[49] Antonio Alcaraz et al. “Salting Out the Ionic Selectivity of a Wide Channel: The Asymmetry of OmpF”. *Biophysical Journal* 87.2 (2004), pp. 943–957.

[50] Gintaras Valincius et al. “Soluble Amyloid beta-Oligomers Affect Dielectric Membrane Properties by Bilayer Insertion and Domain Formation: Implications for Cell Toxicity”. *Biophysical Journal* 95.10 (2008), pp. 4845–4861.

[51] Raquel F. Epand, Paul B. Savage, and Richard M. Epand. “Bacterial lipid composition and the antimicrobial efficacy of cationic steroid compounds (Ceragenins)”. *Biochimica et Biophysica Acta (BBA) - Biomembranes* 1768.10 (2007), pp. 2500–2509.

[52] S. Lopes et al. “Cardiolipin, a key component to mimic the E. coli bacterial membrane in model systems revealed by dynamic light scattering and steady-state fluorescence anisotropy”. *Analytical and Bioanalytical Chemistry* 398.3 (2010), pp. 1357–1366.

[53] M. Montal and P. Mueller. “Formation of Bimolecular Membranes from Lipid Monolayers and a Study of Their Electrical Properties”. *Proceedings of the National Academy of Sciences of the United States of America* 69.12 (1972), pp. 3561–3566.

[54] Mathias Winterhalter. “Black lipid membranes”. *Current Opinion in Colloid & Interface Science* 5.3–4 (2000), pp. 250–255.

[55] Isaac Newton. *Opticks: Or, a Treatise of the Reflexions, Refractions, Inflexions and Colours of Light*. The Prince’s Arms, St. Paul’s Churchyard, London: Royal Society, 1704.

[56] Günther Boheim et al. “Agonist-Activated Ionic Channels in Acetylcholine Receptor Reconstituted into Planar Lipid Bilayers”. *Proceedings of the National Academy of Sciences of the United States of America* 78.6 (1981), pp. 3586–3590.

[57] I. G. Abidor et al. “Electric breakdown of bilayer lipid membranes: 1. The main experimental facts and their qualitative discussion”. *Journal of Electroanalytical Chemistry and Interfacial Electrochemistry* 104 (1979), pp. 37–52.

[58] Edward T. Castellana and Paul S. Cremer. “Solid supported lipid bilayers: From biophysical studies to sensor design”. *Surface Science Reports* 61.10 (2006), pp. 429–444.

[59] Motomu Tanaka and Erich Sackmann. “Polymer-supported membranes as models of the cell surface”. *Nature* 437.7059 (2005), pp. 656–663.

[60] Yee-Hung M Chan and Steven G Boxer. “Model membrane systems and their applications”. *Current Opinion in Chemical Biology* 11.6 (2007), pp. 581–587.

[61] Susanne F. Fenz and Kheya Sengupta. “Giant vesicles as cell models”. *Integrative Biology* 4.9 (2012), pp. 982–995.

[62] Karin A. Riske and Rumiana Dimova. “Electro-Deformation and Poration of Giant Vesicles Viewed with High Temporal Resolution”. *Biophysical Journal* 88.2 (2005), pp. 1143–1155.

[63] Sharon L. Schendel et al. “Channel formation by antiapoptotic protein Bcl-2”. *Proceedings of the National Academy of Sciences of the United States of America* 94.10 (1997), pp. 5113–5118.

[64] Hagan Bayley et al. “Droplet interface bilayers”. *Molecular BioSystems* 4.12 (2008), pp. 1191–1208.

[65] Matthew A. Holden, David Needham, and Hagan Bayley. “Functional Bionetworks from Nanoliter Water Droplets”. *Journal of the American Chemical Society* 129.27 (2007), pp. 8650–8655.

[66] Gabriel Villar, Alexander D. Graham, and Hagan Bayley. “A Tissue-Like Printed Material”. *Science* 340.6128 (2013), pp. 48–52.

[67] Joseph S. Najem et al. “Activation of bacterial channel MscL in mechanically stimulated droplet interface bilayers”. *Scientific Reports* 5 (2015), p. 13726.

[68] Gabrielle de Wit et al. “Dynamic label-free imaging of lipid nanodomains”. *Proceedings of the National Academy of Sciences of the United States of America* 112.40 (2015), pp. 12299–12303.

[69] Shuo Huang et al. “High-throughput optical sensing of nucleic acids in a nanopore array”. *Nature Nanotechnology* 10.11 (2015), pp. 986–991.

[70] D. P Tieleman, S. J Marrink, and H. J. C Berendsen. “A computer perspective of membranes: molecular dynamics studies of lipid bilayer systems”. *Biochimica et Biophysica Acta (BBA) - Reviews on Biomembranes* 1331.3 (1997), pp. 235–270.

[71] Peter J. Bond et al. “Coarse-grained molecular dynamics simulations of membrane proteins and peptides”. *Journal of Structural Biology* 157.3 (2007), pp. 593–605.

[72] Kristyna Pluhackova and Rainer A. Böckmann. “Biomembranes in atomistic and coarse-grained simulations”. *Journal of Physics: Condensed Matter* 27.32 (2015), p. 323103.

[73] Helmut Heller, Michael Schaefer, and Klaus Schulten. “Molecular dynamics simulation of a bilayer of 200 lipids in the gel and in the liquid crystal phase”. *The Journal of Physical Chemistry* 97.31 (1993), pp. 8343–8360.

[74] Erik Lindahl and Mark SP Sansom. “Membrane proteins: molecular dynamics simulations”. *Current Opinion in Structural Biology* 18.4 (2008), pp. 425–431.

[75] Ron O. Dror et al. “Biomolecular Simulation: A Computational Microscope for Molecular Biology”. *Annual Review of Biophysics* 41.1 (2012), pp. 429–452.

[76] Maura Casciola et al. “Properties of lipid electropores I: Molecular dynamics simulations of stabilized pores by constant charge imbalance”. *Bioelectrochemistry* 109 (2016), pp. 108–116.

[77] D. Peter Tieleman. “The molecular basis of electroporation”. *BMC Biochemistry* 5.1 (2004), pp. 1–12.

[78] Hari Leontiadou, Alan E. Mark, and Siewert J. Marrink. “Antimicrobial Peptides in Action”. *Journal of the American Chemical Society* 128.37 (2006), pp. 12156–12161.

[79] W. F. Drew Bennett et al. “Antimicrobial Peptide Simulations and the Influence of Force Field on the Free Energy for Pore Formation in Lipid Bilayers”. *Journal of Chemical Theory and Computation* 12.9 (2016), pp. 4524–4533.

[80] O. H. Samuli Ollila and Georg Pabst. “Atomistic resolution structure and dynamics of lipid bilayers in simulations and experiments”. *Biochimica et Biophysica Acta (BBA) - Biomembranes* 1858.10 (2016), pp. 2512–2528.

[81] Kristyna Pluhackova et al. “A Critical Comparison of Biomembrane Force Fields: Structure and Dynamics of Model DMPC, POPC, and POPE Bilayers”. *The Journal of Physical Chemistry B* 120.16 (2016), pp. 3888–3903.

[82] Masao Yafuso, Stephen J. Kennedy, and Alan R. Freeman. “Spontaneous conductance changes, multilevel conductance states and negative differential resistance in oxidized cholesterol black lipid membranes”. *The Journal of Membrane Biology* 17.1 (1974), pp. 201–212.

[83] J. A. Nollet. *Recherches sur les causes particulieres des phenomenes electriques.* Paris: H. L. Guerin & L. F. Delatour, 1754.

[84] George Warren Fuller. *Report on the investigations into the purification of the Ohio river water at Louisville Kentucky.* New York: D. Van Nostrand Company, 1898.

[85] R. Stämpfli and M. Willi. “Membrane potential of a ranvier node measured after electrical destruction of its membrane”. *Experientia* 13.7 (1957), pp. 297–298.

[86] A. J. H. Sale and W. A. Hamilton. “Effects of high electric fields on microorganisms”. *Biochimica et Biophysica Acta (BBA) - General Subjects* 148.3 (1967), pp. 781–788.

[87] Eberhard Neumann and Kurt Rosenheck. “Permeability changes induced by electric impulses in vesicular membranes”. *The Journal of Membrane Biology* 10.1 (1972), pp. 279–290.

[88] F. André and L. M. Mir. “DNA electrotransfer: its principles and an updated review of its therapeutic applications”. *Gene Therapy* 11.S1 (2004), S33–S42.

[89] G. Küppers and U. Zimmermann. “Cell fusion by spark discharge and its relevance for evolutionary processes”. *FEBS Letters* 164.2 (1983), pp. 323–329.

[90] Sandrine Demanèche et al. “Laboratory-Scale Evidence for Lightning-Mediated Gene Transfer in Soil”. *Applied and Environmental Microbiology* 67.8 (2001), pp. 3440–3444.

[91] Antoni Ivorra and Boris Rubinsky. “Historical Review of Irreversible Electroporation in Medicine”. *Irreversible Electroporation.* 1st Edition. Berlin-Heidelberg: Springer, 2010.

[92] James C. Weaver and Yu. A. Chizmadzhev. “Theory of electroporation: A review”. *Bioelectrochemistry and Bioenergetics* 41.2 (1996), pp. 135–160.

[93] V. F. Pastushenko, Yu. A. Chizmadzhev, and V. B. Arakelyan. “Electric breakdown of bilayer lipid membranes: 2. Calculation of the membrane lifetime in the steady-state diffusion approximation”. *Journal of Electroanalytical Chemistry and Interfacial Electrochemistry* 104 (1979), pp. 53–62.

[94] Yu. A. Chizmadzhev, V. B. Arakelyan, and V. F. Pastushenko. “Electric breakdown of bilayer lipid membranes: 3. Analysis of possible mechanisms of defect origination”. *Bioelectrochemistry and Bioenergetics* 6.1 (1979), pp. 63–70.

[95] V. F. Pastushenko, Yu. A. Chizmadzhev, and V. B. Arakelyan. “Electric breakdown of bilayer lipid membranes: 4. Consideration of the kinetic stage in the case of the single-defect membrane”. *Bioelectrochemistry and Bioenergetics* 6.1 (1979), pp. 71–79.

[96] V. B. Arakelyan, Yu. A. Chizmadzhev, and V. F. Pastushenko. “Electric breakdown of bilayer lipid membranes: 5. Consideration of the kinetic stage in the case of the membrane containing an arbitrary number of defects”. *Bioelectrochemistry and Bioenergetics* 6.1 (1979), pp. 81–87.

[97] V. F. Pastushenko, V. B. Arakelyan, and Yu. A. Chizmadzhev. “Electric breakdown of bilayer lipid membranes: 6. A stochastic theory taking into account the processes of defect formation and death: Membrane lifetime distribution function”. *Bioelectrochemistry and Bioenergetics* 6.1 (1979), pp. 89–95.

[98] V. F. Pastushenko, V. B. Arakelyan, and Yu. A. Chizmadzhev. “Electric breakdown of bilayer lipid membranes: 7. A stochastic theory taking into account the processes of defect formation and death: Statistical properties”. *Bioelectrochemistry and Bioenergetics* 6.1 (1979), pp. 97–104.

[99] J. M. Crowley. “Electrical Breakdown of Bimolecular Lipid Membranes as an Electromechanical Instability”. *Biophysical Journal* 13.7 (1973), pp. 711–724.

[100] D. S. Dimitrov. “Electric field-induced breakdown of lipid bilayers and cell membranes: A thin viscoelastic film model”. *The Journal of Membrane Biology* 78.1 (1984), pp. 53–60.

[101] J. C. Weaver. “Electroporation of biological membranes from multicellular to nano scales”. *IEEE Transactions on Dielectrics and Electrical Insulation* 10.5 (2003), pp. 754–768.

[102] R. Benz and K. Janko. “Voltage-induced capacitance relaxation of lipid bilayer membranes Effects of membrane composition”. *Biochimica et Biophysica Acta (BBA) - Biomembranes* 455.3 (1976), pp. 721–738.

[103] O Alvarez and R Latorre. “Voltage-dependent capacitance in lipid bilayers made from monolayers.” *Biophysical Journal* 21.1 (1978), pp. 1–17.

[104] Peter Atkins and Julio de Paula. *Atkins’ Physical Chemistry*. 7th. Oxford: Oxford University Press, 2002.

[105] R. Benz, F. Beckers, and U. Zimmermann. “Reversible electrical breakdown of lipid bilayer membranes: A charge-pulse relaxation study”. *The Journal of Membrane Biology* 48.2 (1979), pp. 181–204.

[106] Adrian Parsegian. “Energy of an Ion crossing a Low Dielectric Membrane: Solutions to Four Relevant Electrostatic Problems”. *Nature* 221.5183 (1969), pp. 844–846.

[107] Ilja V. Khavrutskii et al. “Free Energy for the Permeation of Na^+ and Cl^- Ions and Their Ion-Pair through a Zwitterionic Dimyristoyl Phosphatidylcholine Lipid Bilayer by Umbrella Integration with Harmonic Fourier Beads”. *Journal of the American Chemical Society* 131.5 (2009), pp. 1706–1716.

[108] P. G. Saffman and M. Delbrück. “Brownian motion in biological membranes”. *Proceedings of the National Academy of Sciences* 72.8 (1975), pp. 3111–3113.

[109] John C. Neu and Wanda Krassowska. “Asymptotic model of electroporation”. *Physical Review E* 59.3 (1999), pp. 3471–3482.

[110] Ralf W. Glaser et al. “Reversible electrical breakdown of lipid bilayers: formation and evolution of pores”. *Biochimica et Biophysica Acta (BBA) - Biomembranes* 940.2 (1988), pp. 275–287.

[111] W. F. Drew Bennett, Nicolas Sapay, and D. Peter Tieleman. “Atomistic Simulations of Pore Formation and Closure in Lipid Bilayers”. *Biophysical Journal* 106.1 (2014), pp. 210–219.

[112] S. Haberl et al. “Cell membrane electroporation - Part 2: the applications”. *IEEE Electrical Insulation Magazine* 29.1 (2013), pp. 29–37.

[113] Martin L. Yarmush et al. “Electroporation-based technologies for medicine: principles, applications, and challenges”. *Annual Review of Biomedical Engineering* 16 (2014), pp. 295–320.

[114] Kyle C. Smith, John C. Neu, and Wanda Krassowska. “Model of Creation and Evolution of Stable Electropores for DNA Delivery”. *Biophysical Journal* 86.5 (2004), pp. 2813–2826.

[115] T. Kotnik et al. “Cell membrane electroporation - Part 1: The phenomenon”. *IEEE Electrical Insulation Magazine* 28.5 (2012), pp. 14–23.

[116] G. Sersa et al. “Electrochemotherapy in treatment of tumours”. *European Journal of Surgical Oncology* 34.2 (2008), pp. 232–240.

[117] Sarah Buchan et al. “Electroporation as a “Prime/Boost” Strategy for Naked DNA Vaccination against a Tumor Antigen”. *The Journal of Immunology* 174.10 (2005), pp. 6292–6298.

[118] Alexander Golberg and Martin L. Yarmush. “Nonthermal irreversible electroporation: fundamentals, applications, and challenges”. *IEEE transactions on bio-medical engineering* 60.3 (2013), pp. 707–714.

[119] Riccardo Lencioni, Laura Crocetti, and Govindarajan Narayanan. “Irreversible Electroporation in the Treatment of Hepatocellular Carcinoma”. *Techniques in Vascular and Interventional Radiology* 18.3 (2015), pp. 135–139.

[120] F. Ting et al. “Focal irreversible electroporation for prostate cancer: functional outcomes and short-term oncological control”. *Prostate Cancer and Prostatic Diseases* 19.1 (2016), pp. 46–52.

[121] Rafael V. Davalos and Boris Rubinsky. “Temperature considerations during irreversible electroporation”. *International Journal of Heat and Mass Transfer* 51.23–24 (2008), pp. 5617–5622.

[122] Liel Rubinsky et al. “Electrolytic Effects During Tissue Ablation by Electroporation”. *Technology in Cancer Research & Treatment* 15.5 (2016), NP95–NP103.

[123] Katsutoshi Sugimoto et al. “Case study to assess the safety of irreversible electroporation near the heart”. *SpringerPlus* 4.1 (2015), p. 74.

[124] Patryk Kambakamba et al. “Intraoperative adverse events during irreversible electroporation - a call for caution”. *The American Journal of Surgery* 212.4 (2016), pp. 715–721.

[125] Katrina F. Chu and Damian E. Dupuy. “Thermal ablation of tumours: biological mechanisms and advances in therapy”. *Nature Reviews Cancer* 14.3 (2014), pp. 199–208.

[126] Mohammad Faroja et al. “Irreversible Electroporation Ablation: Is All the Damage Nonthermal?” *Radiology* 266.2 (2013), pp. 462–470.

[127] Rafael V. Davalos, Suyashree Bhonsle, and Robert E. Neal. “Implications and considerations of thermal effects when applying irreversible electroporation tissue ablation therapy”. *The Prostate* 75.10 (2015), pp. 1114–1118.

[128] Martin J. C. van Gemert et al. “Irreversible electroporation: Just another form of thermal therapy?” *The Prostate* 75.3 (2015), pp. 332–335.

[129] Alexander Golberg et al. “Preventing Scars after Injury with Partial Irreversible Electroporation”. *Journal of Investigative Dermatology* 136.11 (2016), pp. 2297–2304.

[130] M. Sack et al. “Research on Industrial-Scale Electroporation Devices Fostering the Extraction of Substances from Biological Tissue”. *Food Engineering Reviews* 2.2 (2010), pp. 147–156.

[131] M. Morales-de la Peña, P. Elez-Martínez, and O. Martín-Belloso. “Food Preservation by Pulsed Electric Fields: An Engineering Perspective”. *Food Engineering Reviews* 3.2 (2011), pp. 94–107.

[132] James C. Weaver et al. “A brief overview of electroporation pulse strength-duration space: A region where additional intracellular effects are expected”. *Bioelectrochemistry (Amsterdam, Netherlands)* 87 (2012), pp. 236–243.

[133] Gregory P. Walcott, Cheryl R. Killingsworth, and Raymond E. Ideker. “Do clinically relevant transthoracic defibrillation energies cause myocardial damage and dysfunction?” *Resuscitation* 59.1 (2003), pp. 59–70.

[134] Vadim V. Fedorov et al. “Atria are more susceptible to electroporation than ventricles: Implications for atrial stunning, shock-induced arrhythmia and defibrillation failure”. *Heart Rhythm* 5.4 (2008), pp. 593–604.

[135] Yves T. Wang, Igor R. Efimov, and Yuanna Cheng. “Electroporation induced by internal defibrillation shock with and without recovery in intact rabbit hearts”. *American Journal of Physiology - Heart and Circulatory Physiology* 303.4 (2012), H439–H449.

[136] Vladimir P. Nikolski and Igor R. Efimov. “Electroporation of the heart”. *Europace* 7.s2 (2005), S146–S154.

[137] Derek J. Dosdall, Vladimir G. Fast, and Raymond E. Ideker. “Mechanisms of defibrillation”. *Annual Review of Biomedical Engineering* 12 (2010), pp. 233–258.

[138] G. Saulis, M. S. Venslauskas, and J. Naktinis. “Kinetics of pore resealing in cell membranes after electroporation”. *Journal of Electroanalytical Chemistry and Interfacial Electrochemistry* 321.1 (1991), pp. 1–13.

[139] R. P. Joshi and K. H. Schoenbach. “Electroporation dynamics in biological cells subjected to ultrafast electrical pulses: a numerical simulation study”. *Physical Review. E, Statistical Physics, Plasmas, Fluids, and Related Interdisciplinary Topics* 62.1 Pt B (2000), pp. 1025–1033.

[140] Mounir Tarek. “Membrane electroporation: a molecular dynamics simulation”. *Biophysical Journal* 88.6 (2005), pp. 4045–4053.

[141] Sonja A. Kirsch and Rainer A. Böckmann. “Membrane pore formation in atomistic and coarse-grained simulations”. *Biochimica et Biophysica Acta (BBA) - Biomembranes* 1858.10 (2016), pp. 2266–2277.

[142] Bruno Gabriel and Justin Teissié. “Time Courses of Mammalian Cell Electropermeabilization Observed by Millisecond Imaging of Membrane Property Changes during the Pulse”. *Biophysical Journal* 76.4 (1999), pp. 2158–2165.

[143] Gintautas Saulis and Rita Saulė. “Size of the pores created by an electric pulse: Microsecond vs millisecond pulses”. *Biochimica et Biophysica Acta (BBA) - Biomembranes* 1818.12 (2012), pp. 3032–3039.

[144] D C Chang and T S Reese. “Changes in membrane structure induced by electroporation as revealed by rapid-freezing electron microscopy.” *Biophysical Journal* 58.1 (1990), pp. 1–12.

[145] Nicolas Rodriguez, Sophie Cribier, and Frédéric Pincet. “Transition from long- to short-lived transient pores in giant vesicles in an aqueous medium”. *Physical Review E* 74.6 (2006), p. 061902.

[146] Thomas Portet and Rumiana Dimova. “A new method for measuring edge tensions and stability of lipid bilayers: effect of membrane composition”. *Biophysical Journal* 99.10 (2010), pp. 3264–3273.

[147] Ryo Shirakashi et al. “Measurement of the permeability and resealing time constant of the electroporated mammalian cell membranes”. *International Journal of Heat and Mass Transfer* 47.21 (2004), pp. 4517–4524.

[148] Rafael B. Lira, Rumiana Dimova, and Karin A. Riske. “Giant unilamellar vesicles formed by hybrid films of agarose and lipids display altered mechanical properties”. *Biophysical Journal* 107.7 (2014), pp. 1609–1619.

[149] Zachary A. Levine and P. Thomas Vernier. “Life cycle of an electropore: field-dependent and field-independent steps in pore creation and annihilation”. *The Journal of Membrane Biology* 236.1 (2010), pp. 27–36.

[150] Catherine E. Morris. “Mechanosensitive ion channels”. *The Journal of Membrane Biology* 113.2 (1990), pp. 93–107.

[151] Michael J. Ackerman and David E. Clapham. “Ion Channels - Basic Science and Clinical Disease”. *New England Journal of Medicine* 336.22 (1997), pp. 1575–1586.

[152] Dan M. Roden et al. “Cardiac Ion Channels”. *Annual Review of Physiology* 64.1 (2002), pp. 431–475.

[153] Katherine L. Perkins. “Cell-attached voltage-clamp and current-clamp recording and stimulation techniques in brain slices”. *Journal of neuroscience methods* 154.1-2 (2006), pp. 1–18.

[154] Erwin Neher and Bert Sakmann. “Single-channel currents recorded from membrane of denervated frog muscle fibres”. *Nature* 260.5554 (1976), pp. 799–802.

[155] Ricardo A. Cruciani et al. “Magainin 2, a natural antibiotic from frog skin, forms ion channels in lipid bilayer membranes”. *European Journal of Pharmacology: Molecular Pharmacology* 226.4 (1992), pp. 287–296.

[156] Bert Sakmann and Erwin Neher, eds. *Single-Channel Recording*. 2nd Edition. New York: Plenum Press, 1995.

[157] Richard A. Levis and James L. Rae. “Constructing a patch clamp setup”. *Ion Channels*. Ed. by Bernardo Rudy and Linda Iverson. 1st Edition. Vol. 207. Academic Press, 1992, pp. 14–66.

[158] D Axelrod, T P Burghardt, and N L Thompson. “Total Internal Reflection Fluorescence”. *Annual Review of Biophysics and Bioengineering* 13.1 (1984), pp. 247–268.

[159] Joseph R. Lakowicz. *Principles of Fluorescence Spectroscopy*. 3rd Edition. New York: Springer, 2006.

[160] Kazuhiko Kinosita and Tian Yow Tsong. “Voltage-induced conductance in human erythrocyte membranes”. *Biochimica et Biophysica Acta (BBA) - Biomembranes* 554.2 (1979), pp. 479–497.

[161] Iris van Uitert, Séverine Le Gac, and Albert van den Berg. “The influence of different membrane components on the electrical stability of bilayer lipid membranes”. *Biochimica et Biophysica Acta (BBA) - Biomembranes* 1798.1 (2010), pp. 21–31.

[162] D Needham and R M Hochmuth. “Electro-mechanical permeabilization of lipid vesicles. Role of membrane tension and compressibility.” *Biophysical Journal* 55.5 (1989), pp. 1001–1009.

[163] James C. Weaver and Robert A. Mintzer. “Decreased bilayer stability due to transmembrane potentials”. *Physics Letters A* 86.1 (1981), pp. 57–59.

[164] Matthew J. Ziegler and P. Thomas Vernier. “Interface Water Dynamics and Porating Electric Fields for Phospholipid Bilayers”. *The Journal of Physical Chemistry B* 112.43 (2008), pp. 13588–13596.

[165] D. Peter Tieleman and Siewert-Jan Marrink. “Lipids Out of Equilibrium: Energetics of Desorption and Pore Mediated Flip-Flop”. *Journal of the American Chemical Society* 128.38 (2006), pp. 12462–12467.

[166] P. T. Vernier, Z. A. Levine, and M. A. Gundersen. “Water Bridges in Electropermeabilized Phospholipid Bilayers”. *Proceedings of the IEEE* 101.2 (2013), pp. 494–504.

[167] P. Thomas Vernier and Matthew J. Ziegler. “Nanosecond Field Alignment of Head Group and Water Dipoles in Electroporating Phospholipid Bilayers”. *The Journal of Physical Chemistry B* 111.45 (2007), pp. 12993–12996.

[168] R. Benz and U. Zimmermann. “Pulse-length dependence of the electrical breakdown in lipid bilayer membranes”. *Biochimica et Biophysica Acta (BBA) - Biomembranes* 597.3 (1980), pp. 637–642.

[169] P. Thomas Vernier, Yinghua Sun, and Martin A. Gundersen. “Nanoelectropulse-driven membrane perturbation and small molecule permeabilization”. *BMC Cell Biology* 7 (2006), p. 37.

[170] Andrei G. Pakhomov et al. “Membrane permeabilization and cell damage by ultrashort electric field shocks”. *Archives of Biochemistry and Biophysics* 465.1 (2007), pp. 109–118.

[171] P. Thomas Vernier et al. “Nanosecond electric pulse-induced calcium entry into chromaffin cells”. *Bioelectrochemistry* 73.1 (2008), pp. 1–4.

[172] Ming-Chak Ho et al. “Molecular Dynamics Simulations of Ion Conductance in Field-Stabilized Nanoscale Lipid Electropores”. *The Journal of Physical Chemistry B* 117.39 (2013), pp. 11633–11640.

[173] Vasil Dimitrov, Sergej Kakorin, and Eberhard Neumann. “Transient oscillation of shape and membrane conductivity changes by field pulse-induced electroporation in nano-sized phospholipid vesicles”. *Physical Chemistry Chemical Physics* 15.17 (2013), pp. 6303–6322.

[174] Lisa Brown et al. “Through the wall: extracellular vesicles in Gram-positive bacteria, mycobacteria and fungi”. *Nature Reviews Microbiology* 13.10 (2015), pp. 620–630.

[175] Thomas J. Piggot, Daniel A. Holdbrook, and Syma Khalid. “Electroporation of the E. coli and S. Aureus Membranes: Molecular Dynamics Simulations of Complex Bacterial Membranes”. *The Journal of Physical Chemistry B* 115.45 (2011), pp. 13381–13388.

[176] Linda C. M. Gross, Oliver K. Castell, and Mark I. Wallace. “Dynamic and Reversible Control of 2D Membrane Protein Concentration in a Droplet Interface Bilayer”. *Nano Letters* 11.8 (2011), pp. 3324–3328.

[177] Stanisława Koronkiewicz and Sławomir Kalinowski. “Influence of cholesterol on electroporation of bilayer lipid membranes: chronopotentiometric studies”. *Biochimica et Biophysica Acta (BBA) - Biomembranes* 1661.2 (2004), pp. 196–203.

[178] Malgorzata Kotulska. “Natural Fluctuations of an Electropore Show Fractional Lévy Stable Motion”. *Biophysical Journal* 92.7 (2007), pp. 2412–2421.

[179] R. Benz and U. Zimmermann. “Relaxation studies on cell membranes and lipid bilayers in the high electric field range”. *Journal of Electroanalytical Chemistry and Interfacial Electrochemistry* 116 (1980), pp. 723–739.

[180] Linda C. M. Gross et al. “Determining Membrane Capacitance by Dynamic Control of Droplet Interface Bilayer Area”. *Langmuir* 27.23 (2011), pp. 14335–14342.

[181] Vesselin Nikolov et al. “Electrical Measurements of Bilayer Membranes Formed by Langmuir-Blodgett Deposition on Single-Crystal Silicon”. *Langmuir* 23.26 (2007), pp. 13040–13045.

[182] H Rosenboom and M Lindau. “Exo-endocytosis and closing of the fission pore during endocytosis in single pituitary nerve terminals internally perfused with high calcium concentrations.” *Proceedings of the National Academy of Sciences of the United States of America* 91.12 (1994), pp. 5267–5271.

[183] C Solsona, B Innocenti, and J M Fernández. “Regulation of exocytotic fusion by cell inflation.” *Biophysical Journal* 74.2 Pt 1 (1998), pp. 1061–1073.

[184] S. Paula et al. “Permeation of protons, potassium ions, and small polar molecules through phospholipid bilayers as a function of membrane thickness”. *Biophysical Journal* 70.1 (1996), pp. 339–348.

[185] S. Paula, A. G. Volkov, and D. W. Deamer. “Permeation of Halide Anions through Phospholipid Bilayers Occurs by the Solubility-Diffusion Mechanism”. *Biophysical Journal* 74.1 (1998), pp. 319–327.

[186] Monika Naumowicz and Zbigniew A. Figaszewski. “Chronopotentiometric Investigation of the Influence of Cholesterol and Ionic Strength on Lipid Bilayer’s Physicochemical Properties”. *Journal of The Electrochemical Society* 160.3 (2013), H166–H172.

[187] Y Wu et al. “X-ray diffraction study of lipid bilayer membranes interacting with amphiphilic helical peptides: diphytanoyl phosphatidylcholine with alamethicin at low concentrations.” *Biophysical Journal* 68.6 (1995), pp. 2361–2369.

[188] M. F. Mouat and K. L. Manchester. “The intracellular ionic strength of red cells and the influence of complex formation”. *Comparative Haematology International* 8.1 (1998), pp. 58–60.

[189] Rainer A. Böckmann et al. “Effect of Sodium Chloride on a Lipid Bilayer”. *Biophysical Journal* 85.3 (2003), pp. 1647–1655.

[190] Suren Tatulian. “Ionization and Ion Binding”. *Phospholipids Handbook*. Ed. by Gregor Cevc. 1st Edition. New York: Marcel Dekker, 1993.

[191] T. Heimburg. “Lipid ion channels”. *Biophysical Chemistry* 150.1–3 (2010), pp. 2–22.

[192] Marta Pasenkiewicz-Gierula et al. “Computer modelling studies of the bilayer/water interface”. *Biochimica et Biophysica Acta (BBA) - Biomembranes* 1858.10 (2016), pp. 2305–2321.

[193] Andrey A. Gurtovenko and Ilpo Vattulainen. “Effect of NaCl and KCl on Phosphatidylcholine and Phosphatidylethanolamine Lipid Membranes: Insight from Atomic-Scale Simulations for Understanding Salt-Induced Effects in the Plasma Membrane”. *The Journal of Physical Chemistry B* 112.7 (2008), pp. 1953–1962.

[194] Robert Vácha et al. “Mechanism of Interaction of Monovalent Ions with Phosphatidylcholine Lipid Membranes”. *The Journal of Physical Chemistry B* 114.29 (2010), pp. 9504–9509.

[195] Anke Diederich, Günther Bähr, and Mathias Winterhalter. “Influence of surface charges on the rupture of black lipid membranes”. *Physical Review E* 58.4 (1998), pp. 4883–4889.

[196] Sergi Garcia-Manyes, Gerard Oncins, and Fausto Sanz. “Effect of Ion-Binding and Chemical Phospholipid Structure on the Nanomechanics of Lipid Bilayers Studied by Force Spectroscopy”. *Biophysical Journal* 89.3 (2005), pp. 1812–1826.

[197] Lea Rems et al. “Properties of lipid electropores II: Comparison of continuum-level modeling of pore conductance to molecular dynamics simulations”. *Bioelectrochemistry* 112 (2016), pp. 112–124.

[198] V. Sridhara and R. P. Joshi. "Evaluations of a mechanistic hypothesis for the influence of extracellular ions on electroporation due to high-intensity, nanosecond pulsing". *Biochimica et Biophysica Acta (BBA) - Biomembranes* 1838.7 (2014), pp. 1793–1800.

[199] Arnau Cordomí, Olle Edholm, and Juan J. Perez. "Effect of Force Field Parameters on Sodium and Potassium Ion Binding to Dipalmitoyl Phosphatidylcholine Bilayers". *Journal of Chemical Theory and Computation* 5.8 (2009), pp. 2125–2134.

[200] Max L. Berkowitz and Robert Vácha. "Aqueous Solutions at the Interface with Phospholipid Bilayers". *Accounts of Chemical Research* 45.1 (2012), pp. 74–82.

[201] S A Freeman, M A Wang, and J C Weaver. "Theory of electroporation of planar bilayer membranes: predictions of the aqueous area, change in capacitance, and pore-pore separation." *Biophysical Journal* 67.1 (1994), pp. 42–56.

[202] Victor Levadny, Vicente M Aguilella, and Marina Belaya. "Access resistance of a single conducting membrane channel". *Biochimica et Biophysica Acta (BBA) - Biomembranes* 1368.2 (1998), pp. 338–342.

[203] C Wilhelm et al. "Kinetics of pore size during irreversible electrical breakdown of lipid bilayer membranes." *Biophysical Journal* 64.1 (1993), pp. 121–128.

[204] Enrico P. Spugnini et al. "Ultrastructural modifications of cell membranes induced by "electroporation" on melanoma xenografts". *Microscopy Research and Technique* 70.12 (2007), pp. 1041–1050.

[205] Wanda Krassowska and Petar D. Filev. "Modeling Electroporation in a Single Cell". *Biophysical Journal* 92.2 (2007), pp. 404–417.

[206] Kyle C. Smith et al. "Emergence of a large pore subpopulation during electroporating pulses". *Bioelectrochemistry* 100 (2014), pp. 3–10.

[207] Edward W. Lee et al. "Electron Microscopic Demonstration and Evaluation of Irreversible Electroporation-Induced Nanopores on Hepatocyte Membranes". *ResearchGate* 23.1 (2011), pp. 107–13.

[208] S. Kennedy et al. "The role of plasmalemmal-cortical anchoring on the stability of transmembrane electropores". *IEEE Transactions on Dielectrics and Electrical Insulation* 16.5 (2009), pp. 1251–1258.

[209] David J. Stephens and Victoria J. Allan. "Light Microscopy Techniques for Live Cell Imaging". *Science* 300.5616 (2003), pp. 82–86.

[210] Vasilis Ntziachristos. "Going deeper than microscopy: the optical imaging frontier in biology". *Nature Methods* 7.8 (2010), pp. 603–614.

[211] Emily L. Chandler et al. "Membrane Surface Dynamics of DNA-Threaded Nanopores Revealed by Simultaneous Single-Molecule Optical and Ensemble Electrical Recording". *Langmuir* 20.3 (2004), pp. 898–905.

[212] Angelo Demuro and Ian Parker. "Optical single-channel recording: imaging Ca^{2+} flux through individual N-type voltage-gated channels expressed in Xenopus oocytes". *Cell Calcium* 34.6 (2003), pp. 499–509.

[213] Angelo Demuro and Ian Parker. "Imaging the Activity and Localization of Single Voltage-Gated Ca^{2+} Channels by Total Internal Reflection Fluorescence Microscopy". *Biophysical Journal* 86.5 (2004), pp. 3250–3259.

[214] Andrew J. Heron et al. “Simultaneous Measurement of Ionic Current and Fluorescence from Single Protein Pores”. *Journal of the American Chemical Society* 131.5 (2009), pp. 1652–1653.

[215] W. S. Boyle and G. E. Smith. “Charge Coupled Semiconductor Devices”. *Bell System Technical Journal* 49.4 (1970), pp. 587–593.

[216] James R. Janesick. *Scientific Charge-Coupled Devices*. 1st Edition. Washington: SPIE Press, 2001.

[217] Hui Zou et al. “Visualization of Ca^{2+} entry through single stretch-activated cation channels”. *Proceedings of the National Academy of Sciences* 99.9 (2002), pp. 6404–6409.

[218] Johannes Schindelin et al. “Fiji: an open-source platform for biological-image analysis”. *Nature Methods* 9.7 (2012), pp. 676–682.

[219] Eliseo Amado G and Luis H. Blanco. “Osmotic and activity coefficients of aqueous solutions of KCl at temperatures of 283.15, 288.15, 293.15 and 298.15 K”. *Fluid Phase Equilibria* 226 (2004), pp. 261–265.

[220] Joseph A. Rard, Anton Habenschuss, and Frank H. Spedding. “A review of the osmotic coefficients of aqueous calcium chloride at 25 °C”. *Journal of Chemical & Engineering Data* 22.2 (1977), pp. 180–186.

[221] Adéla Melcrová et al. “The complex nature of calcium cation interactions with phospholipid bilayers”. *Scientific Reports* 6 (2016), srep38035.

[222] H. Gögelein and H. Koepsell. “Channels in planar bilayers made from commercially available lipids”. *Pflügers Archiv* 401.4 (1984), pp. 433–434.

[223] V. F. Antonov et al. “Capacitive and ionic currents in BLM from phosphatidic acid in Ca^{2+}-induced phase transition”. *Biochemical and Biophysical Research Communications* 133.3 (1985), pp. 1098–1103.

[224] M. Djabourov et al. “Small-angle x-ray scattering characterization of agarose sols and gels”. *Macromolecules* 22.1 (1989), pp. 180–188.

[225] Nadine Pernodet, Mounir Maaloum, and Bernard Tinland. “Pore size of agarose gels by atomic force microscopy”. *Electrophoresis* 18.1 (1997), pp. 55–58.

[226] H Qian, M P Sheetz, and E L Elson. “Single particle tracking. Analysis of diffusion and flow in two-dimensional systems.” *Biophysical Journal* 60.4 (1991), pp. 910–921.

[227] Lydia M. Harriss et al. “Imaging Multiple Conductance States in an Alamethicin Pore”. *Journal of the American Chemical Society* 133.37 (2011), pp. 14507–14509.

[228] John C. Neu, Kyle C. Smith, and Wanda Krassowska. “Electrical energy required to form large conducting pores”. *Bioelectrochemistry (Amsterdam, Netherlands)* 60.1-2 (2003), pp. 107–114.

[229] M. Kandušer, M. Šentjurc, and D. Miklavčič. “The temperature effect during pulse application on cell membrane fluidity and permeabilization”. *Bioelectrochemistry* 74.1 (2008), pp. 52–57.

[230] Andreas Blicher et al. “The Temperature Dependence of Lipid Membrane Permeability, its Quantized Nature, and the Influence of Anesthetics”. *Biophysical Journal* 96.11 (2009), pp. 4581–4591.

[231] Aljaž Velikonja et al. “Specific electrical capacitance and voltage breakdown as a function of temperature for different planar lipid bilayers”. *Bioelectrochemistry* 112 (2016), pp. 132–137.

[232] Andrey Filippov, Greger Orädd, and Göran Lindblom. “Lipid Lateral Diffusion in Ordered and Disordered Phases in Raft Mixtures”. *Biophysical Journal* 86.2 (2004), pp. 891–896.

[233] Göran Lindblom, Greger Orädd, and Andrey Filippov. “Lipid lateral diffusion in bilayers with phosphatidylcholine, sphingomyelin and cholesterol: An NMR study of dynamics and lateral phase separation”. *Chemistry and Physics of Lipids* 141.1–2 (2006), pp. 179–184.

[234] Ramon Reigada. “Electroporation of heterogeneous lipid membranes”. *Biochimica et Biophysica Acta (BBA) - Biomembranes* 1838.3 (2014), pp. 814–821.

[235] Irep Gözen et al. “Fractal avalanche ruptures in biological membranes”. *Nature Materials* 9.11 (2010), pp. 908–912.

[236] Jacob N. Israelachvili. *Intermolecular and Surface Forces*. 3rd. Massachusetts: Elsevier Academic Press, 2011.

[237] Langzhou Song et al. “Structure of Staphylococcal α-Hemolysin, a Heptameric Transmembrane Pore”. *Science* 274.5294 (1996), pp. 1859–1866.

[238] J. A. Högbom. “Aperture Synthesis with a Non-Regular Distribution of Interferometer Baselines”. *Astronomy and Astrophysics Supplement Series* 15 (1974), p. 417.

[239] Bríd Cronin, Ben de Wet, and Mark I. Wallace. “Lucky Imaging: Improved Localization Accuracy for Single Molecule Imaging”. *Biophysical Journal* 96.7 (2009), pp. 2912–2917.

[240] Hui Zou et al. “Using Total Fluorescence Increase (Signal Mass) to Determine the Ca^{2+} Current Underlying Localized Ca^{2+} Events”. *The Journal of General Physiology* 124.3 (2004), pp. 259–272.

[241] Peigang Deng, Yi-Kuen Lee, and Tong-Yi Zhang. “A nonlinear electromechanical coupling model for electropore expansion in cell electroporation”. *Journal of Physics D: Applied Physics* 47.44 (2014), p. 445401.

[242] K. C. Melikov et al. “Voltage-induced nonconductive pre-pores and metastable single pores in unmodified planar lipid bilayer”. *Biophysical Journal* 80.4 (2001), pp. 1829–1836.

[243] Shihu Wang and Ronald G. Larson. “Water channel formation and ion transport in linear and branched lipid bilayers”. 16.16 (2014), pp. 7251–7262.

[244] Andraž Polak et al. “Electroporation of archaeal lipid membranes using MD simulations”. *Bioelectrochemistry* 100 (2014), pp. 18–26.

[245] Amit Kumar Majhi et al. “Estimation of activation energy for electroporation and pore growth rate in liquid crystalline and gel phases of lipid bilayers using molecular dynamics simulations”. *Soft Matter* 11.44 (2015), pp. 8632–8640.

[246] Evan Evans and Erich Sackmann. “Translational and rotational drag coefficients for a disk moving in a liquid membrane associated with a rigid substrate”. *Journal of Fluid Mechanics* 194 (1988), pp. 553–561.

[247] Jianwei Shuai and Ian Parker. "Optical single-channel recording by imaging Ca^{2+} flux through individual ion channels: theoretical considerations and limits to resolution". *Cell Calcium* 37.4 (2005), pp. 283–299.

[248] David S. Goodsell. "Inside a living cell". *Trends in Biochemical Sciences* 16 (1991), pp. 203–206.

[249] Alessandro Tossi, Luca Sandri, and Anna Giangaspero. "Amphipathic, α-helical antimicrobial peptides". *Peptide Science* 55.1 (2000), pp. 4–30.

[250] Michael Zasloff. "Antimicrobial peptides of multicellular organisms". *Nature* 415.6870 (2002), pp. 389–395.

[251] J. M. Ageitos et al. "Antimicrobial peptides (AMPs): Ancient compounds that represent novel weapons in the fight against bacteria". *Biochemical Pharmacology* 133 (2017), pp. 117–138.

[252] Robert EW Hancock. "Cationic peptides: effectors in innate immunity and novel antimicrobials". *The Lancet Infectious Diseases* 1.3 (2001), pp. 156–164.

[253] Miguel Moreno and Ernest Giralt. "Three Valuable Peptides from Bee and Wasp Venoms for Therapeutic and Biotechnological Use: Melittin, Apamin and Mastoparan". *Toxins* 7.4 (2015), pp. 1126–1150.

[254] Jeffrey R. Brender, Austin J. McHenry, and Ayyalusamy Ramamoorthy. "Does Cholesterol Play a Role in the Bacterial Selectivity of Antimicrobial Peptides?" *Frontiers in Immunology* 3 (2012).

[255] Balazs Leitgeb et al. "The History of Alamethicin: A Review of the Most Extensively Studied Peptaibol". *Chemistry & Biodiversity* 4.6 (2007), pp. 1027–1051.

[256] Alexandra K Marr, William J Gooderham, and Robert EW Hancock. "Antibacterial peptides for therapeutic use: obstacles and realistic outlook". *Current Opinion in Pharmacology* 6.5 (2006), pp. 468–472.

[257] Christopher N. LaRock and Victor Nizet. "Cationic antimicrobial peptide resistance mechanisms of streptococcal pathogens". *Biochimica et Biophysica Acta (BBA) - Biomembranes* 1848.11 (2015), pp. 3047–3054.

[258] Guangshun Wang. "Human Antimicrobial Peptides and Proteins". *Pharmaceuticals* 7.5 (2014), pp. 545–594.

[259] Eileen M. Hotze and Rodney K. Tweten. "Membrane assembly of the cholesterol-dependent cytolysin pore complex". *Biochimica et Biophysica Acta (BBA) - Biomembranes* 1818.4 (2012), pp. 1028–1038.

[260] Stefanie Verherstraeten et al. "Perfringolysin O: The Underrated Clostridium perfringens Toxin?" *Toxins* 7.5 (2015), pp. 1702–1721.

[261] Paulina D. Rakowska et al. "Nanoscale imaging reveals laterally expanding antimicrobial pores in lipid bilayers". *Proceedings of the National Academy of Sciences* 110.22 (2013), pp. 8918–8923.

[262] Ying Li et al. "Single-molecule visualization of dynamic transitions of pore-forming peptides among multiple transmembrane positions". *Nature Communications* 7.1 (2016), p. 12906.

[263] C. E. Meyer and F. Reusser. “A polypeptide antibacterial agent isolated fromTrichoderma viride”. *Experientia* 23.2 (1967), pp. 85–86.

[264] Robert O. Fox and Frederic M. Richards. “A voltage-gated ion channel model inferred from the crystal structure of alamethicin at 1.5-Å resolution”. *Nature* 300.5890 (1982), pp. 325–330.

[265] Jochen Kirschbaum et al. “Sequences of alamethicins F30 and F50 reconsidered and reconciled”. *Journal of Peptide Science* 9.11-12 (2003), pp. 799–809.

[266] Garland R. Marshall et al. “Factors Governing Helical Preference of Peptides Containing Multiple α,α-Dialkyl Amino Acid”. *Proceedings of the National Academy of Sciences of the United States of America* 87.1 (1990), pp. 487–491.

[267] Isabella L. Karle and Padmanabhan Balaram. “Structural characteristics of α-helical peptide molecules containing Aib residues”. *Biochemistry* 29.29 (1990), pp. 6747–6756.

[268] Tim Salditt, Chenghao Li, and Alexander Spaar. “Structure of antimicrobial peptides and lipid membranes probed by interface-sensitive X-ray scattering”. *Biochimica et Biophysica Acta (BBA) - Biomembranes* 1758.9 (2006), pp. 1483–1498.

[269] K He et al. “Mechanism of alamethicin insertion into lipid bilayers.” *Biophysical Journal* 71.5 (1996), pp. 2669–2679.

[270] Fang-Yu Chen, Ming-Tao Lee, and Huey W. Huang. “Sigmoidal Concentration Dependence of Antimicrobial Peptide Activities: A Case Study on Alamethicin”. *Biophysical Journal* 82.2 (2002), pp. 908–914.

[271] Alexander Spaar, Christian Munster, and Tim Salditt. “Conformation of Peptides in Lipid Membranes Studied by X-Ray Grazing Incidence Scattering”. *Biophysical Journal* 87.1 (2004), pp. 396–407.

[272] M. S. P. Sansom. “Structure and function of channel-forming peptaibols”. *Quarterly Reviews of Biophysics* 26.4 (1993), pp. 365–421.

[273] Ke He et al. “Antimicrobial Peptide Pores in Membranes Detected by Neutron In-Plane Scattering”. *Biochemistry* 34.48 (1995), pp. 15614–15618.

[274] L. G. M. Gordon and D. A. Haydon. “The unit conductance channel of alamethicin”. *Biochimica et Biophysica Acta (BBA) - Biomembranes* 255.3 (1972), pp. 1014–1018.

[275] Günther Boheim. “Statistical analysis of alamethicin channels in black lipid membranes”. *The Journal of Membrane Biology* 19.1 (1974), pp. 277–303.

[276] Markus Sondermann et al. “High-resolution electrophysiology on a chip: Transient dynamics of alamethicin channel formation”. *Biochimica et Biophysica Acta (BBA) - Biomembranes* 1758.4 (2006), pp. 545–551.

[277] Katsumi Matsuzaki et al. “Interactions of an antimicrobial peptide, magainin 2, with outer and inner membranes of Gram-negative bacteria”. *Biochimica et Biophysica Acta (BBA) - Biomembranes* 1327.1 (1997), pp. 119–130.

[278] Robert W. Williams et al. “Raman spectroscopy of synthetic antimicrobial frog peptides magainin 2a and PGLa”. *Biochemistry* 29.18 (1990), pp. 4490–4496.

[279] Katsumi Matsuzaki et al. “Physicochemical determinants for the interactions of magainins 1 and 2 with acidic lipid bilayers”. *Biochimica et Biophysica Acta (BBA) - Biomembranes* 1063.1 (1991), pp. 162–170.

[280] B. Bechinger, M. Zasloff, and S. J. Opella. “Structure and orientation of the antibiotic peptide magainin in membranes by solid-state nuclear magnetic resonance spectroscopy.” *Protein Science : A Publication of the Protein Society* 2.12 (1993), pp. 2077–2084.

[281] B. Bechinger et al. “Orientations of helical peptides in membrane bilayers by solid state NMR spectroscopy”. *Solid State Nuclear Magnetic Resonance* 7.3 (1996), pp. 185–191.

[282] Steve J. Ludtke et al. “Membrane Pores Induced by Magainin”. *Biochemistry* 35.43 (1996), pp. 13723–13728.

[283] Chul Kim et al. “Evidence of pores and thinned lipid bilayers induced in oriented lipid membranes interacting with the antimicrobial peptides, magainin-2 and aurein-3.3”. *Biochimica et Biophysica Acta (BBA) - Biomembranes* 1788.7 (2009), pp. 1482–1496.

[284] Khoi Tan Nguyen et al. “Molecular Interactions between Magainin 2 and Model Membranes in Situ”. *The Journal of Physical Chemistry B* 113.36 (2009), pp. 12358–12363.

[285] Davor Juretic et al. “Magainin Oligomers Reversibly Dissipate $\Delta\mu_{H^+}$ in Cytochrome Oxidase Liposomes”. *Biochemistry* 33.15 (1994), pp. 4562–4570.

[286] Katsumi Matsuzaki et al. “Molecular Basis for Membrane Selectivity of an Antimicrobial Peptide, Magainin 2”. *Biochemistry* 34.10 (1995), pp. 3423–3429.

[287] Katsumi Matsuzaki et al. “An Antimicrobial Peptide, Magainin 2, Induced Rapid Flip-Flop of Phospholipids Coupled with Pore Formation and Peptide Translocation”. *Biochemistry* 35.35 (1996), pp. 11361–11368.

[288] Christopher E. Dempsey. “The actions of melittin on membranes”. *Biochimica et Biophysica Acta (BBA) - Reviews on Biomembranes* 1031.2 (1990), pp. 143–161.

[289] J.C. Talbot et al. “Conformational change and self association of monomeric melittin”. *FEBS Letters* 102.1 (1979), pp. 191–193.

[290] Jurgen Lauterwein, Larry R. Brown, and Kurt Wuthrich. “High-resolution 1H-NMR studies of monomeric melittin in aqueous solution”. *Biochimica et Biophysica Acta (BBA) - Protein Structure* 622.2 (1980), pp. 219–230.

[291] T. C. Terwilliger and D. Eisenberg. “The structure of melittin. II. Interpretation of the structure.” *Journal of Biological Chemistry* 257.11 (1982), pp. 6016–6022.

[292] T C Terwilliger, L Weissman, and D Eisenberg. “The structure of melittin in the form I crystals and its implication for melittin’s lytic and surface activities.” *Biophysical Journal* 37.1 (1982), pp. 353–361.

[293] Fuyuhiko Inagaki et al. “Structure of melittin bound to perdeuterated dodecylphosphocholine micelles as studied by two-dimensional NMR and distance geometry calculations”. *Biochemistry* 28.14 (1989), pp. 5985–5991.

[294] Horst Vogel. “Incorporation of Melittin into phosphatidylcholine bilayers”. *FEBS Letters* 134.1 (1981), pp. 37–42.

[295] H Vogel and F Jahnig. “The structure of melittin in membranes.” *Biophysical Journal* 50.4 (1986), pp. 573–582.

[296] B. Stanislawski and H. Rüterjans. “^{13}C-NMR Investigation of the insertion of the bee venom melittin into lecithin vesicles”. *European Biophysics Journal* 15.1 (1987), pp. 1–12.

[297] S. Frey and L. K. Tamm. “Orientation of melittin in phospholipid bilayers. A polarized attenuated total reflection infrared study”. *Biophysical Journal* 60.4 (1991), pp. 922–930.

[298] C Altenbach et al. “Conformation of spin-labeled melittin at membrane surfaces investigated by pulse saturation recovery and continuous wave power saturation electron paramagnetic resonance.” *Biophysical Journal* 56.6 (1989), pp. 1183–1191.

[299] Christopher E. Dempsey and Georgina S. Butler. “Helical structure and orientation of melittin in dispersed phospholipid membranes from amide exchange analysis in situ”. *Biochemistry* 31.48 (1992), pp. 11973–11977.

[300] L Yang et al. “Barrel-stave model or toroidal model? A case study on melittin pores.” *Biophysical Journal* 81.3 (2001), pp. 1475–1485.

[301] Durgesh K. Rai, Shuo Qian, and William T. Heller. “The Interaction of Melittin with Dimyristoyl Phosphatidylcholine-Dimyristoyl Phosphatidylserine Lipid Bilayer Membranes”. *Biochimica et Biophysica Acta (BBA) - Biomembranes* 1858.11 (2016), pp. 2788–2794.

[302] M T Tosteson and D C Tosteson. “The sting. Melittin forms channels in lipid bilayers.” *Biophysical Journal* 36.1 (1981), pp. 109–116.

[303] C. Kempf et al. “Voltage-dependent trans-bilayer orientation of melittin.” *Journal of Biological Chemistry* 257.5 (1982), pp. 2469–2476.

[304] Wolfgang Hanke et al. “Melittin and a chemically modified trichotoxin form alamethicin-type multi-state pores”. *Biochimica et Biophysica Acta (BBA) - Biomembranes* 727.1 (1983), pp. 108–114.

[305] K Matsuzaki, S Yoneyama, and K Miyajima. “Pore formation and translocation of melittin.” *Biophysical Journal* 73.2 (1997), pp. 831–838.

[306] Daniel Allende, S. A. Simon, and Thomas J. McIntosh. “Melittin-Induced Bilayer Leakage Depends on Lipid Material Properties: Evidence for Toroidal Pores”. *Biophysical Journal* 88.3 (2005), pp. 1828–1837.

[307] W F DeGrado et al. “Kinetics and mechanism of hemolysis induced by melittin and by a synthetic melittin analogue.” *Biophysical Journal* 37.1 (1982), pp. 329–338.

[308] A. M. Batenburg, J. H. Van Esch, and B. De Kruijff. “Melittin-induced changes of the macroscopic structure of phosphatidylethanolamines”. *Biochemistry* 27.7 (1988), pp. 2324–2331.

[309] M. Monette and M. Lafleur. “Modulation of melittin-induced lysis by surface charge density of membranes”. *Biophysical Journal* 68.1 (1995), pp. 187–195.

[310] Dirk K. Hincha and John H. Crowe. “The lytic activity of the bee venom peptide melittin is strongly reduced by the presence of negatively charged phospholipids or chloroplast galactolipids in the membranes of phosphatidylcholine large unilamellar vesicles”. *Biochimica et Biophysica Acta (BBA) - Biomembranes* 1284.2 (1996), pp. 162–170.

[311] Alexey S Ladokhin and Stephen H White. “‘Detergent-like’ permeabilization of anionic lipid vesicles by melittin”. *Biochimica et Biophysica Acta (BBA) - Biomembranes* 1514.2 (2001), pp. 253–260.

[312] Geert van den Bogaart et al. “The Lipid Dependence of Melittin Action Investigated by Dual-Color Fluorescence Burst Analysis”. *Biophysical Journal* 93.1 (2007), pp. 154–163.

[313] Joanna Juhaniewicz and Slawomir Sek. “Interaction of Melittin with Negatively Charged Lipid Bilayers Supported on Gold Electrodes”. *Electrochimica Acta* 197 (2016), pp. 336–343.

[314] Jianjun Pan and Nawal K. Khadka. “Kinetic Defects Induced by Melittin in Model Lipid Membranes: A Solution Atomic Force Microscopy Study”. *The Journal of Physical Chemistry B* 120.20 (2016), pp. 4625–4634.

[315] H. Raghuraman and Amitabha Chattopadhyay. “Melittin: a Membrane-active Peptide with Diverse Functions”. *Bioscience Reports* 27.4-5 (2007), pp. 189–223.

[316] M. E. Selsted et al. “Indolicidin, a novel bactericidal tridecapeptide amide from neutrophils.” *Journal of Biological Chemistry* 267.7 (1992), pp. 4292–4295.

[317] C. Subbalakshmi et al. “Requirements for antibacterial and hemolytic activities in the bovine neutrophil derived 13-residue peptide indolicidin”. *FEBS Letters* 395.1 (1996), pp. 48–52.

[318] Timothy J. Falla, D. Nedra Karunaratne, and Robert E. W. Hancock. “Mode of Action of the Antimicrobial Peptide Indolicidin”. *Journal of Biological Chemistry* 271.32 (1996), pp. 19298–19303.

[319] Renato Gennaro and Margherita Zanetti. “Structural features and biological activities of the cathelicidin-derived antimicrobial peptides”. *Peptide Science* 55.1 (2000), pp. 31–49.

[320] Alexey S. Ladokhin, Michael E. Selsted, and Stephen H. White. “Bilayer Interactions of Indolicidin, a Small Antimicrobial Peptide Rich in Tryptophan, Proline, and Basic Amino Acids”. *Biophysical Journal* 72.2 Pt 1 (1997), pp. 794–805.

[321] Annett Rozek, Carol L. Friedrich, and Robert E. W. Hancock. “Structure of the Bovine Antimicrobial Peptide Indolicidin Bound to Dodecylphosphocholine and Sodium Dodecyl Sulfate Micelles,” *Biochemistry* 39.51 (2000), pp. 15765–15774.

[322] Tatyana I. Rokitskaya et al. “Indolicidin action on membrane permeability: Carrier mechanism versus pore formation”. *Biochimica et Biophysica Acta (BBA) - Biomembranes* 1808.1 (2011), pp. 91–97.

[323] H Zhao et al. “Comparison of the membrane association of two antimicrobial peptides, magainin 2 and indolicidin.” *Biophysical Journal* 81.5 (2001), pp. 2979–2991.

[324] Manhong Wu et al. “Mechanism of Interaction of Different Classes of Cationic Antimicrobial Peptides with Planar Bilayers and with the Cytoplasmic Membrane of Escherichia coli”. *Biochemistry* 38.22 (1999), pp. 7235–7242.

[325] Chilukuri Subbalakshmi and Narasimhaiah Sitaram. “Mechanism of antimicrobial action of indolicidin”. *FEMS Microbiology Letters* 160.1 (1998), pp. 91–96.

[326] O Helluin et al. “Lateral diffusion and conductance properties of a fluorescein-labelled alamethicin in planar lipid bilayers”. *Biochimica et Biophysica Acta (BBA) - Biomembranes* 1330.2 (1997), pp. 284–292.

[327] Michael J. Saxton and Ken Jacobson. “Single-Particle Tracking: Applications to Membrane Dynamics”. *Annual Review of Biophysics and Biomolecular Structure* 26.1 (1997), pp. 373–399.

[328] Nicholas B Last, Diana E Schlamadinger, and Andrew D Miranker. “A common landscape for membrane-active peptides”. *Protein Science : A Publication of the Protein Society* 22.7 (2013), pp. 870–882.

[329] P.-H. Puech et al. “Line Thermodynamics: Adsorption at a Membrane Edge”. *Physical Review Letters* 90.12 (2003). Publisher: American Physical Society, p. 128304.

[330] Ming-Tao Lee et al. “Mechanism and kinetics of pore formation in membranes by water-soluble amphipathic peptides”. *Proceedings of the National Academy of Sciences of the United States of America* 105.13 (2008), pp. 5087–5092.

[331] Ronald J Clarke. “The dipole potential of phospholipid membranes and methods for its detection”. *Advances in Colloid and Interface Science* 89-90 (2001), pp. 263–281.

[332] James R. Thompson et al. “Rapid Assembly of a Multimeric Membrane Protein Pore”. *Biophysical Journal* 101.11 (2011), pp. 2679–2683.